Collège Doctoral Languedoc-Roussillon

THÈSE

Pour obtenir le grade de

Docteur

Délivré par

UNIVERSITE DE PERPIGNAN VIA DOMITIA

Préparée au sein de l'école doctorale **305**:

Energie et Environnement

Et de l'unité de recherche

PROMES - CNRS UPR 8521

Spécialité: Sciences pour l'ingénieur

Présentée par Alexandro Joseph Carling Plaza

Vieillissement accéléré et durabilité de matériaux sélectifs pour récepteurs de centrales solaires à concentration

Soutenue le 14 décembre 2021 devant le jury composé de :

Y. Jourlin	Professeur, IUT Saint-Étienne	Rapporteur
Y. Le Maoult	Professeur, IMT Mines Albi	Rapporteur
E. Tomasella	Professeur, U. Clermont-Auvergne	Président
L. Maillé	Maître de conférences, U. Bordeaux I	Examinatrice
B. Claudet	Professeur, Université Perpignan Via Domitia	Examinateur
L. Thomas	Professeur, Université Perpignan Via Domitia	Directeur de thèse
A. Soum-Glaude	Ingénieure de recherche, PROMES-CNRS	Co-directrice

UNIVERSITÉ PERPIGNAN VIA DOMITIA

Acknowledgements

I would like to start this manuscript by thanking all the people who have made it possible for me and have been part of this work. First of all, I would like to thank the members of the jury, the reviewers, Yves Jourlin and Yannick Le Maoult, for their time in correcting my manuscript and for the comments received, in addition to their presence at the defense. Eric Tomasella for agreeing to preside over the jury and for his follow-up during my thesis, as well as Laurence Maillé and Bernard Claudet, for all the support and advice received. I appreciate all the organization and preparation carried out that has made this process more agreeable and enjoyable. I feel honored to have had this jury supporting my work, valuing and enriching the research.

This work arose from European funding from the Occitanie region (FEDER Vadum-CSP), in which I was part of several national projects (ANR ASTORIX, CARAPASS, NANOPLAST), international collaborations (CEFIPRA) and international conferences (SolarPACES). Of course, this work would not have been possible without the supervisory work of Laurent Thomas and Audrey Soum-Glaude. I have always felt very fortunate to have had this opportunity, thanks for the trust they placed in me from the very beginning. Laurent for his forward vision and for giving me motivation and confidence with his good advice, despite the distance that sometimes hampered communication. Audrey, despite the problems encountered, has always been able to see the solution, supporting me and guiding me in the best direction. I am very grateful for having shared long talks and having had your understanding during this process. And to teach me to be patient and trust in the process of research work, something which I have not always found easy. In addition to having given me the strength to make decisions and use the best criteria to guide my work.

Within the small team, Selecteam, I would like to thank Danielle Ngoue, for her good advice and her good communication from a distance, always with her nicest smile. Thanks as well to Aissatou Diop for her availability and her help with the characterization. Also, to Jose Osorio for his help during his stay, for his technical vision and fellowship inside and outside of work, I feel very grateful for everything shared. In addition, within our international collaboration, to our interns, Theo Grifo and Martin Bordas, for their work and dedication, and also to K. Niranjan, for all the information and shared work.

I want to add my thanks to the PROMES-Perpignan Raiselife team, to Reine Reoyo-Prats for her availability at all times, it has been a blessing to have shared the experiment and have had her advice and vision. Also, to Bernard Claudet and Olivier Faugeroux for the recommendations when applying aging protocols. And to Harold Thibault for the help in the technical part at the beginning of my work, which was of great help for the continuation of the experiments. Also, to Roger Garcia for having been able to count on his work in the elaboration of the final support for our experiment.

Within the work carried out in my research, I would like to thank the materials team, especially the active participation of Christophe Escape for the optical characterization of my samples, in addition to his availability at all times to help me and prioritize my tasks. As well as Yonko Gorand for his work on SEM/EDS analysis of samples. Also, to the entire department of solar installations of Odeillo that made possible the proper functioning of solar experiments, a fundamental part of this research. Starting with Emmanuel Guillot, thanks to him for the great knowledge he provided in every detail of the facilities and his availability at all times. And for his help to be part of the SFERA-III program, through collaboration and training. Nicolas Boullet for his help in improving the experimental facility and for the advice about its proper functioning. Régis Rodríguez and Michaël Tessonneaud for the maintenance of the facilities and their quick response when there was a problem. To Marc Garrabos for his training and availability. Jean Louis-Sans for his ideas on future app configurations and for

sharing his work. I would also like to thank Quentin Falcoz for his work, he was the first person I met in the laboratory and he also gave me the opportunity to give practical classes to students. To Laurent Lestrade and Georges Pichelin for their IT support and to Christelle Ferriere, Aurore Thiery and Samia Atmani for organization and help in Odeillo, as well as to Romie Lopez and Naoual Autones in Perpignan.

I would also like to say thanks for everything I shared with the doctoral students, for the camaraderie and the good times during my stay. To Inma and Hadrien in my beginnings, with the first rando ski climbs, and the good dinners that made me feel at home. Also, to Anita for always being there from the beginning, helping me in everything and supporting me when necessary, in addition to all the good climbing trips and moments on the rock. Thanks for the infinite smile of my great friend Srirat, always there for a good time of laughter. Also, to the girls, Segolène, Charlène and Dounia, for the good holidays and their pleasant presence. Thanks to Timothée for his good support and consistent availability. I would like to thank Gabi for his companionship, one of the best people I have met inside and outside the laboratory. Also thank my office colleagues, Joya, Paul, Zu and Freddy.

How not to thank the care received from the laboratory cooks, both Didier and Jean-Pascal, thank you for your work that makes our day in the laboratory so much more enjoyable and special with your delicious food. I would like to give a special dedication inside the laboratory to Sylvie, for her presence, kindness, sympathy and interest, for being there with your best smile and taking care of Kelly. We will both miss you.

I want to thank all my friends who have supported me during this process, thanks for being there, through your messages, calls and those of you who have been able to come to the high mountains to visit me and get to know the center, you have been the best of this time and you will always have a friend to count on. Especially Guille, Olga, Arrate, Adrian, Hector, Manu, Alex, Triana, Cristina, Anton, Tiesto, Nuria, Andy, Deme, Ruben, Emily, Michael, Maitane...

Well, and this is when I open my arms and my heart to thank my family for their unconditional support, from the first day I decided to start this adventure until the last. There are no words to say thanks for everything I have received, you have made me feel your love at all times despite the more than a thousand kilometers that separated us. Thank you, mother, for always seeing the light of everything, thank you Sara for being the sun that never stops shining and thank you Eli for your love and everything you teach me. To my dear uncles, Sue, John, Paqui and Antonio. And I would like to dedicate this work to my father, Brian, for having followed my work from the beginning, giving me the best advice and helping me with proofreading in English. And especially for being the person who instilled in me the scientific vision and infinite curiosity, since I was little, you taught me to put things into practice and be rigorous at work, without forgetting to enjoy every moment. And I end by thanking our dear Uncle Derek for having filled our lives with happiness and joy with his optimism and good music.

Table of contents

General introduction

High carbon emissions in the atmosphere, causing climate change, are notably caused by the combustion of fossil fuels, to produce energy for a growing world population. An increase of renewable energy sources into the energy mix is one of the envisaged responses to this climate and energy crisis. Among renewable technologies, solar energy technologies have a significant role to play to reduce the consumption of fossil fuels while meeting the worldwide energy demand. Indeed, the incoming solar energy on Earth amounts to 437,850 TWh annually, four times the annual global energy consumption of 111,756 TWh. Moreover, increased investment in renewable technologies has led to a fall in the levelized cost of electricity (LCOE) from these technologies, making them economically competitive with fossil fuels. For instance, electricity produced from solar energy is now often cheaper than electricity produced from fossil fuels.

Solar energy technologies comprise Photovoltaics (PV) technologies for direct electricity production, and Solar Thermal (ST) technologies which convert solar energy into heat. This heat can be used to produce domestic hot water and heating, and in many industrial processes where heat is required, in place of consuming electricity to produce heat. When concentrating the incoming solar energy using highly reflective materials as mirrors, the increased amount of heat extracted can be further converted into electricity. This is the principle used in Concentrated Solar Power (CSP) plants, where the incoming solar irradiance can be multiplied up to the level of several hundreds of suns. This concentrated solar energy is sent to a solar receiver that converts it into heat and transfers the latter to a heat transfer fluid (HTF), to be used in a thermodynamic cycle and produce electricity. One of the main advantages of CSP compared to PV is the possibility to easily store the extracted heat before its conversion into electricity, thus allowing for an adjustment of the electricity production to the demands of the electricity market, without suffering from the solar intermittence.

In most cases, solar receivers are made of pipes or flat panels of metallic alloys (e.g. stainless steels or nickel-based high temperature alloys) below which the HTF flows to extract the produced heat. Such materials have desirably high mechanical properties and thermal conductivity. However, their partly reflective intrinsic properties are not suitable for solar absorption. Therefore, their surface can be covered with coatings presenting high solar absorptance in the solar region (0.28 – 2.5 µm), such as black paints. Ideally, these coatings should also have a low thermal emittance in the infrared region (typically above 2 µm), to limit radiative thermal losses and increase their solar-to-heat conversion efficiency. Such functional coatings are called solar selective absorber coatings (SSACs), as they present a spectral selectivity.

In CSP technologies, solar absorber components suffer harsh working conditions for long durations, typically 25 years: high concentrated solar irradiation (30 to 1000 suns), significant temperature levels and temperature variations (several hundreds of °C in seconds/minutes), air, water vapor, pollutants, aerosols, depending on the location and proximity to the sea. Moreover, to make these technologies more economically viable implies the further increase of the working temperature of CSP plants. These working conditions are very demanding for solar absorber materials, especially for coatings. They represent potentially damaging sources of degradation, that may cause their premature aging and degrade the overall efficiency of the plant. The maintenance of the receiver represents a high cost that can be significantly reduced using a highly stable absorber surface, able to maintain its optical performance for long durations.

Therefore, before they can be used in CSP plants, the behavior of solar selective absorber coatings under these harsh working conditions needs to be studied thoroughly to validate their performance and durability. Aging protocols and facilities can be found in the literature for the study of the aging behavior of SSACs. However, these aging procedures need to be further analyzed, adapted and standardized, to offer more reliable and more comparable aging and durability assessment, with the objective that standardized aging procedures can eventually be used as a tool for coating developers to compare the performance of their materials, and for the overall improvement of SSAC technologies.

In this context, this work proposes a critical and extensive literature review of existing aging protocols, aging facilities and aging phenomena used for the study of SSACs, further supported by the experimental application of classical aging protocols (purely thermal aging) and original aging protocols under solar concentration (solar aging), on three different types of SSACs, using two original experimental set-ups that enable to partly decorrelate the effect of the different sources of degradation representative of CSP applications.

To present the work, this manuscript is divided into five chapters. The first chapter demonstrates the principles of concentrated solar energy and its current deployment in the electricity production market. The different technologies of CSP plants and solar receivers are explained. The optical and thermal behavior of solar absorbers are described, considering solar absorptance, thermal emittance and the principle of solar spectral selectivity. The chapter continues with a description of the different types of solar selective absorber coatings and the current research state on each type of absorber, ending with current commercial absorbers used for medium-temperature CSP plants.

The second chapter starts by describing the expected improvements in the next generation of CSP technologies, considering the two most relevant improvements related to the receiver, the increase of the working temperature and the capability of working in atmospheric conditions for long durations. The rest of this chapter is based on an analysis of the scientific literature. From this analysis, the main sources of degradation are identified and described considering the potential impact on CSP receivers, and subsequent aging mechanisms are explained in details. Existing aging procedures, methodologies and tools for failure analysis, that can be applied to SSACs, are then presented and commented. A global scheme linking these different aspects is finally proposed in the conclusions of this chapter.

The following chapters are centered on the experimental application of some of these existing aging protocols, as well as more original ones, on three typical SSACs, with the purpose of evaluating the pertinence of said aging protocols and draw general tendencies regarding the aging behavior of SSACs.

The third chapter presents the materials, facilities and methodologies used for this complementary experimental study. The chapter starts by presenting the three types of SSACs that were tested, looking at their constitutive materials, absorber architecture and manufacturing process in each case. Then are presented the characterization techniques and equipment used to assess the coatings properties, in terms of their optical behavior and microstructure, before and after aging tests. Finally, the global aging methodology and the aging tools used in this study are presented, with detailed descriptions of the experimental set-ups.

The fourth chapter first exposes an analysis of the equivalence of the different samples of each type of absorber in their as-deposited state. Indeed, the equivalence between samples of the same type is essential for a suitable comparability of aging results when applying different protocols. Then a study on purely thermal aging protocols in an electrical furnace begins with the application of aging tests at a typical CSP working temperature, first for short duration tests, as the first step applied to each

absorber, followed by long duration tests as a way of checking the thermal stability under more representative CSP working conditions. Accelerated aging at higher temperatures is then applied to the absorbers with good thermal stability at working temperature. The influence of other aging parameters such as thermal cycling and aging atmosphere are also studied. Correlations between tests in representative aging and accelerated aging are established in an attempt to understand the degradation behavior and the more suitable way of applying purely thermal aging.

The fifth and last chapter deals with the application of solar aging using a unique solar aging facility. First, adaptations of the existing solar aging facility are proposed to allow for a more generalized application of solar aging procedures on SSACs samples. The chapter continues with a comparison of the effects of purely thermal aging and solar thermal aging, in an attempt to decorrelate the impact of the presence of concentrated solar irradiance at similar levels of temperature. The main differences between the two types of aging, particularly in terms of temperature and irradiation profiles, are also discussed. Then the influence of other sources of degradation in solar aging, such as solar irradiance levels and cycling amplitude, are studied with the aim of observing which of these sources have a more significant impact on the aging behavior of SSACs. Finally, a discussion on the pertinence of applying solar aging in addition to purely thermal aging for more representative aging studies, as well as recommendations for applying solar aging procedures, are provided.

Overall, this work confronts the existing state of the art on the aging behavior assessment of solar selective absorber coatings with the experimental application of classical (purely thermal) and original (solar) aging procedures, using original aging facilities and typical R&D solar absorber coating configurations, in view of helping in the development of a more broadly applicable test standard for the prediction of thermal stability, reliability and service life of solar selective absorber coatings operating at high temperatures under atmospheric conditions.

Chapter 1 – Solar absorbers for CSP

1. Introduction and context

1.1. Climate change

The evidence of climate change in our daily life is ever clearer, with devastating events around the world. Extreme weather conditions are observed when and where they are not expected, as in 2018, with remarkable icy storms in Europe and the north-eastern US and an increase of 20°C of average temperatures in the Arctic [1]. This situation creates dry areas and also some even more humid areas. One of the main reasons of this problem is the increase of greenhouse gases (GHG) emissions toward the atmosphere, caused mainly by human activities.

According to the International Energy Agency (IEA), there has been an increase of almost 20% in the concentration of carbon dioxide (CO_2) emissions from 1980 to 2017, with current values of 404.98 ppm (parts per million) of CO_2 and an average growth of 2 ppm/year in the last ten years [2]. In addition, there has been a significant increase in the levels of methane (CH_4) and nitrous oxide (N_2O). These increases can be linked to the ever-intensifying anthropogenic activities following the Industrial Revolution.

One of the clearest evidence of these CO_2 emissions being produced by human activity has been shown recently with the COVID-19 pandemic that drastically altered the energy demand due to the confinement of most of the world population. The daily global CO_2 emissions then decreased by 17% by early April 2020, compared to the previous year [3].

Looking at the figures by sectors, the energy sector (electricity and heat generation, and transportation) accounts for approximately two-thirds (68%) of total green-house gas emissions through the combustion of fossil fuels, and around 80% of CO_2 total emissions [4]. Indeed, the generation of electricity and heat worldwide still relies heavily on coal, the most carbon-intensive fossil fuel. This therefore makes the energy sector one of the major sectors contributing to such a global situation. Meanwhile, there is an increasing demand for energy coming from worldwide economic growth and development, with a growth of 150% between 1971 and 2015 [4].

This state of affairs has attracted considerable attention from major players. The engagement of the industrialized and developing countries is very important for national and global GHG mitigation. This was formalized by the United Nations Framework Convention on Climate Change (UNFCCC) Conference of the Parties (COP), to support countries through the provision of energy and emissions statistics, and the training of countries officials in policy, modelling and energy statistics, with the final objective of stabilizing GHG concentrations in the atmosphere. In 2015, China contributed 28% of the total CO_2 emissions (9,084 $MtCO_2$), the United States 17% (4,998 $MtCO_2$), Europe 16% (5,080 $MtCO_2$) and India 6.5% (2,066 $MtCO_2$) [4].

A state of transition has started towards a clean, sustainable, affordable and accessible global energy system. To this day, non-fossil energy (without GHG emissions) accounts for 26.3% of the global energy production share (not including hydroelectricity), with 1.01 terawatts of installed renewable capacity [5]. In the wake of COP 21, most nations across the world agreed to accelerate their reductions in carbon emissions, namely through renewable electricity production and lower carbon-emitting transportation. Renewable energy is indeed at the center of the transition to a less carbon-intensive and more sustainable energy system, and represented almost two-thirds of new net electricity capacity additions in 2016 with almost 165 GW_e [6]. Renewable energy has indeed grown rapidly in recent years, accompanied by sharp cost reductions for solar PV and wind power in particular. The IEA expects renewable electricity generation to increase by more than one-third by 2022 to over 8000 TWh.

In this global context, solar energy is a most valuable candidate. It is predicted that solar energy can produce up to 27% of global electricity by 2050 (16% from solar photovoltaic systems and 11% from solar thermal electricity), and become the top source of electricity as early as 2040 [7].

1.2. Potential of solar energy

Solar energy is the most abundant energy resource on Earth, with about 885 millions of TWh reaching the surface of the planet every year, which means 8,100 times the primary energy consumed by humankind in 2015 [8] (the world final energy consumption was 109,135 TWh in 2015). It is abundant in many parts of the world [9]. Figure 1 shows the direct normal irradiance (DNI) levels around the globe. This irradiance is the relevant irradiance for the concentration of solar energy, and is measured on surfaces normal to the direct sunbeams.

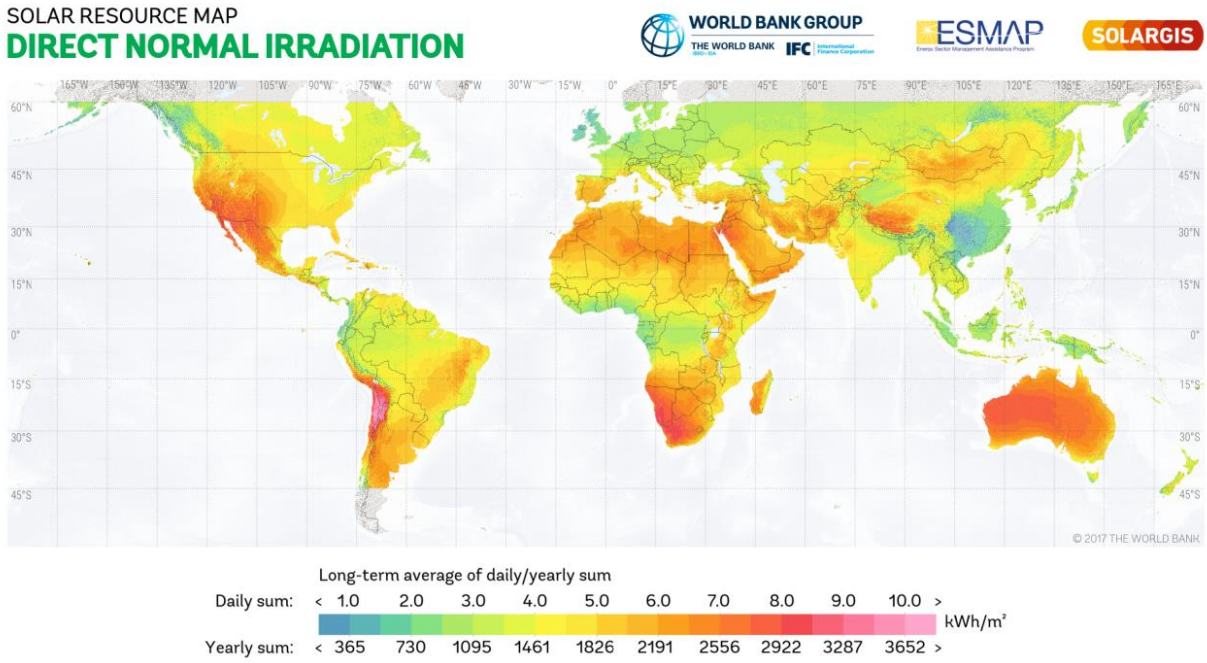

Figure 1. Global map showing the DNI levels for each location [9]

It can play a major role as an alternative energy resource, producing heat or electricity by capturing the radiation of the Sun. Indeed, solar radiation can be captured by photovoltaic devices using semiconductor materials that convert sunlight directly into electricity, or using solar thermal devices that convert the solar radiation into heat. These solar thermal devices can work at large and small scale. The small scale is used to heat water or air at low temperatures (T < 300°C) for buildings (domestic hot water, heating and cooling) and industries (mining, food, textile, etc.). The large scale is used to produce steam for electricity generation at higher temperature in solar power plants. This configuration is obtained by using mirrors to concentrate sunlight, transfer heat at high temperature to a fluid to produce steam then electricity via a steam turbine. These types of systems using solar concentration are called Concentrated Solar Power (CSP) technologies.

In the following section, the principles of CSP technologies, the current commercial technologies available and the needed improvements of these technologies to increase the efficiency are discussed.

2. Concentrated solar power (CSP)

2.1. Main advantage of CSP: thermal storage

The main disadvantage of solar energy is its intermittent nature, with fluctuations due to cloud cover during the day, and total absence during the night, especially after sundown and in the early morning when power demand steps up. To compete with other sources of energy, this intermittence must be overcome. Therefore, the question of energy storage is crucial for the development of solar technologies, both photovoltaic and thermal.

For photovoltaics (and wind energy), electricity is directly produced and must be stored. The currently available energy storage systems for electricity are pumped hydro, compressed air energy storage (CAES), a large family of batteries, flywheels and hydrogen storage. Each technology has its own performance characteristics that make it optimally suitable for certain grid services.

Pumped hydro and CAES can be considered high scale storage adapted to the geographic location, making them site-dependent. Both are capable of discharge times in tens of hours and with high module sizes that reach 1,000 MW. Pumped hydroelectric energy storage is a large, mature, and commercial utility-scale technology currently used at many locations around the world. CAES systems are similar, but less mature, in their use as they store energy in the form of pressurized air, usually in underground caverns.

In contrast to the capabilities of these two technologies, various electrochemical batteries and flywheels are positioned around lower power and shorter discharge times, ranging from a few seconds to six hours. Several different electrochemical battery technologies are currently available for commercial applications. The more robust technologies include lithium-ion (Li-ion), sodium sulfur (NaS), and lead acid batteries. Li-ion batteries tend to be best suited for relatively short discharges (under two hours) but do not handle deep-discharges well. The main disadvantage is the cost of battery storage with capital costs from near 300 $/kWh [10]. Flywheels are currently commercially deployed primarily for frequency regulation, ensuring a steady power supplied to the grid. Hydrogen systems are another type of storage, still at the early stage. It requires careful analysis to fully capture the value stream. While energy efficiencies might be at a level of 40%, this is balanced by energy storage potential that may last days, weeks, or longer.

In contrast, in concentrated solar power technologies for electricity production, the solar radiation is harnessed **first to produce heat** then electricity. This first conversion step allows for much easier and cheaper large-scale heat storage. Thermal storage used in CSP plants has a medium-long discharge time with five to ten hours of storage, optimally run for about 4,000 hours per year, depending on the solar conditions of the site. Thermal storage is used to increase the capacity factor of the CSP plant, and it reduces the average cost of solar thermal electricity. Thermal storage also has remarkable efficiency, especially when the storage medium is also used as the heat transfer fluid, such as with molten salts, with limited energy losses of 2%. It is expected to be able to improve such technology, with a decrease of the system capital cost. It is estimated that costs can be reduced to under 15 $/kWh, from the current cost of 20-25 $/kWh, with a high system efficiency of up to 95% and being able to have a lifetime of 10,000 cycles [11]. Thus direct thermal storage is the main advantage of CSP over PV (and wind), and allows for continuous electricity generation, which solves the problem of the intermittent nature of solar energy. This advantage gains importance with respect to renewable energy sources such as PV and wind power. Electric Thermal Energy Storage (ETES) is even considered by some as an alternative to store and spread at a reasonable cost the power generated by PV or wind, using the produced electricity to heat a fluid, then generate electricity again via a steam turbine [12].

2.2. Current situation in CSP deployment

Concentrated solar power or CSP technologies are one of the most mature renewable energy technologies to produce electricity, together with photovoltaic and wind energy. Research activities on CSP started in the 1970s with several pilot plants, such as THEMIS tower in Targasonne, France, with 2 MW of output power built in 1979. This brought CSP technology to the industrial and commercial level, with the first CSP plant, called Solar One, installed in 1982 in the United States. The first commercial CSP plants were built without storage in California, in the context of tax incentives for renewable energy. After that, there was a period of stagnation due to the drop in price of fossil fuels. The development of CSP projects resumed in the 2000s, mainly in Spain and the United States, as a consequence of energy policies and incentives to mitigate CO_2 emissions and diversify the energy supply. It strongly increased from 2010, emerging in new markets such as the Americas, North and South Africa, the Middle East, Australia, China and India. It was not until 2006 that large-scale CSP plants were built, particularly in the aforementioned countries. The world's largest CSP plant, in the Mojave Desert in the USA, with 392 MW, was connected to the grid in 2013.

While Spain and the United States are still the leading countries in CSP installations, CSP plants are 103 in operation, 21 under construction or planned in many Sun Belt countries. In January 2020, the global installed CSP capacity amounted to about 6.1 GW with an additional of 1.5 GW under construction and 1.6 GW in the development stage, as can be seen in Figure 2. The emerging CSP countries are China with 514 MW under construction, Chile with 1.1 GW in development, and the MENA countries with 910 MW under construction.

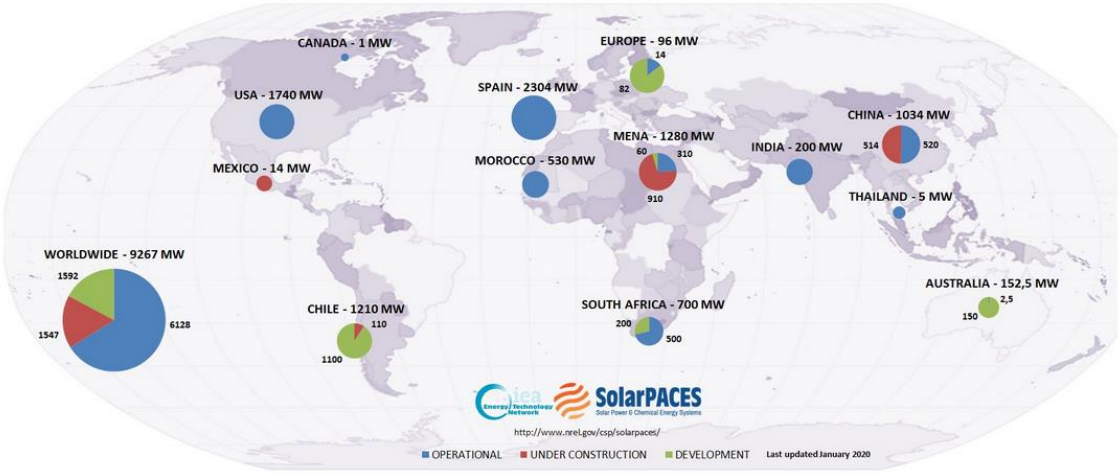

Figure 2. CSP plants and projects around the world

Despite its advantages due to thermal storage, the implementation of CSP is lagging behind PV and other renewable energies. About 6.3 GW of solar thermal electricity were installed worldwide in 2019, compared to 580 GW for PV [13]. The growth of concentrating solar power was relatively slow with just 601 MW additional installed capacity in 2019, and it represented only 0.2% of the global installed capacity of renewable energy technologies of that year. The integration of CSP technology is however highly recommended for the energy market.

For instance, CSP plants with thermal storage are counted as promising flexible power supply, especially when the net load power curve is duck-shaped due to the high photovoltaic penetration in the power grid, as can be seen in Figure 3. The latter illustrates the fact that the peak demand often occurs after sunset (> 18:00), when solar power is no longer available, which leads to large-capacity power shortage. CSP with storage can mitigate this problem. Therefore, while they are competitors on some projects, CSP and PV are ultimately complementary.

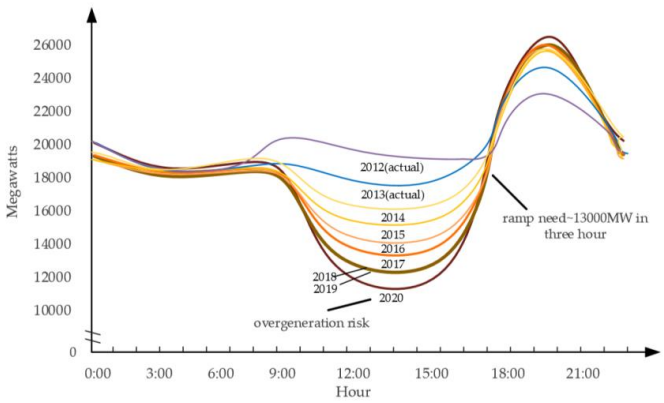

Figure 3. The predicted duck curve (total load power curve minus renewable energy generation curve) reported by California Independent System Operator in 2015. (Source: http://www.caiso.com/Documents/FlexibleResourcesHelpRenewables_FastFacts.pdf.)

Overall, the implementation of CSP technologies is expected to reach a global share of 11% by 2050, equivalent to 1,000 GW of total installed capacity, avoiding the emissions of up to 2.1 gigatons of carbon dioxide annually. CSP technology has the capacity to provide for about 7% of the total electricity needs projected for the world by 2030, and 25% by 2050 (considering a high-energy-saving, high-energy-efficiency scenario) [14].

2.3. CSP technologies

The main principle of CSP plants is illustrated in Figure 4. It consists in concentrating the incoming solar irradiation onto a solar absorber (receiver), to be able to convert this concentrated solar energy into useful heat. The concentration is done with highly reflective mirrors. The level of concentration and absorber temperature depend on the area and optical efficiency of the mirrors. The former is the concentration ratio given by Eq.(1), where A_m is the total area of the mirrors and A_r is the area of the receiver.

$$C = \frac{A_m}{A_r} \tag{1}$$

The absorbed useful heat is transferred to a heat transfer fluid (HTF), which transfers the heat to a steam generator to finally run a steam turbine and produce electricity. The three main subsystems are the solar collector field, or mirror field, the solar receiver and the power conversion system.

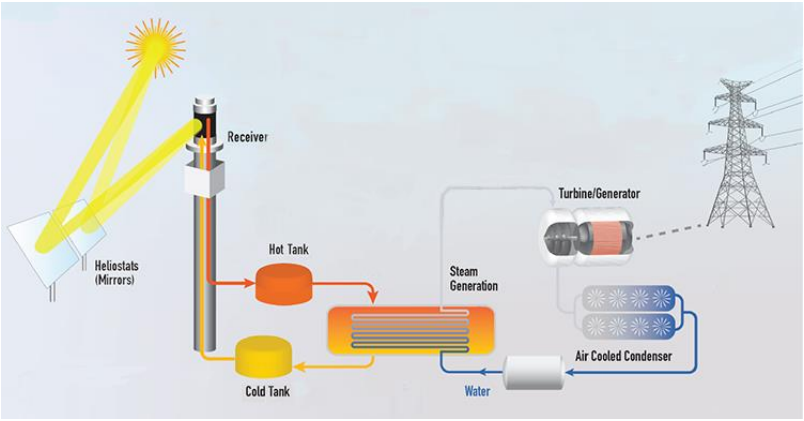

Figure 4. Principle of a Concentrated Solar Power (CSP) plant

In hybrid plants, a storage or back-up system is added to improve performance and therefore increase the capacity factor. The storage is usually done with liquid molten salt, used as the heat transfer fluid

which has already been proven effective for 7 to 15 hours [15]. Steam can be also used for storage, but it is considered a short term storage, viable for just 0.5 to 4 hours [16–18]. The power conversion systems are Rankine cycles, Brayton cycles, combined cycles and Stirling cycles, depending on the CSP technology. The back-up is usually done with natural gas, enabling the plant to function continuously, even during cloudy days.

The differences between CSP technologies are in the optical design, the solar field layout, the tracking system, the type of receiver, the type of heat transfer fluid, the heat storage capability and the conventional power system generating electricity. Currently, there are four different configurations of commercial CSP plants: Linear Fresnel reflector, Parabolic trough, Central receiver and Parabolic dish. Table 1 shows the design, main characteristics and images (left: global view, right; receiver) of each configuration. These technologies are detailed in the following sections.

Table 1. Four types of concentrated solar power plants

Linear receiver (single axis)			
Linear Fresnel reflector	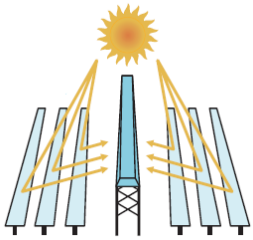	Cost effective Low capacity C = 20 – 80 T_{max} ~ 300°C	 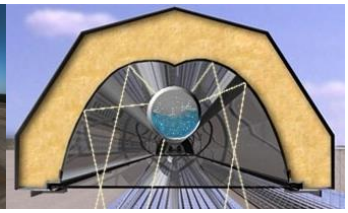
Parabolic trough	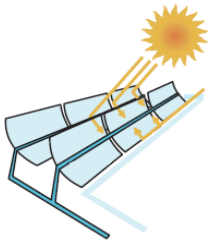	Most commercial technology C = 80 – 150 T_{max} ~ 390°C	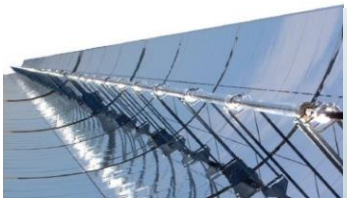 
Single point receiver (two axis)			
Central receiver	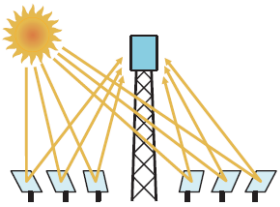	Large capacity C = 500 – 1000 T_{max} ~ 565°C	 
Parabolic dish	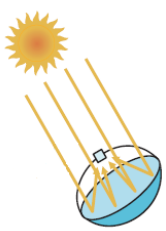	Highest concentration C > 1000 Low investment	 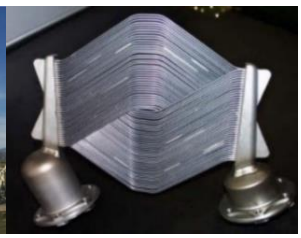

2.3.1. Parabolic trough collectors

Parabolic trough (PT) is one of the most commercial, advanced and mature CSP technology, with 2,000 hours of performance, and a history of commercial plants operation dating from the early 1980s. Currently, there are over 4,000 MW in operation with 80 plants operating worldwide commercially and 11 plants under construction. The power of PT plants is between 5 and up to 280 MW. It can be said that this technology has the lowest operational risk compared to other CSP technologies, making PT the most competitive in the field. This system provides the best land-use factor of any solar technology. Figure 5 shows the set-up of this kind of CSP plant.

PT collectors track the sun on one axis: the cylindrical-parabolic reflector concentrates the incoming solar rays onto a linear metallic receiver tube insulated in an evacuated glass envelope, which moves with the reflector. The concentration ratio for PT is between 70 and 100 and the operating temperature varies from 350°C to 400°C.

The efficiency of the system is measured by the amount of heat collected by the fluid from the collectors divided by the amount of incoming solar radiation, also called solar-to-electricity conversion. The overall efficiency of PT plants is 15 to 16%, with the highest peak efficiency reaching 20%. The annual capacity factor is between 25 and 40%: this factor is the ratio of the actual electrical energy output to the maximum possible electrical energy output, both over the same period.

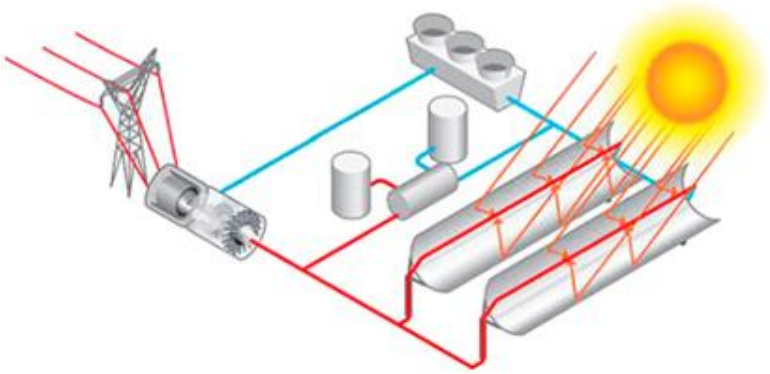

Figure 5. Schematic of a parabolic trough power plant (Source: European Solar Thermal Electricity Association ESTELA, www.estelasolar.org.)

There are several variations of this technology depending on the heat transfer fluid used and the inclusion of heat storage. The possible heat transfer fluids are synthetic oils, molten salts and direct steam generation (DSG). While molten salts or DSG are not yet commercially proven, synthetic oils are the most used configuration with a maximum working temperature reaching 400°C. In most cases, the synthetic oil is used as the heat transfer fluid circulating in the solar field, and then, using a heat exchanger, the heat collected by the oil is transferred to a molten salt storage medium. Normally, with a full thermal reservoir the turbines can run for about 7.5 hours at full-load, even if it rains or long after the sun has set.

Pioneer countries in this technology are Spain, with a 2.3 GW capacity installed in 49 plants, the last plants commissioned in 2013. Since 2006, almost half of this capacity has been equipped with thermal energy storage with two tanks of molten salts and 7 hours of nominal capacity, and the United States, with a 1.7 GW capacity installed in plants with six-hour storage such as the Solana plant in Arizona.

Here are some of the currently operating PT plants:

- Andasol-1 (and Andasol-2 & 3) (50 MW, Spain)
- Arcosol 50 (50 MW, Spain)
- Ashlim (Negev) (121 MW, Israel)
- Chabei Molten Salt PT Project (64 MW, China)
- Solnova 1 (50 MW, Spain)

2.3.2. Central receiver

The central receiver plant, or solar tower plant, is one of the emerging solutions for high capacity CSP plants. The first commercial central receiver plant, called PS10, was commissioned in June 2007 in Spain. Currently, the capacity of these types of plants can reach up to 100 MW for a single receiver. By concentrating sunlight 600 up to 1,000 times, the operating temperature can reach levels from 300°C to over 565°C, with a high potential to increase the operating temperature up to 800°C. This technology has proven to be technically feasible in projects with 15 years of experience worldwide. It can be said that this is one of the most promising technologies in the CSP field: thanks to the possibility of achieving such high temperatures, plants can also drive gas turbines or combined cycle systems, reaching peak efficiencies of 35%.

The main components of solar tower plants are a heliostat (mirror) field, a tower and an electricity generation system. The tower has a height from around 100 meters to up 150 meters. The multitude of movable heliostats track the Sun and concentrate the sunrays upon the receiver at the top of the tower, where the fluid is circulating (Figure 6). As a usual CSP configuration, the working fluid absorbs the solar energy and is then used to generate steam to power a conventional turbine.

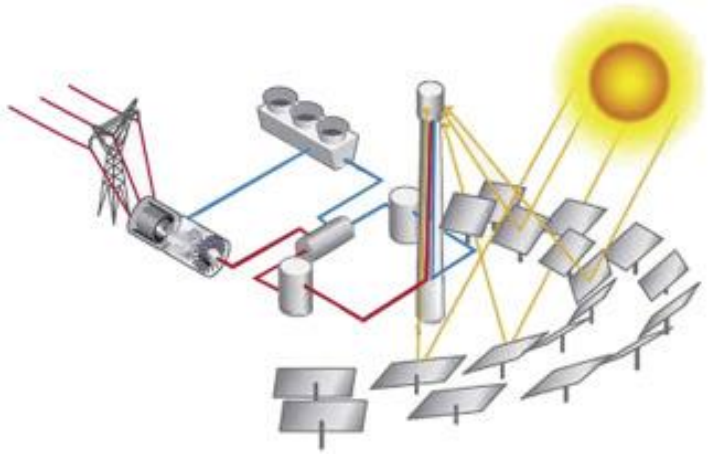

Figure 6. Solar tower plant configuration (Source: European Solar Thermal Electricity Association ESTELA, www.estelasolar.org)

There are different configurations depending on the heat transfer fluid (steam, air, molten salts), the storage system and the heliostat design. One option is to use molten salts both as heat transfer fluid and heat storage medium, such as for the Crescent Dunes Solar Energy Project, located in Nevada with a capacity of 110 MW and 10-hour thermal storage, and Gemasolar in Spain, with a capacity of 20 MW and 15 hours of thermal storage. Plants such as PS10 and PS20, near Seville, Spain, use direct steam generation (DSG) with steam as the heat transfer fluid. The largest CSP capacity so far at a single place is the one built at Ivanpah in California, totaling 377 MW (net). This plant includes three distinct towers – each with its own turbine – based on DSG technology and no storage.

It is important to note a different configuration for solar tower plants, called the beam-down [19], where the tower receiver is substituted by a down-facing convex mirror. In this way a second reflection stage is added and the receiver can be located on the ground. This emerging configuration avoids having to send the heat transfer fluid up to the top of the tower with pumps.

There are several central receiver plants around the world, with a capacity ranging between 10 and 100 MW per tower. In 2020, there are around 18 plants operating and 7 plants are on the way to become operational in the next few years, most of them located in China and Chile.

Some of the currently operating solar tower plants are:

- NOOR III (150 MW, Morocco)
- ACME Solar Tower (2.5 MW, India)
- Planta Solar 10 (11 MW, Spain)
- Planta Solar 20 (20 MW, Spain)

2.3.3. Linear Fresnel reflectors

This type of technology is one of the least mature technologies in the CSP field together with the parabolic dish configuration, which will be described in the following section. It is also the technology with the lowest concentration ratio, thus the operational temperature stays low and so does the system efficiency. Currently, long-term performance and cost data are still lacking for further improving this technology. The main components of LFRs are the reflective mirrors, the receiver tube and the tubing system.

This technology is similar to parabolic troughs, but uses a line of mirrors instead of one single curved mirror. Indeed, this system concentrates sunlight with a series of long, narrow, shallow-curvature (or flat) mirrors, each oriented differently, so as to approximate the concentration profile of a parabolic trough, as can be seen in Figure 7. Each line of single-axis mirror tracks the movement of the Sun. It is structurally simpler and cheaper than a parabolic trough concentrator. Also, the loads caused by wind are lower and it has higher land-use efficiency, suitable for rooftop or limited industrial areas. Sunlight is concentrated onto a receiver mounted at the focal line of the Fresnel mirrors, placing it parallel to and above them. The design of the receiver is a thermally-insulated inverted cavity with a secondary mirror, covered by a glass enclosing the absorber tubes in static atmospheric conditions.

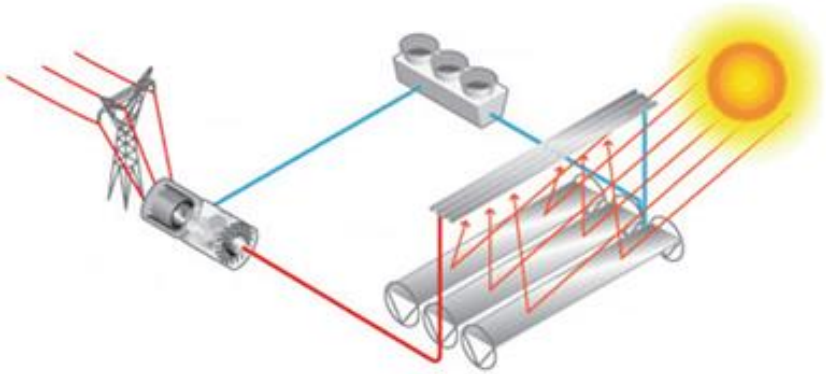

Figure 7. Schematic of a Linear Fresnel reflector (Source: European Solar Thermal Electricity Association ESTELA, www.estelasolar.org)

As mentioned before, this technology has greater optical losses than troughs, especially when the Sun is low in the sky. As a result, there is lower production in the early morning and late afternoons, and also in winter, but this can be overcome in part by the use of higher operating temperatures than trough plants. Thus, LFR technology uses direct steam generation, with direct storage of the steam.

Current research is underway to use molten salts as the heat transfer fluid, to be able to use it as the direct storage media in both parabolic trough and linear Fresnel systems. The greatest challenges to commercializing this change in the technology are to use materials compatible with rotary joints and concerns over salt freezing in the solar field.

The first prototypes of LFR technology were built in 2010, and after that, two commercial plants were operating, in 2012, with a 30 MW plant in Spain and in 2014, with a 125 MW plant in India, both of them without storage. Nowadays, only 5 plants (166.4 MW) are operating and 3 are under construction (65 MW):

- Dhursar (125 MW, India)
- Puerto Errado 1 (1.4 MW, Spain)
- Puerto Errado 2 (30 MW, Spain)
- Lanzhou Dancheng Dunhuang (50 MW, China)
- eLlo Solar Thermal Project (Llo) (9 MW, France)

2.3.4. Parabolic dish

Parabolic dish is the least commercialized CSP technology, with just 3 MW of installed capacity worldwide. Despite having the highest optical efficiency within CSP technologies, there is very little research to further improve this technology. The main reason why this technology has low commercial investment while it has a good overall performance is the lack of storage, making it difficult to reduce the higher costs and risks of the technology. Therefore, it is not able to compete with other CSP technologies or photovoltaic.

It comprises a main parabolic dish and a Stirling engine or a micro-turbine, which are heat-to-electricity engines, located at the focal point. It is based on a two-axis solar tracking system, which concentrates the solar energy onto a receiver positioned at the focal point of the dish (Figure 8). Having most of the system moving, due to the tracking system, and a direct production of electricity with the Stirling engine, it is not possible to integrate thermal storage into the system, making the overall investment price too high to compete directly with a photovoltaic system.

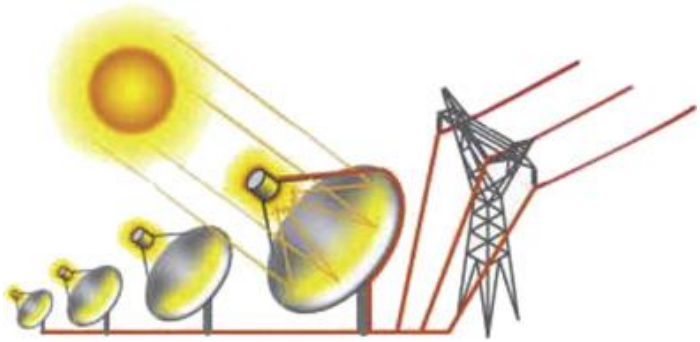

Figure 8. Parabolic dish plant (Source: European Solar Thermal Electricity Association ESTELA, www.estelasolar.org)

There are only two plants built worldwide with just 3 MW of capacity but they are currently in a non-operational state:

- Maricopa Solar Project (Non-Operational, 1.5 MW, US)
- Tooele Army Depot (Non-Operational, 1.5 MW, US)

A possible use of this technology is at small scale, as a source of heat in community kitchens and other service or small industry facilities in countries such as India.

2.4. Solar thermal receiver

The receiver is one of the most important subsystems of a solar thermal plant. It is where the conversion of concentrated solar radiation into thermal energy takes place. They are responsible for collecting solar energy and transferring the heat collected to the heat transfer fluid (HTF). It is located at the focal point of a CSP system, and its configuration depends on the type of technology. It is generally composed of one or more metal tubes.

The efficiency of the receiver is equal to the thermal energy transported out of the receiver by the working fluid, divided by the concentrated solar irradiance hitting the receiver surface, which depends on the receiver design. There are possible losses on the receiver due to back-reflection, re-radiation, convection and conduction. This efficiency is strongly related to the optical efficiency and dimensions of the CSP plant, influencing the density and homogeneity of the flux that arrives on the receiver.

2.4.1. Central receiver

The central receiver design depends mostly on the type of fluid that is flowing through the tubes. As mentioned previously the fluid used can be molten salts, steam, atmospheric air or compressed air. The two basic receiver configurations used in large central tower receiver plants are the external receiver and the cavity receiver. Both configurations can be used for all the heat transfer fluids. A typical external receiver is shown in Figure 9.

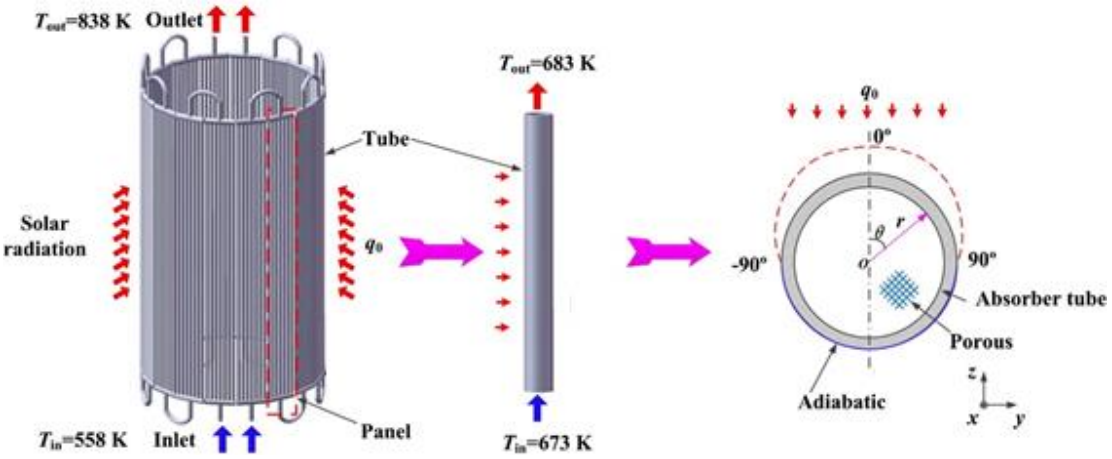

Figure 9. External receiver with single tube and cross-section [20]

In external receivers, the tubes are installed on the outside of a surface, such as a cylinder when used in a surrounding heliostat field configuration. The solar flux density can reach levels of up to 1,000 kW/m^2 with this type of receiver. The level of deterioration of the coating is higher compared to other receivers that have a higher protection from the atmosphere. An example of commercial plants with external receiver is the Gemasolar plant in Spain.

In cavity receivers (Figure 10), the tubes are arranged on the inner walls of a large cavity with a small aperture. The solar radiation is distributed inside the cavity over a large area with the absorber tubes. In this way, even though the solar heat flux at the aperture is in the same range as for external receivers, the solar flux on the absorber tubes is increased, due to multiple reflections inside the cavity. Also, convection losses are reduced. A cavity receiver is used on the PS10 and PS20 plant in Spain.

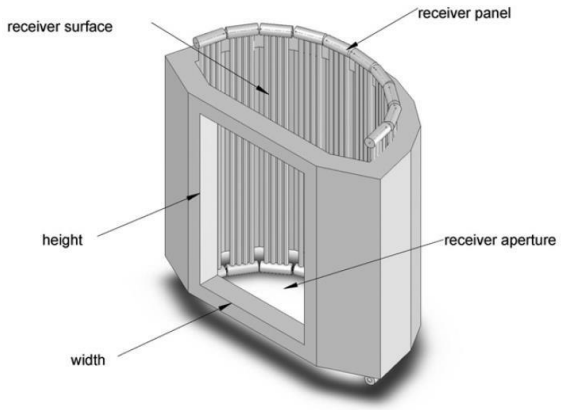

Figure 10. Cavity receiver for solar tower plant [21]

For air receivers, volumetric absorbers are a possible option, which is still under research and development. These absorbers are structures with high open porosity, mostly made of ceramic materials (Figure 11). The solar radiation penetrates into the volume of the absorber, and is then transferred to an airflow passing through the open structure. The receivers can be operated at both ambient pressure or in pressurized mode, by closing the receiver aperture with a quartz window. Small systems may use this type of receiver.

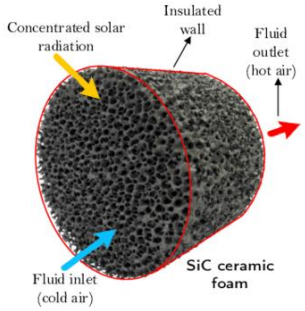

Figure 11. An example of porous media used for volumetric absorbers [22]

Central receivers are large compared to other CSP receivers, which produces significant heat losses, especially with the external and open-air types. These losses impose restrictions on the working temperature of this type of plant, in addition to the optical concentration limitations.

2.4.2. Parabolic trough linear receiver

In parabolic trough systems, the receiver tube works under vacuum conditions. The key components in this type of heat collector element are the metallic tube material, the selective absorber and the outer glass tube, to maintain the tube under vacuum conditions. The selective absorber is the main element responsible for the optical and thermal efficiency of a receiver tube. The thermal losses of the receiver tube are: partly conductive and convective, the latter being reduced in a vacuum environment; mostly radiative, the latter being minimized by the low thermal emittance of the selective absorber.

The use of evacuated tubes on this type of CSP plant is mandatory, considering the large surface of absorbers (several tens of kilometers), the relatively high operating temperature (350-390°C) and the low concentration ratio (typically 80 suns). Not having the receiver under vacuum conditions would have a significant negative impact on the performance of the receiver (due to high thermal losses not being compensated by sufficient concentrated solar input) and therefore of the plant compared to other types of CSP plants.

Glass to metal seals (bellows), the connection at both ends of the receiver tubes, are used to maintained a high vacuum condition [23], created during the manufacturing of the receiver (Figure 12). The vacuum pressure inside of the tube is ~ 10^{-4} mbar (below the Knudsen conduction range) [24]. In these conditions, the gas is in the free molecular flow regime and convective heat transfer is negligible. The typical values of the inner and outer annulus diameters are 70 and 110 mm.

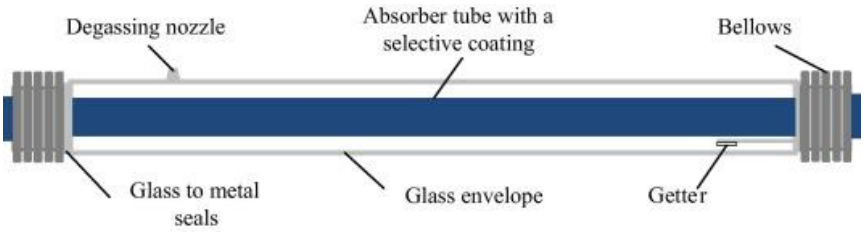

Figure 12. Parabolic trough receiver tube [25]

The bellows are one of the most critical parts of this configuration because it is where most of the non-radiative heat losses occur. The vacuum conditions can also be disturbed by hydrogen from the working fluid perspiring through the inner receiver tube and into the evacuated zone between the tubes. Even low levels of hydrogen concentration of around $1 \cdot 10^{-7}$ bar may cause significant losses, for this reason special getters are designed to mitigate this effect.

2.4.3. Linear Fresnel receiver

The LFR receiver is the only commercial CSP receiver equipped with a secondary reflector to improve the efficiency of the collector by increasing the solar flux reaching the receiver, as shown in Table 1 and Figure 13. Due to the low optical efficiency of the plant, the receiver deals with low level of concentrated solar energy (< 60 suns) and often low operating temperatures (250-350°C). These working conditions avoid a significant deterioration of the secondary reflector.

This type of receiver is enclosed between the secondary reflector and a glass cover and atmospheric conditions are maintained around the receiver. This enclosure protects the receiver from the wind, which decrease the heat losses. Compared parabolic trough, the natural convection losses are higher due to the lack of the vacuum conditions around the receiver.

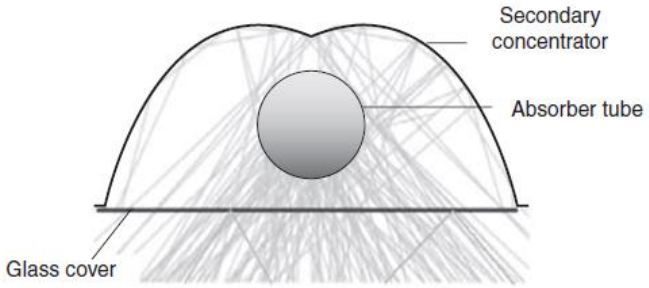

Figure 13. Single tube receiver for LFR receiver [26]

For a good performance of this receiver, a good tracking system needs to be reached, to ensure a homogenized flux on the secondary reflector, and in this way, avoid hotspots and high deterioration of the reflector. In addition, the intensity distribution of the flux on the absorber surface has an impact on the stresses on the absorber system, as due to the concentrator system, usually one side of the absorber tube receives an overwhelming fraction of the total irradiation of the tube.

The secondary reflector is one of the key components of a LFR and one the most popular topics of research for the improvement of the collector's optical performance. Its shape is one of the aspects to optimize and adapt, considering the primary mirrors layout [27,28].

One of the purposes of LFR technologies is to be potentially lower cost than PT technologies, with both quasi-flat collectors instead of troughs, and receivers working in static air instead of vacuum. LFR receivers are however specifically designed for a particular plant, and no off-the-shelf component is commercialized to this day, contrarily to PT receivers. Thus, no cost data for LFR receivers is yet publicly available, to compare with PT receivers.

3. Optical and thermal behavior of solar absorbers

This section introduces notions relevant to the understanding and optimization of solar absorbers, related to their interaction with solar radiation and their thermal behavior in conditions of use.

3.1. Optical behavior of a surface towards incident radiation

As energy is conserved during light-matter interaction, an incident radiation on a material can only be either reflected at its surface, transmitted through the material, or absorbed by it (Figure 14).

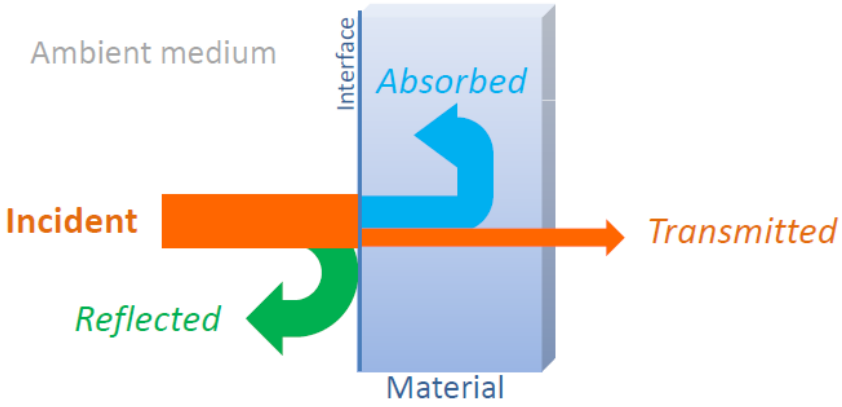

Figure 14. Interaction between light and matter

The relative distribution between the three phenomena depends on the radiation wavelength λ and incident angle θ, and the material temperature *T*, as illustrated by Eq.(2).

$$R(\lambda,\theta,T) + Tr(\lambda,\theta,T) + A(\lambda,\theta,T) = 1 \quad (2)$$

$R(\lambda,\theta,T)$, $Tr(\lambda,\theta,T)$ and $A(\lambda,\theta,T)$ are the spectral reflectance, transmittance and absorptance of the material, respectively. Solar receivers are usually made of opaque materials so $Tr(\lambda,\theta,T) = 0$ (no transmission).

Also, Kirchhoff's law of radiation states that, at thermal equilibrium, any radiation that can be absorbed by a material at temperature *T* at a given wavelength λ and angle θ can also be reemitted at the same wavelength and angle in order to maintain its temperature constant, and thus respect thermal equilibrium. From these, Eq.(3) can be established.

$$A(\lambda,\theta,T) = E(\lambda,\theta,T) = 1 - R(\lambda,\theta,T) \quad (3)$$

As spectral absorptance and emittance are difficult to measure, it is thus possible to estimate them from spectral reflectance, which is the intrinsic ability of a material to reflect light. From these spectral quantities, the performance of a solar absorber can be deduced. It is illustrated by its solar absorptance and thermal emittance, which are defined in the following.

3.2. Absorption of solar radiation

3.2.1. Solar radiation incident on the absorber

The solar radiation or sunlight is a fraction of the electromagnetic spectrum, which is emitted by the Sun. Most of the incoming radiation from the Sun reaching the top of the Earth's atmosphere is absorbed or scattered far up in the ionosphere, the ozone layer or the troposphere. The solar irradiation that reaches the surface of the Earth varies due to atmospheric scattering and absorbing components (cloud cover, aerosol content, ozone layer conditions, time of day, Earth/Sun distance, etc.) which influence the path of the rays that traverse the atmosphere.

Depending on their latitude, a different air mass (AM) value is attributed to each site (Figure 15). The AM illustrates the direct optical path length through the atmosphere, expressed as a relative ratio to the path length at the zenith.

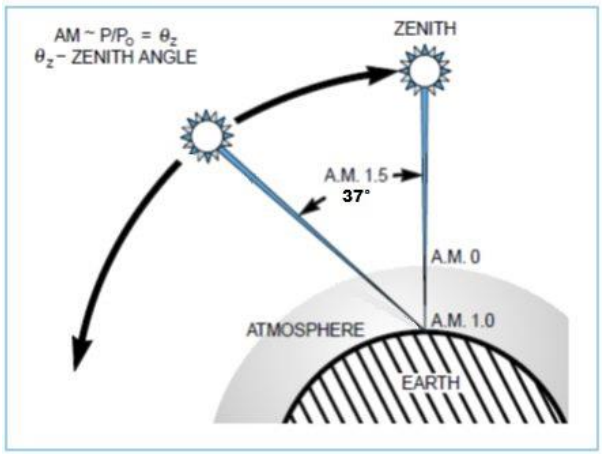

Figure 15. Air Mass (AM) changing with the zenith angle [29]

The amount of solar spectral irradiance that reaches the surface of the Earth is commonly defined for specific atmospheric standard conditions of an absolute air mass of 1.5 and a sun-facing surface tilted at 37°, as calculated by the American Society for Testing and Materials using SMARTS-2 software [30]. This is known as the ASTM G173-03 AM1.5 standard solar spectrum [31]. Figure 16 shows the corresponding extraterrestrial spectral irradiance (AM0) and the Global Tilt (GT) and Direct + Circumsolar (DC) spectral irradiance on the 37° sun-facing tilted surface, at AM1.5, for each wavelength in nanometers (nm) [32].

The extraterrestrial spectral irradiance shows the solar radiation received at the top of the Earth's atmosphere. As it passes through no atmosphere, it is at Air Mass 0 (AM0). The global tilt spectral irradiance is a measure of the density of the available solar resource per unit area considering both the direct (+ circumsolar) and diffuse solar radiations. The direct + circumsolar irradiance is the radiation that comes from the Sun disc and its corona through the atmosphere without getting scattered. The diffuse irradiance is the solar radiation scattered by the particles and molecules in the atmosphere, but still makes it down to the Earth's surface. The Direct + Circumsolar (DC) is the relevant irradiance to consider for the concentration of solar energy, as only these parallel sun rays can be reflected by the mirrors towards the receiver.

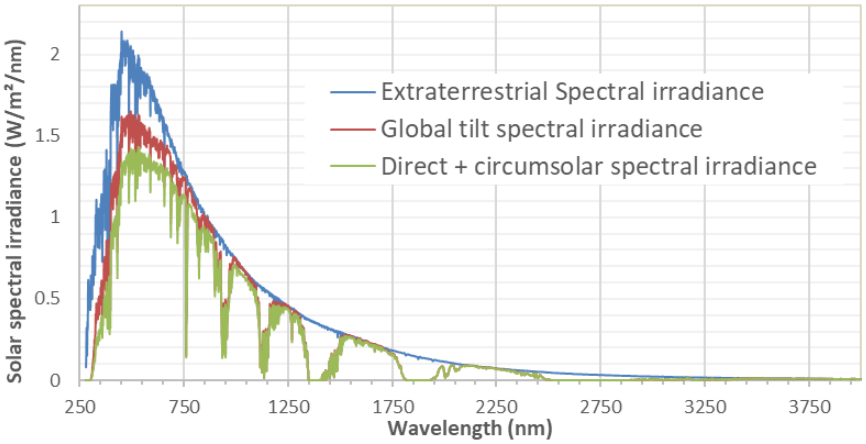

Figure 16. ASTM G173-03 Solar Reference Spectra [31]

The DC solar spectrum ranges from the ultraviolet to the infrared, mostly between 0.28 and 2.5 µm (Figure 16). The radiation coming from the Sun has a small amount of ultraviolet radiation (3% of the total solar radiation occurs between 0.28 and 0.4 µm); a higher amount of visible light (42% of the solar radiation is emitted between 0.4 and 0.7 µm); a large amount of infrared radiation (55% is emitted between 0.7 and 4 µm).

The total amount of solar radiation *I* (W/m²) in a given location is obtained by integrating the solar spectral irradiance *G*(λ) (W/m²/nm) in this region over its wavelength range (λ_1 , λ_2), as shown in Eq.(4).

$$I = \int_{\lambda_2}^{\lambda_1} G(\lambda) \cdot d\lambda \tag{4}$$

As an example, integrating between 0.25 µm and 4 µm (with a step of 5 nm) and considering the solar spectrum ASTM G173-03 AM1.5 DC, the total amount of solar radiation is 901.26 W/m².

3.2.2. Solar absorptance

The solar absorptance α_S is the fraction of incident solar radiation that is actually absorbed by a material. The incident solar flux density (in W/m²) can be obtained by integrating the solar spectrum $G(\lambda)$ (in W/m²/nm) over wavelength (Eq.(5)). The flux density that is actually absorbed by the material is obtained by weighting the spectral solar irradiance $G(\lambda)$ with the hemispherical spectral absorptance $A(\lambda,\cap,T)$ of the material at each wavelength λ, and then integrate it over wavelength in the solar range as well. The following expression is obtained for solar absorptance, which is a total value (i.e., independent of wavelength) comprised between zero (no absorption) and one (maximum absorption) and has no unit.

$$\alpha_S = \frac{\int_{\lambda_1}^{\lambda_2} [1 - R(\lambda)] \cdot G(\lambda) \cdot d\lambda}{\int_{\lambda_1}^{\lambda_2} G(\lambda) \cdot d\lambda} \tag{5}$$

Eq.(3) (p.28) implies that hemispherical spectral absorptance $A(\lambda,\cap,T)$ is considered to be equal to $[1 - R(\lambda,\cap,T)]$, which is the near-normal ($\theta_i = 8°$) hemispherical spectral reflectance of the sample measured at room temperature T_a (see Chapter 3 for more details). Therefore, a good solar absorptance is associated with a low reflectance in the range of the solar spectrum. $G(\lambda)$ is taken as the standard solar irradiance spectrum for CSP (ASTM-G173 AM1.5 direct + circumsolar) [31]. The boundary wavelengths are λ_1 = 0.25 µm and λ_2 = 2.5 µm in this study.

3.3. Emission of thermal radiation

3.3.1. Blackbody emission

When an object is heated, it emits thermal electromagnetic radiation due to molecular and atomic agitation. The wavelength and intensity of this radiation depend on the temperature of the object and its optical characteristics. For a solar receiver, this thermal emission amounts to radiative thermal losses, as the corresponding heat will be emitted towards the environment and not be conducted towards the heat transfer fluid.

To estimate the emissive power of real objects, an ideal object, called a blackbody, is used as a reference. A blackbody is an object that absorbs any and all radiation it receives, and to maintain its temperature constant (thermal equilibrium), is able to reemit it. The Sun is for instance considered as a blackbody at a temperature of 5800 K. The blackbody emission at a given wavelength λ and temperature *T*, or spectral emittance $M_\lambda^0(\lambda, T)$, is given by Planck's law, using Eq.(6).

$$M_\lambda^0(\lambda, T) = \frac{2\pi hc^2}{\lambda^5} \cdot \frac{1}{\exp\left(\frac{hc}{\lambda k_B T}\right) - 1} = \frac{c_1}{\lambda^5 \left[e^{\frac{c_2}{\lambda T}} - 1\right]} (W \cdot m^{-2} \cdot \mu m^{-1}) \quad (6)$$

h is Planck's constant (6.6261×10^{-34} J · s), k_B is Boltzmann's constant (1.3807×10^{-23} J/K), *c* is the light velocity in vacuum (2.9979×10^8 m/s), and $c_1 = 3.7405 \cdot 10^8\ W \cdot \mu m^4 \cdot m^{-2}$ and $c_2 = 1.4388 \cdot 10^4\ \mu m \cdot K$ are the first and second Planck´s radiation constants, respectively. This law is illustrated in Figure 17, which shows the blackbody spectra at different temperatures. The total emitted energy can be obtained by integrating the spectrum over the whole wavelength range.

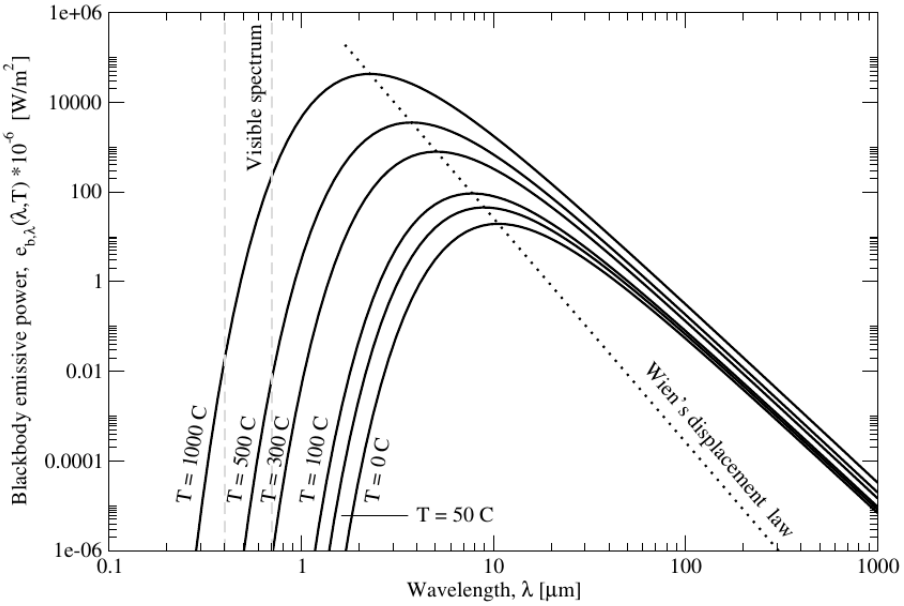

Figure 17. Spectral emissive power of a blackbody for each wavelength [33]

Figure 17 shows that the intensity of emitted radiation increases with temperature, and this emission is shifted towards shorter wavelengths. By the derivation of Eq.(6), the wavelength where the maximum emission occurs, λ_{max}, can be obtained for a given temperature *T:* this is called Wien's displacement law (Eq.(7)).

$$\lambda_{\max} \cdot \mathrm{T} = 2898\ \mu m \cdot K \quad (7)$$

The solar radiation (5800 K) is for instance centered in the visible region (hashed in Figure 17). For ambient temperatures (around 300 K), the radiation is centered in the infrared region. For the case of 800 K of temperature, the radiation is centered between the infrared and visible region. The higher the temperature the closest is the center to the visible region.

Eq.(6) can be integrated over wavelength to obtain the total emissive power of a blackbody, resulting in the Stefan-Boltzmann law (Eq.(8)) that gives the hemispherical total emitted energy for a blackbody at temperature *T* per unit area in all directions and all wavelengths.

$$M(T) = \int_0^\infty M_\lambda^0(\lambda, T) = \sigma T^4 \tag{8}$$

$\sigma = 5.6696 \cdot 10^{-8}\ W \cdot m^2 \cdot K^{-4}$ is the Stefan-Boltzmann constant.

3.3.2. Thermal emittance

Thermal emittance is used to characterize the optical properties of a real body in the infrared wavelength range as compared with an ideal blackbody. Thermal emittance can be defined as the fraction of radiant flux density (in W/m^2) actually emitted by a material at temperature *T*, compared with the radiant flux density that would be emitted by a blackbody at the same temperature. The latter part is given by Stefan-Boltzmann law, i.e., the integration of Planck's law (blackbody spectral emittance $M_\lambda^0(\lambda, T)$ in W/m^2/µm) over wavelength. The former part is obtained by weighting the blackbody spectral emittance $M_\lambda^0(\lambda, T)$ with the spectral emittance of the material $E(\lambda, \theta, T) = 1 - R(\lambda, \theta, T)$ (Kirchhoff's law) and integrate it over wavelength, as shown in Eq.(9).

$$\varepsilon_\theta(T) = \frac{\int_{\lambda_1}^{\lambda_2} [1 - R(\lambda, \theta, T)]\ \cdot M_\lambda^0(\lambda, T) \cdot d\lambda}{\int_{\lambda_1}^{\lambda_2} M_\lambda^0(\lambda, T) \cdot d\lambda} \tag{9}$$

Spectral emittance $E(\lambda, \theta, T)$ and reflectance $R(\lambda, \theta, T)$ depend on the emission/reflection angle θ, therefore $\varepsilon_\theta(T)$ is the total directional thermal emittance of a material at temperature *T* and angle θ.

Since radiation can be emitted in all directions, another quantity of interest is the hemispherical thermal emittance $\varepsilon_H(T)$. It is calculated by angularly integrating directional thermal emittance $\varepsilon_\theta(\theta, T)$ at different angles, as shown in Eq.(10).

$$\varepsilon_H(T) = 2 \cdot \int_0^{\pi/2} \varepsilon_\theta(\theta, T) \cdot \sin\theta \cdot \cos\theta \cdot d\theta \tag{10}$$

This value represents the propensity of a surface illuminated from all directions of the hemisphere surrounding it to emit radiation in the same hemisphere.

In our case, it was previously measured and as found rather close to the near-normal ($\theta = 10°$) emittance value, with a relative deviation of 2–3% [34].

Eq.(10) shows the dependence with temperature. One assumes that $E(\lambda, \theta, T) = 1 - R(\lambda, \theta, T)$, so ideally reflectance should be measured at temperature *T* to estimate $\varepsilon_\theta(\theta, T)$. For practical reasons however, reflectance is more often measured at ambient temperature T_a. This requires the assumption that $R(\lambda, \theta, T) = R(\lambda, T_a, \theta)$. This assumption is not always met, but in our case leads to a good approximation of the real emittance at high temperature, at least up to 500°C [34,35].

3.4. Optical performance of solar absorbers

3.4.1. Principle of solar spectral selectivity

On one hand, a good solar receiver should be able to efficiently capture the solar radiation, in order to transmit the highest amount of energy possible to the heat transfer fluid. In other words, its absorption should be high for wavelengths in the solar range (0.28 - 4 µm).

On the other hand, when reaching a high temperature, due to its absorption of the solar irradiance and subsequent heating, the solar receiver should emit as little thermal radiation as possible, in order to limit radiative losses towards the ambient environment. Thus, its emission should be low for wavelengths in the infrared (thermal) range.

Therefore, at a given wavelength, high spectral absorptance and low spectral emittance are incompatible, and one must be preferred over the other. Therefore, a good solar receiver must ideally be **spectrally selective**, i.e., present a different optical behavior depending on the wavelength range: high absorption in the solar range, low emission (low absorption) in the infrared range.

Figure 18 shows the solar irradiance spectrum (ASTM G173-03 AM1.5 Direct + Circumsolar [31]) and blackbody radiation spectra at 100°C, 300°C, 500°C and 800°C (given by Planck´s law, Eq.(6)), all normalized to 1, and the ideal solar selective reflectance spectrum for a temperature of 500°C.

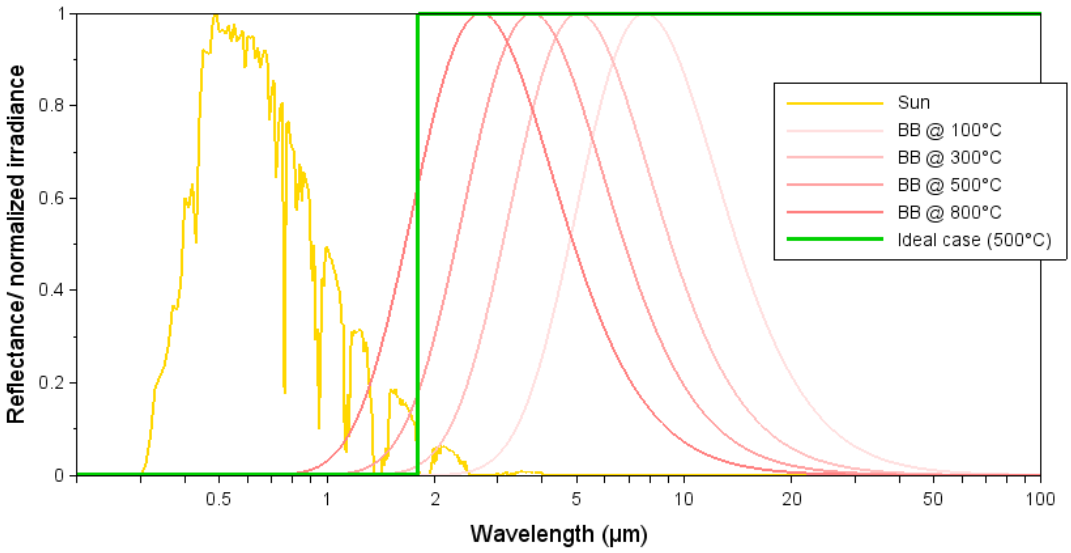

Figure 18. Solar spectrum (yellow), blackbody at 100°C, 300°C, 500°C and 800°C spectra and reflectance spectrum for an ideal selective coating working at 500°C (green)

As in the near infrared range, the solar and blackbody irradiance spectra tend to overlap, the optical behavior of an ideal receiver must switch as drastically as possible from high absorption (low reflectance) to low emission (high reflectance) in that spectral range. The position of this switch, or cut-off wavelength, depends on the receiver temperature. For low operating temperatures $T < 100$°C, the ideal absorption cut-off may be placed anywhere in the 2 to 4 µm region, since thermal emission is low and happens mainly beyond the solar range, so that there is very little or any overlap. Therefore, it is easier to create a surface that absorbs the maximum possible of the incident solar radiation, but does not re-emit the absorbed energy for such temperatures. For higher temperatures, this overlapping occurs at lower wavelength, depending on the temperature (Figure 18). The transition in the ideal case must therefore be placed at a lower position, typically between 1.5 and 2 µm.

3.4.2. Heliothermal efficiency

The efficiency of a solar absorber is illustrated by its solar-to-heat conversion efficiency, or heliothermal efficiency, $\eta(T)$. The heliothermal efficiency of an absorbing surface is equal to the ratio of the net radiative energy absorbed by the surface (i.e., absorbed − emitted) to the radiative energy received from the concentrating mirrors (Eq.(11)).

$$\eta\,(T) = \frac{\text{absorbed} - \text{emitted}}{\text{incident}} = \frac{\alpha_S \cdot \mathrm{C} \cdot \mathrm{I} \cdot \eta_{opt} - \varepsilon(T) \cdot \sigma \cdot (T^4 - T_0^4)}{\mathrm{C} \cdot \mathrm{I} \cdot \eta_{opt}} = \alpha_S - \frac{\varepsilon(T) \cdot \sigma \cdot (T^4 - T_0^4)}{\mathrm{C} \cdot \mathrm{I} \cdot \eta_{opt}} \quad (11)$$

α_S is the solar absorptance, $\varepsilon(T)$ is the thermal emittance at temperature T (measured at 8°). C is the concentration ratio, I is the incident solar flux density, σ is Stefan-Boltzmann's constant, T is the surface temperature (K) and T_0 (K) is the ambient temperature. η_{opt} is the optical efficiency of the concentrating mirrors. The values used to calculate the heliothermal efficiency were the same for the different types of samples studied in this work. These values are shown in Table 2.

Table 2. Value of the parameters used for the heliothermal efficiency

Parameter	Value
I	1000 W/m²
C	100
η_{opt}	1
T	500°C
T_0	25°C
σ	$5.67 \cdot 10^{-8}$ W/m²/K⁴

The absorbed energy depends on solar absorptance and incident concentrated solar flux (W/m²) ($\alpha_S \cdot \mathrm{C} \cdot \mathrm{I} \cdot \eta_{opt}$). Thermal losses are considered to be only radiative and are given by Stefan-Boltzmann law, which takes into account the temperature of the absorber (T) and its thermal emittance $\varepsilon(T)$. Convective and conductive losses are neglected, radiative losses being much higher.

By deriving Eq.(11), the sensitivity of heliothermal efficiency to the solar absorptance and thermal emittance of the absorber can be quantified for given incident flux and absorber temperature. For example, using parabolic trough conditions, with an incident flux Q_{sol} of 100 kW·m^{-2} ($Q_{sol} = C \cdot I \cdot \eta_{opt}$ with C = 100, I = 1000 W/m², η_{opt} = 1) and a coating temperature of 400°C (Eq.(12)):

$$\frac{\partial \eta(T)_{coating}}{\partial \alpha_S} = 1\,; \quad \frac{\partial \eta(T)_{coating}}{\partial \varepsilon(T)} = \frac{-\sigma T^4}{Q_{sol}} = -0.116 \quad (12)$$

It can be seen that the heliothermal efficiency of the coating is much more sensitive to the variation of its solar absorptance than to the variation of emittance. Indeed, when solar absorptance increases by 1%, heliothermal efficiency also increases by 1%, whatever the operating conditions ($\partial \alpha_S = \partial \eta(T)$). Meanwhile, a decrease of 8.6% in thermal emittance is necessary to obtain the same increase of 1% in heliothermal efficiency ($\partial \varepsilon(T) = -\partial \eta(T)/0.116 = -0.01/0.116$). For a solar flux of 500 kW/m² and a surface temperature of 650°C (e.g. solar towers), the sensitivity to emittance is -0.082. Therefore, for these conditions, increasing solar absorptance by 1% has the same impact on heliothermal efficiency as reducing thermal emittance by 12.2%. At this higher temperature, even though radiative losses are higher, the absorbed solar flux is much higher due to high concentration, and losses have a lesser impact on efficiency.

Heliothermal efficiency is the most relevant parameter to design and evaluate solar absorbers, as it not only takes into account their intrinsic optical properties, i.e., solar absorptance and thermal emittance, but also the CSP operating conditions in which they will be used. Therefore, in this manuscript, solar absorptance, thermal emittance and heliothermal efficiency will systematically be followed as performance parameters.

The existing structures of solar selective absorbers are explained in the following section, where their principle and behavior are discussed.

4. Solar selective absorbers

4.1. Types of solar selective absorbers

Solar absorbers are usually based on a metal or alloy structure. These materials are chosen for their durability at high temperatures in contact with potentially corrosive heat transfer fluids. Another advantage of these materials is that they conduct heat very easily, because they have electrons free to move through their crystalline structure, and the electrical field of the incoming solar radiation drives these electrons to oscillate and dissipate (transfer) heat. The most common materials used for high temperature receivers are stainless steels and Inconel (nickel-based alloy). For low temperature receivers, copper can also be used.

In the case of a shiny metal surface, little of the incoming radiant energy is absorbed as heat however, as it is mostly reflected. This reflection can be minimized by treating the surface of the metal. One of the simplest ways is to paint the metal surface black, so both light and heat are absorbed, and the surface gets warmer than a white or shiny surface. This is called a solar absorber, where a metallic surface is coated with a high-temperature paint that increases the solar absorption levels up to 95%.

This type of configuration is very mature and it has been improved over recent years, creating a durable coating that can be used in solar receivers working under atmospheric conditions and at temperatures higher than 500°C. Another important aspect of these solar absorbers is their high emittance reaching levels similar to that of absorptance. The emittance is an important factor when considering the overall performance of the absorber, following Eq.(11)). Indeed, high emittance will cause high radiative thermal losses and a reduced heliothermal efficiency.

To obtain metal surfaces with a low emittance while maintaining a high absorptance level, a material with spectrally selective properties can be added, creating what is called a solar selective absorber. This type of absorber has the property of absorbing as much as possible of the incident sunlight in the solar spectrum range and emitting as little thermal radiation as possible in the infrared region.

There are no natural materials with intrinsic selective properties that can be used as efficient selective absorbers. To create such absorbers, transition metal compounds and semiconductors have been found to act as selective materials. In most cases, absorbers with selective properties are obtained by adding several thin layers of different materials to the metallic surface, normally layers of different materials and compositions, to vary the complex refractive index between the layers, and in this way increase the solar absorption of the surface. To be able to decrease the emittance value of the surface, an infrared reflective layer is added between the stack and the substrate, which is in most cases also a metal. The design of solar absorber coatings is optimized taking into account two important parameters, intrinsic to each type of material used, called its optical constants, the extinction coefficient, k, and the refractive index, n.

A general structure of a solar selective absorber is normally based on three principal layers (Figure 19). The main layer is the absorptive layer, which aims at absorbing the highest amount of the incoming radiation. An infrared reflective sublayer is often added between the absorber layer and the receiver (substrate), to block and collect backwards the radiation emitted by the hot receiver. In some cases, it is also used to avoid having interdiffusion between the absorptive layer and the receiver. The topmost layer is an antireflective layer. The main purpose of this layer is to improve the absorptance of the absorptive layer by decreasing its reflection of the incoming solar radiation. In many cases, it also protects the coating from oxidation, acting as a diffusion barrier against oxygen, especially when working at atmospheric conditions. Each of these principal layers can in fact consist in an arrangement of several thin layers.

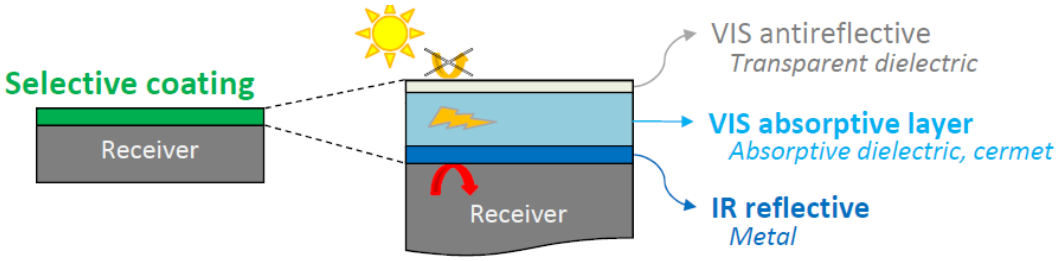

Figure 19. General structure of a solar selective absorber

There are several possible mechanisms to trap the incoming solar radiation: intrinsic absorbers; semiconductor-metallic layers; light trapping or textured absorbing surfaces; metal-dielectric composite coatings; interference stacks (multilayer absorbers); and tandem absorbers.

The first step to take when designing a solar selective coating is to decide on the materials to be used, normally alternating metals with dielectrics, metal-dielectric composites or metals with semiconductors. Selective properties can also be obtained by texturing the surface. In the following sections, the different types of selective coatings are explained in more details.

4.1.1. Intrinsic absorber

This is the simplest absorber configuration. It is not always considered to be a selective coating, due to the lack of efficient selective properties in most cases but is classified as a solar absorber. One of the simplest absorbers used since ancient times is achieved by covering the support surface (receiver) with a black paint, as can be seen in Figure 20.

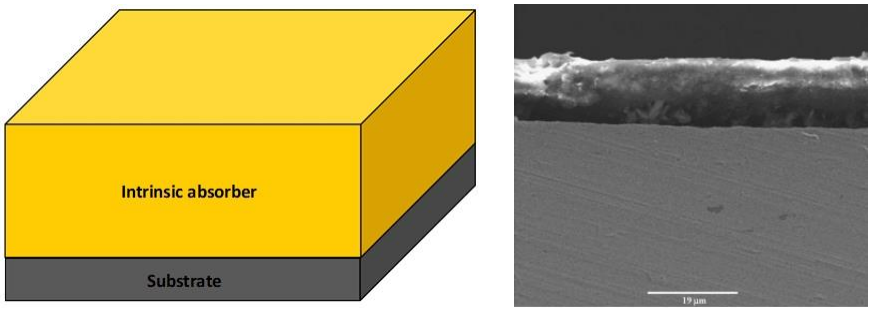

Figure 20. Structure of intrinsic absorber (left) and cross-section image of an as deposited intrinsic coating (SOLPHYCO) (right) [36]

This type of absorber is ideally obtained by adding to the metal substrate a specific material, which has intrinsic solar selective properties. It is not easy to find materials with natural intrinsic selective absorption properties. Materials with these properties are transition metals and semiconductors, such as W, TaC, TiC, MoO_3-doped Mo, Si doped with B, CaF_2, HfC, ZrB_2, V_2O_5 and LaB_6, as shown in most

selective coating reviews [37]. These types of materials were studied for the first time in the late 70s and early 80s [38]. Thanks to the energy level gaps of semiconductor materials, they are appropriate to absorb the photons of visible light. They absorb photons having energies greater than the band gap as a result of raising the material's valence electrons into the conduction band.

This type of coating has a low cost, especially due to the application method. It can be found in the form of paints, making it easy to be applied on a surface. Solar selective paints are inspired by the well-known highly absorptive, highly emissive, non-selective paint coating used in high temperature receivers, called Pyromark® 2500. It is a silicone-based solar paint that can survive thousands of heating and cooling cycles at temperatures between 600 and 1000°C. It has non-selective properties with high solar absorptance of 0.96 and high thermal emittance of 0.8 at 800°C. This high emittance is compensated by the high absorptance value when working under highly concentrated radiation, e.g., in solar towers. This type of coating is in fact the most used for solar tower plants and other receivers working under atmospheric conditions. There are also paint coatings with spectral selectivity, which combine the advantages of paints and maintains a moderate thermal emittance value around 0.55 at 77°C, called thickness insensitive spectrally selective (TISS) paint coatings [39], suitable for glazed and unglazed solar absorbers working at low temperatures (< 100°C).

4.1.2. Textured surface

Textured surfaces have been investigated for micro- and nanotechnologies. It has been widely used in photovoltaic technologies, mainly to improve the light absorption of solar cells. Various structures can be used, such as nanometric pyramidal textures (Figure 21). Compared to flat surfaces, these structures enhance light reflection and diffraction inside an intricate geometric shape created on the surface, increasing its mean free path in the material and generating light trapping phenomena. The solar absorptance of materials with high intrinsic absorption, i.e., bulk materials and substrates, or absorber coatings, can thus be further increased by carving a texture at its surface. This allows very high solar absorption [40], even in very thin materials, leading for instance to a price reduction of PV panels [41–43]. Some examples of these structures are gratings [44–46], cavity arrays [47,48], metamaterials [49,50] and nanoparticle arrays [51–53].

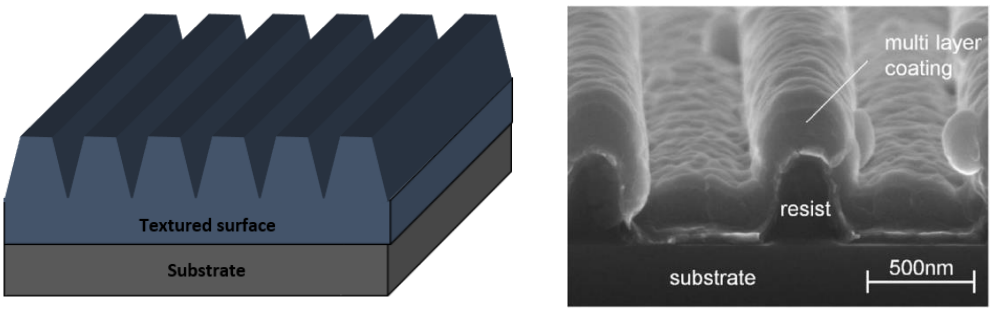

Figure 21. Textured coating structure (left) and microscopic image of a multilayered textured coating (right) [44]

The dimensions of the texturing can be microscopic or macroscopic, and light scattering can be isotropic or anisotropic. The resulting absorption and emission are defined by the geometrical parameters of the structure, such as the dimensions of the patterns (height/depth, distance), its orientation and the layer thicknesses.

With this type of configuration, the absorptance can reach up to 0.99 for wavelengths below 1.0 µm [54]. For instance, Barshilia et al. [55] show a nanometric multi-functional zinc oxide (ZnO) super-hydrophobic layer, fabricated on a surface to improve the absorptance (α_S = 0.97), also with good water repellence and anti-reflection properties in the visible range. This coating was stable up to 450°C in air and vacuum. In a paper by Sai et al. [56] a 2D surface grating with submicron holes is shown,

fabricated by fast atom beam etching with highly ordered porous alumina masks, demonstrating good thermal stability at high temperatures (800°C) under vacuum conditions, with an absorptance value over 0.85 and thermal emittance of 0.075 at 527°C. In [54], reactive sputter etching was used to texture a silicon wafer. The texturing was made of pillars with diameters and spacing smaller than the visible and near-infrared wavelengths and height comparable to these wavelengths. It showed an overall solar absorptance of 0.85 and thermal emittance of about 0.25, due to multiphoton absorption processes normally observed in thick Si crystals.

Bichotte et al. [44] (Figure 21, Figure 22) show a good example of diffractive periodic gratings, where a TiAlN multilayer structure deposited on a textured substrate has been optimized and tested. This work shows the improvement of the optical performance of the coating with the use of microtexturing, with solar absorptance changing from 0.91 to 0.95 while thermal emittance at 550°C increases from 0.32 to 0.38, compared to the same flat absorber. Surface texturing leads to an absolute improvement of the heliothermal efficiency from 1% to 3% depending on the solar power plant working conditions (concentration ratio and temperature).

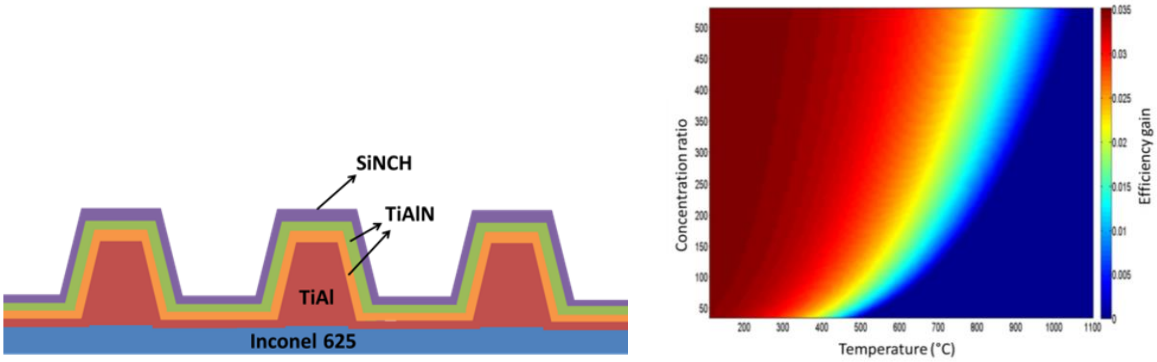

Figure 22. TiAlN multilayer coating structure with texturing: schematics (left) and efficiency gain (right) [44]

Overall, compared to more conventional solar absorber coatings, this type of textured surface is however usually more fragile and easily oxidized, with a catastrophic influence on its lifetime [57].

4.1.3. Metal-dielectric composite (cermet)

Metal-dielectric composites for solar applications, also called cermets, are composite materials made of nanosized metal particles embedded in a dielectric matrix, usually a porous oxide or other ceramics. This type of material is designed to take advantage of the properties of ceramics, such as high thermomechanical stability and good resistance to corrosion. The metal particles influence the optical response of the ceramic host, creating an effective medium with strong absorption properties. This is caused by Surface Plasmon Resonance (SPR) phenomena: the metal conduction electrons are excited by incident solar radiation, generating an electric field at the surface of the metal nanoparticles, which resonates with the electromagnetic field of the incident light. In cermets, these plasmons are localized at the surface of the metallic nanoparticles in contact with the dielectric phase, due to their differences in refractive index. These plasmons are thus called Localized Surface Plasmons (LSP) [58].

Good solar absorption can be obtained by finely adjusting the nature of constituents (e.g. for high temperature applications, transition metals and refractory ceramics), the composite thickness, and its metal particle concentration, size, shape and orientation. The metal volume fraction is usually below the percolation threshold (typically < 20%) and the size of the metal particles is lower than 100 nm.

Cermets are thus considered to have great possibilities for solar thermal applications and are widely used commercially on parabolic trough collectors, with strong absorption of the VIS and NIR radiation and a good thermal stability at medium temperatures (~ 400°C) under vacuum conditions.

One of the ways to improve this type of absorber is to create a double cermet coating, with High and Low Metal Volume Fraction cermet solar absorption layers, known as HMVF and LMVF, respectively. It is often associated with a metal infrared-reflective bottom layer, whose function is to reflect the thermal emission from the heated substrate, as the absorber layer is not always intrinsically selective. Also a top antireflective (AR) layer with low refractive index can reduce the surface reflection effectively [59] and is often added to the configuration to further improve the absorption performance. In this configuration, shown in Figure 23, the refractive index and subsequent transmission towards lower layers increase from surface to substrate, to better capture the incident solar light and favor its absorption. Commonly, an optimization is done for layer thicknesses, number of layers and composition of each layer.

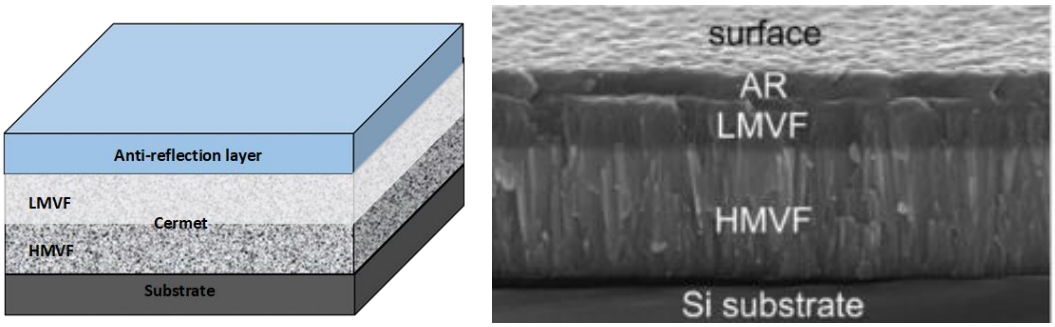

Figure 23. Double cermet structure (1) and cross-section of an as-deposited double cermet coating (2) [60]

Granqvist and Niklasson [61] first proposed the use of cermet materials in solar selective absorbing coatings in 1978. Many cermet absorbing coatings have been studied since, such as black Cr [62], Co-Al_2O_3 [63], Ni–Al_2O_3 [64], Pt-Al_2O_3 [65–67], black Co [68], Mo-Al_2O_3 [69–72], etc. Zhang and Mills [73] first proposed the double cermet absorption layer structure with a solar absorptance of 0.92 and a thermal emittance of 0.05 at 300°C. Afterwards, such kinds of coatings were extensively reported, for example Metal-AlN [74–76], Mo-SiO_2 [77,78], Mo-Si_3N_4 [79], W-Al_2O_3 [80,81], W–SiC(N)H [82], Zr-ZrO_2 [83], AlNi-Al_2O_3 [84], Ag-Al_2O_3 [85], NbTiON/SiON [60], Nb–NbN [86], black Ni [87], Nb–TiO_2 [88] and a-Si:C:H/Ti [89]. All these cermet examples have good solar absorptance ranging from 0.91 to 0.96 and significantly low thermal emittance around 0.10 at temperatures from 350°C to 500°C.

There are also other interesting options, such as multi-scaled Si–Ge coating layers ($Si_{0.8}Ge_{0.2}$) in SiO_2 [90], black oxide materials such as cobalt oxide (Co_3O_4) nanoparticles inserted in a SiO_2 matrix [91] or in a forest of copper oxide (CuO) nanowires [92].

One of the main disadvantages of this type of coating is the lack of high temperature durability in air and its potential high emittance, which limits its development. It is nevertheless easier to fabricate double cermet solar selective absorbing coatings than textured surfaces.

4.1.4. Multilayer absorber

Multilayer absorbers, also called multilayer interference stacks, or Dielectric-Metal-Dielectric (DMD) absorbers [58] consist in alternating thin layers of transparent dielectric and semitransparent metallic materials (Figure 24). This configuration uses multiple reflections between the layers to absorb light. As for cermets, Surface Plasmon Resonance (SPR) phenomena can occur when the metal layer is extremely thin. In DMD absorbers however, the metal particles are not separated by the dielectric matrix as they constitute a continuous layer. Consequently, their conductive electrons are free to

oscillate collectively when excited by incident light, creating Surface Plasmon Polaritons (SPP) that propagate as a wave along the interface between the metal and dielectric layers. SPPs are attenuated and scattered, causing destructive interference with incident light. As a result, reflection is strongly decreased and absorption is increased in the solar range, while the DMD is transparent in the thermal infrared range. If an IR-reflective (metallic) bottom layer and/or substrate is used, providing low emittance, a solar selective absorber coating is obtained.

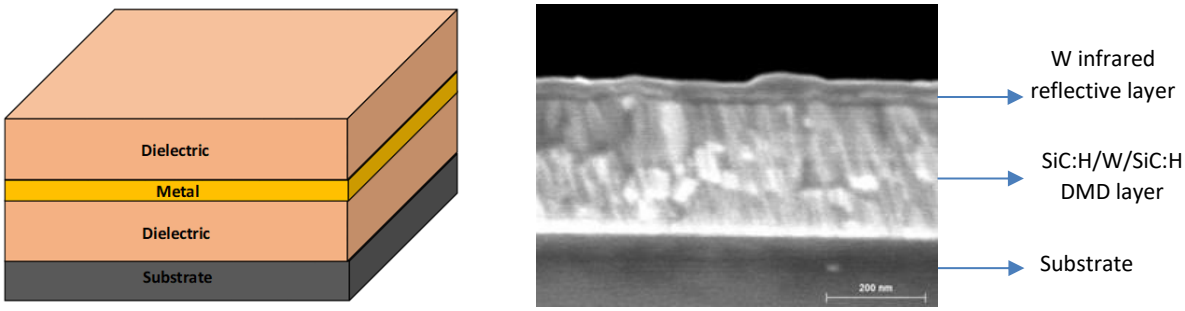

Figure 24. Dielectric–metal-dielectric stack structure (left) and example of SiC:H/W/SiC:H DMD (right) [93]

By applying optical theory for multilayer systems [94] using computer modelling [95,96], the optical properties of the multilayer design can be simulated and optimized, considering the candidate materials and their optical constants. For instance, in the case of a W/SiC/W/SiC multilayer absorber [93], the influence on simulated reflectance when adding each consecutive layer of the absorber is shown in Figure 25. The best absorptance (lowest reflectance in the visible range) was clearly obtained after adding the complete SiC/W/SiC multilayer absorber on top of the infrared reflective layer of tungsten (brown line).

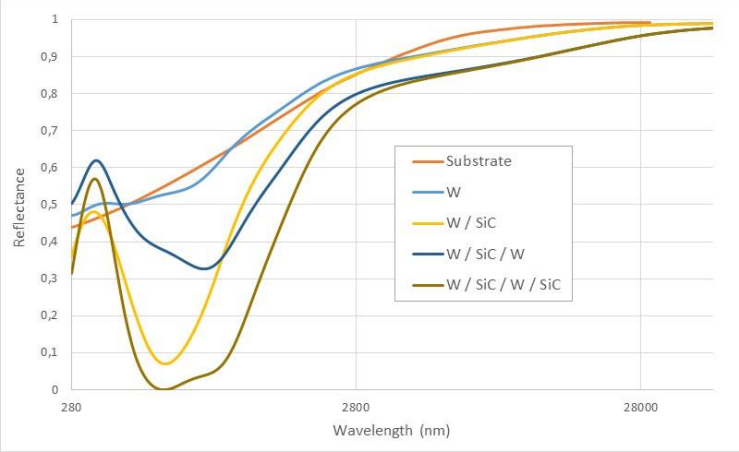

Figure 25. Spectral reflectance variation when adding consecutive layers to a W/SiC multilayer absorber [93]

Common dielectric materials used for multilayer absorbers are Al_2O_3, SiO_2, AlN, CeO_2, ZnS, MgF_2, MgO, HfO_2, CrO_2, TiO_2, etc. and the metals used are classically Al, Mo, Ag, Cu, Cr, Ti, Ni, Au, Pt, Zr, etc. Other multilayer absorber configurations using refractory metal silicides (TiSi, TiAlSi, etc.) in combination with TiO_2 or SiO_2 were also proposed by Kennedy et al. for parabolic trough applications [97].

Many such absorbers have been developed for high temperature solar thermal conversion applications [101–109] and cited in the literature for high temperature applications [99], as they are stable at medium-high temperatures (≥ 400°C). Overall, these coatings have a better stability after annealing in air compared to double cermet coatings [78]. A classic example is the AMA coating (Al_2O_3-Mo-Al_2O_3) with α_S = 0.92–0.95, ε(20°C) = 0.06–0.10 that shows a good thermal stability at 550°C in air [109]. Barshilia et al. [110] studied a multilayer absorber of Al_xO_y/Al/Al_xO_y deposited on copper showing

thermal stability up to 400°C with a significant drop of absorptance at 450°C, and better durability at higher temperatures with a Mo substrate, especially in vacuum. Another interesting work from the same research group was shown in [108] by Selvakumar et al. Their DMD stack of HfO_x/Mo/HfO_2 was also tested with a copper substrate and maintained its high selectivity after 2 hours at 500°C in air. At higher temperatures, there was a decrease in solar selectivity due to the formation of oxides. This illustrates the difficulty of finding good thermal stability while maintaining satisfactory spectral selectivity.

Also, multilayer absorbers are often fabricated by vacuum deposition techniques such as Physical Vapor Deposition, and fabrication costs can be high. Some researchers instead adopt wet chemical methods to reduce fabrication costs [111–113]. Chemical methods however lead to many structural defects, for example, their purity and density are not controlled well enough. Chemical interactions including oxidation and diffusion can consequently occur when high temperature is applied.

Overall, these disadvantages restrict the development of this kind of coating [114,115]. So far, to our knowledge no successful long-term high temperature (≥ 400°C) durability trials for multilayer absorbers have been recorded in the literature.

4.1.5. Tandem absorber

A tandem absorber is composed of two layers of materials with different optical behaviors: one behaves like a metal and the other like a semiconductor. Semiconductors with band gaps of about 0.5–1.5 eV and corresponding absorption edges from 0.8 to 2.5 µm will absorb the visible and near infrared spectrum of solar radiation. Metals are highly reflective in the thermal infrared range.

The simplest configuration is the absorber-reflector or metal-semiconductor tandem, combining a highly absorbing surface in the solar region (the semiconductor) and a highly reflecting surface in the infrared (the metal). A dark mirror can be made by covering a base metal of high infrared reflectance with a highly solar absorbing thin coating, or a heat mirror by covering an absorbing surface with a solar transparent infrared reflective coating. Semiconductors of interest include Si (1.1 eV), Ge (0.7 eV) and PbS (0.4 eV) [116–118].

More recently, transition metal oxides, nitrides and oxynitrides have successfully been used in tandem absorbers. A gradient of refractive index is created in the tandem by varying the composition of the two layers to obtain a metallic-like (higher N and/or O concentration and higher *n*) and semiconductor-like (higher N and/or O concentration and lower *n*) optical behaviors. Thanks to the metallic-like nature of the underlying component of the tandem (closest to the support metal), the use of an infrared reflective underlayer is not always necessary. An antireflective top layer is often added on top of the semiconductor-like upper layer of the tandem, to minimize optical losses. This way, the complete tandem absorber coating (Figure 26) presents a decreasing gradient of refractive index from the metallic substrate with high *n* towards air with *n* = 1.

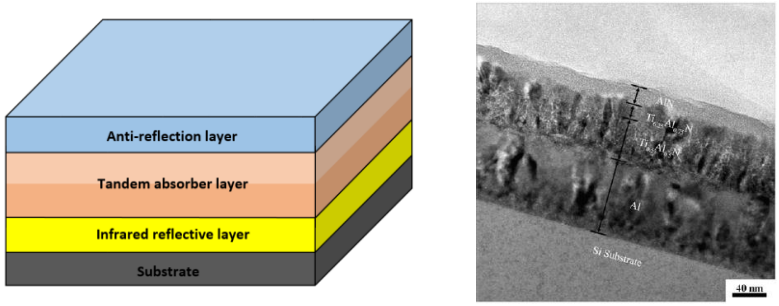

Figure 26. Tandem absorber structure (left) and microscopic image of a tandem absorber coating (right) [119]

Due to their excellent oxidation resistance and thermal stability, these materials have high potential as medium/high temperature solar selective absorber coatings. They are also known for their diffusion barrier properties that can prevent the diffusion of elements of the support material inside the absorber coating, a common source of degradation of optical performance, especially emittance. They can also act as diffusion barriers for oxygen, preventing or limiting oxidation. They are therefore suitable for high-temperature solar receivers operated in air [120].

Many such tandem configurations were reported in the literature, including TiAlN/TiAlN [119,121], TiAlN/TiAlON [120,122–125], TiAlN/TiAlSiN [126], TiAlSiN/TiAlSiON [127], TiAlN/AlON [128], TiAlC/TiAlCN/TiAlSiCN [129], HfMoN/HfON [130], NbTiON/NbTiON [60], AlSiN/AlSiON [80], NbAlN/NbAlON [131] and CrMoN/CrON [132]. The most proven thermally stable tandem absorber coatings are made by combining titanium and aluminum. $TiAlN_x/TiAlN_y$ has demonstrated long-term thermal stability at 500°C after 1,000 hours of isothermal treatment under static air conditions with a α_S equal to 0.91 and a $\varepsilon(500°C)$ equal to 0.31 [121]. TiAlN/TiAlON has been shown to be stable up to 1,000 hours in air after cyclic heating from room temperature to 347°C (α_S = 0.93, $\varepsilon(500°C)$ = 0.07) [125]. A coating comprised of TiAlCrN/TiAlN tandem absorber was also found with good optical properties (α_S = 0.91, ε = 0.07) and thermal stability up to 600°C in air after 4 hours [133]. In [60] a NbTiON/SiON tandem absorber exhibited high absorptance of 0.95 and low emittance of 0.07 with good thermal stability for 40 hours at 500°C under vacuum conditions.

Despite their diffusion barrier properties, metal diffusion from the substrate is one of the major sources of degradation of optical performance for this type of absorber, since it can strongly modify the composition/structure and refractive index gradients. A diffusion barrier layer can prevent metal diffusion inside the coating [120].

4.2. Main commercial absorber configurations for medium-temperature CSP plants

Most commercial CSP plants operate at medium temperatures, ranging from 250°C up to 400°C. This temperature range correspond to both Parabolic Trough and Linear Fresnel collectors working with oil as heat transfer fluid. The operating temperature limit is predicted to increase to levels of around 500°C with the development of Direct Steam Generation. Also, in the case of parabolic troughs, most of the commercial receivers work under vacuum conditions inside a glass tube, as explained in section 2.4.2 p.26.

For these technologies at 250-400°C, cermet absorbers (Mo-Al_2O_3, W-Al_2O_3, etc.) are the most widely used solar selective absorber coatings. The most common commercial cermets are: for mid-temperatures, SS–C, SS–AlN, CrN–Cr_2O_3, $TiNO_x$, a-C:H/Cr, Ni–NiO, etc.; for high-temperature applications, Mo–SiO_2, W–Al_2O_3, Mo–Al_2O_3, SS–AlN, W–AlN, Mo–AlN, etc. Nitto Kohki, Turbosun, GRINM, Alanod Solar, Almeco-TiNOX, Ikarus Coatings, S-Solar, Archimede and Rioglass companies are some examples of commercial coating manufacturers. The configuration, optical properties and thermal stability limit of each commercial coating of the aforementioned companies is shown in Table 3.

Cermet coatings based on titanium oxynitrides as the absorbing layer are produced by a German company named Almeco-TiNOX. They are deposited on aluminum, copper or stainless steel sheets by PVD (electron beam vapor deposition and sputtering) [134]. A TiC diffusion barrier is deposited at the bottom, to prevent metal atoms from entering the absorber layer at high temperatures. The top layer is a protective and antireflective layer made of fused quartz, extremely hard and scratch-resistant. The coatings are thermally stable in vacuum up to 400°C [135–137].

Table 3. Main commercial solar absorber coatings [135]

Application	Company	Country	Products	Absorber materials	Solar absorptance	Emittance	Thermal stability in vacuum	Ref.
Low temperature solar thermal	Almeco-TiNOX	Germany	TiNOX®	Ti oxynitrides	0.95±0.02	0.04±0.02 @ 100°C	400°C	[134]
	Alanod Solar	Germany	Mirosol® TS	Metal oxide	0.95	0.05 @ 100°C	-	[138]
	Asoluna (ex S-Solar)	Sweden	SunStrip Lazerplate	Graded Ni-NiO	0.95	0.05-0.08 @ 100°C	300°C	[139,140]
	TurboSun	China	_	SS-AlN	0.92-0.96	0.08-0.10	330-500°C	-
	GRINM	China	GRIST 70/90/42	_	0.96	0.09 @ 400°C	400°C	-
Medium/high temperature CSP	Rioglass Solar Ex-Siemens Solel Ex-SCHOTT	Spain Israel Germany	UVAC 70-7G PTR 70-4G	W-Al_2O_3, Mo-Al_2O_3	0.96 0.94	0.095 @ 400°C	350-500°C	[141,142]
	Angelantoni-ENEA Archimede	Italy	HCEOI-12 Oil HCEMS-11 MS HCESH-12 DSG	Mo-SiO_2, WN-AlN, W-Al_2O_3	≥ 0.95	0.103 @ 600°C	580-600°C	[143]

Another cermet composite coating based on SS-AlN is manufactured by TurboSun in China [74], this type of configuration is widely used in low temperature solar collector tubes in China [144]. China is a leader in the solar water collector market (87.5 GW installations) [145] with companies such as TurboSun that had already produced 3.5 million U-shaped vacuum solar collectors by the end of 2011. The SS–AlN coatings are deposited by magnetron sputtering [73,144,146]. The top layer of this cermet coating is made from aluminum nitride that works as an antireflective layer. Their solar absorptance is within the range of 0.94–0.95, emittance is within 0.12–0.14 at 350°C, and the coatings are thermally stable in vacuum up to 500°C.

Another example is a multilayer coating with a nickel diffusion barrier layer, an absorbing layer of graded Ni–NiO and an antireflective layer on aluminum sheets, manufactured for Sunstrip fins in Sweden. It has been also developed for low temperature solar thermal applications. These commercial solar absorber coatings have a high solar absorptance of 0.95 and a low thermal emittance of 0.05-0.10 at 100°C [147,148].

The most standard commercial receiver tubes for Parabolic Trough collectors are manufactured by Rioglass Solar, funded in 2007. It is nowadays the world leader in the development and production of receiver tubes and mirrors, with the latest receiver tubes “UVAC 70-7G” (ex. Siemens-Solel) and “PTR 70-4G” (ex. Schott Solar) that guarantee solar absorptance higher than 0.95 and thermal emittance lower than 0.10 at 400°C, for oil-based parabolic trough technology [141]. Rioglass acquired the technology from Siemens/Solel, based on W-Al_2O_3 and Mo-Al_2O_3 with good thermal stability in the range of 350/500°C under vacuum conditions [69,149]. Afterwards, Rioglass also signed an agreement with Schott Solar in 2015 for the acquisition of its receiver business. Currently, Rioglass Solar has signed a contract for the largest Parabolic Trough CSP project in the world.

Most of the previous commercial coatings have a thermal stability up to maximum level of 500°C under vacuum conditions. It is difficult to find thermally stable coatings at higher temperature. One exception is also a double cermet configuration, manufactured by Archimede in Italy for products “HCEMS-11 Molten Salts” and “HCESHS-12 Direct Steam Generation”, with an absorptance of 0.95 and an emittance of 0.10-0.13 at 600°C [77,81,143,150–152]. This coating has been proven to withstand a temperature of 600°C under vacuum conditions. As these commercial coatings are developed for and tested under vacuum conditions in view of their application on PT receivers [153], there is a lack of information on their thermal stability under atmospheric conditions. Thus they cannot be directly envisaged for receivers intended to work in air, such as LFR and central tower technologies.

5. Conclusion

Global climate problems are principally caused by the increase of CO_2 emissions due to human activity, closely related to the combustion of fossil fuels. The high potential of concentrated solar power (CSP) has been identified as an alternative to conventional electricity production, with more than 6 GW_e already installed worldwide. Four main CSP technologies exist, but parabolic trough and solar towers represent the almost entirety of the installed capacity. Different types of solar receivers are used depending on the technology, but their ideal optical and thermal behavior is similar: high solar absorptance, low thermal emittance in the infrared, resulting in high solar-to-heat conversion (heliothermal) efficiency are the main performance parameters for solar absorbers. To achieve this, they must present a spectral selectivity, with high spectral reflectance in the solar range and low reflectance in the infrared range. These characteristics can be obtained using different types of solar selective absorbers, in the form of surface treatments or coatings on metallic pipes, from the simplest configuration to more complex and optimized configurations: multilayer, cermet and tandem absorbers. Solar selective absorbers have been intensively studied in the past ten years. Great improvements have been attained on the optimization of coatings, reaching very high solar absorptance, between 0.95 and 0.96, and low emittance levels of 0.10 at 400°C. Some of these configurations are found in commercial CSP plants.

Nonetheless, the durability of such coatings during the lifetime of the plant, around 25 years, has not yet been demonstrated, although it is of vital importance for the deployment of CSP technologies. This thesis thus investigates the thermal stability and durability of typical solar absorbers. It can be seen that: i) absorbers are mainly developed for receiver tubes protected under vacuum (parabolic troughs); ii) high temperature stability tests are specific to each supplier; iii) very few aging tests are carried out in air, whereas this is imperative for LFR and central tower technologies; iv) in most aging studies, only solar absorptance and thermal emittance are considered when following the evolution of the absorbers optical performance with aging, while said performance is better represented by the solar-to-heat conversion (heliothermal) efficiency, also taking into account the absorber working conditions (concentration, temperature). Representative aging studies are therefore necessary to correctly predict the absorbers operating life.

In the next chapter, the problematic of selective absorber aging will thus be discussed at length. Possible sources of degradation and subsequent aging phenomena will be explained, as well as a critical literature review of existing aging facilities and protocols.

Chapter 2 - Aging and durability of solar absorbers: a critical analysis

To encourage CSP deployment, there is a crucial need to improve current technologies to achieve both lower costs and higher efficiencies. For example, the SolarPACES program [154], a collaborative research program of the International Energy Agency, has identified several tasks for the improvement of CSP plants and other relevant applications in this field. The task for "Solar technology and advanced applications" deals with the advancement of the technical and economic viability of emerging solar thermal technologies and their validation. The main objective of this task is to achieve a further significant cost reduction for new plants while guaranteeing a high performance over the lifetime of the plant.

For this purpose, two main levers are available, i.e., working at higher temperatures and under atmospheric conditions. These enhanced requirements can evidently become very demanding for CSP receiver materials, causing potentially harsher sources of degradation and subsequent aging phenomena. The latter need to be studied thoroughly so as to validate the performance and durability of new and improved CSP components. Aging protocols and facilities already exist for this purpose, as can be found by reviewing the literature, but they need to be adapted and standardized to offer more reliable aging and durability analyses. This chapter will develop these different topics at length.

1. Expected improvements in next generation CSP technologies

1.1. Increasing working temperatures

As mentioned before, the role of a solar receiver/absorber is to convert solar radiation into heat. The efficiency of this conversion is the heliothermal efficiency, defined in Chapter 1 (Eq.(11) p.34). This heat can be used directly or injected in a thermodynamic cycle to produce electricity (heat-to-mechanical work conversion).

The ideal case of a thermodynamic cycle is called the Carnot cycle, the efficiency of which is given by Eq.(13), for a solar absorber at temperature T_{abs} and ambient temperature T_0.

$$\eta_{carnot} = 1 - \frac{T_0}{T_{abs}} \tag{13}$$

A good approximation of a semi-ideal case is represented by the Chambadal-Novikov (C-N) efficiency, which is the efficiency of a semi-ideal heat engine operating at maximum power output, where the heat transfer is irreversible (Eq.(14)).

$$\eta_{C-N} = 1 - \sqrt{\frac{T_0}{T_{abs}}} \tag{14}$$

Figure 27 illustrates the Carnot and Chambadal-Novikov efficiencies as a function of temperature. As can be expected from Eq.(13) and (14), these efficiencies increase with temperature. Figure 27 also shows an estimated range of the net annual average thermal-to-electric conversion efficiencies of common heat engines that can be integrated in solar thermal systems. They all follow the Chambadal-Novikov efficiency trend.

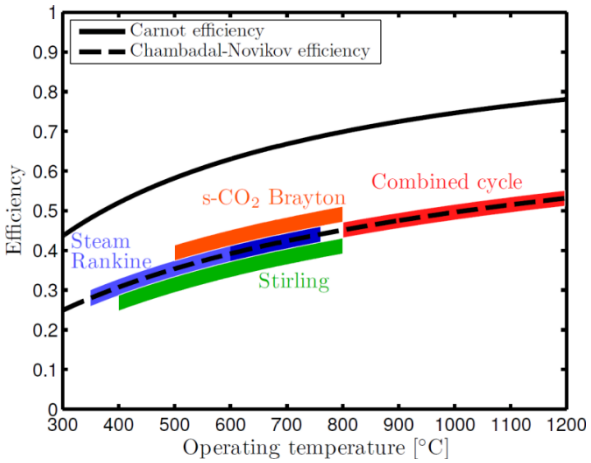

Figure 27. Thermal cycle efficiency vs. temperature [155,156]

Most current CSP plants operate at temperature ranges from 250°C up to 565°C, depending on the type of technology, the configuration used (especially the heat transfer fluids) and the scale of the plant. As the global efficiency of a concentrated solar power plant is the combination of optical and thermodynamic efficiencies, reaching higher temperatures would be one way to further increase the global efficiency of the plant. It also allows increasing storage densities by increasing the temperature difference of the process, following Eq.(15). This increase in the energy stored directly reduces the total cost of the solar collector field and the specific cost of the storage units.

$$Q = mC_p\Delta T \tag{15}$$

Q is the energy stored by the storage medium, m and C_p are its mass and specific heat, and ΔT is the temperature change during the process (maximum – minimum temperature of the storage medium).

This objective can be found in many ongoing research projects, where the main aim is to increase the operating temperature. In the case of solar tower plants, there are projects such as: the Next-CSP EU project using ceramic particles as the heat transfer fluid, reaching operating temperatures up to 800°C; the Polyphem EU project using pressurized air at 750°C; the Gen3 US DOE project using nanoparticles at 700°C, etc. For parabolic troughs, the High Performance Solar 2 (HPS2) project investigates the use of a higher temperature heat transfer fluid (such as molten salts) on this type of technology. For Linear Fresnel technology, the French ADEME LFR500 project used pressurized steam at 500°C.

Under these enhanced working conditions, there is also a need for more robust and durable components, able to withstand these fluids at high temperatures. Thus another important research topic, that runs parallel with the search for a new heat transfer fluid, is the development of cost effective, efficient and durable absorber materials for the receivers, where the most extreme working conditions are met.

1.2. Working under atmospheric conditions

Most CSP plants in operation around the world today are parabolic troughs, where the receiver works in vacuum (Figure 12 p.27). As higher working temperatures are sought for, central towers are meant to come into play at an increasingly larger scale. For these technologies, the receiver at the top of the tower cannot be maintained in vacuum, for practical reasons. Also, Linear Fresnel technologies propose cost reductions via the use of receivers operating at ambient static air, without having recourse to expensive bellows to maintain them under vacuum, as is the case for parabolic trough receivers. Consequently, new absorber materials for solar receivers are now expected to sustain simultaneously high temperatures and atmospheric conditions.

The latter can however be very demanding for absorber materials, as CSP operating conditions, and especially these enhanced ones, generate many sources of potential degradation of the materials microstructure and optical performance. The nature of these sources of degradation is presented in section 2. Their impact on materials and subsequent aging phenomena will be detailed in section 3.

2. Correlated sources of degradation for CSP receivers

CSP receivers are submitted to extreme conditions of use, that can be challenging to their integrity and durability. The main suspected causes for material degradation are summarized in this section.

2.1. Concentrated solar radiation

The concentrated solar radiation is the solar flux density (in kW/m^2) concentrated by a collector (mirror) onto the receiver, with a concentration ratio from few tens to few hundreds or higher, depending on the type of CSP plant (Table 1 p.20). All solar receivers in CSP systems, by definition, receive this concentrated solar radiation, and the absorber material must be able to withstand it. This radiation varies in both spectral range and intensity, depending on the materials used as collectors (mirrors), on the concentration ratio of the technology and on the climate and weather conditions under which the receiver operates.

2.1.1. Spectral range and UV flux density

Collectors are reflecting surfaces with high specular reflectance in the solar spectrum. They are usually made of silver or aluminum, due to their excellent reflective properties in the spectral range of interest. Most commercial CSP plants use Ag-based collectors [157]. The two metals have a different spectral behavior. Ag is partly absorptive in the UV range of the solar spectrum (280 – 400 nm), as shown by its low reflectance below 350 nm (Figure 28, left), then becomes highly reflective. Thus when considering the standard solar spectrum (ASTM G173-03 AM1.5 Direct + Circumsolar [158], interpolated with a 1 nm step), the solar reflectance of Ag in the UV range is 0.73, while it is 0.96 in the whole solar range (Table 4). Al is less reflective than Ag, but over a larger spectral range including UV (Figure 28, right), leading to the same solar reflectance in the UV range than in the whole solar range of around 0.92.

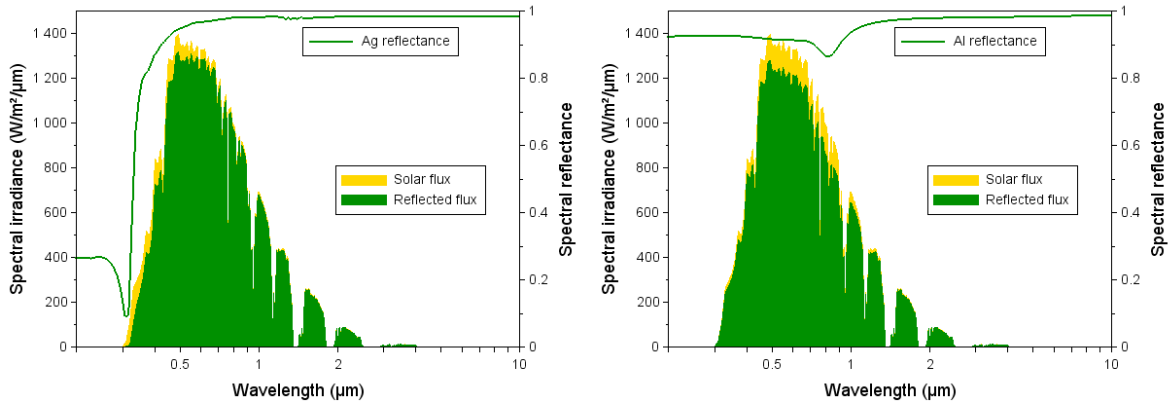

Figure 28. Solar spectrum, spectral reflectance and reflected spectrum of Ag (left) and Al (right)

Considering a receiver with solar absorptance α_S = 0.95, the absorbed UV flux density can amount to as high as 2-3 kW/m² for a concentration ratio C = 100 (parabolic troughs), and 20-30 kW/m² with C = 1000 (solar towers). UV photons being highly energetic (3 – 4.5 eV), they can be potentially damaging for materials, especially at such high flux densities. Indeed, they are energetic enough to break some chemical bonds and cause chemical reactions, such as photodissociation.

Table 4. Solar flux densities incident, reflected (collector) and absorbed (receiver) in UV and complete solar ranges (based on standard ASTM G173-03 AM1.5 Direct + Circumsolar solar spectrum [158], interpolated with a step of 1 nm)

Spectral range	Sun	Collector			Receiver (α_S = 0.95)	
	Solar flux density (kW/m²)	*Material*	*Reflected flux density (kW/m²)*	*Solar reflectance (integrated over spectral range)*	*Absorbed concentrated flux density (kW/m²)*	
					C = 100	*C = 1000*
UV (0.28 – 0.4 µm)	0.031	Ag	0.022	0.732	2.1	21
		Al	0.028	0.926	2.7	27
Complete solar (0.28 – 4 µm)	0.900	Ag	0.864	0.960	82.1	821
		Al	0.830	0.922	78.9	789

Moreover, CSP plants are installed in regions with high DNI, often in dry and high elevation regions. For instance, the highest DNI resource in the world (3536 kWh/m²/year) is found in the Atacama Desert in Chile (mean elevation ~ 2500 m). At high elevation and in dry weather, both the atmosphere thickness and water vapor content, that solar radiation encounters before reaching the ground, are smaller, so that the relative amount of incident UV radiation (280 – 400 nm) is even higher: e.g. 4.8% of the complete solar spectrum of the Atacama desert, vs. 3.9% for the standard solar spectrum [159]. Therefore, the concentrated UV flux density actually seen by CSP receivers can be even higher than already mentioned in Table 4.

2.1.2. Weather fluctuations

Weather fluctuations have a direct impact on the solar radiation incident on the collector, and consequently on the concentrated solar radiation seen by the receiver. Two typical configurations can be considered: sunny days and cloudy days. Figure 29 shows examples of such configurations, where Direct Normal Irradiance (DNI) levels were recorded during a statistical study conducted by Boubault et al. [36] at the Odeillo solar furnace (France).

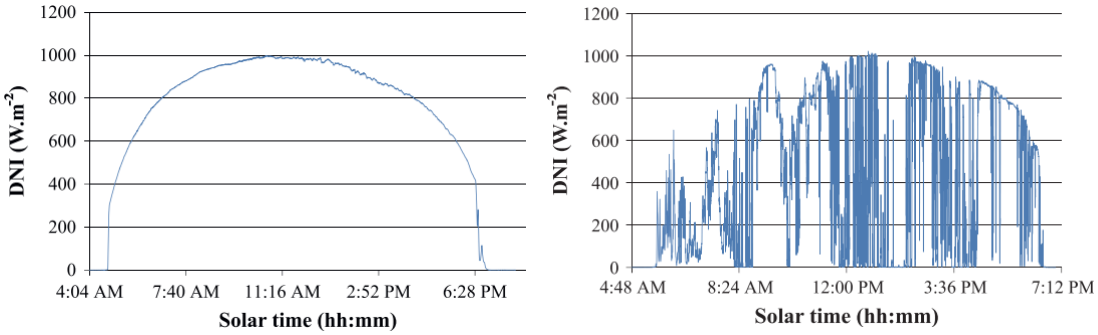

Figure 29. DNI level for a sunny day (left) and a cloudy day (right) for the site of Odeillo [36]

During the cloudy day (Figure 29, right) there were 427 DNI peaks, equivalent to 214 cloudy spells. The average amplitude of the DNI peaks (raise or drop) was 316 W/m², with an average DNI variation velocity of 23 W/m²/s. What is more, in a concentrating system, these DNI variations are multiplied by the concentration ratio *C*. With *C* between 40 and 1000 in CSP systems, the variation of the concentrated solar radiation seen by the receiver is typically between 0.9 and 23 kW/m²/s. This causes very fast variations of high amplitude of flux density received by the absorber materials, and consequently, intense thermal cycling and thermal shocks. Moreover, the flux density is not perfectly homogeneous throughout the receiver due to the imperfections of the collector, causing local gradients of concentrated solar flux and temperature.

Sunny day operation (Figure 29, left) also causes thermal cycling, with lower period and velocity, due to day/night cycles. In any case, this intense thermal cycling can be strongly detrimental to the thermomechanical integrity and optical performance of the receiver/absorber, as will be further explained in section 3.

2.2. Temperature

As mentioned, the direct corollary to the incident concentrated solar radiation on the absorber is the temperature profile it imposes on it. Indeed the receiver absorbs this radiation and consequently heats up, generating high levels of temperature, rapid heat ramps (°C/s) and thermal shocks. An example of the dependence of the surface temperature of a sample cyclically illuminated in a solar furnace, to the concentrated solar flux density it receives, is illustrated in Figure 30. When the concentrated solar flux density is varied from 250 to 500 kW/m² (typically corresponding to C = 250 – 500), the sample surface temperature varies from 450°C to 650°C. This occurs in only a few minutes, causing quick temperature variations of around ± 20°C/s.

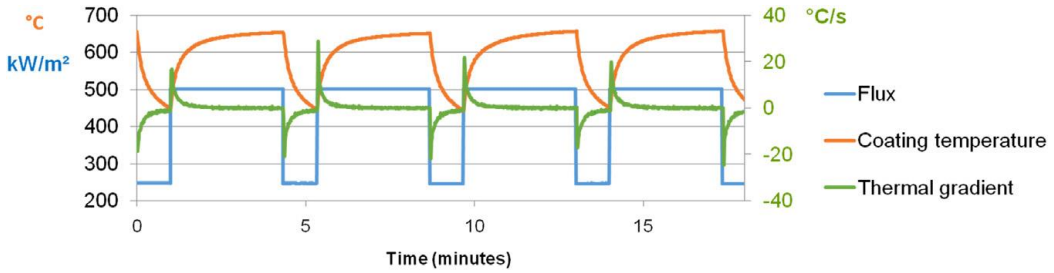

Figure 30. Example of correlation between concentrated solar flux (kW/m²), surface temperature (°C) and velocity of temperature variation (°C/s) [160]

Overall, the temperature reached by the receiver surface depends on many factors, influencing the energy balance of the receiver (Figure 31):

- the concentrated solar irradiance received from the collector (P_{sol}), the solar absorptance of the receiver (α_S), the ambient temperature, all accounting for thermal input;
- the thermal emittance of the receiver (ε), its thermal conductivity, the convection coefficient with the heat transfer fluid (HTF) and the mass flow rate of the latter, all causing thermal output for the receiver, via useful heat transfer (P_u) or heat losses (P_{rad}).

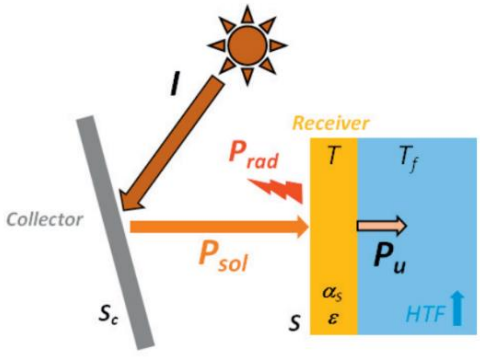

Figure 31. Conversion from incident solar flux to useful heat by a CSP receiver

It is worth noticing that the highest temperature is reached at the receiver surface, where the solar flux is concentrated, and where most of it is absorbed. The heat generated is then transferred by conduction towards the inner part in contact with the HTF. The receiver surface is typically 40-50°C higher than the operating temperature of the heat transfer fluid itself.

Moreover, when considering the receiver temperature, it is also paramount to take into account:

- its rapid and frequent fluctuations by several hundreds of degrees, directly linked to that of the concentrated solar flux density incident on the receiver (section 2.1 and Figure 30), causing thermal cycling and thermal shocks;
- the duration for which high temperature is maintained, i.e., several hours each day, up to 24-hour operation if large enough thermal storage is installed (e.g. 15-hour storage at Gemasolar central tower), and this cumulatively up to the 25 years of operation corresponding to the typical lifetime of a CSP plant;
- the fact that receivers usually associate several materials, especially in the case of solar selective absorber coatings, that do not physically react in the same way to temperature. For instance, ceramics and metals have very different thermal expansion coefficients, which can generate mechanical stress in the architecture of the absorber (Figure 32). Tensile or compressive stress can appear under temperature increase, taking into account that coating-to-substrate stress is classically compressive before heating and that differential dilatation can induce in this case tensile stress. Such fact can lead to degradations of the whole coated system (cracking, delamination of the coatings).

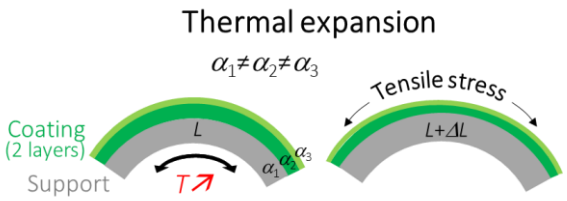

Figure 32. Illustration of thermal expansion on a tubular solar receiver covered with an absorber coating associating materials of different thermal expansion coefficients (α) [161]

High temperatures (> 400°C) for long durations, and especially associated with thermal shocks, can cause irreversible physicochemical changes in the absorber, and subsequent degradations of their optical performance, as will be further explained in section 3.

2.3. Atmospheric conditions

In parabolic trough systems, the receiver is protected with an evacuated glass tube, so the receiver works under vacuum conditions. Contrarily, central tower and LFR receivers are exposed to atmospheric conditions by design. Consequently, all the environmental factors can have an impact on the absorber surface. Atmospheric conditions can have damaging chemical effects on the absorbers, especially at high temperature, when compared to vacuum conditions for PT receivers.

Ambient air is usually composed of 78.09% N_2, 20.95% O_2, 0.93% Ar, 0.04% CO_2, and small amounts of other gases. It also contains a variable amount of H_2O vapor, with an average of around 1% at sea level, and 0.4% over the entire atmosphere. Other compounds such as pollutants can also be present, for instance NO_x and SO_2. If N_2 and Ar are inert gases, all these other species contain O and can chemically interact with absorber materials, sometimes dramatically, as will be further explained in section 3.

Atmospheric conditions strongly depend on the location and elevation, which influence ambient temperature, cloudiness, dryness, wind, rain, etc. CSP plants often operate in deserts with high DNI levels, in order to maximize the heat production of the plant. Such environments are often found in dry regions, some at high elevations (e.g. Atacama region in Chile). In some sunny regions, deserts are however close to sea coasts (e.g. United Arab Emirates, Saudi Arabia, etc.), and the presence of rain,

high humidity, dew and salt sprays are also to be considered. Sand and dust particles can also be found in the atmosphere, with potentially high kinetic energy able to also cause physical damage.

2.4. Heat transfer fluids

The use of most heat transfer fluids, such as air, steam or molten salts, especially at high temperature, can be chemically damaging for the inner wall of the receiver [162–164]. New generations of high thermal conductivity HTFs now include liquid sodium and chloride salts, posing even bigger challenges in terms of receiver materials durability [165]. These issues will however not be considered at length, since this thesis focuses on the outer surface of CSP receivers covered with solar selective absorber coatings and the durability of their optical performance.

More to our point are the high mechanical stresses induced for long durations on the receiver and its coatings, by pressurized HTF (steam, air) at levels around 100 bars (Figure 33). Also in some cases, the HTF distribution inside the receiver, due to gravity, does not match the concentrated flux distribution, generating temperature inhomogeneities and thermal gradients on the receiver (Figure 34).

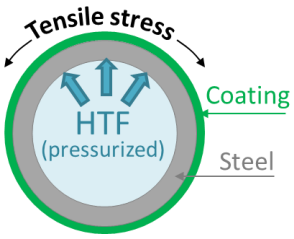

Figure 33. Illustration of mechanical stress generated by pressurized heat transfer fluid [161]

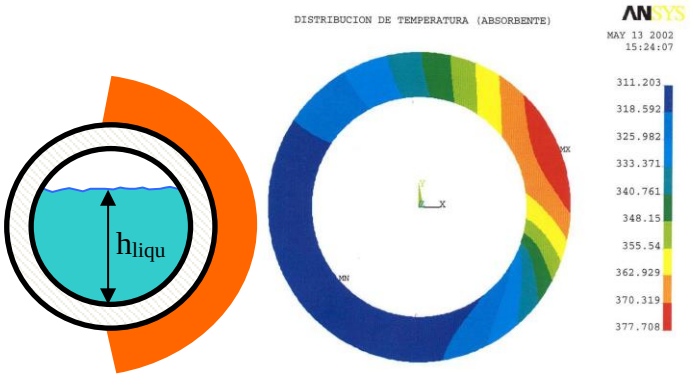

Figure 34. Steam HTF (left) and subsequent temperature (right) distribution on a PT receiver with Direct Steam Generation (on the left, the PT reflector in symbolized in orange) [courtesy E. Zarza, CIEMAT/PSA]

2.5. Conclusion on the sources of degradation

As a summary, Table 5 gathers the different sources of degradation listed above, depending on the type of CSP technology, and the potentially damageable impact they can have on the receiver (ranging from strong = + + + to null = - - -). It becomes evident that receivers in central towers are the most at risk, cumulating high concentrations, temperatures and exposure to ambient atmosphere. LFR receivers are also at risk as they operate in air, especially since the next generation of LFR is meant to work at higher temperatures (e.g. Dacheng Dunhuang 50 MW LFR/molten salts plant in China).

Overall, these many sources of degradation create harsh working conditions with potentially dire consequences on the absorber materials integrity and performance. The physicochemical phenomena occurring in the materials under the influence of these combined sources of degradation, amounting to material aging, are detailed in the next section.

Table 5. Sources of degradation vs. CSP technologies

Sources of degradation	*Central tower*	*PT*	*LFR*
Concentrated solar radiation	+ + + High (*C* = 1000)	+ Medium - Low (C = 80 - 120)	+ Low (*C* < 50)
Temperature (HTF)	+ + + Up to 565°C so far (molten salts, DSG) Towards higher T (air)	+ + 350 – 400°C (oil) 565°C (molten salts)	+ + 250 – 350°C (steam, oil) 535°C (molten salts)
Atmospheric conditions	+ + + Ambient atmosphere	- - - Vacuum	+ + Static air (receiver behind glass window)

3. Subsequent aging mechanisms for CSP receivers

3.1. Aging vs. degradation

In the previous section, several sources of degradation for CSP absorber materials were identified. As a response to the application of these sources of degradation, the microstructure and functional properties of the exposed materials will evolve as a consequence of physicochemical phenomena that will be described in this section. However not all these phenomena are necessarily damaging to the materials or their performance. Therefore in this section the notion of aging will be preferred. As a matter of fact, in metallurgy, aging even refers to the extended heat treatment processes for strengthening alloys, with positive impact in that case.

Here aging will designate the exposure of materials to real or artificially reproduced working conditions related to their use in CSP applications, using aging protocols and facilities that will be presented in section 4. Aging phenomena are considered as the consequence of this exposure on the materials microstructure, investigated by material characterization, after aging tests are applied.

Performance requirements for CSP absorber materials can be formulated on the basis of many criteria, but none is as paramount for the global efficiency of the CSP system as the absorber optical performance. Therefore, it is the evolution of their optical properties (spectral reflectance, solar absorptance α_S, thermal emittance ε, heliothermal efficiency, selectivity ratio α_S/ε) with time and temperature that is used to characterize the stability and durability of their performance, evaluate their aging behavior and determine if this aging gives rise to a degradation in performance.

3.2. Thermally-induced aging phenomena

The application of high temperatures to a material can cause well-known thermally-induced phenomena, following temperature-dependent laws. They are discussed in the following.

3.2.1. Chemical phenomena

3.2.1.1. Atomic diffusion

Atomic diffusion is a process of mass transfer inside a single material (“intradiffusion”, self-diffusion) or between adjacent materials (interdiffusion), by movement of atoms from regions of high atomic concentrations to regions of low atomic concentrations. These concentration gradients act as a driving

force for atomic diffusion. Fick's first diffusion law at steady-state (Eq.(16)) illustrates how the diffusion flux J (atoms/m²/s or kg/m²/s) along direction x is related to the concentration gradient $\partial C/\partial x$ (atoms/m³/m or kg/m³/m) through the diffusion coefficient D (m²/s).

$$J = -D \cdot \frac{dC}{dx} \tag{16}$$

To be able to move in the material lattice, atoms need to break their bonds with surrounding atoms and locally distort the lattice. They need to acquire the activation energy of diffusion E_a to do so. The thermal energy of an atom is related to temperature, and increases with it, as lattice vibrations increase: $E = k_B T$. The diffusion coefficient D is thus highly temperature-dependent, following an Arrhenius law, as indicated by Eq.(17), where D_0 is the temperature-independent preexponential term (m²/s), E_a is the activation energy for diffusion (J/mol or eV/atom), R the gas constant (8.314 J/mol/K) and T is the temperature (K).

$$D = D_0 \cdot exp(-E_a/RT) \quad \Leftrightarrow \quad \ln D = \ln D_0 - \frac{E_a}{R} \cdot \frac{1}{T} \tag{17}$$

The formulation on the right of Eq.(17) gives rise to an Arrhenius plot of D vs. $1/T$, with a linear expression, the slope of which ($-E_a/R$) is proportional to the diffusion activation energy E_a: the higher E_a, the harder it is for atoms to diffuse in the material, the steeper the linear Arrhenius plot.

As an example, Figure 35 illustrates such temperature dependence for diffusion coefficients of several elements in titanium [166]. It can be seen that it is easier for transition metals such as Al to diffuse in Ti (left) than for O (right, E_a = 200 kJ/mol) although usually light elements such as O, C or N diffuse much more easily than larger metallic atoms (e.g. through interstitial diffusion in the crystalline lattice). It is suggested that strong covalent-like bonds form between the host titanium atoms and the "impurity" metal atoms. This example emphasizes the need to investigate diffusion behaviors in materials of interest when developing materials and coatings for high temperature applications. It also highlights that the diffusion behavior of an element strongly depends on the surrounding elements and their chemical bonds it has to progress in.

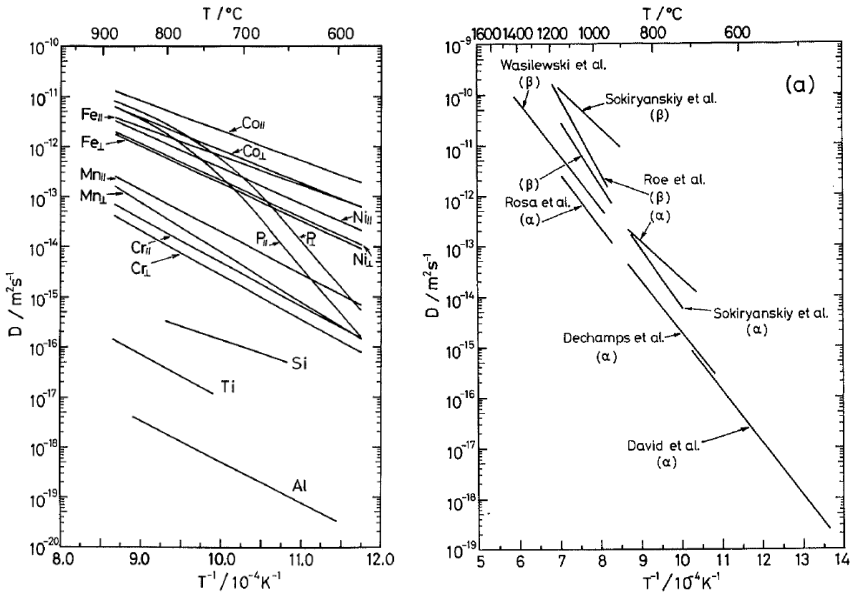

Figure 35. Temperature dependence of diffusion coefficients in α-Ti (left) for Co, Fe, Ni, Mn, Cr and P in single crystals, and Si, Al and Ti (self-diffusion) in polycrystals; for O in α-Ti and β-Ti (right) [166]

The diffusion behavior is also closely related to the materials microstructure. For instance, columnar structures (e.g. Figure 36, bottom left) are often obtained in coatings deposited by sputtering vacuum techniques, with various grain sizes, densities, grain boundary widths, etc. In crystalline solids, grain boundaries typically account for 50% of the total volume of the material, and the atomic concentration at grain boundaries is 10–30% lower than in the rest of the material. Grain boundary diffusion is therefore much faster than volume diffusion, and is a classical diffusion path. Diffusion in amorphous materials is thus supposedly slower as there are no grain boundaries, but can also occur.

Multilayer architectures such as receivers covered by solar selective absorber coatings associate materials with various chemical compositions. Thus strong atomic concentration gradients exist in these structures, and interdiffusion or interlayer diffusion often take place between the receiver support material (metallic substrate) and the coating, or within the individual layers of said coating. Diffusion phenomena are thus frequently observed in solar absorbers as one of the main degradation phenomena, as reported in many publications.

An example of such diffusion is shown in Figure 36 for a low temperature CrON/SnO_2 solar selective absorber coating deposited on Cu [167]. After aging in air for 600 h at 278°C, the inward interdiffusion of O into the absorber layer and the substrate, and the outward diffusion of Cr and Cu into the upper layers, are clearly visible. While solar absorptance is barely affected by this aging (it only decreases from 0.932 to 0.930), said diffusion phenomena cause an increase in emittance from 0.069 to 0.123, due to the loss of metallic-like behavior of the absorber close and into the Cu substrate, with the inward diffusion of O.

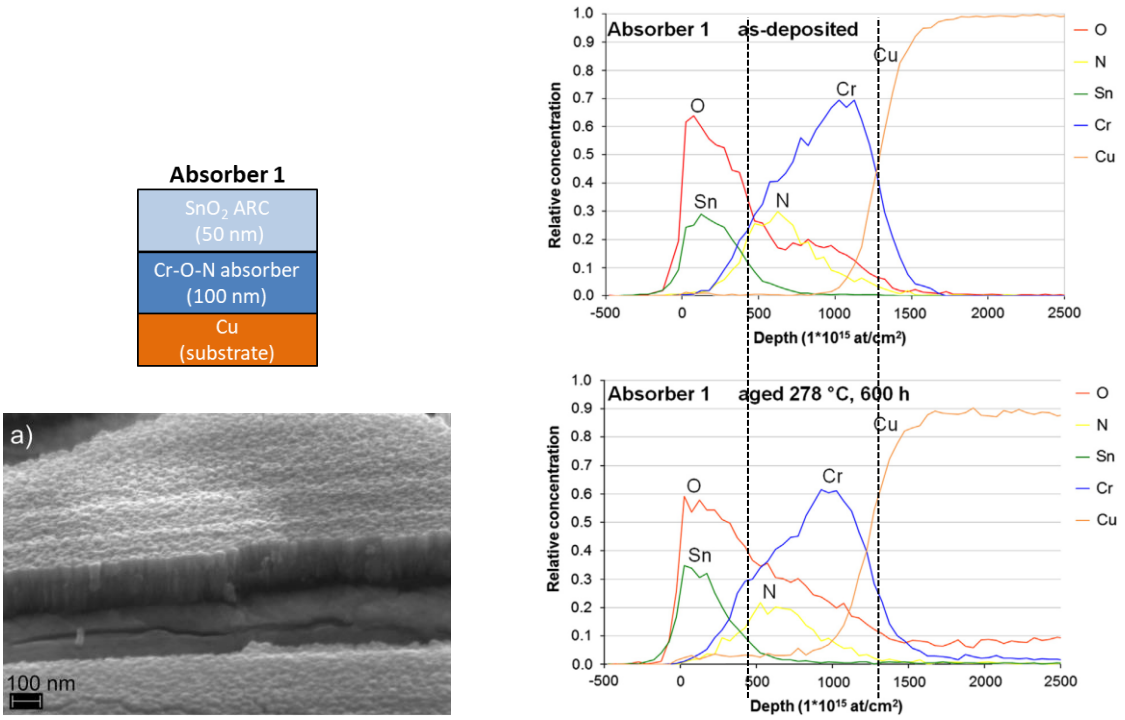

Figure 36. Atomic depth profiles (TOF-ERDA) for a chromium oxynitride selective coating on copper, as-deposited and aged at 278°C for 600 h in air [167]

Liu et al. [60] established that for NbTiON/SiON absorber coatings on Cu substrates, Cu diffusion into the absorber was the main reason for its aging, i.e., decrease of α_S from 0.95 to 0.84 and increase of ε from 0.07 to 0.14, after 40 h at 600°C in vacuum. The same coating on SS substrate had lower optical performance as-deposited (0.91/0.13) but exhibited better thermal stability (0.90/0.13 at 600°C), as Cu is known for its tendency to diffuse. This study underlines the impact of the substrate material on the degradation of the absorber coating, which otherwise would be thermally stable in itself.

Xinkang et al. [71] found that Mo diffused in Mo-Al_2O_3 cermets through inner self-congregation inside the cermet, and infiltration through the Al_2O_3 layer in Mo/Al_2O_3 tandems (after 5 h at 800°C in vacuum). They also surmised that defects appearing in Al_2O_3 at temperatures above 650°C, such as widened boundaries, cracks and holes, create pathways for Mo diffusion. Finally, when using Mo IR-reflective layer above SS substrates, they underlined the necessity to "produce an Fe_2O_3 layer on SS substrate by a way of oxidation of the substrate surface to avoid mutual diffusion across the interface between SS and base metal Mo layer". Even with the Fe_2O_3 layer, the coating optical properties were degraded when annealed for 2 h above 500°C, especially emittance ($\Delta\alpha_S$ = -0.01, $\Delta\varepsilon$ = +0.01-0.08).

Liu et al. [168] also observed that after 10 h at 800°C in vacuum, the interdiffusion between the SS substrate and the Mo IR-reflective layer caused the coating degradation ($\Delta\alpha_S$ = -0.01, $\Delta\varepsilon$ = +0.05). Mn outward diffusion from SS substrate in TiAlCrN/TiAlN/AlSiN tandem absorber coatings was also observed by Valleti et al. [133] after 4 h at 600°C with a critical effect on their emittance ($\Delta\varepsilon$ = +0.08).

Overall, it is often found that the diffusion of elements from the metallic substrate causes the degradation (increase) in the emittance of solar selective absorber coatings at high temperature [133,169]. Indeed, this type of diffusion tends to degrade the low-emissive metallic nature of the substrate and IR-reflective layer.

It is thus critical to knowledgeably select the constitutive materials with regard to their diffusion behavior at high temperatures. The design of SSACs aims at reducing diffusion rates or avoid diffusion altogether: known diffusion barrier materials with high thermal stability are used as additional barrier layers between substrate and IR reflector, or even as one or all of the optically active layers. For instance Al_2O_3 [169,170], W [171–174] or titanium aluminum nitrides [133] have been successfully used to reduce diffusion within SSACs.

3.2.1.2. Oxidation/corrosion

The presence of oxygen-containing species in the surroundings of a material, coming from the atmosphere (O_2, H_2O vapor, CO_2, NO_x, etc.) or even from adjacent materials (oxides), can cause its oxidation and/or corrosion (chemical erosion), i.e., the incorporation of oxygen atoms in its microstructure, and their diffusion, to locally or globally form a compound containing (more) oxygen, such as an oxide. CSP absorbers can be subject to dry corrosion in air (O_2, H_2O vapor), especially at high temperature, and wet/aqueous corrosion in water (dew, rain).

Dry corrosion, i.e., oxidation in air at high temperature, is a common phenomenon for solar absorbers. Its principle is illustrated in Figure 37 (left) for a metallic surface. First, ambient O_2 molecules are adsorbed and dissociate on the material surface (1). This leads to the nucleation and growth of an oxide film (2): the adsorbed oxygen atoms react with the material to form oxide clusters, which laterally grow until they connect to form a continuous film. Then the oxide film grows in thickness (3), due either to the diffusion of O_2 towards the material/oxide interface (inward growth), adding interstitial oxygen in the lattice; and/or to the diffusion of one or more elements of the material towards the oxide/ambient interface (outward growth), creating vacancies in the material. Both phenomena induce stress and defects can appear in the oxide layer as its thickness grows: cavities, pores, microcracks, grain boundaries, etc. (4). This can lead in some cases to the cracking, unsticking and eventually failure of the oxide film, giving rise to further oxidation paths (5).

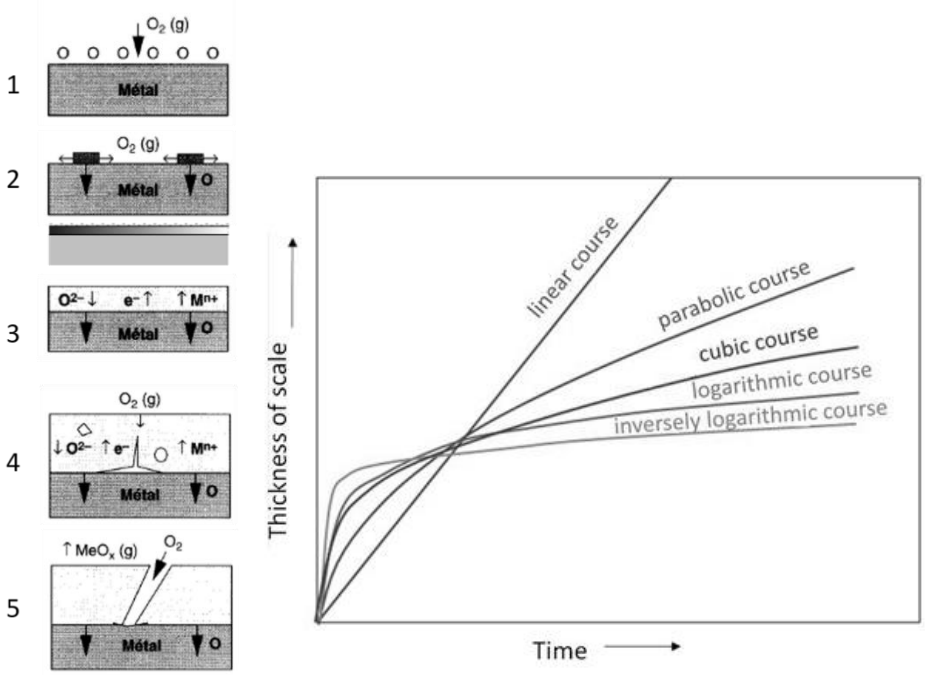

Figure 37. Typical oxidation steps of a metallic surface (left) and typical oxidation profiles of materials illustrated by the evolution of oxide thickness vs. time (right [175])

Different materials have different oxidation behaviors, as can be observed when following the mass/weight gain Δm or thickness of a material exposed to an oxidizing atmosphere vs. time (Figure 37, right [175]). The linear profile indicates an ever ongoing oxidation of the material with formation of a volatile oxide, eventually leading to the failure of the material (steps 1 to 5). At low, medium and high temperatures, oxidation typically follows cubic, logarithmic and parabolic laws, respectively [175]. A material resistant to oxidation will form an adhesive, dense and stable oxide layer at its surface (steps 1 to 3). This oxide layer will act as a diffusion barrier for oxygen, and its thickness will stabilize with time following a parabolic profile. This is the case for instance of Al and Cr, that respectively form thin Al_2O_3 and Cr_2O_3 protective layers. Both metals are thus often included in oxidation-resistant materials and alloys (e.g. Ni-Cr stainless steels).

The parabolic law, or Wagner's law, was first derived by Wagner et al. [176] for metal oxidation and concerns thick oxide films (> 600 nm). The rate of oxidation is expressed with Eq.(18), where x is the oxide thickness (cm), K_P is the parabolic rate constant (cm²/s) and t is time (s).

$$\frac{dx}{dt} = \frac{K_P}{x} \quad \Leftrightarrow \quad x^2 = 2K_P \cdot t + C^{te} \tag{18}$$

This law is applicable to uniform, continuous and protective oxide scale layers. In many cases, more complex or mixed growth rules can be observed. Cabrera and Mott further developed Wagner's theory for thinner films (< 3 nm), proposing an inverse logarithmic law [177] (Figure 37, right). The parabolic rate constant K_P is nevertheless very often used for the description and comparison of the oxidation behavior of materials.

Oxidation, as a particular case of diffusion, is also a temperature-dependent phenomenon, following an Arrhenius law. The activation energy E_a and temperature dependence of oxidation are thus expressed by Eq.(19) and can be deduced from an Arrhenius plot, as explained for diffusion.

$$K_P = A \cdot exp(-E_a/RT) \quad \Leftrightarrow \quad \ln K = \ln A - \frac{E_a}{R} \cdot \frac{1}{T} \tag{19}$$

Apart from temperature, many other parameters influence the oxidation behavior and resistance of a material, either intrinsic to the material itself (chemical composition, thermodynamic properties) or linked to its fabrication technique (microstructure, diffusion resistance).

The presence of water vapor in the oxidizing atmosphere is also a known factor affecting material oxidation kinetics, through the adsorption of water molecules and the formation of hydroxides at the surface, that can accelerate the formation of oxides. If these are stable oxides (parabolic law), the material can be more quickly protected from further oxidation and water vapor then has a beneficial effect on oxidation resistance [178]. In some cases [179], after this initial protective oxidation, breakaway oxidation is observed in the presence of water vapor, i.e., a rapid acceleration of the oxidation rate (linear law), leading to the degradation of the material.

Oxidation is a frequently encountered aging mechanism in solar selective absorber coatings working in air or degraded vacuum at high temperature, even though highly oxidation-resistant materials at high temperatures are often used, such as Al_2O_3 [20, 21, 23, 31–41] and Si_3N_4 [79,123,131,188–190].

The top antireflective (AR) layer can be oxidized, as evidenced by Rebouta et al. [80] with SS/W/W-Al_2O_3/SiO_x architectures, where SiO_x is further oxidized towards SiO_2 and emittance slightly decreases as a consequence. A stable surface oxide can form, protecting the rest of the coating from further oxidation by slowing down the diffusion of oxygen and other elements (parabolic law with $\sqrt{t}$).

In other cases, oxygen diffuses from/through the top antireflective layer, often a porous stable oxide, then reaching and oxidizing the underlying absorber layers, and degrading their optical properties. Such scenario was observed by Gao et al. [191] with SS/TiN/Al_2O_3 architectures: after 2 h in air above 250°C, TiN was oxidized into TiO_2, degrading solar absorptance ($\Delta\alpha_S$ = -0.05-0.12, $\Delta\varepsilon$ = -0.01). Liu et al. [168] observed that Mo/LOCL/MOCL/HOCL (Low/Middle/High Oxygen Content CrAlO) heat-treated at 600°C for 200 h in air suffered from mild optical degradation ($\Delta\alpha_S$ = -0.02, $\Delta\varepsilon$ = -0.02) due to the further oxidation of the underlying LOCL, as well as the formation of a thin layer of surface oxide. Barshilia et al. [192] surmised the oxidation of Al layer in Cu/Al_xO_y/Al/Al_xO_y above 400°C, and observed the diffusion of Cu atoms from the substrate and their oxidation to form CuO, strongly degrading solar absorptance ($\Delta\alpha_S$ = -0.06-0.18, $\Delta\varepsilon$ = -0.01). This study highlights the possible synergy between diffusion and oxidation.

Finally, after oxidizing the AR and absorber layers, oxygen can continue to diffuse downwards and reach the IR-reflective layer and substrate, also forming oxides with the metals they contain. This was evidenced for instance by Khamlich et al. [193] with Cr/α-Cr_2O_3 nanoparticles grown on Ta substrates, where fast oxygen diffusion at the α-Cr_2O_3/Ta interface generated Ta_2O_3, after heat-treatments in H_2 at 600°C, leading to a dramatic degradation in optical performance ($\Delta\alpha_S$ = -0.05, $\Delta\varepsilon$ = +0.17, vs. sample annealed at 500°C). It is worth noticing that for the same architecture, annealing at 500°C produced a contrary effect ($\Delta\alpha_S$ = +0.18, $\Delta\varepsilon$ = -0.14, vs. sample annealed at 300°C), again highlighting that aging phenomena do not necessarily induce degradations of optical performance.

Overall, oxidation phenomena seem to mostly affect, and degrade, the solar absorptance of selective absorber coatings. Indeed, the efficiency of the latter is based on the intricate optical interference phenomena generated by the association of thin layers of different materials. Such interference phenomena strongly depend on the materials optical indices, chemical nature and layer thicknesses, all of which notably vary with the formation and growth of oxides within and/or at the surface of the coating. In some cases, an accommodation in refractive index between the layers can arise and absorbing performance can even improve. In most cases however, it is degraded, as the structure is

no longer optically optimized. As a consequence, their spectral reflectance varies both in intensity and spectral distribution, causing optical performance to evolve undesirably.

Figure 38 presents an illustration of this fact. The simulated spectral reflectance and optical performance of a simple stack composed of Fe substrate, SiC absorber and SiO_2 antireflective layer are shown: initially (a), the SiC absorber layer is 20 nm-thick and the SiO_2 antireflective is 70 nm-thick; then, the SiC absorber is oxidized into SiO_2, (b) half (SiC 10 nm / SiO_2 10 nm / SiO_2 70 nm) then (c) entirely (SiO_2 20 nm / SiO_2 70 nm), without any change in total thickness (90 nm); finally (d) the thickness of the entirely oxidized SiC is increased (SiO_2 130 nm / SiO_2 70 nm). At a wavelength of 600 nm, the refractive indices are (n = 3.41, k = 0.31) for SiC and (n = 1.46, k = 0) for SiO_2, thus the oxidation of SiC into SiO_2 causes drastic changes in optical behavior. The increase in O content, and subsequent decrease in refractive index, tend to modify the intensity of the reflectance maxima and minima that are due to optical interferences, but not their position (wavelength) which is linked to thickness. The increase in oxide thickness tends to increase the number of these interferences (reflectance oscillations) and causes their spectral shifting towards the infrared range. Both evolutions cause a degradation in solar absorptance, as the coating structure diverts from its optimal parameters, initially giving rise to low reflectance in the solar range. Meanwhile, emittance is barely affected by the changes in the absorber, as it mostly depends on the substrate material itself. However as thickness further increases, eventually the reflectance spectral shift towards the infrared range and the increase in the number of oscillations also affect emittance. Some previous and recent results have shown the relation between the increase in thickness and variations of the optical properties [194]. In any case, further analysis from experimental results need to be considered after each aging test to better understand the changes on the absorber and confirm this relation.

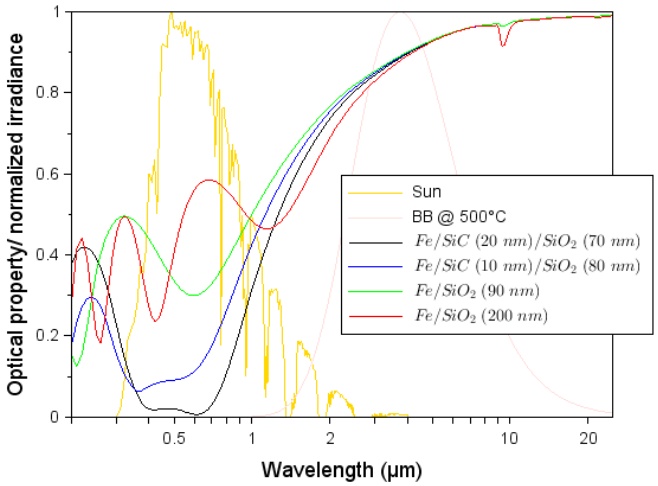

Stack	α_S	ε(500°C)
(a) Fe / SiC (20 nm) / SiO_2 (70 nm)	0.80	0.08
(b) Fe / SiC (10 nm) / SiO_2 (80 nm)	0.71	0.08
(c) Fe / SiO_2 (90 nm)	0.56	0.08
(d) Fe / SiO_2 (200 nm)	0.49	0.09

Figure 38. Simulated spectral reflectance and optical performance of model solar selective absorber coating at different stages of oxidation for the absorber layer

To summarize, the oxidation behavior of selective coatings is difficult to anticipate due to their complex architecture associating different materials, and its impact on optical performance is very strong and hard to predict.

3.2.2. Physical phenomena: densification, recrystallization etc.

As a consequence of temperature increase, as well as of diffusion and oxidation phenomena, materials may undergo other physicochemical phenomena such as phase changes, crosslinking, recrystallization, densification of porous materials, that can also modify their microstructure and related optical properties. Usually materials are preselected for their known thermal stability in the temperature

range of interest in the aimed applications, so that these phenomena have a limited impact. Most fabrication techniques however give rise to microstructures that are not entirely stabilized as-deposited (Figure 39), so as to reduce fabrication costs, for instance by depositing at low or even room temperature [71,195]. As a consequence, only partly crystallized and disorganized/amorphous microstructures are fabricated, that can sometimes be further densified and reorganized during aging, especially when this aging occurs at temperatures higher than the fabrication temperature, in combination with diffusion and/or oxidation phenomena (Figure 40).

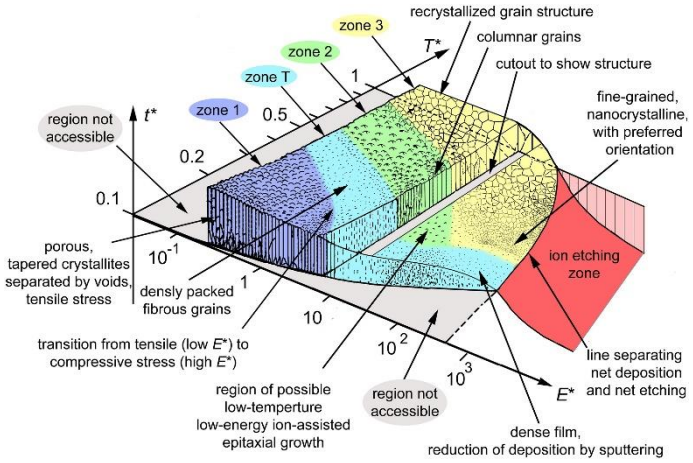

Figure 39. Microstructure of coatings prepared by plasma techniques vs. process parameters (generalized substrate temperature *T, normalized ion energy flux *E**) and film thickness (*t**) [196]**

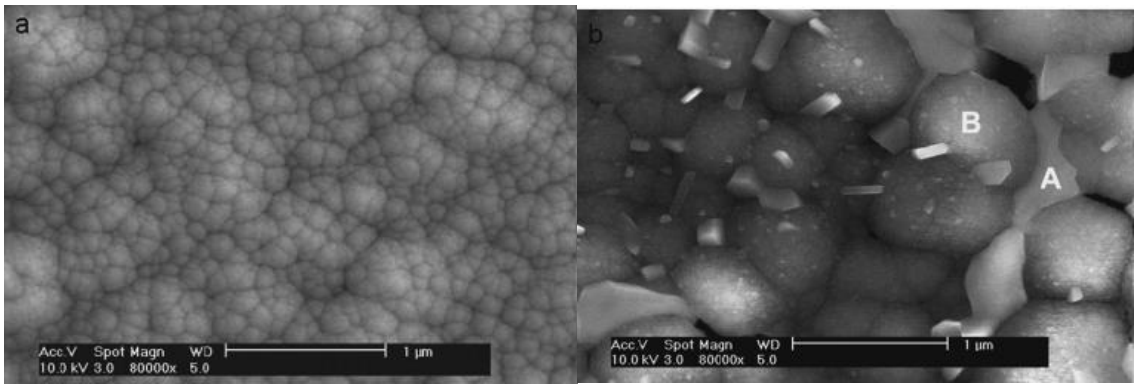

Figure 40. Change in surface morphology of SS-(Fe_2O_3)/Mo/Al_2O_3 coatings (a) before and (b) after heat treatment at 800°C for 5 h, due to Mo diffusion in Al_2O_3 (Mo enrichment at point A) [71,72]

In solar selective coatings, this restructuring may lead to less efficient absorbers. For instance, the antireflective top layer needs to present a low refractive index to ensure the antireflective effect ($n_{absorber\ material} = \sqrt{n_{AR\ material}}$). This is often achieved by using porous oxides [124,127,130], as incorporating vacuum or air (n = 1) in a material (n > 1) logically reduces its refractive index. When exposed to higher temperatures, these porous materials may be densified, increasing again their refractive index and reducing their thickness, thus lessening the antireflective effect and decreasing the solar absorptance and efficiency of the solar absorber coating. On the contrary, densified absorber layers are preferable, as illustrated by a study of Cheng et al. [72], where a denser Al_2O_3 matrix for Mo-Al_2O_3 cermets improved the durability of their optical performance, by limiting the diffusion and oxidation of Mo into the matrix above 400°C.

Xinkang et al. [71] found that the surface restructuring in Figure 40 led to an increase in thermal emittance, due to an increase in surface roughness or asperity. Ke et al. [197] also observed optical degradation ($\Delta\alpha_S$ = -0.05, $\Delta\varepsilon$ = +0.01, after 342 h at 308°C), due to abnormal grain growth after aging (Figure 41). Moreover, these grains being larger and looser, the authors suppose there are many open

pores among the grain boundaries, which would act as fast diffusion paths for atoms, further degrading the material and its performance.

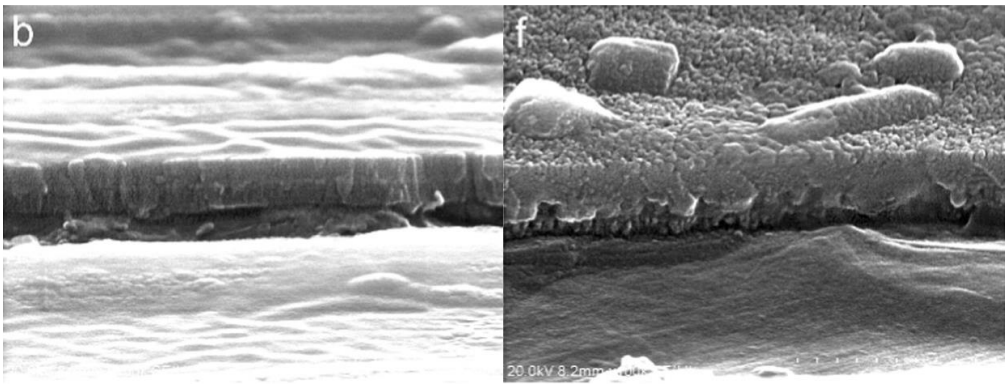

Figure 41. Change in morphology of Al/Cr-O/Cr-N/SiO_2 coating (b) before and (f) after 200 h heat treatment at 400°C [197]

3.3. (Thermo)mechanical aging phenomena

3.3.1. Mechanical behavior of materials

3.3.1.1. Mechanical stress and strain

Materials in conditions of use are subjected to mechanical stress σ (N/m² or Pa), i.e., the application of a force *F* (N) on an area *A* (m²) of the material, due to its surroundings (ambient pressure, temperature, adjacent materials), offering resistance or imposing changes. As such forces can be normal or parallel to the surface, the resulting stress can be tensile ("pulling"), compressive ("pushing") and/or shear (lateral) stress, uniaxial or biaxial, etc. For instance, Figure 42 illustrates the growth of an oxide layer at the surface of a material, in the case of a linear oxidation behavior (see section 3.2.1.2 p.57): the mismatch of their lattice parameters causes the thin oxide to break under tensile (upper case) or compressive stress (lower case), forbidding the formation of a stable protective oxide layer and allowing for endless oxidation.

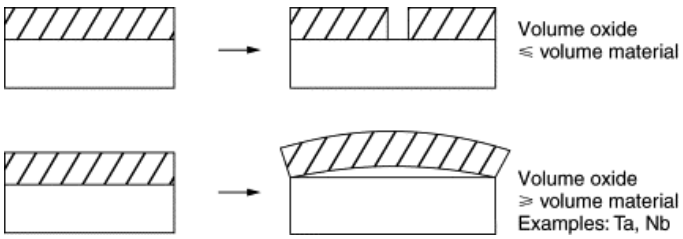

Figure 42. Possible mechanical stress causing the breakdown of oxide films [57]

As a response to stress, materials strain, i.e., deform. Tensile, compressive and shear stress respectively result in tensile, compressive and shear strain ε. Strain can also be in volume (dilatation). Since strains are ratios of two lengths or volumes, they are dimensionless.

3.3.1.2. Elastic and plastic behavior

According to Hooke's law, for small strains, strain is proportional to stress, via the elastic (Young) modulus *E*: $\sigma = E \cdot \varepsilon$, for simple tension. The material presents a linear elastic behavior: strain is reversible and the material returns to its initial shape when stress is released. *E* can be measured via tensile testing (Figure 43), where tensile stress is applied to a sample and its resulting strain is measured, *E* being the slope of the linear part.

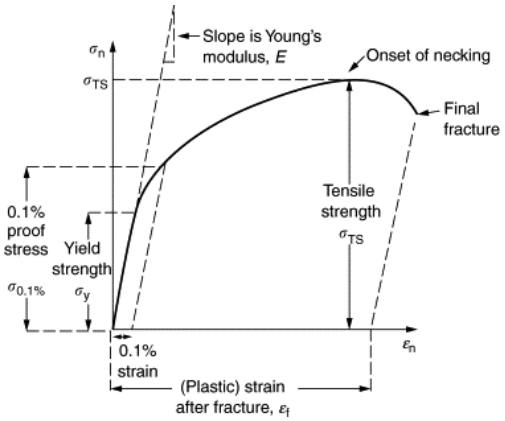

Figure 43. Tensile test of a ductile material and main mechanical properties [57]

For most materials, this elastic behavior only occurs at very low strain, typically ≤ 0.001, e.g., 1 mm deformation for an initial length of 1 m. Beyond this point, some materials start to deform plastically, i.e., their shape irreversibly changes. Materials with such ability are called ductile, and include metals. The transition between elastic and plastic domains occurs when applying a stress equal to the yield strength σ_y of the material, also called its elasticity limit *Re*. Plastic deformation is a way for the material to accommodate mechanical stress without breaking. Contrarily to ductile materials, brittle materials such as ceramics cannot deform plastically and simply break beyond the elastic behavior zone. Yet they are stronger than ductile materials, meaning they have a greater ability to withstand stress without failure.

As stress is further increased, plastic deformation can only be sustained until the tensile strength (σ_{TS} or Rm) of the material is reached. Beyond that, plastic instability leads to the material weakening and final fracture. The tougher the material, the later fracture will occur. Indeed toughness is the ability of a material to plastically deform without fracturing, represented by the area under the stress-strain curve. In order to be tough, a material must be both strong and ductile.

Plastic deformation is rendered possible by the formation and propagation of dislocations in the material crystalline lattice: atomic planes locally slide past one another and move by gradual rearrangement of chemical bonds breaking and reforming (Figure 44).

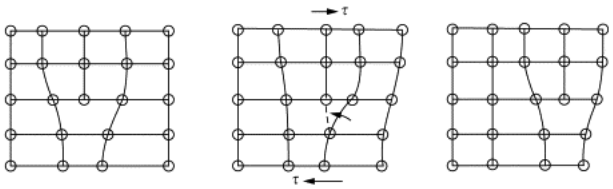

Figure 44. Propagation of a dislocation in a crystal lattice [57]

This is possible in materials with weak atomic bonds, such as metals (metallic bonds). Ceramics having strong covalent bonds, the energy required to allow dislocations to propagate is very high, so that their plastic deformation is only possible at very high temperatures close to their melting point.

To limit plastic deformation and delay fracture in ductile materials, polycrystalline structures such as metal alloys can be used. The presence of atomic inclusions and grain boundaries in such materials act as obstacles and oppose a resistance to the propagation of dislocations, strengthening the material but reversely, non-continuous (micro or polycrystalline) materials are more sensitive to oxidation/corrosion phenomena. Finally, alternating metals (ductile) and ceramic coatings (fragile) in multilayers is a way to limit cracks propagations under stress and increase lifetime when in solar use (see section 3.3.2).

3.3.1.3. Influence of temperature on the mechanical behavior of a material

Temperature has a strong influence on mechanical properties, as illustrated in Figure 45 for $Ti_{0.35}Al_{0.65}N$ coatings and in Figure 46 for Inconel 718. A heat treatment can be used to toughen the material at a given temperature (e.g. 150°C in the first case). Heat treatment/aging at higher temperature can cause the deterioration of mechanical properties, often due to thermally-induced phenomena (see section 3.2 p.54). This degradation can impact the integrity and lifetime of the material, by impairing its ability to resist external and internal stress.

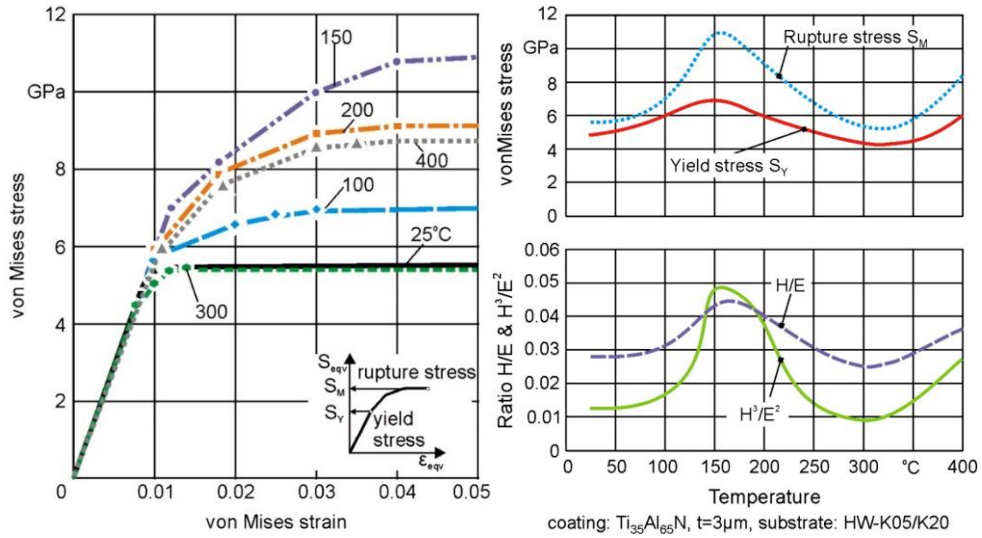

Figure 45. Stress-strain curves, yield and rupture stress, H/E and H^3/E^2 ratios of $Ti_{0.35}Al_{0.65}N$ coating vs. temperature [199]

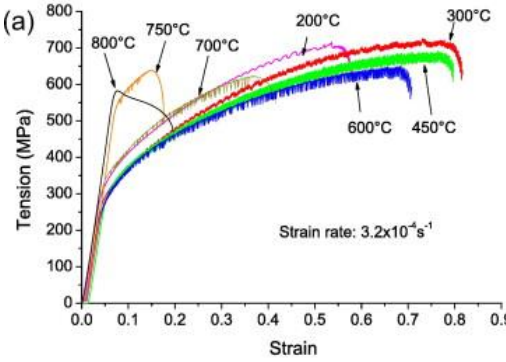

Mechanical property	Temperature (°C)						
	200	300	450	600	700	750	800
σ_{YS}	274	261	272	251	328	523	543

Figure 46. Stress-strain curves and yield strength for Inconel 718 vs. temperature [199]

3.3.2. (Thermo)mechanical degradations

3.3.2.1. Cracks formation

Defects such as atomic impurities, grain boundaries, porosities, etc., represent intrinsic stress concentrations in materials. Such stress can be initially present, as a result of the fabrication method (e.g. Figure 39 p.61 illustrates residual stress in plasma-deposited coatings), the type of material [200], or the shape of the support material (notch, shoulder, gorge, hole, etc.). Thermomechanical stress on materials can also be induced during use, in particular at high temperature, where differences in thermal behavior (e.g. thermal expansion, oxide growth, etc.) between adjacent materials can generate stress inside and at their interface.

The relaxation of such intrinsic, residual or induced stress leads to the formation and enlargement of cracks (Figure 47), especially in coatings. Moreover, the stress close to the crack σ_{local} is greater than the average stress σ in the material: the crack has the effect of concentrating stress [57].This tends to favor its propagation in the material.

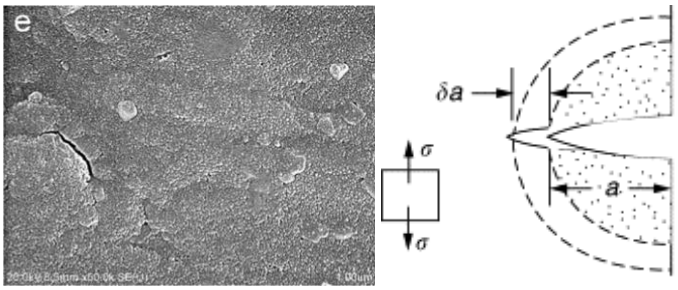

Figure 47. Example of cracked surface after heat treatment of Al/Cr-O/Cr-N/SiO_2 coating at 400 °C for 200 h [197] (right); release of stored energy as a crack grows [57] (left)

3.3.2.2. Cracks propagation and fracture

Fracture and mechanical failure of materials result from the propagation of cracks, according to several fracture modes initiated by tensile or shear stress (Figure 48).

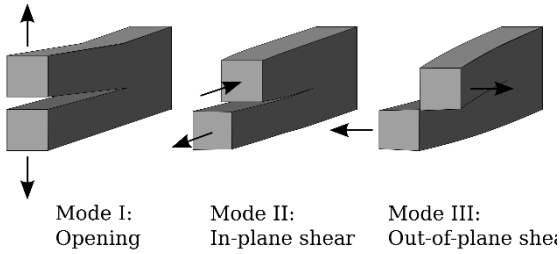

Figure 48. Fracture modes allowing cracks propagation in materials

If a material containing a crack is sufficiently stressed, the crack can become unstable and grow in the material, to cause catastrophically rapid fracture, or fast fracture, at a stress lower than the yield stress [198]. Fast fracture occurs when, in a material subjected to a stress, a crack reaches some critical size *a*, or when a material containing cracks of size *a* is subjected to some critical stress. Figure 49 illustrates a case of fast fracture, initiated by intragranular cracking which escalated into transgranular cleavage and final fracture.

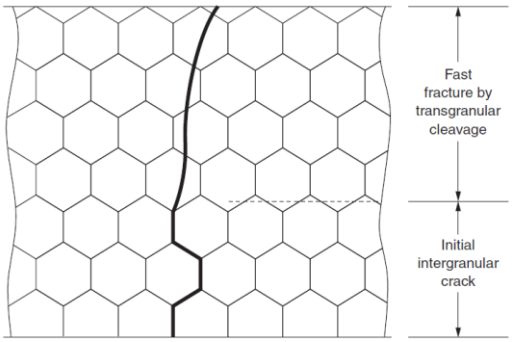

Figure 49. Fast fracture and subsequent failure of a material [57]

One way of delaying crack propagation and subsequent fracture is by disposing obstacles to such propagation in the component architecture, as in fiber-reinforced polymers (Figure 50). At a smaller scale, solar absorber coatings also associate materials with high strength (ceramics) and materials with high toughness (metals), that can lead to similar delays in cracks propagation.

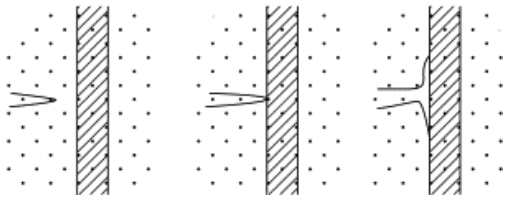

Figure 50. Principle of crack stopping in composites [57]

3.3.2.3. Fatigue failure

Cracks can also form and grow slowly in materials even under low mechanical stress, typically below the yield strength of the material (Figure 43), if this stress is applied cyclically (Figure 51) and for a large number of cycles. This phenomenon is called fatigue and can also lead to material fracture and failure over time. Fatigue failure occurs more rapidly and dramatically if cracks or stress concentrations pre-exist in the material. The applied stress $\Delta\sigma$ can be mechanical (e.g. tensile or compressive), thermal (high/low temperature cycles) or thermomechanical, i.e., combining mechanical and thermal cyclic stresses.

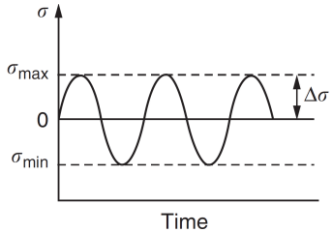

Figure 51. Cyclic stress leading to fatigue failure [57]

Fatigue behavior can be illustrated on a Wöhler or S-N curve (Figure 52), showing the applied stress vs. the number of cycles that need to be applied to provoke failure at this particular level of stress. It reveals two main regimes of fatigue:

- high-cycle fatigue (green area in Figure 52) where the material deformation is mostly elastic due to lower stress (below cyclic yield strength) and the number of cycles needed to reach failure is high (typically above 10^4 cycles). In some materials a fatigue limit is reached, where the material can sustain an infinite number of cycles without fracture, if the applied stress is lower than the cyclic yield strength of the material. It is the most desirable design. Most steels present such fatigue limit. Other soft ductile materials such as Al will inevitably fail under cyclic solicitation, however low the applied stress, as they have no fatigue limit.
- low-cycle fatigue (grey area in Figure 52) where the applied stress is higher, leading to plastic strain, and the number of cycles to failure is lower (typically below 10^4 cycles). Figure 52 (left) also illustrates that the stress level needed to plastically deform a material under cyclic stress is lower than under constant stress: cyclic solicitation is more damaging than constant load.

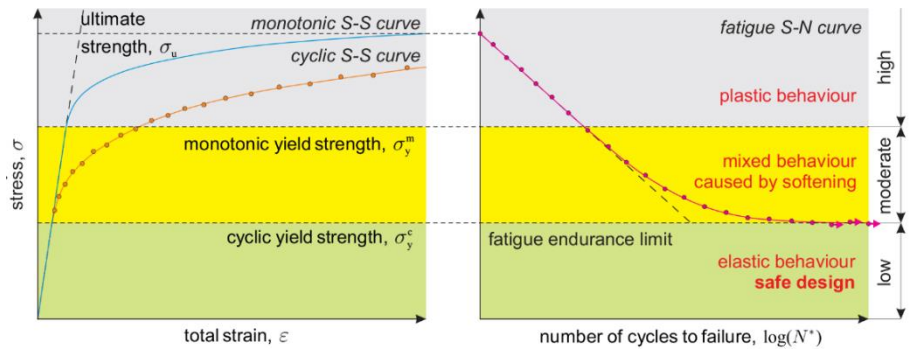

Figure 52. Applied stress vs. material strain (S-S curve) and vs. number of cycles to failure (S-N curve) [201]

3.3.2.4. Creep damage and fracture

As the temperature of a material increases, mechanical stress that would only lead to reversible deformation at room temperature can cause the material to creep: creep is a slow, continuous and irreversible deformation with time. This deformation depends not only on the applied stress but also on temperature and time. The temperature T at which a material starts to creep depends on its nature and on its melting point T_M (in K): T = 0.3-0.4 · T_M for metals and 0.4-0.5 · T_M for ceramics.

Creep damage and resistance can be tested by applying a constant mechanical load to a specimen placed in a hot furnace and following its deformation with time (Figure 53). After an initial elastic strain, three stages of creep can appear. Primary creep occurs quickly and causes only small deformation slowing with time, illustrating the resistance or consolidation of the material. Secondary creep, or steady-state creep, is a deformation steadily increasing with time. In this stage, the creep rate $\dot{\varepsilon}_{SS}$ can be expressed by the Arrhenius law of Eq.(20) where σ is the applied stress, T is the temperature, R is the gas constant, A is called the creep constant, n is called the creep exponent (typically between 3 and 8) and E_a is the activation energy for creep (in J/mol). In other words, the steady creep rate increases exponentially with temperature.

$$\dot{\varepsilon}_{SS} = A\sigma^n \cdot exp(-E_a/RT) \tag{20}$$

This temperature dependence arises from the role of atomic diffusion in creep: at the atomic level, the diffusion of atoms, activated by temperature, facilitates the propagation of dislocations in the lattice of crystalline materials (Figure 44). Diffusion usually becomes significant around T = 0.3 · T_M, explaining why it is around this temperature that materials start to creep.

Finally, during tertiary creep, damage accumulates as internal cavities in the material, especially at grain boundaries, rapidly accelerates with time, until it causes the fracture of the material (Figure 54).

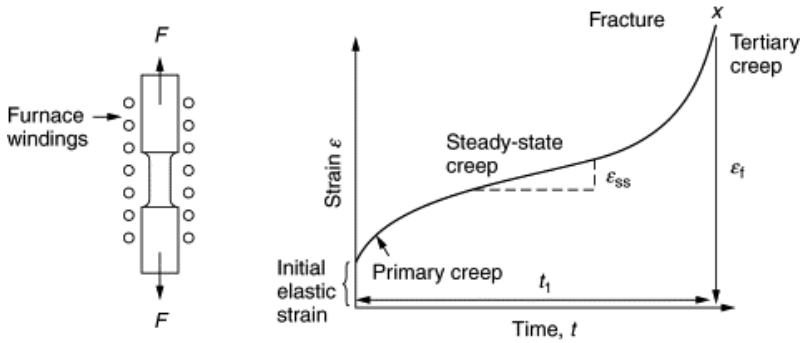

Figure 53. Example of creep testing [57]

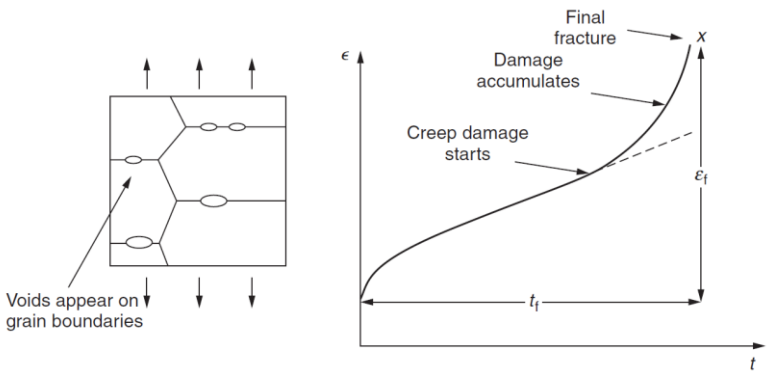

Figure 54. Creep damage accumulation at tertiary stage leading to material fracture [57]

3.3.2.5. Thermomechanical phenomena in CSP receivers

In CSP, receivers are often considered to mostly sustain slow cyclic thermal stress due the day/night variations of the incident concentrated solar irradiance (see sections 2.1.2 and 2.2 of this chapter), which causes fatigue damage. However CSP receiver materials also have to bear:

- rapid thermal stress due to cloudy spells: when a cloud passes in the sky, the solar input on the receiver decreases dramatically while the heat transfer fluid flowing inside it still extracts its heat, leading to a rapid decrease of the receiver wall temperature for a short duration. For this reason, infra-hour solar resource assessment and forecasting is a developing and critical area of research in CSP to better adapt operating strategies and limit their impact on materials;
- long-term cyclic mechanical stress (creep-fatigue) at their attachment points with other parts of the structure (support rods, welding, etc.), especially when they suffer thermal expansion at high temperature;
- long-term mechanical stress at constant load and in temperature (creep) due to the weight of the receiver itself, and the weight of the heat transfer fluid inside it, the latter sometimes also being pressurized (giving rise to additional radial stress, see Figure 33). This is especially true for linear receivers, which are only supported every few meters to limit shading.

Moreover, oxide phases and/or layers formed by thermally-induced phenomena (see section 3.2) bring defects in the crystal lattice, and often have different thermal expansion than the initial absorber materials. This, coupled with mechanical stress mentioned above, can in turn cause crack formation in the oxide, propagating in the underlying material, leading to later thermomechanical failure. Thermomechanical and thermally-induced aging phenomena are thus all intricately linked.
CSP receivers are therefore subjected to complex thermomechanical stress leading to complexly coupled fatigue-creep and thermally-induced physicochemical aging phenomena that are hard to predict, since they depend on the solar resource.
In the literature, thermomechanical stress and failure analysis mostly concerns receiver bulk materials for high temperatures and/or high solar concentrations, e.g. metallic alloys, sometimes covered by Pyromark® absorber paint [202–206] (Figure 55) or ceramics [207,208]. Apart from rare, recent exceptions [209–211], very little information can be found about the thermomechanical behavior of receivers covered with more complex selective absorber coatings, and the impact of thermomechanical stress on such coatings. These elements are rarely taken into account by selective coating developers, beyond the preselection of materials from other thermomechanical applications such as aeronautics/automotive, turbines, cutting tools, etc. [212–214], and simple mechanical characterization, e.g. hardness measurements on as-deposited samples [120]. For instance, Barshilia et al. [192] just indicate that their $Al_xO_y/Al/Al_xO_y$ multilayer absorber coatings suffered from differences in thermal expansion between metal and ceramic layers, leading to crack formation and delamination, causing subsequent oxidation.

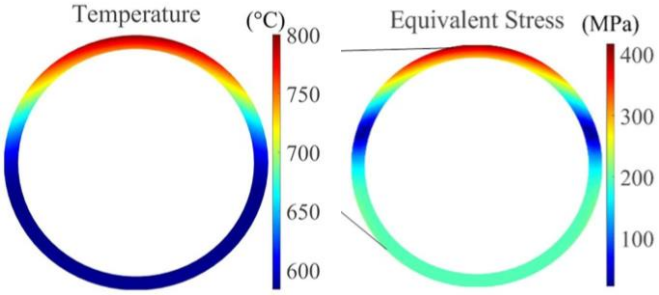

Figure 55. Calculated temperature and equivalent thermomechanical stress distributions on the cylindrical tubes of an Inconel 625 central receiver covered with Pyromark® paint [202] (graphical abstract)

3.4. Summary and conclusions on aging mechanisms

An overview of the main aging mechanisms concerning solar absorber coatings was presented, to better understand the aging behavior of solar receivers and their selective absorber coatings. These mechanisms were found to be intricately correlated and interdependent. They lead to material deteriorations, through the formation of microstructural defects such as cracks that can propagate and ultimately fracture the coating, causing the loss of optical performance and reduced lifetime. This is illustrated by the summary schematic in Figure 57, showing the interconnection between CSP plant configuration, correlated sources of degradation (section 2, p.49), aging mechanisms and subsequent material deterioration, for a system consisting in a metallic receiver with a solar selective absorber coating (SSAC).

Figure 56 more specifically illustrates how microdefects in the coating microstructure, existing as-deposited and evolving with aging (grain boundaries, cavities, porosity) are preferential oxidation and diffusion paths. For instance, the long-term cyclic exposure to high temperature in air can simultaneously cause atomic diffusion and related oxidation, thermal cycling, thermal expansion, mechanical tensile stress, fatigue, creep, etc. In particular, literature review and optical simulation both reveal that diffusion phenomena tend to increase thermal emittance, whereas oxidation tends to decrease solar absorptance, both being detrimental to the optical performance of the solar receiver.

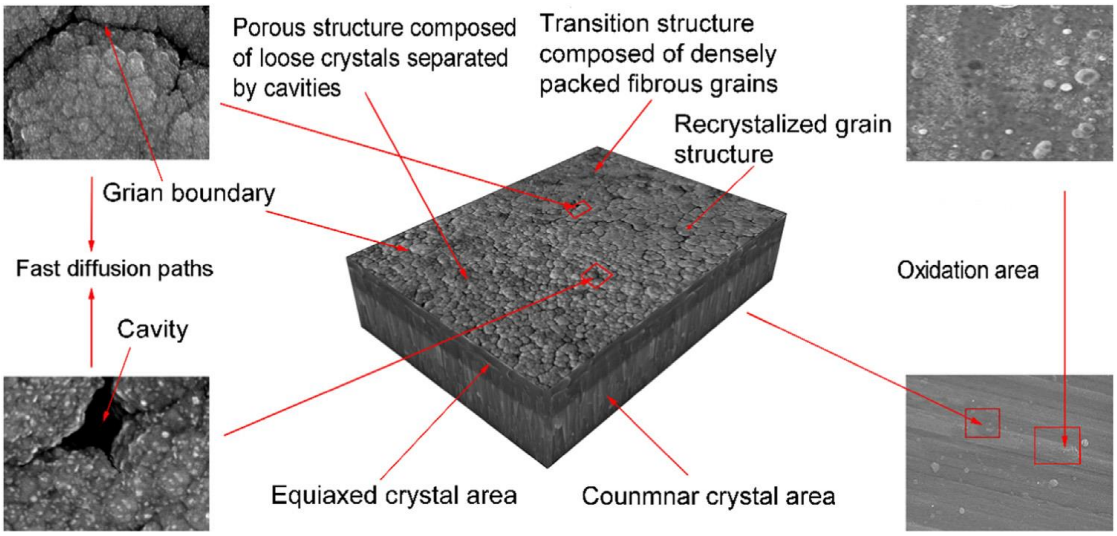

Figure 56. Schematic of microdefects of an aged solar absorber coating [135]

Depending on the type of CSP technology, the relative impact of the sources of degradation may vary. In the case of parabolic troughs, the receiver is protected with an evacuated glass tube and works under vacuum conditions, avoiding the degradations linked to atmospheric conditions. However it should ideally be capable of withstanding high temperatures in degraded vacuum, to anticipate the loss in performance of the vacuum protection over the years and minimize SSAC damage if vacuum is lost, especially when considering the high cost of replacing such components. Such coatings could also serve for Linear Fresnel Reflectors working in static air. Solar tower and linear Fresnel technologies are corresponding to the worst degradation cases.

Figure 57. Schematic of the interconnections between CSP plant configuration, correlated sources of degradation, aging mechanisms and subsequent material degradations for the receiver with solar selective absorber coating (SSAC)

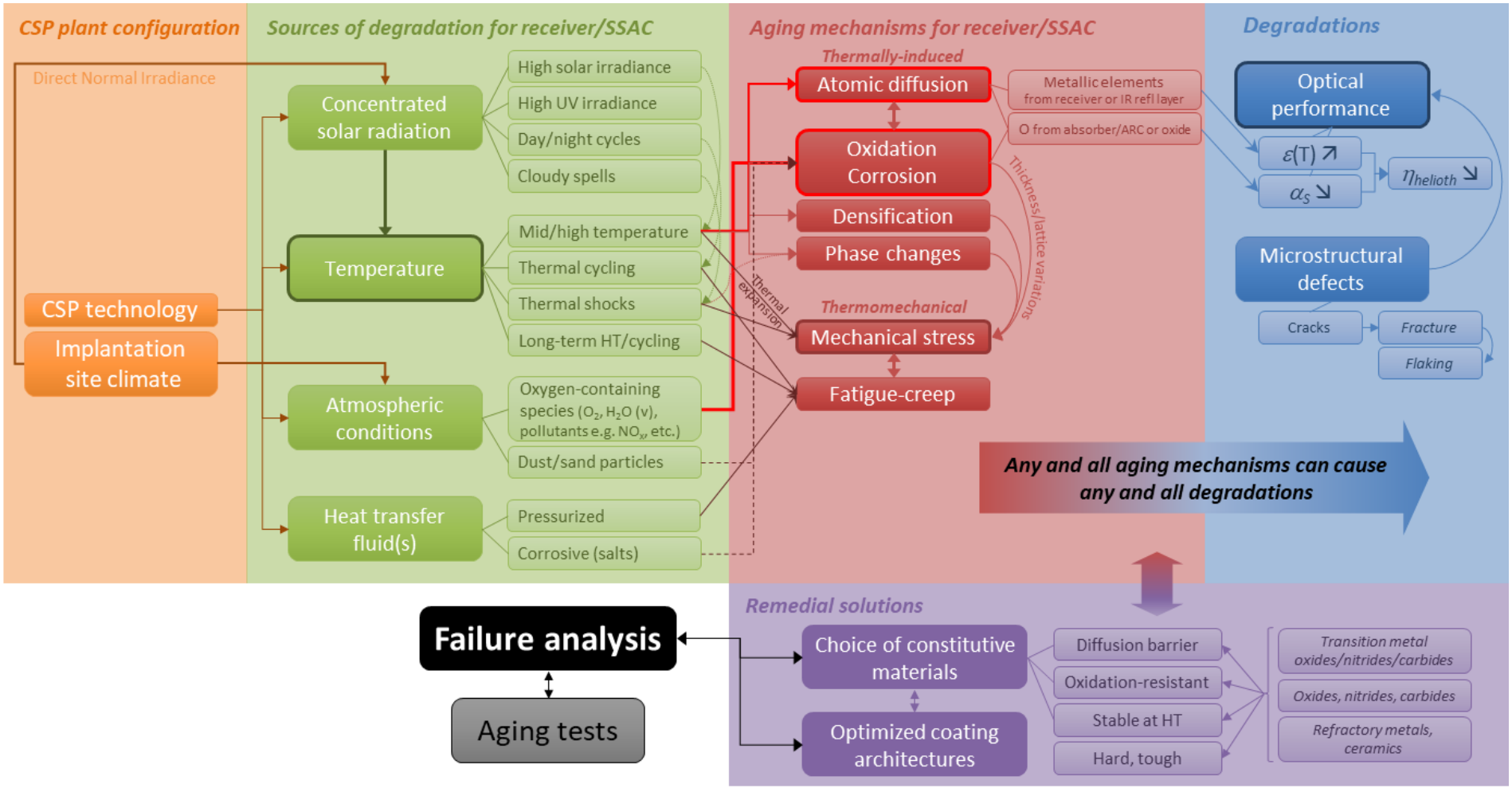

In central towers, the impact of solar and UV irradiance is higher, as the concentration ratio is much higher, also leading to higher operating temperatures and their related degradation phenomena, what is more in ambient/humid/polluted/ dusty air. However in this case thin absorber paints (e.g. silicone-based Pyromark®) are widely used, with very simple structure (typically one 15 µm-thick SiO_2 layer) and excellent thermal stability, strongly limiting degradations: few changes in solar absorptance levels were observed after thousands of hours of testing at 650°C [215]. Yet such paints: are not spectrally selective (high emittance of 0.87) leading to large thermal losses at high working temperatures; must be reapplied every few years (typically 5 years [216]) leading to high maintenance costs and difficulty (the receiver being at the top of a high tower). Thus R&D efforts are still put to develop more complex and efficient SSACs for central towers.

Figure 57 also summarizes possible remedial solutions to prevent or limit aging mechanisms and subsequent degradation, as previously discussed and found in the literature. They are mostly based on choosing SSACs constitute materials that are known to be intrinsically resistant to these aging mechanisms, i.e., the diffusion barrier, oxidation-resistant, high temperature materials discussed in Chapter 1: transition metal oxynitrides for tandem absorbers [119,121], refractory metals/ceramics for multilayer absorbers and composites [109], antireflective oxides [127], etc.

Adapting the coating architecture is also paramount. For instance, to prevent the degradation of thermal emittance via the diffusion of metallic elements from the receiver material, the diffusion barrier layer/material must be placed between the latter and the coating. Similarly, to prevent the oxidation of the absorber material(s) in air, the oxygen diffusion barrier layer must be placed at the top of the coating (e.g. antireflective oxide) in contact with ambient conditions.

As can be expected, the efficiency of such preventive measures may suffer from the large amount of uncertainty regarding the evolution of the materials and architectures with aging. When considering a single material, aging mechanisms are easier to anticipate, or even predict and simulate. However with the complex architecture of solar selective absorber coatings, there is a much larger number of factors to take into account: materials chemical composition and microstructure (crystallinity, porosity/density, defects, depending on fabrication methods), layer order, chemical affinity and thicknesses, interdiffusion behavior, thermal expansion and lattice parameters matching, etc.

This complexity makes the prediction of material degradation and failure very difficult, explaining why there is no common acceptable model to describe the aging of solar absorber coatings. Each type of coating requires specific degradation and failure analysis. The only consensus is the definition of failure for such coatings, based almost entirely on their optical performance. Simple models may have some significance and serve as reference, e.g. pure metal oxidation models for metallic-containing SSACs. The oxidation of metal alloys and metallic oxides is however more complicated to predict than the oxidation of pure metals [217]. Literature in other research areas can also help better understand and anticipate their behavior at high temperature, for instance regarding oxidation [218–223].

The solar receiver is one of the crucial elements to consider in the overall lifetime of a CSP plant. A small change in the performance of the receiver can significantly affect the global performance of the plant [224]. Despite the difficulty, anticipating the evolution in performance of the absorber is thus a major issue for CSP developers, to predict its lifetime and also plan its technical maintenance [224]. Indeed, it is not desirable for CSP plants to be stopped for components replacement or maintenance, as they lead to decreased energy production and subsequent loss of income for plant operators. It is thus intended that each component and its materials should be able to function for the complete lifetime of the CSP plant, which is around 20 to 25 years. Aging behavior and durability of the selected solar absorbers thus need to be understood, controlled and anticipated as much as possible.

For this purpose, a number of aging procedures for CSP selective absorber coatings have been developed in the literature, which are discussed in the next section.

4. Aging procedures and failure analysis of solar absorber coatings

4.1. Aging methodologies

The literature on solar selective absorber coatings mentioning aging studies is extensive. As a statistical illustration, we have considered 79 aging conditions from 59 research articles relating aging tests on selective absorber coatings [55,56,60,62,71,72,78,79,81,84–86,88,108,110,119–121,123–128,130–133,144,150,169–174,180,181,183–186,188,189,225–240] (Table 6). Out of these 59 articles, 33 (i.e., 42%) were published between 2015 and 2020, showing that the study of aging behavior is becoming an increasingly important step for the development of solar absorbers. Out of the 79 tests, most are applied on tandem (42/79 = 53%) and cermet (31/79 = 39%) configurations, as they are considered to be the most promising absorbers for CSP applications at mid-high temperatures.

When looking more closely, it appears that most of these studies focus on three main parameters to test the aging behavior of a solar selective absorber, with no clear consensus on their respective values. These parameters are the temperature, atmosphere and duration applied to the materials during their aging tests. Their values are chosen considering the CSP operating conditions for which the absorber is intended, and adjusted to apply more or less harsh treatments to the absorber, sometimes increasing them gradually to find the materials stability limit (failure), usually defined as a significant loss in optical performance. Temperature and atmosphere are chosen first and the tests are applied for a certain amount of time, usually until there is a significant deterioration of the absorber.

In some conditions, failure occurs after long aging durations. In this case, the tests are in fact applied in several aging steps of shorter duration that accumulate on the sample (e.g. in [235], samples were treated up to 600 hours, using eight different cycles with short duration before 100 hours and then long duration of 100 hours for the next cycles). In addition to being easier to apply, this method has the advantage of allowing for the evolution of the coating to be measured at regular intervals, to understand to some extent the kinetics of aging mechanisms. This procedure however amounts to thermal cycling (heating-cooling cycles) that can have a different and more deleterious effect than continuous aging (fatigue), so the former must be distinguished from the latter, especially since there is no consensus on the intermediate steps durations or number of cycles applied.

The tests were categorized according to their temperature range, atmosphere chosen and number of hours applied (Table 6). Most of these tests (62/79 = 78%) were applied in the [400-600°C] temperature range, where most of the absorbers failed. The most used atmosphere for the tests is vacuum (42/79 = 53%) rather than air (35/79 = 44%). Almost half of the tests (36/79 = 46%) did not exceed 100 hours, mostly due to the low thermal stability shown by the absorber.

Figure 58 shows the correlation between the temperature and duration of the different tests, for the different atmospheres. To illustrate the relationship between the aging duration and temperature applied during the considered tests, their correlation coefficient was calculated using the Spearman correlation r_s shown in Eq.(21). This coefficient is determined by dividing the covariance of the rank (*rk*) variables by the product of the standard deviations σ_i of the rank variables.

$$r = \frac{cov(rk_x, rk_y)}{\sigma_{rk_x} \cdot \sigma_{rk_y}} \tag{21}$$

Table 6. Tendencies for aging tests on selective absorbers, based on 79 aging conditions from 59 articles

Type of absorber			
Textured surface	Multilayer absorber	Cermet	Tandem absorber
1 [240]	**5** [86,108,133,192]	**31** [60,62,71,72,79,81,85,88,144,150,170,171,180,181,183–186,188,225,226,241]	**42** [60,119–121,123–128,130–132,172–174,189,225,227–236,238,239,242]
Temperature			
< 400°C	400 - 499°C	500 - 599°C	≥ 600°C
7 [88,108,110,124,127,150,239]	**17** [119,125,128,130,150,173,184,189,225,229,236,238,242]	**29** [60,62,72,81,86,120,121,126,131,132,144,150,169,170,172,181,186,188,189,225,227,231,232,234,239,240,242]	**26** [60,71,72,79,84,123,130,133,171,174,180,183,185,187,226,228,230,233,236,238,239,241,242]
Atmosphere			
Vacuum	Nitrogen	Air	
42 [60,62,71,72,79,81,84–86,88,124,125,130,132,144,169,173,174,180,183–186,188,226,228,230–234,236,238,239,241,242]	**2** [170,181]	**35** [108,110,119–121,123,124,124,126,128,130,131,133,150,171,172,189,225,227,229,235,236,238,239,242]	
Numbers of hours				
< 10 h	10 - 99 h	100 - 499 h	500 - 999 h	≥ 1000 h
17 [71,72,85,86,108,123,126,131,133,144,172,185,227,228,233]	**9** [62,110,120,130,170,180,239]	**29** [60,79,119,128,132,169,171,174,183,186,189,226,229–232,238–242]	**13** [81,84,121,124,127,173,225,239,242]	**11** [88,125,150,181,184,188,225]

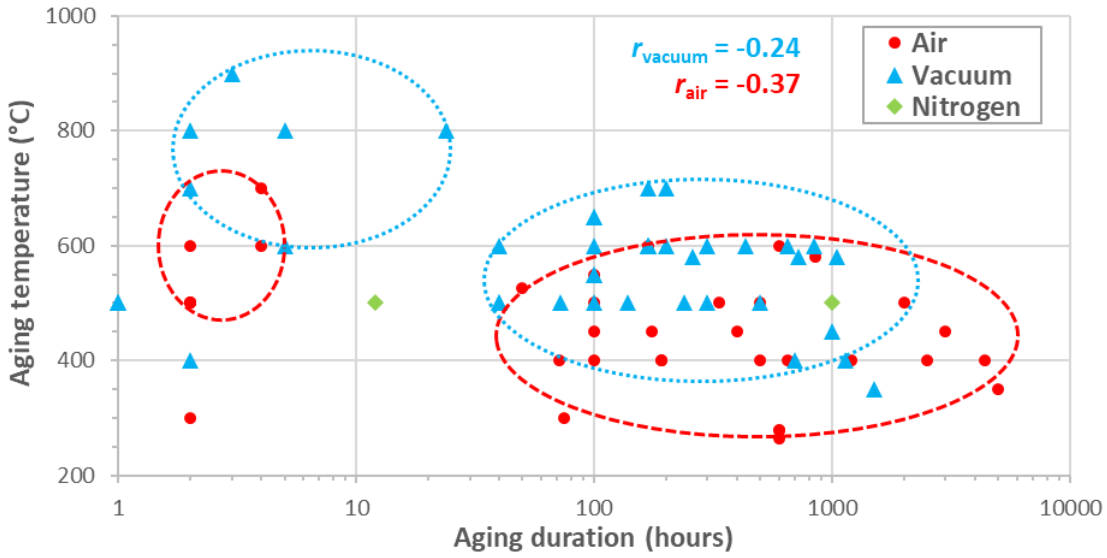

Figure 58. Correlation between aging temperature and duration based on 79 aging conditions from 59 articles

The large disparity in Figure 58 shows that there is no consensus on the aging protocols applied to solar absorber coatings: each manufacturer applies different aging to their absorber, without following any standard procedure. Most tests are for temperatures between 400°C to 600°C and durations between 100 and 1000 hours. The applied temperatures are higher in vacuum conditions than in air, underlining the deleterious effect of oxidation on the coatings durability. Test durations in vacuum and air are similar, although there seems to be a tendency for longer durations in air, as CSP applications now demand it. The longest durations (≥ 1,000 hours) are applied at temperatures between 350°C and 600°C, mostly in air. The maximum duration applied to an absorber in this review is 5000 hours in air for a temperature of 350°C [150], to prove the durability of a commercial absorber. At the highest temperatures (≥ 700°C), the duration is short (≤ 10 hours), the tests being just intended to rapidly observe a deterioration of the coating and be able to make conclusions about failure mechanisms [72,180,228,233]. Overall, the negative values of the temperature-duration correlation coefficients, equal to -0.24 for vacuum tests and -0.37 for air tests, reflect that the aging duration is reduced as temperature increases, especially in air, as the time to failure also decreases in harsher conditions. Their weak values (closer to 0 than -1) further illustrates that no clear relationship exists between temperature and duration, especially in vacuum.

On the whole, this bibliographic study shows that there is no common standard in aging procedures. This is in part due to the large variety of coating solutions explored, and their different thermal stability. However, it is mostly due to differing goals for coating developers. If some authors explore in detail the aging behavior of their coatings [181,184,225], most developers simply aim at demonstrating the stability of their coating performance [171,185,188,226]. They do not always push their coatings to failure, applying only temperatures too low and/or durations too short to reach it. In addition, they tend to carry out optical measurements only, but no further material characterization. Therefore, the thermal stability limit and aging mechanisms occurring in their coatings remain unexplored. Aging test standardization does not seem to be actively pursued in the solar selective absorber coating community.

To better understand existing aging procedures and aspire to their standardization, we have divided them into two main categories, depending on the temperature, atmosphere and duration applied to the absorbers: representative aging and accelerated aging. These two ways of applying aging are detailed in the following.

4.1.1. Representative aging

Representative aging is the first (and often the last) step taken to test a solar selective absorber. The main objective with this type of aging is to prove the thermal stability of the coating under atmospheric and/or vacuum conditions close to that of the intended CSP application. An absorber coating is considered thermally stable when it is capable of maintaining its initial optical properties and integrity after being exposed to aging conditions. It is observed from the evolution of optical properties, i.e. solar absorptance and thermal emittance, with temperature and time.

The chosen temperature for this type of test is slightly higher than the real operating temperature intended for the absorber, usually around 50°C higher. The chosen atmosphere also depends on the final use of the absorber. The most used options are:

- air, an oxidant atmosphere that can be:
  - static (natural convection) or dynamic (forced convection);
  - dry (without H_2O) or humid;
  - filtered (e.g. without H_2O and CO_2), or with added pollutants (e.g. NO_x);
  - recreated using an equivalent partial pressure of oxygen [243];
- vacuum, with levels between $5 \cdot 10^{-5}$ and 10 mbar [84];
- inert gases, such as nitrogen or argon [170,181].

The last two are suitable for parabolic trough applications where the receiver is maintained under vacuum, or simply to compare with aging in air and highlight the specific effects of the oxidant atmosphere. Testing in air is mandatory for the other CSP technologies.

In practice, representative aging tests can be initiated with short duration tests at increasing temperatures, to observe the thermal behavior and find the failure temperature of the absorber. These short duration tests last typically less than 10 hours, 2 hours being a popular choice [119,128,233,237]. Due to their short duration, they are only applied in one cycle, consisting of a controlled heating ramp, stable plateau at the testing temperature, then natural cooling.

Afterwards, tests at longer durations (> 100 hours) are applied, cumulatively (on the same sample) or continuously (on different equivalent samples), below or around this failure temperature, to get an idea of the coating durability (long-term stability) in conditions representative of the CSP application.

4.1.2. Accelerated aging

After applying representative aging to a solar selective absorber coating to find its thermal stability limit, accelerated aging can be applied, for the main purpose of predicting the lifetime of the absorber coating, by accelerating its aging over much shorter durations (e.g. several days or weeks) than its intended operating time (e.g. several years or tens of years).

Methods for accelerated aging tests of solar absorber coatings were first introduced in the work of the International Energy Agency (IEA) Solar Heating and Cooling (SHC) Programme, under Task 10 “Solar materials R&D”(1985-1991) [244]. As a continuation of Task 10, the IEA Working Group of Materials in Solar Thermal Collectors (MSTC) was founded in 1994 [245–249]. These studies concerned low temperature solar thermal collectors working below 280°C, mostly for Domestic Hot Water (DHW) systems. Predictions of long-term stability of coatings for such solar collectors by accelerated aging in Task 10 were confirmed by examples in the field, e.g. in [250] for a selective absorber coating on a single glazed flat plate collector, assessed by performing constant load tests in the laboratory, where a temperature-dependent Arrhenius behavior was suggested for the degradation of optical properties. This type of testing method was submitted to the International Organization for Standardization (ISO)

in January 1997 [251] for standardization, later named ISO/CD 12592, 2 "Solar Energy – Materials for flat plate collectors – Qualification test procedures for solar surface durability". Based on this standard, a qualification method of accelerated aging at higher temperature was presented by the European Committee for Standardization, named ISO standard draft EN 12975-3-1 (2011) [252]. It is now used for qualification evaluation and service life prediction for commercial products in low temperature solar collectors.

Yet to this day no such standard was ever proposed for the accelerated aging and lifetime prediction of solar selective absorbers used in CSP. However similar aging procedures were attempted by SSACs developers. These procedures are therefore explained in further detail in the next subsections.

4.1.2.1. Thermal stability and lifetime prediction with Arrhenius method

Exposing the coatings to aging temperatures higher than the operating temperature is the most popular method of applying accelerated aging. It allows to activate and speed up thermally-induced physicochemical phenomena that can be responsible for the coating deterioration (see section 3.2). Thus for degradation caused by diffusion, oxidation or other chemical reactions, the temperature dependence of the process can be described by an Arrhenius relationship. The aging process rate *K* is then expressed with Eq.(22).

$$K = A \cdot exp(-E_a/RT) \tag{22}$$

E_a is the activation energy in kJ/mol, i.e., the minimum energy required to start the aging process. *A* is the characteristic parameter of the process (e.g. for diffusion, *A* is D_0 as in Eq.(17) p.55). *T* is the temperature applied during the accelerated aging test. *R* is the gas constant.

For SSACs, the aging of interest relates to the changes in solar absorptance $\Delta\alpha_S$ ($\Delta\alpha_S(t) = \alpha(t) - \alpha(t=0)$) and/or thermal emittance $\Delta\varepsilon$ before and after the aging test. The rate in Eq.(22) is thus considered proportional to the variation of the optical properties with time $\left(K \sim \frac{\Delta\alpha_S}{\Delta t} or \frac{\Delta\varepsilon}{\Delta t}\right)$ and expressed in h^{-1}.

The evolutions $\Delta\alpha_S$ and $\Delta\varepsilon$ can also be followed simultaneously through the performance criterion PC (ISO 22975-3 standard [252], Eq.(23)). If degradations occur (decrease in solar absorptance and increase in thermal emittance), the value of PC increases: the higher PC, the higher the degradation. Once PC reaches 0.05, the coating is considered fully degraded. The degradation rate of Eq.(22) can therefore also be expressed as the evolution of PC with time.

$$PC = -\Delta\alpha_S + 0.5 \cdot \Delta\varepsilon \tag{23}$$

It is usually presumed that there is only one mechanism of degradation [246] so that its activation energy E_a and parameter *A* can classically be attributed to said mechanism. Nevertheless, since the process rate is expressed as the change in optical properties with time, the Arrhenius relationship represents in this case a global degradation of the coating including all thermally-induced mechanisms, with a global activation energy E_a for optical degradation. If the kinetics of these phenomena differ too much, the estimation of E_a can become tricky. More to the point, to apply Arrhenius method one must verify by material characterization (e.g. EDS, XPS, TGA, etc.) that thermally-induced phenomena are the main cause for optical degradation in the chosen temperature range, so that they can be correctly represented by an Arrhenius law.

To predict the lifetime of solar selective absorber coatings, this global activation energy must be estimated. It can be determined using an Arrhenius plot vs. $1/T$ (Eq.(24) derived from Eq. (22)). Its linear slope $-\frac{E_a}{R}$ gives direct access to E_a.

$$ln(K) = ln\left(\frac{\Delta\alpha_S \; or \; \Delta\varepsilon}{\Delta t}\right) = -\frac{E_a}{R}\cdot\frac{1}{T} + ln\, A \qquad (24)$$

To obtain this plot, several equivalent samples of the same coating are used. Each sample is treated at a different temperature, called accelerated temperatures T_{acc}, that must be chosen carefully. Indeed they must be higher than the aimed operating temperature T_{op} by a meaningful amount, to significantly accelerate aging, though not too high and not too far from one another, so that the aging mechanisms at play remain the same than at T_{op} and also the same for all T_{acc} values. For good accuracy, at least three temperatures are needed for pertinent linear regression; a step in temperature of less than 50°C is used; several samples are treated for each temperature T_{acc}; the variation of optical properties at each T_{acc} must be monitored at regular intervals and the test must reach a reasonable total duration, typically around or longer than 100 hours. As an example, Figure 59 illustrates an accelerated aging test in air previously carried out at PROMES laboratory on a TiAlN tandem absorber [253] intended for T_{op} = 350 - 500°C. Accelerated temperatures of 600, 620 and 650°C were applied with durations of 150, 100 and 40 hours respectively. An activation energy around 155 kJ/mol was deduced from the corresponding Arrhenius plot.

Knowing the activation energy, the yearly decay rate $d(T_{op})$ in %/year of the optical property of interest at the operating temperature T_{op} can be estimated using Eq.(25). It takes into account the number of hours of operation over a year, typically 8 hours/day for 365 days = 2920 hours/year. The absolute decay at T_{op} can then be deduced by multiplying the yearly decay rate by the number of years of operation intended for the coating (Eq.(26)), typically 25 years.

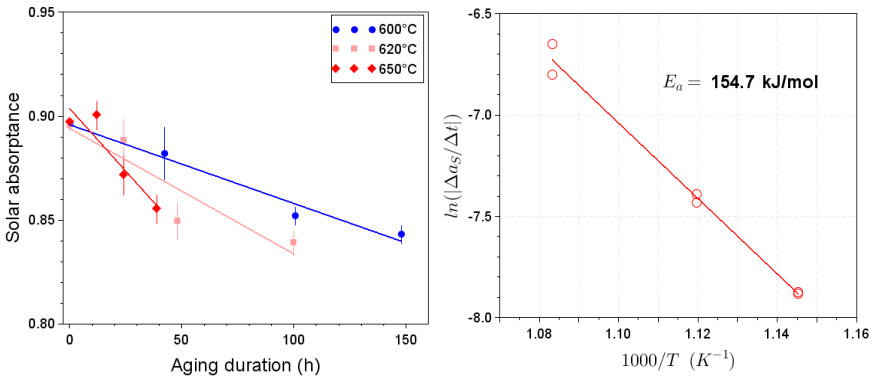

Figure 59. Solar absorptance evolution with accelerated aging tests of a TiAlN coating at PROMES and corresponding Arrhenius plot [253]

Knowing the activation energy, the yearly decay rate $d(T_{op})$ in %/year of the optical property of interest at the operating temperature T_{op} can be estimated using Eq.(25). It takes into account the number of hours of operation over a year, typically 8 hours/day for 365 days = 2920 hours/year. The absolute decay at T_{op} can then be deduced by multiplying the yearly decay rate by the number of years of operation intended for the coating (Eq.(26)), typically 25 years.

$$d(T_{op})\ [\%/year] = -exp\left(\frac{-E_a}{R\cdot T_{op}}\right)\cdot N°\ hours/year \qquad (25)$$

$$Absolute\ decay\ (\%) = d(T_{op})\cdot N°\ of\ years \qquad (26)$$

These values are illustrated in Figure 60 for the previous example. At T_{op} = 500°C a drop in absorptance of 7 points/year gives rise to an unacceptable decrease in absorptance of 10 points after only 2 years. At T_{op} = 350°C the estimated lifetime is higher than 25 years with a decrease in absorptance lower than 1 point.

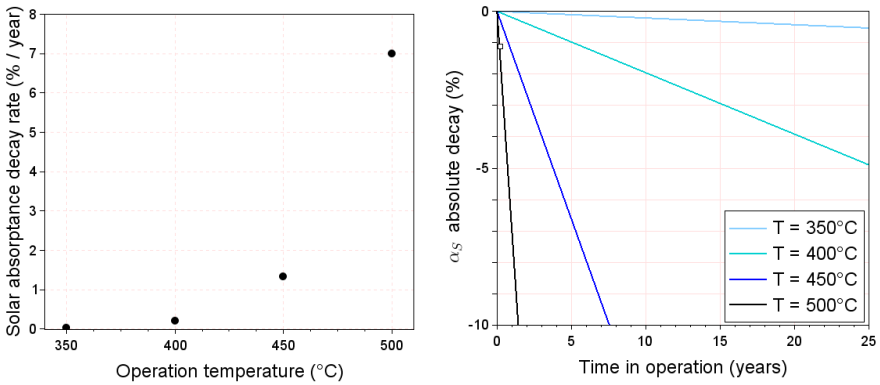

Figure 60. Solar absorptance yearly decay rate vs. operation temperature (left) and solar absorptance absolute decay vs. time in operation (right) of a TiAlN coating at PROMES [253]

An acceleration factor $a_{T_{acc}}$ of the aging at T_{acc} can be deduced from the activation energy (Eq.(27) derived from Eq.(22)). It allows estimating the test duration t_{acc} needed to be applied to the coating at temperature T_{acc} to reach the same state as after the operation time t_{op} at temperature T_{op}. These values are illustrated in Figure 61 for the previous example: for instance, the accelerated aging duration needed to represent 25 years of operation for 8 hours/day (73000h) at T_{op} = 500°C is t_{acc} ≈ 6 months (193 days) at T_{acc} = 600°C, or 2 months at 650°C. In another work [151], the time to reach PC = 0.05 (Eq.(23)), considered as irreversible optical degradation, was calculated as a function of T_{op} following a similar procedure. The coating was declared stable at 375°C for 25 years of standard operation.

$$a_{T_{acc}} = \frac{t_{op}@\,T_{op}}{t_{acc}\,@\,T_{acc}} = exp\left(-\frac{E_a}{R}\cdot\left[\frac{1}{T_{acc}}-\frac{1}{T_{op}}\right]\right) \qquad (27)$$

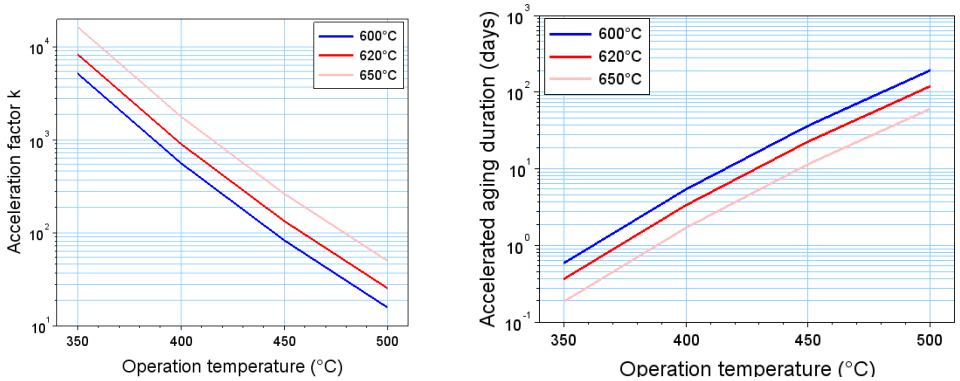

Figure 61. Acceleration factor and accelerated aging duration calculated for a TiAlN coating at PROMES [253]

The example in Figure 61 shows that the acceleration factor accessible with accelerated aging strongly depends on the operation temperature: the higher T_{op}, the longer the necessary aging to become representative of the real time in operation (e.g., 25 years at T_{op}). It is also possible to increase T_{acc}, but one must still ensure that aging phenomena remain similar at both temperature levels (T_{op} and T_{acc}) for Arrhenius method to stay valid. Higher aging temperatures may induce new phenomena such as phase changes or densification.

Figure 62 [161] further illustrates this notion and also considers the influence of the activation energy of optical degradation, based on two examples found in the literature: a mid-temperature selective coating (SCHOTT PTR70 receiver coating, E_a = 170 kJ/mol, T_{op} = 400°C [254]) and a high temperature selective coating (TiAlN/AlON tandem absorber, E_a = 100 kJ/mol, T_{op} = 500°C [128,151]). At 700°C, the acceleration factors are respectively 25 and 11700, giving rise to aging durations of respectively 19h and 8940h (more than a year). This example highlights that the Arrhenius method, first suggested for low temperature absorber coatings (solar thermal collectors), may be suitable for accelerating the

aging of mid-temperature coatings [254], but in most cases the aging will not be accelerated enough for new generations of SSACs intended for operation at higher temperatures: test durations exceeding a few weeks or months mobilize too many technical and financial resources.

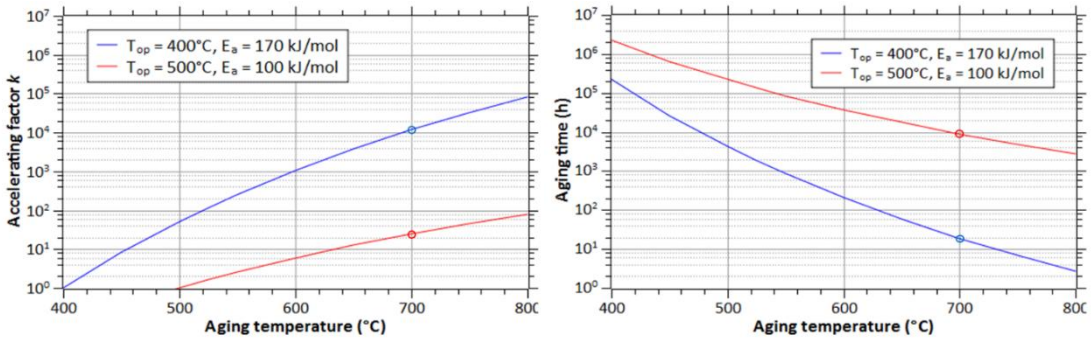

Figure 62. Acceleration factor and accelerated aging duration calculated for two different cases [161]

4.1.2.2. Influence of thermal load: effective mean service temperature method

A solar absorber is exposed to temperatures that may vary greatly during its lifetime. The effective mean service temperature T_{eff}, deduced from Eq.(28) [251] and derived from Arrhenius method, is a good representation of this thermal load.

$$exp\left(-\frac{E_a}{RT_{eff}}\right) = \int_{T_{max}}^{T_{min}} exp\left(-\frac{E_a}{RT}\right) \cdot f(T) \cdot dT \qquad (28)$$

$f(T)$ is the yearly frequency function for the service temperature of the absorber surface, i.e., the time fraction of a year when the service temperature is in the interval $[T\ ;\ T + dT]$. T_{min} and T_{max} are the minimum and maximum service temperatures. E_a is the Arrhenius activation energy of the optical degradation. R is the gas constant. Figure 63 shows the function $f(T)$ (left) and effective temperature T_{eff} vs. activation energy (right) of the absorber, for two cases:

- a standard profile for low temperature solar thermal collectors (blue), suggested by the IEA Working Group Materials in Solar Thermal Collectors, with T_{min} = -10° and T_{max} = 180°C [251];
- an estimated profile for mid-high temperature (red), typical of parabolic trough or Fresnel technologies using molten salts as heat transfer fluid (melting point around 230°C, stability limit of 565°C) with T_{min} = 200° and T_{max} = 540°C [161]. T_{eff} is much higher in this case.

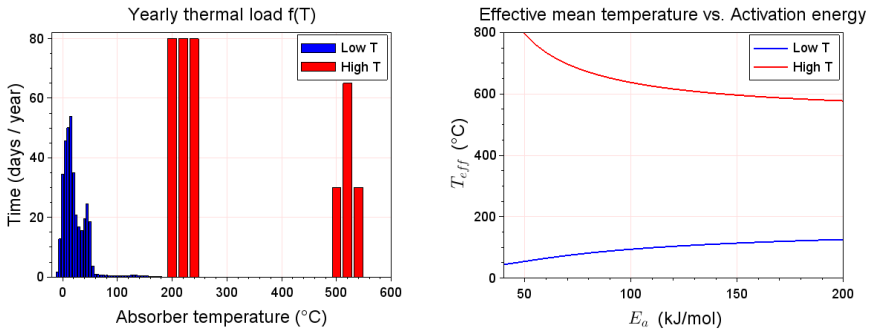

Figure 63. Examples of yearly frequency function *f(T)* (left) for low (blue [251]) and high temperature (red [161]) solar absorbers, and corresponding effective mean service temperature vs. activation energy [161]

An accelerated aging methodology can be designed based on the effective temperature. Eq.(29) is used to convert the intended 25-year service life (considering PC remains below 0.05, see Eq.(23)) into a "shortest failure time" t_{fail} at a given accelerated temperature T_{acc}. Figure 64 illustrates the shortest

time to failure vs. activation energy at two values of T_{acc}: 250°C for the low temperature absorber (blue) and 700°C for the high temperature absorber (red). For low temperature solar absorbers, the time to failure considering degradation mechanisms with $E_a \geq 50$ kJ/mol is t_{fail} = 10 days when aging at 250°C, which are very acceptable conditions for aging tests. For higher temperature absorbers however, the time to failure considering degradation mechanisms with $E_a \geq 100$ kJ/mol reaches 11 years when aging at 700°C. In other words, it would take 11 years of aging tests at 700°C to be representative of 25 years of operation at the effective mean service temperature: this is hardly accelerated aging anymore. Once again, this aging methodology is not suitable for high temperature absorbers.

$$t_{fail}\,[years] = 25 \cdot exp\left(-\frac{E_a}{R} \cdot \left[\frac{1}{T_{eff}(E_a)} - \frac{1}{T_{acc}}\right]\right) \quad (29)$$

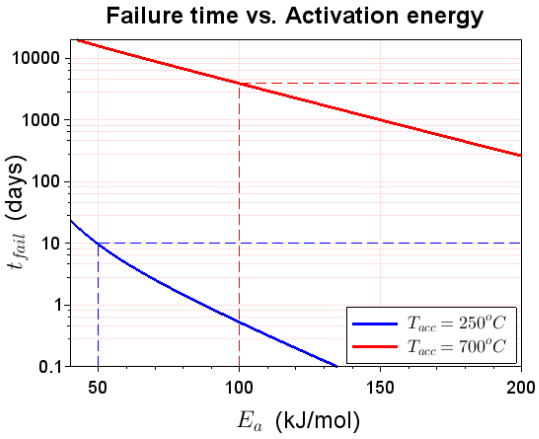

Figure 64. Failure time vs. activation energy for two different accelerated temperatures (low in blue, high in red) [161]

4.1.2.3. Towards more suitable accelerated aging methods?

As discussed, the previous classical accelerated aging methods are not always well suited for testing high temperature solar absorber coatings, due to the low acceleration factor they provide. Also they do not take into account parameters other than the temperature levels reached by the absorber. Other aging methodologies may be of interest in this field, and some of them are proposed in this section.

4.1.2.3.1. Considering thermal fatigue

Thermal cycling is inherent to the life of solar absorbers. This cycling results in thermomechanical fatigue (see section 3.3.2), that can lead to the failure of the absorber. Therefore, the response of candidate SSACs to thermal cycling should be tested. The Coffin-Manson relationship (Eq.(30)) is commonly used to model the low-cycle fatigue failure of materials subjected to thermal cycling [255–257]. The same formalism can be applied to CSP solar absorbers [258]. It is based on the notion that a power-law dependence β exists between the material optical degradation (e.g. the evolution of solar absorptance with the number of cycles: $d\alpha/dn$) and the temperature change ΔT during the cycles ($\Delta T = T_{max} - T_{min}$). $f(\alpha)$ represents the time-dependence of the degradation mechanism (e.g. in [258], the evolution of absorptance with thermal cycling could be fitted with $\alpha(t) = a \cdot t^{\gamma} + \alpha_0$ power law, which they derived to obtain $f(\alpha) = -(\alpha_0 - \alpha)^{\frac{\gamma-1}{\gamma}}$.

$$\frac{d\alpha}{dn} = k(\Delta T) \cdot f(\alpha) = A \cdot (\Delta T)^{\beta} \cdot f(\alpha) \quad (30)$$

Thermal cycling accelerated aging can be applied using this formalism, to obtain a lifetime prediction. Considering the cycles seen by the absorber in real operating conditions (e.g. for the Ivanpah central receiver plant, the annual load consists in Δn = 430 thermal cycles with temperature change ΔT_{op} = 672 K + 2300h of isothermal load at 716.7°C [258]), the aging can be accelerated with an acceleration factor a_{C-M} by applying cycles with $\Delta T_{acc} > \Delta T_{op}$ (Eq.(31), with β the Coffin-Manson coefficient from Eq.(30)). For the method to remain valid, the accelerated testing maximum temperature should not exceed the temperature of thermal stability limit of the absorber.

$$a_{C-M} = \left(\frac{\Delta T_{acc}}{\Delta T_{op}}\right)^{\beta} \tag{31}$$

As an example, a lifetime prediction for an industrial absorber coating (paint) using this method is presented in Figure 65 [258]. It compares the effects of isothermal (expected lifetime 36 years), cyclic (16 years) and coupled isothermal + cyclic loads (12 years), showing how the last two cases have a strong influence of the lifetime of the absorber. This example underlines that thermal fatigue testing is critical when developing a solar absorber coating, although rarely taken into account.

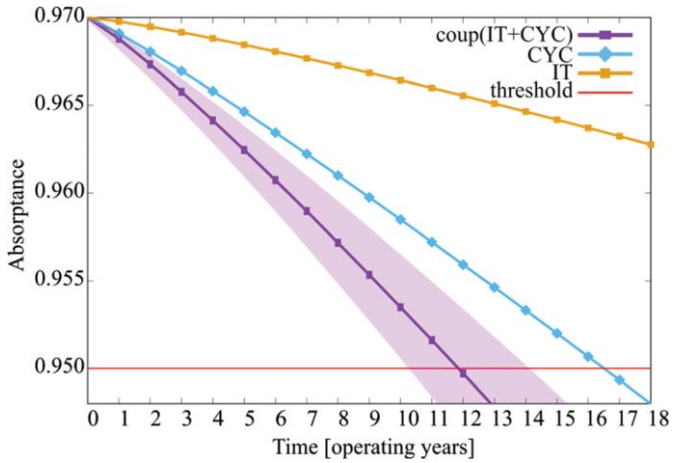

Figure 65. Optical degradation of HSA coatings under isothermal (IT), cyclic (CYC) and coupled (IT + CYC) loads, with limiting threshold at absorptance = 0.95 [258]

4.1.2.3.2. Considering thermomechanical fatigue-creep phenomena

As mentioned before (section 3.3.2.5), few research efforts regarding the thermomechanical aspects of aging for solar absorber thin coatings can be found in the literature. Among them, Montero-Chacón et al. [211] proposed a thermomechanical analysis of a tubular receiver with TiN/TiC:a-C/Al_2O_3 selective coating, using bottom-up multiscale simulation: from Molecular Dynamics at the nanoscale, to Representative Volume Element (RVE) at the microscale, to Finite Elements Method (FEM) at the receiver scale (Figure 66). Considering the materials thermal and mechanical properties (specific heat, thermal conductivity, coefficient of thermal expansion, elastic modulus, stress-strain curves), they were able to estimate stress distributions in the single layers and inside the absorber nanocomposite (a-C matrix with TiC inclusions). Although it does not constitute an aging procedure per se, nor provides a lifetime prediction, such analysis can be useful to foresee potential critical zones that could lead to the failure of the coating. However, the authors concede that their method is not straightforward as "it requires the expertise of the computational material scientists and is time-consuming".

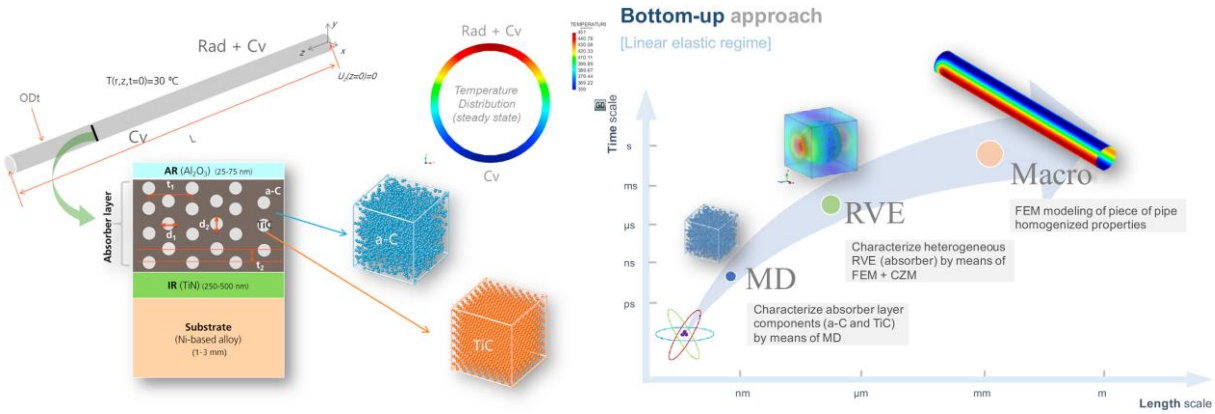

Figure 66. Multiscale thermomechanical analysis of a tubular receiver coated with TiN/TiC:a-C/Al_2O_3 [211]

Regarding experimental aging procedures, during the ASTORIX project (ANR 2014-2019, PROMES-CNRS partner), it was advised that thermomechanical aging tests must be applied to SSACs for more realistic lifetime prediction, in the same manner as for high temperature thermal power plant materials. As a first approach in the ASTORIX project, TiAlN absorbers were for instance submitted to bending tests at 150 MPa inside a furnace, first with constant temperature of 600°C at different durations up to 192h, then with thermal cycling between 600°C (8 hours) and 250°C (16 hours, natural cooling), and their microstructure and optical properties were studied to follow the impact of aging (unpublished work).

High temperature tensile or bending tests were proposed as they can effectively combine cyclic (fatigue) and long duration (creep) thermomechanical loads, with controlled strain rate (Figure 67). Tests at different temperatures and strain rates are classically used for bulk materials and provide accelerated aging and time to failure/lifetime predictions (e.g. [259]), in a similar manner as with the previously discussed thermal aging and thermal fatigue protocols, except thermomechanical failure is more often determined by the apparition and fast propagation of microcracks. These methods could also be adapted to receivers covered with SSACs, as was initiated in the ASTORIX project, considering failure as loss of optical performance.

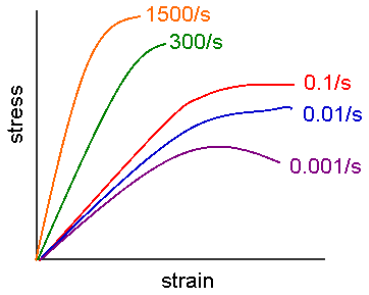

Figure 67. Typical stress-strain curves and corresponding strain rates (in relative deformation $\Delta L/L$ per second)

4.1.2.3.3. Considering atmospheric conditions

Contrary to solar mirrors [260–262], the influence of water vapor (humidity), salt sprays or sand particles in the operating atmosphere of the solar absorber are rarely considered factors when testing their durability. However only some authors have considered it [258,263]. For instance, Noč et al. [258] found that in similar thermal conditions, the addition of humidity had a notably aggravating effect on the degradation of solar absorptance (Figure 68). Chen et al. [263] found that salt spraying (NaCl 50 g/L) resulted in the corrosion of some SSACs at temperatures as low as 35°C and durations as short as 24h.

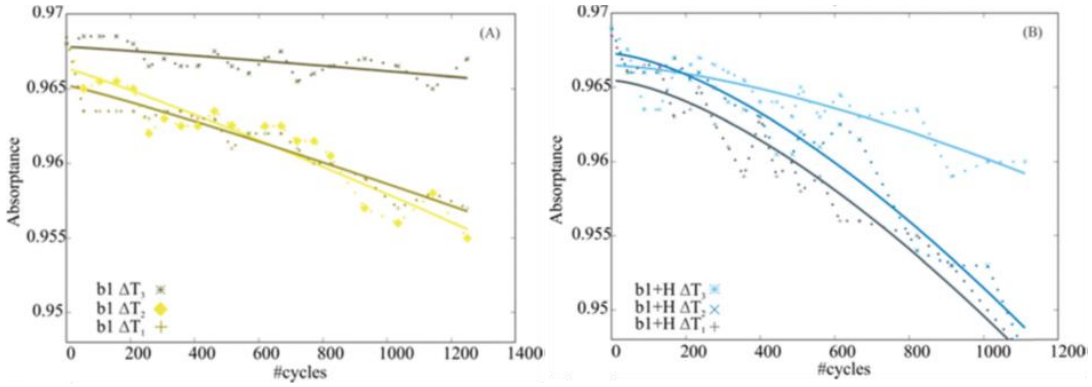

Figure 68. Optical degradation under similar cyclic thermal load, in dry (A) and humid (B) air [258]

To apply accelerated aging tests with humidity, a well-accepted model of the humidity stress factor known as Peck's model (Eq.(32)) can be used [264–266]. This model includes the effect of relative humidity (RH), and of temperature using an Arrhenius term with activation energy E_a.

$$t_f = (RH)^n \cdot exp\left(\frac{E_a}{RT}\right) \tag{32}$$

t_f is the time to failure, *RH* is the relative humidity and *n* is the kinetic parameter, which depends on the materials. To estimate E_a under humidity, tests at three different temperatures and constant humidity can be applied. In a similar manner, tests at three levels of humidity and constant temperature can be applied to determine *n*.

This is also a type of accelerated aging, with an acceleration factor a_P. The latter is given by Eq.(33) where RH_{op} and T_{op} represent the real operating conditions depending on the type of CSP technology and its implantation site, while RH_{acc} and T_{acc} are the relative humidity and temperature applied during the aging tests.

$$a_P = \left(\frac{RH_{op}}{RH_{acc}}\right)^n \cdot exp\left(\frac{E_a}{RT} \cdot \left[\frac{1}{T_{op}} - \frac{1}{T_{acc}}\right]\right) \tag{33}$$

4.1.2.3.4. Considering concentrated solar irradiance

As solar absorbers are intended to be exposed to concentrated solar radiation, accelerated thermal aging protocols can be designed using said radiation, to be more representative of the CSP application, especially regarding high temperature gradients and high flux densities with energetic UV-visible photons, that cannot be produced with simple thermal aging in a furnace. Only few attempts were made using concentrated solar irradiance as aging accelerant, mostly due to the technical complexity and cost of the required facilities (see section 4.2.2). Previous work in PROMES-CNRS laboratory proposed such aging procedures [36,160,267,268], using a unique solar facility that will be presented in details in the next chapters, as it was also implemented and further developed in this thesis. The facility was calibrated and designed to be as representative as possible of thermal flux profiles seen by solar receivers in real CSP operation (Figure 69). It allowed for high irradiance levels, high temperature gradients, rapid thermal cycling and thermal shocks, as a way to apply representative and accelerated aging. Similar efforts were made in other concentrated solar and solar-simulated facilities [35,224].

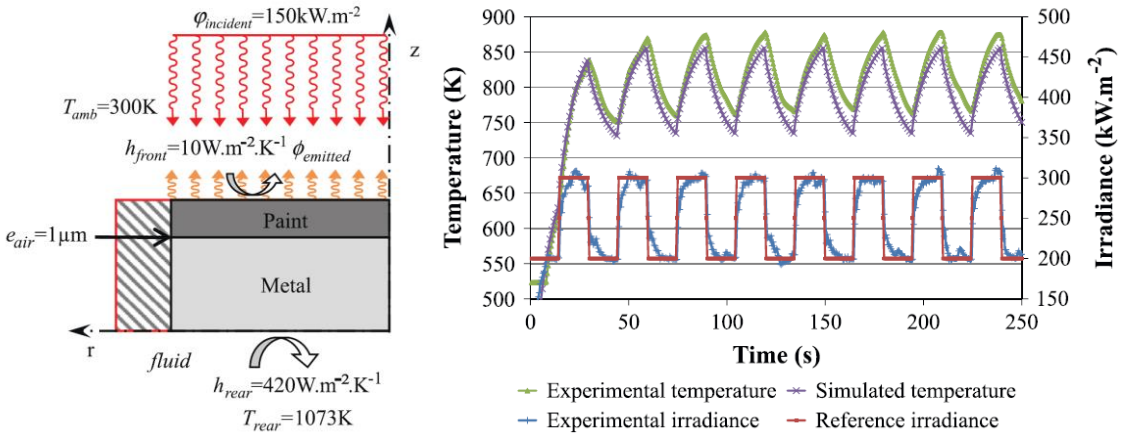

Figure 69. Configuration (left) and experimental/simulated temperature responses to cyclic irradiance (right) in solar aging facility developed in PROMES-CNRS [36]

However little to none experimental data regarding materials aged in real working conditions for several years is publicly available to this day. It is thus all the more difficult to determine which acceleration parameters would pertinently represent or accelerate real solar aging. Solar accelerated aging protocols were proposed, mostly based on the knowledge of thermal stability, but no consensus exists in this domain and no lifetime prediction is yet derived from these types of studies.

Overall, a large variety of solutions to test and ensure the stability and durability of solar absorbers exists. However the technical means to apply the more complex aging tests proposed in section 4.1.2.3 are not always accessible to developers. Indeed, these tools can be very specific, as presented in the next section.

4.2. Aging facilities

Aging facilities are specific equipment used to apply the possible sources of degradation (section 2) and accelerated aging methodologies (section 4.1) to determine the durability of solar selective absorbers. By using chambers and furnaces, different harsh environments can be created, where aging parameters (temperature, cycling, humidity, irradiance, etc.) are controlled, and adjusted to partly simulate the conditions that can be seen by the solar absorber of a CSP plant.

4.2.1. Thermal aging/cycling in electric furnaces

Programmable tubular or muffle electric furnaces (Figure 70), capable of reaching high temperatures up to 1800°C, are the most used aging equipment for solar selective absorbers (e.g. [121,269,270]). They are mostly used to apply isothermal aging, and in some cases slow thermal cycling, often for long exposure (> 1000 hours) and/or multiple cycles (> 200 cycles). In many studies, they are used for service lifetime prediction of absorbers, applying long term testing at different temperatures to apply the Arrhenius method [258] (section 4.1.2.1).

Figure 70. An example of muffle furnace (Nabertherm furnace) used for thermal aging

The configuration of these furnaces ensures a good thermal uniformity inside the heating chamber, by using ceramic heating plates. It also offers a good control of the temperature using a PID (proportional-integral-derivative) controller and thermocouples installed along the inside of the furnace. This way, heating can be applied as a linear profile with a fixed heating ramp, though the latter is limited by the furnace inertia and power. The cooling phase is often not controlled but simple natural cooling with decreasing exponential profile, also dependent on the furnace inertia.

Most electric furnaces work in atmospheric conditions, however some are also equipped to obtain vacuum conditions, with vacuum levels down to 10^{-5} mbar. Both configurations are widely used for solar absorbers, with tests done under atmospheric conditions for central receiver and LFR absorbers and under vacuum conditions for PT absorbers.

Overall, this type of aging facility can give access to a good prediction of the thermal stability of solar absorbers. However the relatively slow heating ramp accessible (e.g. 20°C/min) and the radiation (mid-infrared) applied to the absorbers create non-realistic conditions compared to real CSP working conditions, where the rise in temperature can be very quick (e.g. 20°C/s) and the absorbed radiation is in the solar range (UV-Vis-NIR). Other types of aging facilities offer more realistic conditions, as explained in the following subsection. The main advantage of electric furnaces is that they allow for a more precise control and reproducibility of the aging tests over long durations.

4.2.2. Thermal cycling under concentrated solar radiation

4.2.2.1. Solar furnaces

A solar furnace is a facility that uses a concentrating system to produce high irradiance levels and subsequent high temperatures at the focal point of such system, where materials are placed to test them. This type of aging device can thus simulate more realistic CSP conditions than electric furnaces.

Representative or accelerated aging conditions can be simulated with adapting the solar flux density, temperature level and temperature/flux gradients: irradiance levels can be adapted by using shutters, that can also give a rapid variation of the incoming solar flux. The most used concentrating system for solar furnaces is the parabolic dish (Figure 71), due to the good optical efficiency that gives high-flux solar radiation levels and also an easy access to the focal point. This technology enables to reach very high temperatures, thanks to the high optical efficiency of the parabolic dishes used with a concentration factor often higher than 10,000 [267].

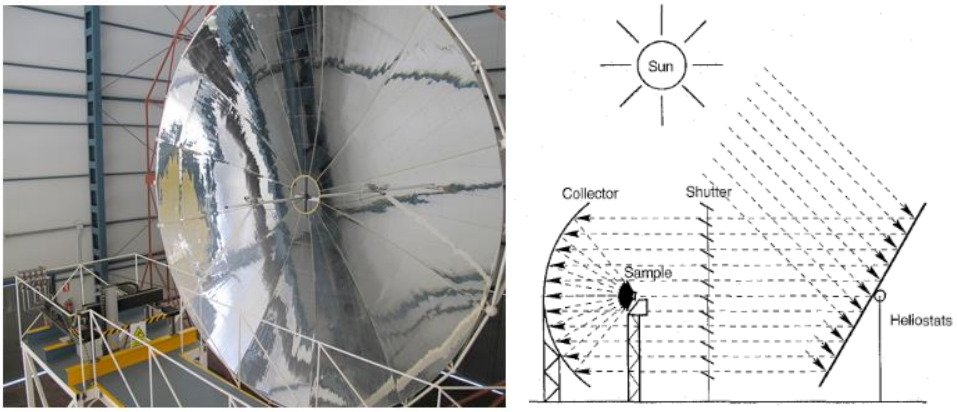

Figure 71. Example of a solar furnace located at the Plataforma Solar de Almeria [271]

There are three well-known solar furnace installations used for aging research purposes: PSA (Plataforma Solar de Almeria) laboratories in Almeria (Spain) [271] (Figure 71), PROMES-CNRS laboratory in Odeillo (France) [267] and Sandia National Laboratory NSTT (National Solar Thermal Test Facility) in Albuquerque, New Mexico (US) [224]. These laboratories have long experience in the field, which has enabled an optimization of such facilities. One of the reference works done on solar furnaces for research purposes is presented by Berenguel et al. [271] with the 20 kW solar furnace in Almeria. It shows several types of PID with gain scheduling and a self-tuning controller, as well as experimental results for temperature control with a law developed for this type of furnace [272].

In practice, irradiance levels are highly dependent on atmospheric conditions and sky clarity over time, so there is some uncertainty about the applied aging parameters, due to the dependence on weather fluctuations during the experiment. Also the aging duration is limited to the number of hours of direct sunlight during the day, therefore the total aging duration is necessarily shorter than with electric furnaces, due to the large number of days needed to accumulate hours of aging on the samples (e.g. 6 hours of aging under concentrated solar irradiance correspond to 2 half-days of tests, often spread over several days, weather pending). Finally, these facilities imply relatively high investment costs and require specific know-how. These are all disadvantages for this aging technology, which however remains the closest to real CSP operation.

4.2.2.2. High-flux solar simulators

Solar simulators are based on a light source that duplicates the solar spectrum and beam characteristics, to recreate an artificial emission spectrum similar to real solar radiation. A high-flux solar simulator is a type of solar simulator that gives access to high irradiance fluxes with the help of optical concentrators and high-powered lamps to be used indoors [273].

High-flux solar simulators combine the advantages of the previous aging facilities. As for electric furnaces, tests can be applied for long durations, and this whatever the climate, weather or DNI conditions, also providing more stable and reproducible experimental conditions. As for solar furnaces however, the tested materials can be heated with high heating ramps and irradiated with concentrated “solar-like” radiation instead of infrared thermal radiation, thus reaching irradiance and temperature levels more representative of the CSP application.

The light sources used in high flux simulators are xenon arc, metal halide or argon lamps, emitting near-solar light, and equipped with an ellipsoidal back reflector serving as concentrator (Figure 72). The first designs were built in the 1960s, to be used in space applications research projects sponsored by NASA for spacecraft ground-testing by simulating environments at orbital altitudes [274–276]. In the 1970s, low-flux solar simulators were first used for the development of solar collectors, then in the

1990s, high-flux simulators were built, mostly for testing thermochemical and CSP components. The first design of a high-flux simulator was proposed in 1991 for the study of chemical reactions under high temperature and flux, at the Lawrence Berkeley Laboratory [277]. With the help of an ellipsoidal concentrator, it delivered 3 kW on a 7 x 7 cm target and the peak flux reached 16 MW/m^2.

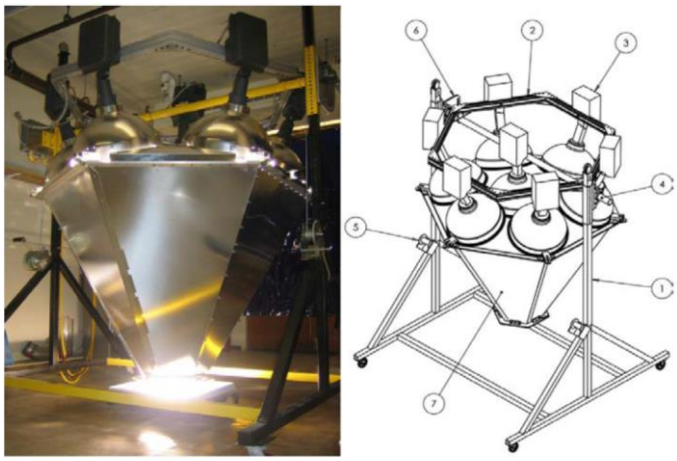

Figure 72. MIT CSP solar simulator [278]

Currently, there are several high-flux solar simulators around the world, capable of achieving high fluxes (1000 - 15000 kW/m²), used mostly for research purposes. The Paul Scherrer Institute (PSI) [277], the Swiss Federal Institute of Technology in Zurich [279,280], the German Aerospace Center (DLR) [281], the University of Minnesota [282], the Massachusetts Institute of Technology (MIT) [278], the Spectrolab (T-HIPSS) in USA and the Universidad Politécnica de Madrid in Spain [283], all have designed and built such systems for studying thermochemical processes and materials under very high concentration. One of the references for solar simulators for CSP purposes is the one developed at PSI [277]: 50 kW or 11000 suns, with 10 independent arrays of xenon arc lamps and their ellipsoidal concentrators, making it easier to apply various power capacities. Hence the same designs are successfully used in DLR and University of Minnesota.

The main drawbacks of this technology are the associated costs, in most cases higher than $100k, and also the difficult assembly and operation due to the large size, customized components, and significant safety requirements regarding fire hazard, ozone extraction, etc. Xenon arc lamps, the most used in this type of simulator, are also quite expensive and must be replaced regularly (e.g. every 1000 hours). To solve the cost problem, a low cost reduced-size solar simulator was built at MIT [278]. It uses seven 1.5 kW metal halide lamps as light source and offers mid flux levels: peak 60 kW/m² and average 45 kW/m². The peak irradiance is therefore lower (due to poorly concentrating reflectors), but the total cost is maintained below $10k. In any case, a very high level of concentrated irradiance is not necessary for testing materials intended for much lower concentration CSP systems such as parabolic troughs.

4.2.3. Atmospheric conditions: controlled atmosphere chambers

Controlled atmosphere or climate/weathering chambers are another type of aging technology. Climate chambers allow testing absorbers with Damp Heat, Humidity Freeze, sand erosion or Neutral Salt Spray. These types of chambers are more widely used to test solar reflectors and PV modules, due to the low operating temperatures and exposure to conditions at ground level. However they can also be relevant for testing solar absorbers [284].

A Damp Heat (DH) tester is a climate test chamber usually set to work at 85°C and 85% relative humidity (HR). Damp heat tests are relevant when the receiver is not in operation, for example during the night or in the absence of sun, with a humid atmosphere or dew [285,286]. The standards used for

this type of test are IEC 62108 Test 10.7 and IEC 61215-1 [287,288]. The Humidity Freeze (HF) test is similar to the Damp heat test, except it adds thermal cycling between 85°C and -40°C, with 85%HR for temperatures higher than 0°C. The standard used for this test is also the IEC 62108, Test 10.8. Both of these tests are usually applied for long durations, typically 2000 hours [260].

The Neutral Salt Spray (NSS) chamber is particularly relevant to test solar absorbers intended for CSP plants located near the coast, because of the saline atmosphere. This low temperature corrosion test method is standardized (ISO 22975-3:2014 [289]) with a typical exposure of 3000 hours at 35°C and 100%HR with NaCl 50 g/L sprayed solutions. It is a popular method to check the corrosion resistance of materials and coatings, and was applied to solar absorber coatings [284].

Sand erosion tests (Figure 73) can also be considered as testing procedures to estimate the lifetime of solar absorbers. This test is more widely used for solar reflectors [290] due to their larger aperture and proximity to the ground. For solar absorbers, the standard used for this test is MILSTD 810 G, where parameters such as wind profiles and particle size are chosen.

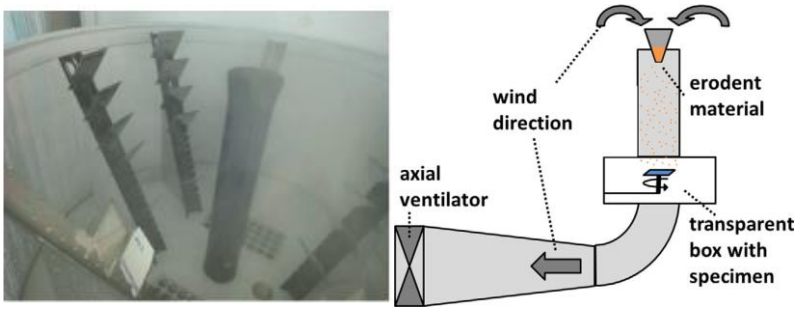

Figure 73. Sand erosion tests at PSA lab [290]

If these weathering tests amount to accelerated aging for low temperature materials such as mirrors and PV cells, for CSP absorbers they often relate to representative conditions rather than accelerated ones. However they can serve as a first indication of the absorbers stability to atmospheric conditions. As a general rule, the tests can be adapted to be close to the expected environmental loads on the absorber in real working conditions (e.g. corrosivity class of the location of the CSP plant, exposure to/velocity of sand particles, etc.), which differ for each CSP technology and implantation site.

4.2.4. Thermomechanical aging (fatigue-creep)

High temperature tensile or bending tests (Figure 74) consist in applying a mechanical load on a sample placed inside a hot furnace and following the response of the material (specifically its deformation or strain, see section 3.3). They are widely used to test the thermomechanical behavior of bulk materials for thermal and thermomechanical applications. Although they rarely are, they could also be used on coated solar receiver samples. For instance, during the ASTORIX project (ANR 2014-2019), the thermomechanical aging of high temperature TiAlN solar absorber coatings was tested (see section 4.1.2.3.2 p.81): a specific sample holder was developed to apply controlled bending loads on the samples while inserted in a furnace at 600°C (Figure 74, right).

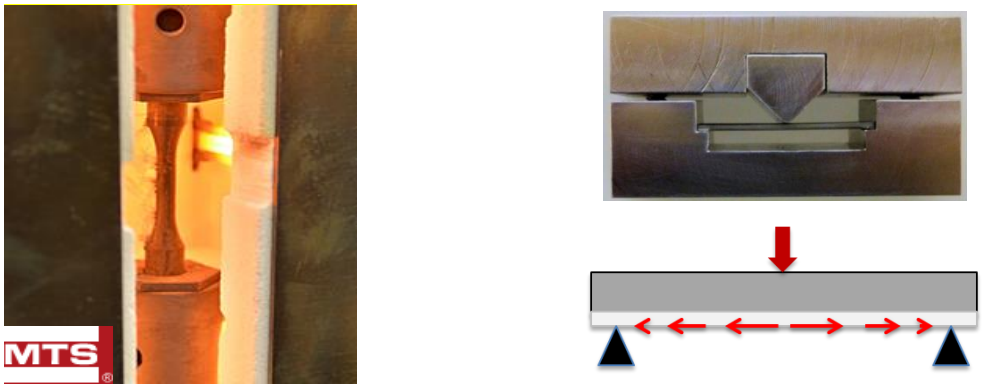

Figure 74. High temperature tensile tester (left), custom bending tester applied to TiAlN absorber coatings (right, courtesy of ANR ASTORIX project and Mines Saint-Etienne)

5. Conclusions on aging studies and justification of the present work

The main goal for current and next generation CSP plants is to increase the plant global efficiency by increasing the operating temperature, so as to increase the heat-to-electricity conversion efficiency. This also increases the temperature that solar receivers, the components in charge of absorbing solar radiation, will have to withstand, typically between 550 and 800°C, ideally in air. Yet the surface of the receiver still needs to be optically functionalized to guarantee high solar-to-heat conversion efficiency. This is achieved with spectrally selective absorber coatings (SSACs), combining high solar absorptance and low infrared emittance. The temperature stability limit of current commercial coatings is however between 400°C and 580°C in vacuum, so far they exhibit poor thermal stability at high temperatures under atmospheric conditions. Thus, there is still a need to find solar selective absorber coatings with satisfying thermal and mechanical stability at high temperatures in atmospheric conditions, and this for long durations, i.e., durability. As a consequence, research in the field of air-stable high temperature SSACs is very active.

The harsher working conditions these new SSACs are intended for however calls for a thorough evaluation of their aging behavior, in order to validate their suitability. Indeed, CSP absorbers are subjected to many potential and interdependent sources of degradation: high flux solar radiation, high temperatures, thermal cycling, thermal shocks, oxidant/corrosive/erosive atmospheres, etc. Yet often such aging analysis remains limited. Current aging tests in the literature focus on conservative tests at laboratory scale, not representative of CSP applications. In most cases, they are purely thermal treatments applied in electric furnaces heating with infrared radiation, due to the simplicity and availability of the technology. Often no thermal cycling is applied (continuous tests) and the materials are tested at moderate temperatures in air (< 400°C) or higher temperatures but in vacuum, mostly for short durations (< 100 h).

The most frequently identified aging mechanisms are therefore necessarily thermally-induced, and directly linked (with an Arrhenius law) to temperature. The main ones are: atomic interdiffusion of the chemical elements from the support material (usually a metallic alloy) and the different layers constituting the SSAC (metallic infrared-reflective sublayer, absorber layer, antireflective top layer); oxidation of any or all materials of the absorber (including the support and all layers of the SSAC), by surface adsorption, inward diffusion and insertion/bonding of oxygen atoms in the structure. Oxidation and diffusion often enhance one another as they both create defects and diffusion pathways in the crystal lattice. Although other phenomena are less studied in SSACs, the extensive know-how from other applications such as turbines, aeronautics or tools leads one to realize that CSP harsh working conditions can also cause phase changes, densification, thermal expansion, and related physical degradations such as the formation and propagation of cracks, which in turn enhance diffusion and

oxidation, as well as generate thermomechanical fatigue and creep. All these aging phenomena can potentially lead to deteriorating the SSACs, and subsequently to the failure of the absorber thermo-optical performance, due to significant and deleterious changes in its initial optical properties (i.e., decrease in solar absorptance, increase in thermal emittance). Therefore, to validate new efficient and durable SSACs, their aging behavior needs to be more deeply investigated, anticipated, corrected.

In this context, alternative aging methods need to be proposed and more systematically be applied to SSAC-covered absorbers, to get closer to the CSP application and more representative of its working conditions, for instance:

- tests in electric furnaces for long durations (e.g. > 1000 hours) and several temperatures above the thermal stability limit of the absorber, to apply accelerated aging and attempt lifetime prediction, although the acceleration factor may be limited;
- tests under concentrated solar irradiation and offering rapid thermal cycling: this calls for less standard aging tools such as solar furnaces or solar simulators;
- tests in controlled atmosphere chambers, to assess the long-term resistance of the coated absorber to corrosive and erosive atmospheres: salt sprays, humidity, dew, pollutants, sand, dust, etc.);
- tests combining high temperatures and mechanical stress for long durations, to study thermomechanical degradation occurring on the different absorbers.

A needed improvement in aging strategies would be to better investigate the specific effects of each source of degradation encountered by solar absorbers in CSP applications as well as the synergy between them, leading to the failure of the absorber. It would indeed give more representative information about the aging behavior of the absorber in realistic conditions. This calls for complementary aging methodologies and tools, able to decouple as much as possible the potential sources of degradation. Some, among many possibilities, are suggested in Table 7.

Table 7. Examples of complementary aging methodologies decoupling the sources of degradation encountered in CSP, each with thermal cycling option (slow: period ≈ h, rapid: period ≈ s)

Applied source(s) of degradation	**Type of heating**	**Type of illumination**	**Type of thermal cycling**	**Aging tool**
High temperature *+ thermal cycling*	Thermal (IR)	–	None *Slow*	Electric furnace
High temperature + Sun *+ thermal cycling*	Sun or sunlight lamps		None *Rapid*	Solar furnace or solar simulator
High temperature + UV *+ thermal cycling*	Sun or thermal (IR)	Sun or sunlight lamp + filter, or UV lamp	– *Slow*	Solar furnace, solar simulator or UV chamber
Mid-temperature + UV *+ thermal cycling*	Thermal (IR)	UV lamp	– *Slow*	Controlled atmosphere chamber
Mid-temperature + humidity *+ thermal cycling*	Thermal (IR)	–	– *Slow*	
High temperature + mechanical *+ thermal cycling*	Thermal (IR)	–	– *Slow*	Tensile or bending tester

As a first step towards with ideal aging strategy, following the critical analysis of literature exposed in this chapter, this thesis will present original experimental studies focused on the following elements:

- for practical reasons, not all the sources of degradation mentioned in Table 7 could be applied, as they are not all available at PROMES-CNRS, and the extensive corresponding work would go beyond the scope of a thesis. Therefore, the first two methodologies described in Table 7 were applied. They were compared with one another, with the objective to observe the synergy and decorrelate the specific effects of several critical aging parameters: high temperature, concentrated solar exposure, slow and rapid thermal cycling. For this purpose, a series of complementary aging tests, including representative and accelerated aging, were derived from the knowledge of aging factors under real CSP conditions and devised as explained in details in the following chapters. As a general rule, aging was increased or accelerated using higher values of aging parameters and/or repeated stress level variation (cycling).

- the tests were applied on sets of equivalent samples, presenting three typical configurations for next-generation high temperature air-stable SSACs, and following the line of research and previous work done in our laboratory: two architectures based on tandem absorbers, provided by project collaborators (HEF-IREIS Saint-Etienne and CSIR-NAL Bangalore), and one with a dielectric-metal-dielectric multilayer absorber, developed at PROMES-CNRS in Perpignan [194]. The exact SSACs configurations will be presented in Chapter 3 and the equivalence of the sets of samples will be discussed in Chapter 4, as a prerequisite to comparable aging tests.

- two PROMES-CNRS dedicated experimental aging facilities were implemented, calibrated, adapted and further developed during this thesis: an electric furnace that applies long-term thermal aging and slow thermal cycling, and a solar furnace that applies solar radiation for shorter durations and allows rapid thermal cycling. These aging tools and their characteristics will be presented extensively in the next chapters, as the control of their aging parameters is key to decoupling them and observe their specific effects. Aging tests performed thanks to the first tool will be presented at length in Chapter 4 on thermal aging. Chapter 5 will focus on solar aging results and their comparison with thermal aging.

- in all cases, the impact of the different aging methodologies on the materials was mainly observed via the evolution of their optical properties, surface morphology and atomic composition, to establish the links between aging parameters, aging mechanisms and optical failure. On this basis, the pertinence of the different aging methodologies tested in this thesis will finally be discussed in Chapter 5.

As a general rule, aging strategies for solar selective absorbers have two main goals:

- the first, most popular one is to study the aging behavior occurring in the absorber for the ultimate purpose of determining if they are suitable for CSP applications, i.e., if they are thermally stable in air at high temperatures, for long durations, or in other words, durable. Indeed, there is a need to find durable solar selective absorber coatings, to guarantee the long-term efficiency of solar receivers and minimize the overall cost of electricity generation in CSP plants. Although it is not the main objective of this thesis, as a collateral result, our aging studies provided pertinent information in that regard concerning the three configurations considered.

- the second goal we found almost absent in the literature, although it appears to us to be decisive for future CSP deployment with technologies operating at high temperatures in air. It is a more long-term and global objective, and the subject of this thesis: to gather in-depth knowledge on the synergy and separate effects of the main sources of degradation seen by solar selective absorber coatings during their CSP operation, in the ultimate view of eventually drawing up broadly applicable test standards for the prediction of thermal stability, reliability and service life of solar absorber coatings operating in these demanding conditions, as is already the case for other solar thermal materials, such as solar mirrors and low temperature solar thermal collectors.

Chapter 3 - Materials and methods

1. Absorber coatings used for aging studies

In this section, the three different solar absorber coatings that were used for the experimental analysis of aging procedures are described, looking at the architecture and constituting materials of the absorber, and techniques and equipment used for the manufacturing of the tested samples. The first two types of absorbers were designed, optimized and manufactured by project collaborators, where PROMES-CNRS laboratory is in charge of the thermo-optical and aging characterization of the absorbers. The last type of absorber was developed at PROMES-CNRS.

1.1. $TiAlN_x/TiAlN_y$ tandem absorber

This type of absorber was developed within the framework of the ASTORIX project (2014-2019) [34,44,82,291–295], in collaboration with HEF-IREIS (Institut de Recherches en Ingérierie des Surfaces) in Saint-Etienne [296], a surface engineering company specializing in tribology and functionalization of surfaces, thermochemical treatments and physical vapor deposition (PVD). HEF was in charge of the optimization and fabrication of $TiAlN_x/TiAlN_y$ tandem absorbers, intended as a new absorptive selective coating for central tower and linear Fresnel receivers working under atmospheric conditions at temperatures above 500°C. This project has ended and is continued by the NanoPlaST project (2019-2024) [297].

1.1.1. Materials and structure

Titanium aluminum nitride (TiAlN) was developed in the late 1980s as an alternative to TiN films for cutting tool applications such as dry and high-speed cutting [298,299]. TiAlN exhibits superior oxidation resistance, abrasion resistance, high thermal stability, chemical inertness and low electrical resistivity at higher temperatures than TiN [300–303]. Although TiAlN films were initially developed for hard coating applications due to its good performance at high temperatures [298], it has been proven that it can also be used as a solar selective absorber with an absorptance value for a single layer of 0.8 [304].

The solar selective absorber studied in this thesis is based on a tandem absorber configuration (see Chapter 1 section 4.1.5), using titanium aluminum nitride TiAlN as the main material for the absorber layers, deposited on Inconel and stainless steel (SS) substrates (Figure 75). Following the structure of tandem absorbers, the $TiAlN_x/TiAlN_y$ absorber has two layers with low and high content in nitrogen, thus switching from metallic-like to semiconductor-like behavior, with refractive index gradation from high to low [34,44,120,124,291] (Figure 76).

A TiAl infrared reflector sublayer [293] with intermediate *n* is added between the metallic substrate and the tandem absorber. On top of the absorber layers, a SiNCH antireflective layer is added to enhance solar absorption [292]. These types of materials are high temperature ceramic materials, suitable for antireflective coatings, with low refractive index, high hardness and good thermal stability up to 650°C in air [82,294]. A multilayer stack (Inconel/TiAl/$TiAlN_x/TiAlN_y$/SiNCH, Figure 75), with refractive index continuously decreasing from metallic substrate (high *n*) to ambient air ($n = 1$) is thus created, with complementary and optimal selective optical properties for CSP applications. These configurations were validated for both flat [34,44,291] and textured coatings [44,293].

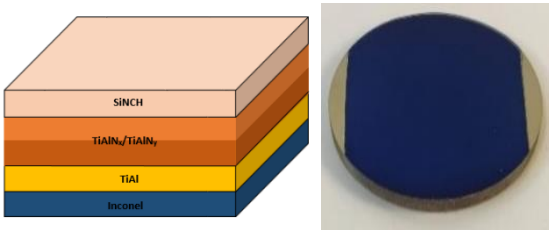

Figure 75. $TiAlN_x/TiAlN_y$ tandem absorber structure (1) and macroscopic image (2)

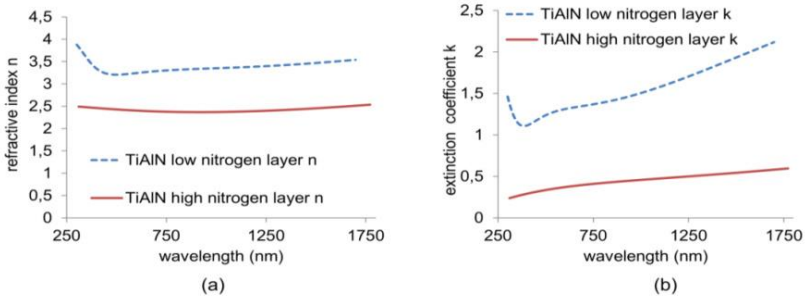

Figure 76. Refractive index *n* (a) and extinction coefficient *k* (b) variation for low and high nitrogen content, measured by ellipsometry [293]

In this thesis, the heliothermal efficiency of this absorber was systematically estimated for the following operating conditions, typical of new generations of Fresnel technologies: temperature of 500°C, concentration ratio of 50, concentrator optical efficiency equal to 0.5 and for an incoming solar irradiance of 900 W/m².

1.1.2. Manufacturing process

For the deposition of these samples an industrial pilot-scale deposition machine (TSD 2800R) was used [291] (Figure 77). This machine has been developed over 15 years. This equipment can treat large surfaces (long tubes of 2.57 meters) in a single batch. Three types of deposition sources can be used: cathodic arc, magnetron sputtering and distributed microwave plasma-enhanced chemical vapor deposition (PECVD). This machine has been described and used in previous studies [44,291,293].

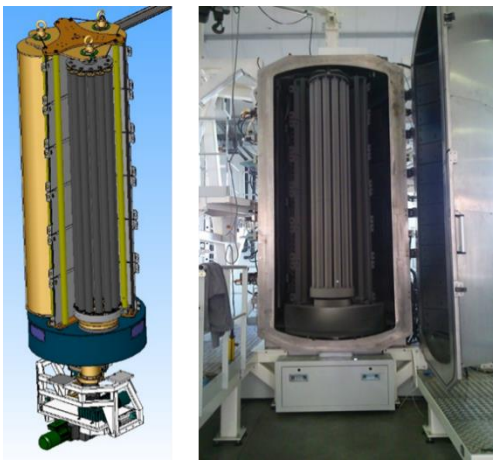

Figure 77. Industrial pilot-scale deposition machine at HEF-IREIS (TSD 2800R)

For the manufacturing of this solar selective absorber, the samples were fixed on a tube dual rotation system and were deposited by two different vacuum plasma deposition methods, physical vapor deposition (PVD) direct current magnetron sputtering of a TiAl target for the TiAl IR-reflective layer (in Ar plasma) and TiAlN absorber layers (in Ar / N_2 plasma), and microwave PECVD for the SiCNH antireflective layer (in Ar / tetramethylsilane $Si(CH_3)_4$ / N_2 reactive plasma).

1.2. WAlSiN tandem absorber

This second absorber is developed at the CSIR-NAL (Council of Scientific & Industrial Research-National Aerospace Laboratories) in Bangalore, India, by the Surface Engineering Division (SED), within the framework of the CEFIPRA (Indo-French Center for the Promotion of Advanced Research) project n°5908-1 led by Pr. Harish C. Barshilia [305]. The objective of this collaboration is to design and develop new selective coatings for CSP receivers that can withstand high temperatures in air while maintaining their thermo-optical properties, using facile manufacturing processes.

1.2.1. Materials and structure

The structure studied in this thesis is a tandem absorber configuration of W/WAlSiN/SiON/SiO_2 on SS 304 substrates. SS 304 was chosen for its high thermal stability and high corrosion resistance. The absorber is composed of a Tungsten sublayer, WAlSiN absorber layer and SiON/SiO_2 antireflective layers [195] (Figure 78).

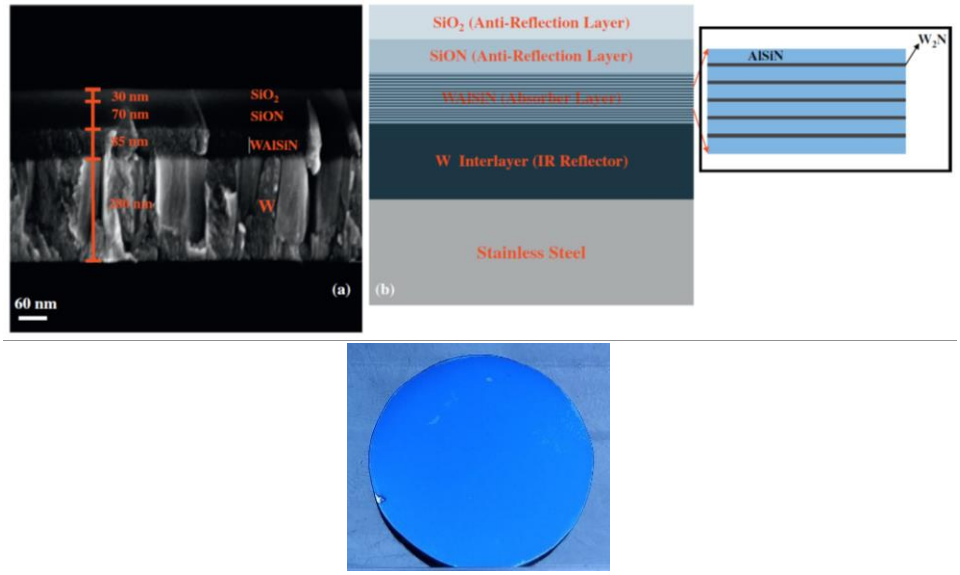

Figure 78. W/WAlSiN/SiON/SiO_2 tandem absorber: cross-sectional SEM image and structure (top) [195], macroscopic image (bottom)

The WAlSiN absorber layer is itself a multilayered tandem structure, consisting of 18 layers of W_2N and 18 layers of AlSiN [306]. This multilayered structure strongly enhances the thermal stability of WAlSiN, as AlSiN is a highly thermodynamically stable material [307]. The use of metal nitrides as solar absorber coatings has been extensively studied because of their thermal stability, high oxidation resistance and high degree of spectral selectivity [136]. The presence of tungsten in the absorber composition further enhances the solar absorption in the solar (UV/Vis/NIR) region [308].

The SiON/SiO_2 double antireflective layer ensures broadband absorptance (0.2-1.5 µm). SiON/SiO_2 are optically thin dielectric films which suppress the reflection of the light by destructive interference effects [309,310]. The gradual increase in refractive index from bottom to top layer results in high absorption and low thermal emittance [236]: n_{WAlSiN} = 2.65, n_{SiON} = 1.50 and n_{SiO2} = 1.40 (at 632 nm).

The low emittance is ensured by the IR-reflective W interlayer, which exhibits very high reflectance in the wavelength range of 3-20 µm. This layer also protects from the outer diffusion of substrate elements into the absorber layer (diffusion barrier). This accounts for the overall improved thermal stability of the tandem stack.

To optimize the absorber and achieve optimal optical properties, i.e., high solar absorptance and low thermal emittance, different combinations of W/WAlSiN/SiON/SiO_2 stacks were deposited at various individual layer thicknesses and compared [195].

1.2.2. Manufacturing process

These coatings were deposited by CSIR-NAL/SED on stainless steel 304 substrates (30 x 30 mm^2 x thickness of 2 or 3 mm) using a four-cathode reactive unbalanced direct current (DC) magnetron sputtering system (Figure 79):

- W layer was deposited by sputtering a W target in an Ar plasma;
- W_2N layers were deposited by reactive sputtering of a W target in Ar/N_2 plasma;
- AlSiN layers were deposited by reactive sputtering of Al and Si targets in Ar/N_2 plasma;
- SiON and SiO_2 layers were deposited by reactive sputtering of a Si target, in $Ar/N_2/O_2$ and Ar/O_2 plasmas, respectively.

Figure 79. Four-cathode reactive unbalanced direct current magnetron sputtering system [311]

The main deposition parameters are the targets power density and flow rates of the reactive gases (N_2 and O_2), which control the layers compositions, and the deposition times of the individual layers which control their thicknesses.

1.3. W/SiCH absorber coating

The development of these absorbers was also carried out in the framework of the ANR ASTORIX (2014-2019) [34,44,82,291–294] and ANR NanoPlaST projects (2019-2024) [297] (see section 1.1), with the aim of developing new absorptive selective coatings for solar receivers for working temperatures above 500°C. This solar absorber was designed, optimized and manufactured at PROMES-CNRS laboratory during the PhD theses of Laurie Di Giacomo (2014-2017), Danielle Ngoue (2017-2021) and Aissatou Diop (2019-2022).

1.3.1. Materials and structure

Samples presenting the structure shown in Figure 80 were used for aging tests. This structure consists in a SiCH/W/SiCH dielectric/metal/dielectric multilayer absorber (see Chapter 1 section 4.1.4) with W infrared reflective sublayer, deposited on Inconel (2 mm-thick, diameter 2''). The layer thicknesses were previously optimized by optical simulation [93]. Structures consisting in W/SiCH periodic bilayers (2 nm / 60 nm) were also used in specific cases [194].

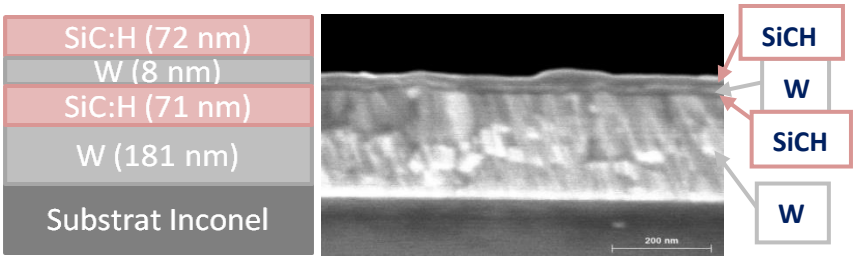

Figure 80. W/SiCH/W/SiCH optimized coating [93]

1.3.2. Manufacturing process

The PROMES-CNRS laboratory has worked on the elaboration of selective solar absorbers since 2014, for which the IDEFIX deposition reactor was developed (Figure 81).

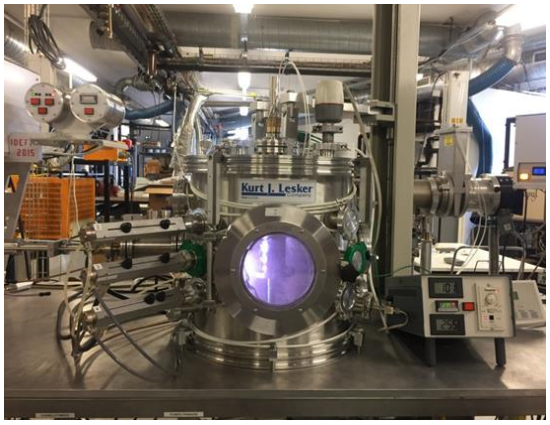

Figure 81. IDEFIX reactor in PROMES-CNRS [93]

The IDEFIX reactor allows implementing microwave Plasma Enhanced Chemical Vapor Deposition (PECVD) for the dielectric layers and radiofrequency (RF) magnetron sputtering (a type of Physical Vapor Deposition or PVD) for the metallic layers. The 4-layer stack presented in Figure 80 was prepared with substrate temperature of 350°C. W layers were deposited by PVD in Ar plasma, without substrate bias and W target bias of -300 V. SiCH layers were deposited by PECVD with 50% of tetramethylsilane precursor (TMS) in the Ar/TMS gas flow (25 sccm) and without substrate bias. The coatings were deposited on Inconel (diameter 2" and 1"), T91 steel and silicon substrates.

2. Characterization of materials

To follow the aging of solar selective absorbers, the changes in the optical properties, structure and composition of the coatings were systematically studied, using different techniques.

2.1. Optical properties

The samples spectral reflectance was systematically measured to study the aging behavior of the coatings. The evolution of their optical performance, i.e., solar absorptance, thermal emittance and heliothermal efficiency can be estimated from spectral reflectance (see Chapter 1 section 3).

2.1.1. UV-Vis-NIR spectrophotometer

A Perkin Elmer Lambda 950 spectrophotometer (Figure 82) was used to measure the quasi-normal (8°) hemispherical spectral reflectance in the UV-Vis-NIR range. It is equipped with tungsten halogen and deuterium lamps that emit light in the 190 - 3300 nm range, a monochromator for wavelength selection, and beamsplitters to compare the beam reflected by the sample with the reference beam

(Figure 82, right). It is calibrated using a white diffuse reflectance standard from Labsphere as reference. It also features a 150 mm integrating sphere covered with highly reflective Spectralon®, that allows collecting all the radiation reflected by the sample in all directions (specular and diffuse), and sending it to the detectors at the bottom of the sphere: a PMT R955 photomultiplier detector for the UV-Visible region (200 - 860 nm) and a InGaAs detector for the near infrared region (860 - 2500 nm). Overall, the detection range in the sphere is 250 - 2500 nm. The error for the measurements obtained from this equipment is less than 1%.

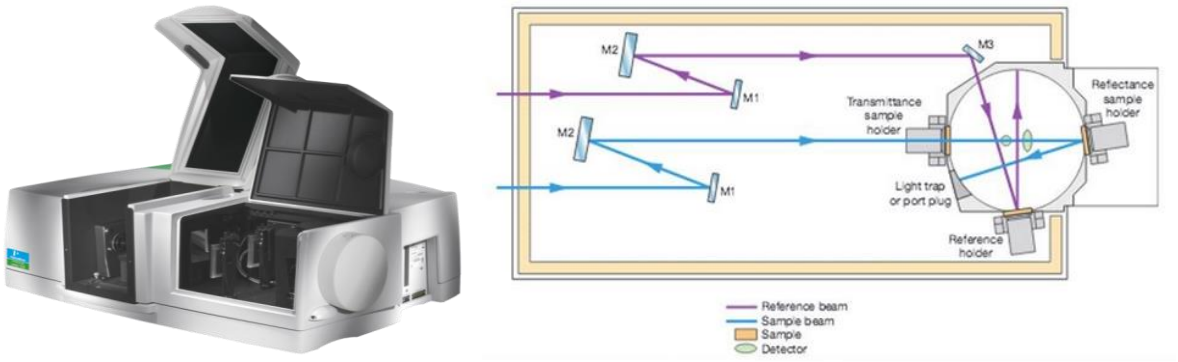

Figure 82. Picture (left) and principle (right) of Perkin Elmer Lambda 950 spectrophotometer [312]

2.1.2. IR spectrophotometer

A Surface Optics SOC-100 HDR reflectometer coupled with a Nicolet 6700 FTIR spectrophotometer (Figure 83) is used for hemispherical directional spectral reflectance measurements in the infrared region from 1.25 to 25 µm.

Figure 83. SOC-100 HDR with Nicolet 6700 FTIR spectrophotometer (left), principle of SOC-100 HDR (right)

The SOC-100 HDR reflectometer is composed of a blackbody infrared source at 700°C placed at one of the foci of a hemi-ellipsoidal gold mirror. A gold-coated specular reflectance standard calibrated by NIST is used as a reference (Figure 84). The reference, then the sample, are placed at the other focus point of the mirror thanks to a moveable holder, so that they are irradiated from all directions (Figure 83, right). A moveable overhead mirror collects the light reflected by the reference/sample, at a chosen detection angle (between 8° and 80°). Then a set of mirrors directs the collimated beam into the FTIR spectrophotometer for signal treatment. The FTIR is equipped with InGaAs and DTGS/KBr detectors respectively for the NIR and mid-IR range, as well as a Michaelson interferometer and quartz and KBr beamsplitters. At least 64 interferograms are acquired on the reference then on the sample, for all wavelengths at once, to obtain the reflectance spectrum by Fourier transform. For each scan, a chopper is used above the source to also acquire interferograms of the radiation naturally emitted by the sample in the IR range (considered as noise) and subtract it. For this equipment, the error is negligible up to about 6 µm and reaches 2.5% around 15 µm.

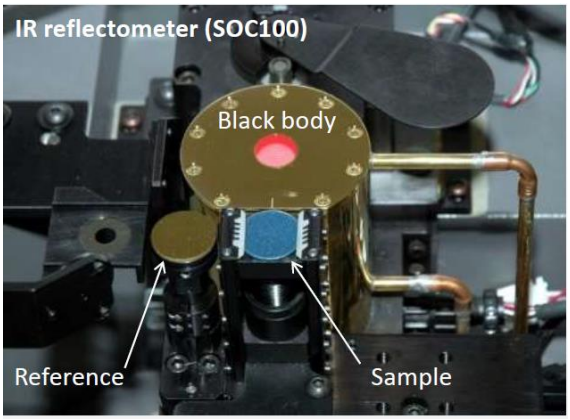

Figure 84. Blackbody at 700°C, reference and sample to be measured

2.2. Material microstructure

In this work, Scanning Electron Microscopy (SEM) and Energy Dispersive Spectroscopy (EDS) were used to study the samples microstructure before and after aging tests.

Scanning Electron Microscopy (SEM) is based on the detection of signals arising from the multiple collisions between energetic electrons (called primary electrons), emitted in ultra-high vacuum by an electron gun (e.g. tungsten Field Emission Gun, or FEG), and the atoms of the analyzed sample. The volume of interaction (Figure 85, left) is approx. 1 μm^3, depending on the average atomic number (density) of the sample and the energy of the incident electrons.

Inelastic collisions with primary electrons (PE) can cause secondary electrons (SE) to be ejected from the sample surface (Figure 85, right). They can be detected to provide high-resolution imaging of the sample surface. If an electron from an internal electronic layer is ejected, an electron from a more external layer can take its place. This transition releases energy through the emission of an X-ray photon. The energies of these electron transitions are characteristic of chemical elements and have been tabulated. Therefore, the detection of these X-ray photons as a function of their energy (Figure 86) can be used to determine the material chemical composition. This technique is called Energy Dispersive Spectroscopy (EDS) and is not valid for elements with only one electronic layer such as H.

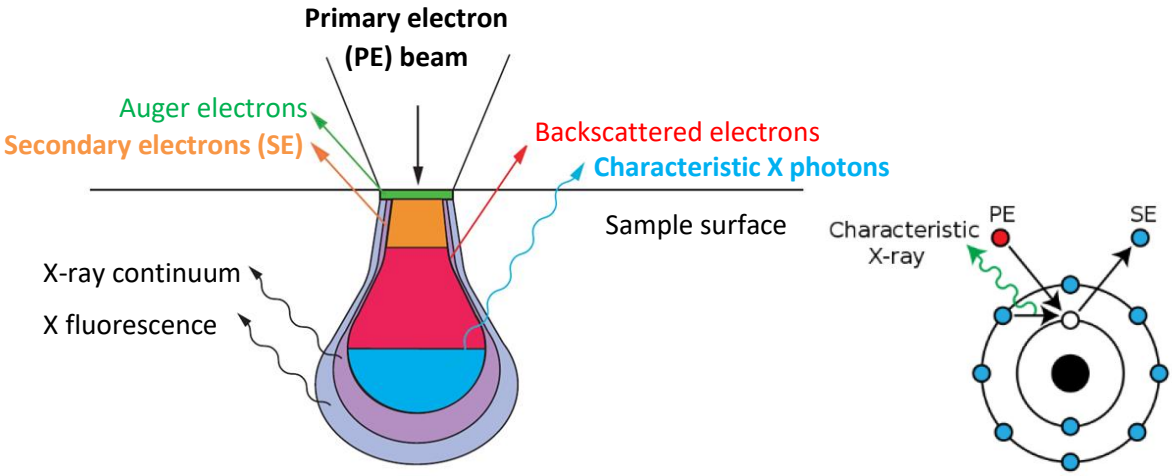

Figure 85. Interaction between the electron beam and the material at the microscopic (left [313]) and atomic levels (right)

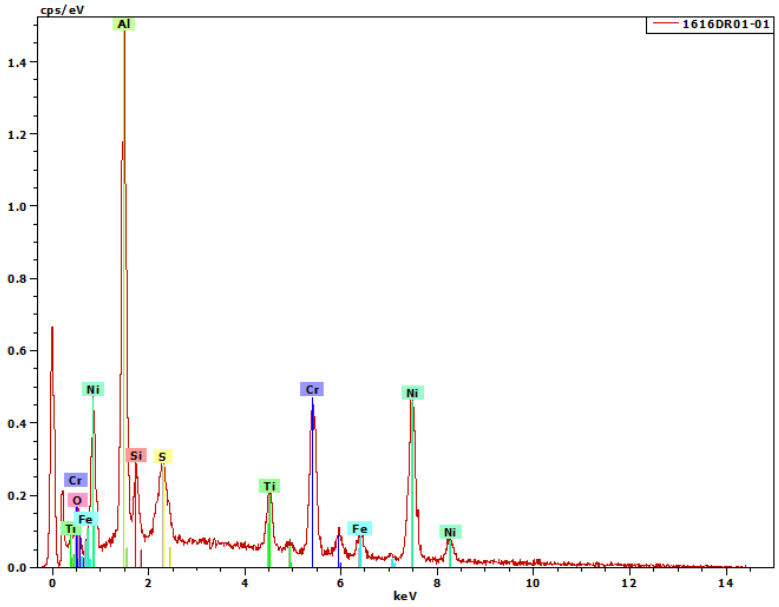

Figure 86. Example of EDS spectrum obtained for the TiAlN absorber on Inconel substrate

In this work, a Hitachi S-4500 FEG-SEM (Field Emission Gun) with 1.5 nm resolution at 15 kV was used to observe the samples surface morphology and its evolution with aging. It is coupled with a Kevex EDS analysis system (Bruker Nano GmbH, Germany) to follow the samples atomic composition, with an error of ± 2 at.%. Thus an element with low content in the sample may not be properly detected. Also the energy resolution of EDS is rather poor, typically around 0.3 keV. This sometimes causes difficulties in resolving overlapping transitions from two different elements. It is for instance the case for Si-K and W-M transitions (1.77 – 1.87 keV), and N-K and Ti-L transitions (0.39 – 0.46 keV). Therefore the exact quantification of such pairs of elements in the same sample can be tricky. This concerns the three absorber types considered in this thesis (TiAlN, WAlSiN, W/SiCH). However it was used for practical reasons, as the only non-destructive technique that could systematically be implemented for chemical analysis at PROMES-CNRS, not requiring sample cutting or preparation and adapted to the small thickness of the coatings.

3. Aging

In this section, the global aging methodology applied to our absorbers is explained and the different aging tools available at PROMES-CNRS are described.

3.1. Aging methodology

Inspired by literature review (Chapter 2), the global methodology applied to study the impact of aging on sample series of the three types of absorbers will be justified in more details in the following chapters, in light of the obtained results. In summary, it consists in systematically:

1. Assessing the microstructure and optical properties of each series of samples in their as-deposited state, to serve as reference, by:
    - SEM, to observe their surface morphology;
    - EDS, to obtain their atomic composition;
    - spectrophotometry, to measure their spectral reflectance in the 0.25 – 25 µm range and deduce their optical performance: solar absorptance, thermal emittance, heliothermal efficiency;

2. Applying different types of aging tests on different samples of the same series, with different degradation sources, using the aging tools presented in section 3.2:

    - starting by "representative" (purely thermal) aging to assess the absorber thermal stability behavior/limit, i.e., applying thermal aging at a temperature typical of the aimed CSP applications, here 400 to 500°C in ambient air (depending on the type of absorber), cumulatively on the same sample, starting with short durations of up to 24h, reaching at least 100h in total (Figure 87), and up to 1000h (see Chapter 4);

    - if the samples show thermal stability after 100h at 400 to 500°C, their series can be considered for accelerated aging, purely thermal at higher temperatures to attempt lifetime prediction (see Chapter 4), and/or with additional degradation sources such as concentrated solar irradiance, rapid thermal cycling and thermal shocks (see Chapter 5).

3. Observing the evolution of the morphology (e.g. apparition of cracks), composition (e.g. oxidation) and optical properties of the sample by the previous techniques (step 1), systematically after every aging step by spectrophotometry, and periodically by SEM and EDS.

4. Comparing the results obtained for the different aging protocols, applied on series of similar samples, and concluding on their suitability and pertinence to estimate the durability of solar selective absorber coatings.

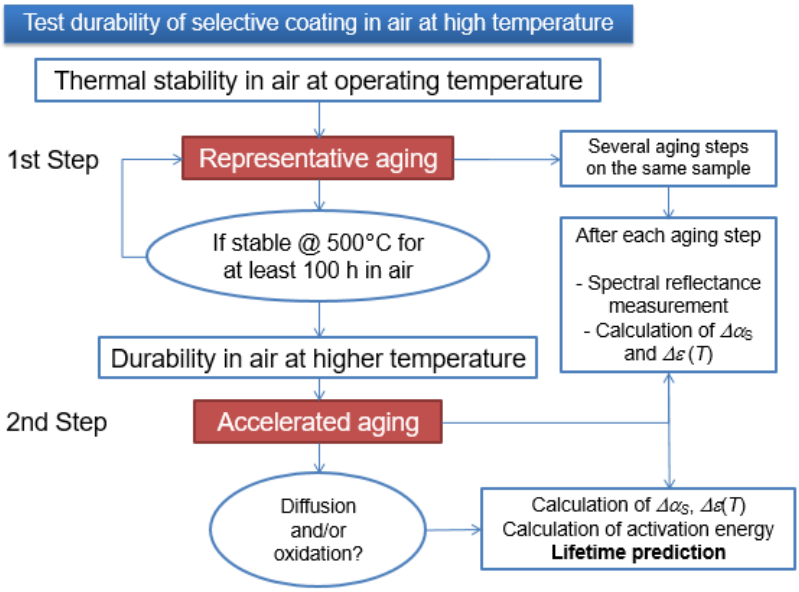

Figure 87. Aging methodology for the study of the durability of selective absorber coatings

3.2. Aging tools

To apply the different sources of degradation to the solar selective absorber coatings, two aging tools were used, an electric furnace and a solar furnace.

3.2.1. Thermal aging: ALTHAIA

3.2.1.1. Experimental set-up

An aging facility called ALTHAIA (Aging Long-Term Tests in Humid Air or Inert Atmosphere) is located at PROMES-CNRS laboratory in Odeillo. It is based on a 3.5 kW electrical tubular furnace from Thermconcept®, model ROS 105/900/12 (Figure 88), with maximum temperature of 1200°C, mounted

on a stainless steel table. The furnace is equipped with a ceramic tube of 1200 mm in length and an inner diameter of 105 mm. The heated length is 900 mm, with the central 400 mm at ΔT = ± 5°C. Samples are positioned at the center of the furnace. The ceramic tube is encased in a high-grade ceramic fiber insulation material with low thermal mass, protected with a metal casing. During heating, insulating caps are placed at each end of the ceramic tube for better thermal insulation and stability, limiting forced convection and giving a static air atmosphere.

Figure 88. Thermconcept ROS 105/900/12 with Eurotherm 3508 temperature controller, insulating caps, independent thermocouples and Graphtec data logger

3.2.1.2. Control of temperature

Heating ramps and temperatures can be adjusted to the desired values using a Eurotherm® 3508 controller. It operates on the principle of a PID regulator allowing a temperature correction to be made by comparing the setpoint and the measured value. The controller also makes it possible to program heating cycles of several hours or several days, and therefore easily achieve long-term aging.

Temperature in the furnace is independently measured using three thermocouples (jacketed, diameter 3 mm, length 750 mm), one positioned at the center of the furnace, and two at 5 cm on each side of the central position. Temperature profiles are recorded by a Graphtec GL220 data logger (Figure 88). Table 8 shows the difference between the setpoint temperature and the temperature measured inside the furnace (average and standard deviation of measurements from the three thermocouples). Therefore, the setpoint temperature was systematically adapted to obtain the desired temperature in the furnace, as indicated in Table 8.

Table 8. Temperature correspondences

Desired *T*	Setpoint *T*	Measured *T*	Difference between measured & desired *T*
300°C	320°C	299 ± 9°C	1°C
400°C	425°C	404 ± 11°C	4°C
500°C	525°C	496 ± 7°C	4°C
600°C	630°C	596 ± 7°C	4°C
630°C	665°C	645 ± 2°C	15°C
660°C	705°C	673 ± 4°C	13°C
690°C	740°C	712 ± 2°C	22°C

3.2.1.3. Heating and cooling rates

The furnace heating ramp can be adjusted using the Eurotherm® controller. Temperature profiles recorded using the independent thermocouples were analyzed to verify the agreement between heating ramp setpoints and real heating rates, for different setpoint values: 5, 10, 15, 20 and 100°C/min (Figure 89). The heating ramp seen by a sample equipped with a welded thermocouple on its backside, when placing it directly inside the already hot furnace (rapid heating), was also considered. In all cases, a linear regression on the heating ramp from 150 to 450°C was used to estimate the heating rate (slope).

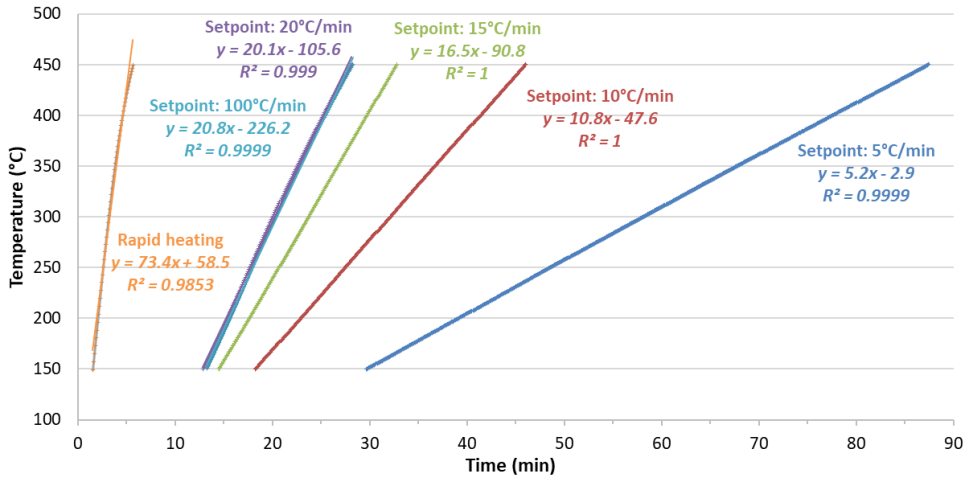

Figure 89. Heating ramps and their linear regressions for different heating rate setpoints

Table 9 compares setpoint and measured heating rates from Figure 89. For low heating rates between 5 and 20°C/min, the agreement is good. For a setpoint of 100°C/min, the measured heating rate is 21°C/min, showing the limitation in heating rate due to the furnace thermal inertia: due to its configuration, the furnace itself cannot provide a heating rate higher than 21°C/min. When introducing the sample directly into the already hot furnace (rapid heating), the heating rate seen by the sample reaches approximately 73°C/min (the temperature profile is less linear than the others, since there is no temperature regulation in this case). Such heating rate is closer to the kind of thermal shock that materials may encounter in CSP operating conditions.

Table 9. Different heating rates setpoint and calculated heating rates obtained from linear regression

Heating rate setpoint (°C/min)	Measured heating rate (°C/min)
5	5.2
10	10.8
15	16.5
20	20.1
100	20.8
Rapid heating	73.4

As a rule, samples were thus systematically introduced in the hot furnace at the desired stabilized temperature. This allows reaching higher heating rates while preventing temperature overshoots due to the PID regulation. Samples were then maintained under the desired temperature plateau for the desired duration thanks to the controller. At the end of the heating plateau, they were allowed to cool naturally inside the furnace, following its cooling kinetics (decreasing exponential). Temperate profiles gave access to the natural cooling rate, which was estimated between -3 and -0.2°C/min, depending on the temperature range (cooling is fast at high temperature but slows down below 200°C).

3.2.1.4. Typical temperature profile

The typical temperature profile applied to the samples (Figure 90) is similar for each aging test. It consists in a rapid heating at the desired heating rate (typically 20°C/min) followed by a temperature plateau of the desired duration (typically 24h) and finally the sample is left in the furnace during its natural cooling.

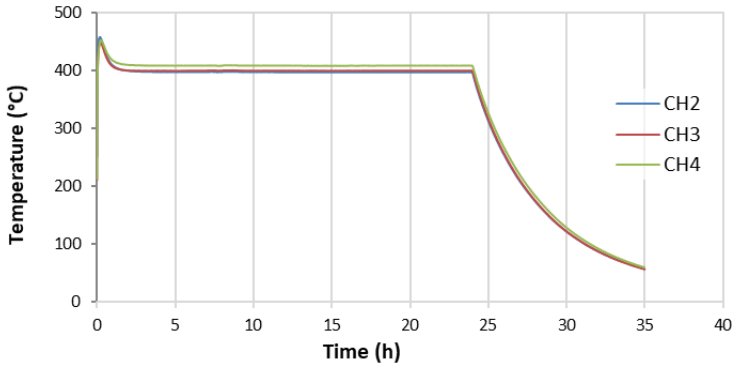

Figure 90. Electrical furnace performance for a setpoint temperature of 400°C during 24h, as measured by the three thermocouples placed at the center of the furnace (CH3), and 7 cm apart on each side of it (CH2, CH4)

3.2.1.5. Development of ALTHAIA experimental set-up

The ultimate aim of ALTHAIA experimental set-up is to provide a versatile aging tool, able to apply heat treatments to solar absorber coatings under different atmospheres, i.e., vacuum and air with controlled humidity, to study, decorrelate and compare the influence of additional sources of degradation: purely thermal aging (high temperature without air), thermal aging in oxidant (HT with air) and corrosive atmospheres (HT with humid air), influence of water vapor content.

ALTHAIA set-up was therefore further developed, with additional features to control the inner atmosphere of the furnace (Figure 91). The extended set-up was designed and fabricated at PROMES-CNRS by Audrey Soum-Glaude and Emmanuel Hernandez, and further implemented during this thesis.

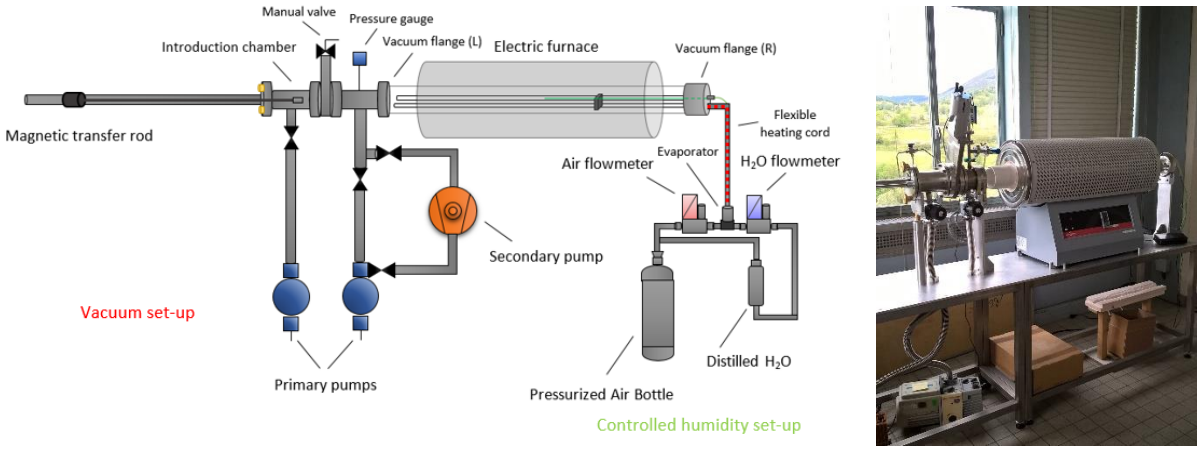

Figure 91. ALTHAIA extended experimental set-up

It mainly consists in:

- a vacuum chamber system, composed of a quartz tube (O.D. 100 mm) inserted inside the furnace ceramic tube (I.D. 105 mm), equipped with custom vacuum flanges at its extremities, connected to a system of pumps providing primary vacuum inside the chamber ($\approx 4 \cdot 10^{-3}$ mbar).

- an injection system for air with controlled humidity (air and water flowmeters with mixing valve) that can provide an absolute humidity in primary vacuum equivalent to a large range of typical atmospheric conditions: from 10°C and 10%RH (0.8 g/kg of dry air) to 58°C and 100%RH (138 g/kg of dry air).

This set-up would provide valuable additional testing conditions, relevant to this thesis. Unfortunately, an accidental overheating damaged the vacuum system and prevented its use for the present work. Nonetheless, it did not affect the tests carried out under ambient air presented in this manuscript. The vacuum system was lately rehabilitated with the implementation of new components designed by Roger Garcia and will be available for future work on aging studies following this thesis.

3.2.1.6. Additional thermal aging tools

In some cases, the W/SiCH absorber coatings were instead aged in a Nabertherm programmable muffle furnace. This furnace was used to perform aging at 500°C up to 96h in filtered (H_2O + CO_2) air, thanks to an injection system of compressed air with H_2O and CO_2 filters.

In some cases the WAlSiN absorber coatings were aged at CSIR-NAL Bangalore laboratory [314]:

- in vacuum ($5 \cdot 10^{-5}$ mbar), using a tubular quartz furnace surrounded by resistive heating coils. Temperature is measured in three areas connected to the temperature control unit, to maintain the temperature within ±2°C. A heating rate of 10°C/min is applied.
- in air, using a resistive ceramic tubular furnace, with a heating rate of 10°C/min.

3.2.2. Concentrated solar + thermal aging: SAAF – Solar Accelerated Aging Facility

SAAF, for Solar Accelerated Aging Facility, is a unique concentrated solar facility developed at PROMES-CNRS laboratory in Odeillo. It was initially designed to test the solar and thermal performance of absorber paint coatings for CSP tower receivers, by applying accelerated aging experiments, during the thesis of Antoine Boubault (2013) [36,267,268,315]. It was then used to test the thermomechanical behavior of ceramic materials for CSP receivers during the thesis of Yasmine Lalau (2017) [207,208,316], and the thermal stability of absorber coatings during the thesis of Reine Reoyo-Prats (2020) [317], in the framework of the EU project RAISELIFE [160].

3.2.2.1. Experimental set-up

SAAF facility consists in the following elements.

- a movable heliostat (20 m^2), installed on the 1st floor of the building, tracks the Sun and reflects parallel beams of solar irradiance toward the 6th floor, through a trap door equipped with controllable shutters to regulate the solar irradiance sent inside the building;
- a 1.5 m fixed parabolic dish concentrator, suspended horizontally above the trap door and shutters, receives solar irradiance from the heliostat and concentrates it at its focal point;
- a kaleidoscope (made of four mirrors facing one another) at the focal point homogenizes the concentrated solar flux (from a Gaussian profile to a rectangular profile);
- a sample holder mounted on a movable cart is placed after the kaleidoscope to irradiate samples with a homogenized concentrated solar irradiance, whose flux density is controlled via the shutters;
- a pyrometer suspended to the parabola right above the sample holder measures the sample temperature during the tests;

- a data acquisition system including a Graphtec data logger records input and output data (temperatures, voltages, flows, etc.).

All these elements are illustrated in Figure 92 (pictures) and Figure 93 (schematics). The main components are described in more details in the following subsections.

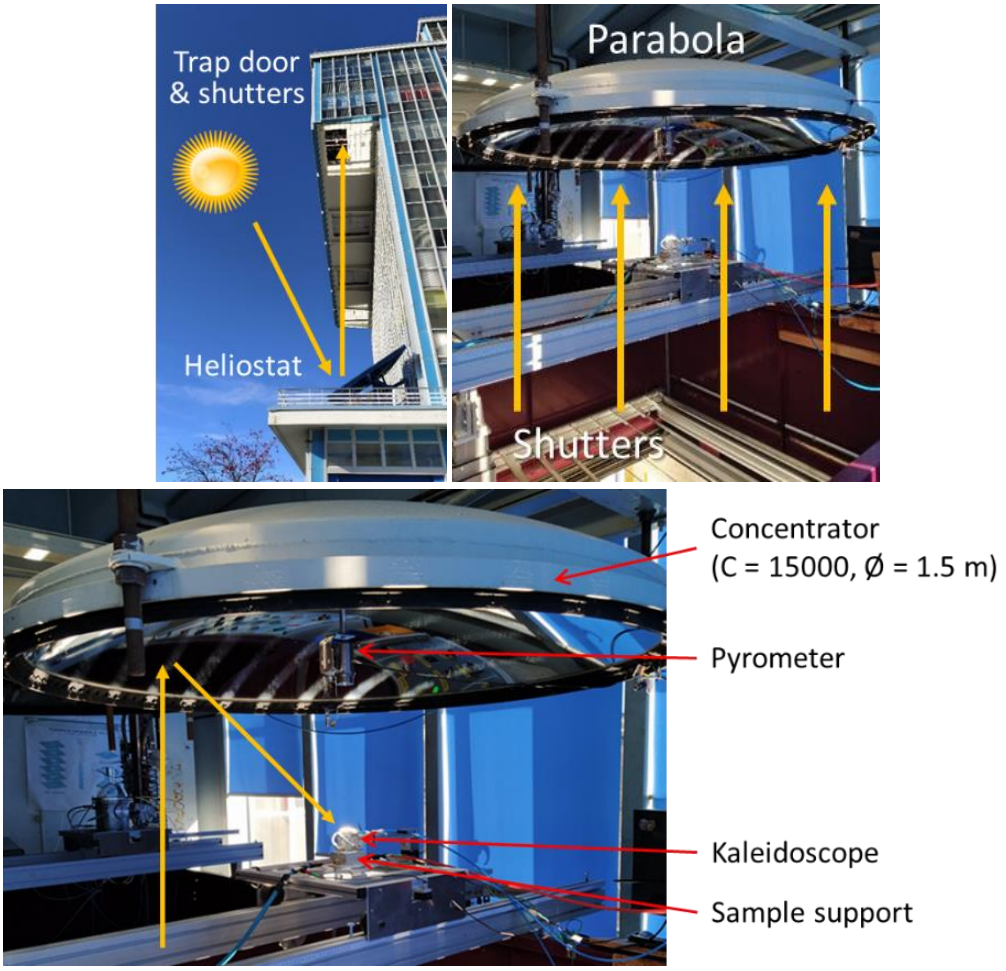

Figure 92. Pictures of the SAAF experimental set-up at PROMES-CNRS laboratory

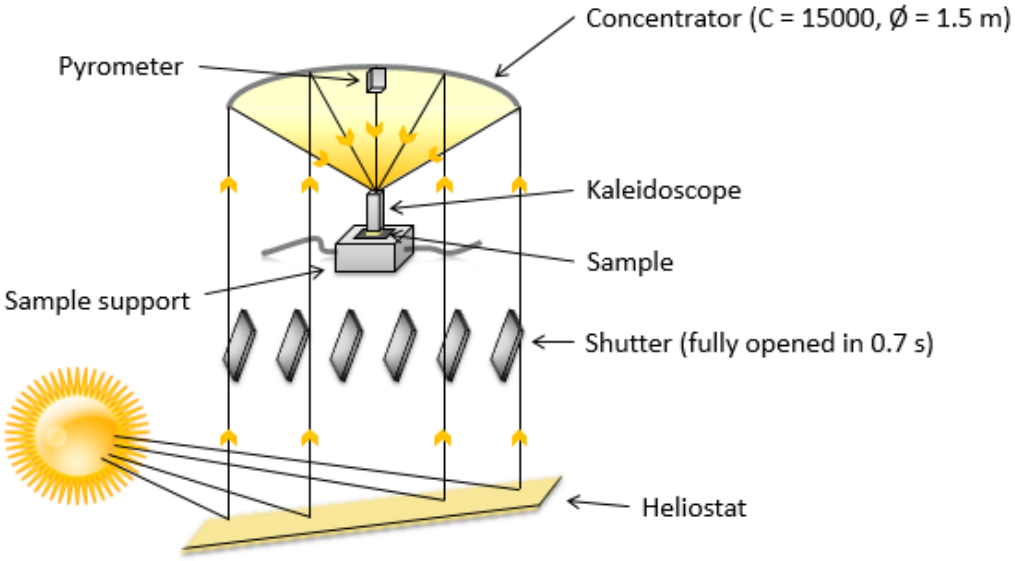

Figure 93. Schematics of the SAAF experimental set-up

3.2.2.1.1. Adjustable shutter - EGSésame

The amount of concentrated solar flux given to the samples is adjustable thanks to a system of 13 movable flaps (Figure 92) that enable precise control via an irradiance sensor coupled with a PID regulation loop. This system is called the Sésame shutters and is located above the closing trapdoor, between the heliostat and the parabolic concentrator.

The shutter opening is controlled automatically by an external voltage with a 0-10 VDC analog signal and a PC running a specific software called EGSésame. This software written in C++ programming language was developed by Emmanuel Guillot and adapted for this specific project. It controls the external voltage given to the Sésame controller trough an InstruNet that acts as a "power buffer". The voltage depends on the actual DNI, which is the only feedback given to the software. This voltage is calculated depending on the needed concentrated solar flux at the focal point and the available incoming solar radiation. The shutters allow precise control of the amount of incident solar power.

3.2.2.1.2. Parabolic dish concentrator

The parabolic dish concentrator has a thermal power output of 850 W, a concentration ratio of about 15,000 with a diameter of 1.5 m. It can reach a power density of around 16,000 kW/m^2 at the focal point with a focus diameter of around 15 mm. The focal point is located at 639 mm as indicated by the manufacturer. Figure 94 shows the distance of the pyrometer, kaleidoscope and sample support from the parabolic dish. The latter is equipped with two crossed lasers allowing visualization of the focal point and facilitating the adjustments for sample treatment. It is suspended horizontally in a fixed position with a metallic structure, to face the heliostat and have the focal point close to our accessible working area, enabling us to locate the samples at the focal point with a movable cart.

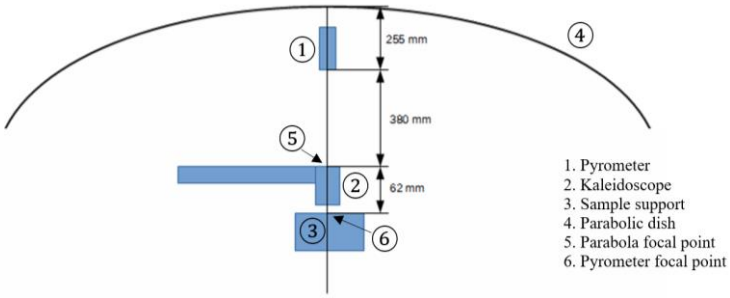

Figure 94. Distances of the different equipment to the parabola

3.2.2.1.3. Kaleidoscope

A parabolic dish concentrator has a very high concentrator factor and a small focal point diameter. This makes it difficult to work at the focal point. To ensure a less damaging area and adapt the incoming concentrated solar radiation, a device called a kaleidoscope is placed at the focal point of the concentrator, above the sample (Figure 95, left). The kaleidoscope consists in four metal walls made of polished aluminum, with reflectance values greater than 66%, and good resistance to concentrated solar radiation. It is 60 mm high and has a square aperture of 20 mm². It is mounted on a movable arm to adjust its position between the focal point and the sample (Figure 96).

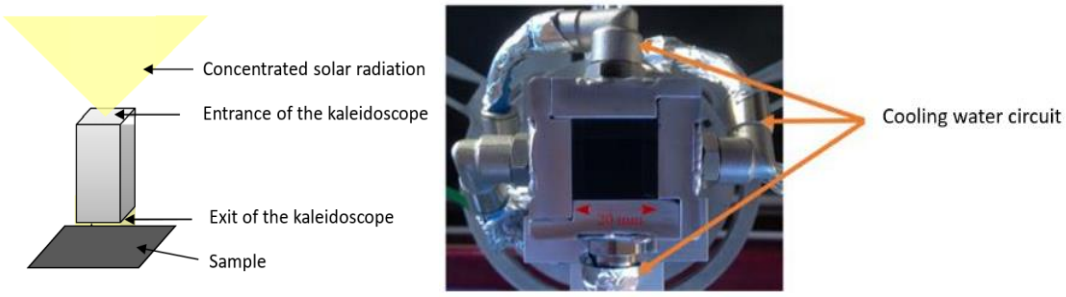

Figure 95. Path of the concentrated solar radiation through the kaleidoscope (left [317]) and picture of the kaleidoscope (right)

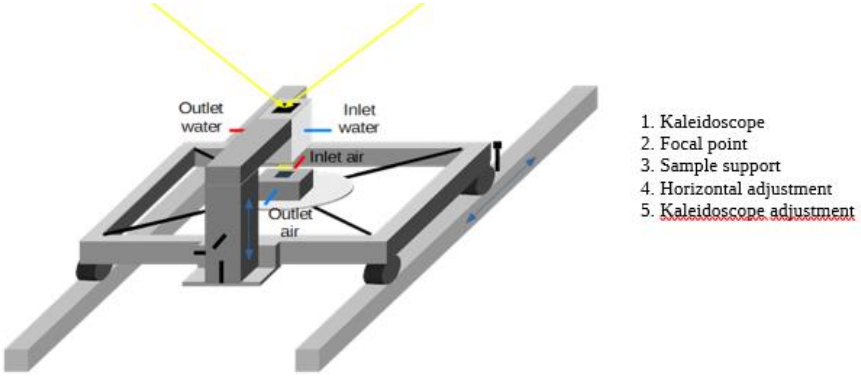

Figure 96. Movable cart holding the kaleidoscope and sample support

Due to the multiple reflections within, the kaleidoscope homogenizes the incoming solar flux from the parabolic dish concentrator, so instead of the input Gaussian profile with peak irradiance over a few mm² (Figure 97 - blue), the sample receives the output rectangular profile of approximately 15 mm² with homogeneous irradiance (Figure 97 - red). Due to this size, samples are treated one at a time.

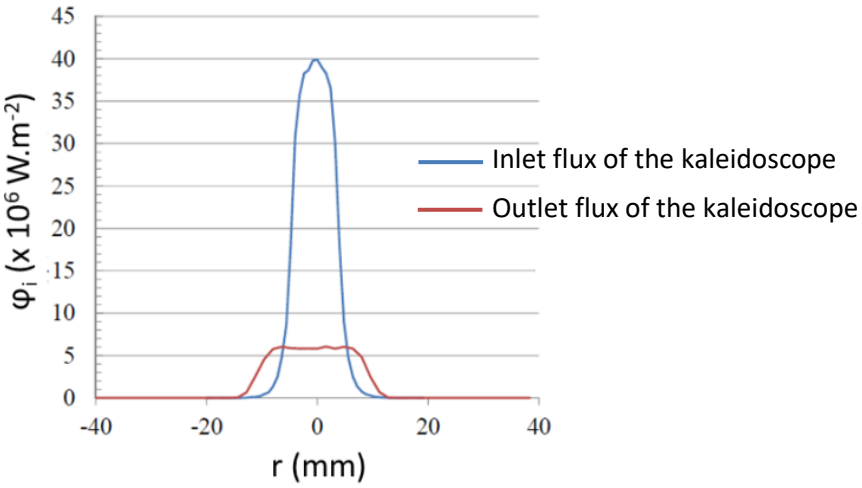

Figure 97. Flux distribution at the entrance and exit of the kaleidoscope [267]

The aluminum walls are cooled down with a water cooling system to avoid their overheating and deterioration (Figure 95, right). This device has a low efficiency, due to thermal losses toward the cooling system and optical losses caused by the high number of reflections inside the kaleidoscope. As an example, optical simulation predicts that a flux density of 40 MW/m² incident on the kaleidoscope results in a flux density of 6 MW/m² on the sample (Figure 97). The solar irradiance at the exit of the kaleidoscope was calibrated as a function of the shutter aperture (see Annex 1 p.235).

3.2.2.1.4. Sample support

For the aging tests, the samples are placed on a specific support. The main purpose of this support is to have the sample fixed in position at the exit of the kaleidoscope. It is also designed, when possible, to allow for effectively adjusting the desired temperature of the sample, thanks to air cooling that can be regulated. The cooling system is integrated into the support with two orifices, one being the inlet and the other the outlet (Figure 96). A rubber O-ring is placed between the support and the sample, to seal the sample to the support and ensure an optimum use of the cooling air. In this way, heat can be extracted from the backside of the sample. The compressed air network used for the cooling has a regulator installed on the structure of the dish to modify the pressure of the incoming air and thus the flow rate.

Four different supports were used, depending on the shape and dimensions of the samples. They are built with different materials and configurations (Table 10).

- Support 1 is an old sample holder in MACOR®, now used without air cooling as the sample cannot be sealed to the support, but with the main advantage of being adapted for round and square samples of different sizes.
- Support 2 is an aluminum support usable only for square samples of 30 x 30 mm², as the sample is sealed to the support using an O-ring and screws, allowing for efficient back cooling and temperature regulation.
- Support 3 is an alumina support usable only for square samples of 50 x 50 mm², also with an efficient back cooling system.
- Support 4 was recently developed to accommodate many sample sizes and shapes. It is made of stainless steel. It includes a cooling system, though not as efficient as for supports 2 and 3 because the outlet air does not flow in a restricted space in this case.

Table 10. Different supports used for SAAF experiments

	Support 1	***Support 2***	***Support 3***	***Support 4***
Support material	MACOR	Aluminum	Alumina	Stainless steel
Sample cooling	No cooling	Efficient cooling	Efficient cooling	Not efficient cooling
Sample size	30 x 30, 50 x 50 mm², O.D. 2”	30 x 30 mm²	50 x 50 mm²	1” to 2” side/diameter
Sample shape	Round and square	Square	Square	Round and square
Max sample thickness	None	3 mm	Up to 6 mm	Up to 6 mm
Image				
Funding project	–	–	RAISELIFE	SFERA-III

3.2.2.1.5. Pyrometer

An Optris CTlaser G5H infrared pyrometer equipped with CF4 optics is fixed on the parabola, in direct view of the sample surface (Figure 92), at around 43.5 cm from the sample (Figure 98), close to the focal point of the pyrometer (45 cm). It allows measuring temperatures between 250°C and 1650°C.

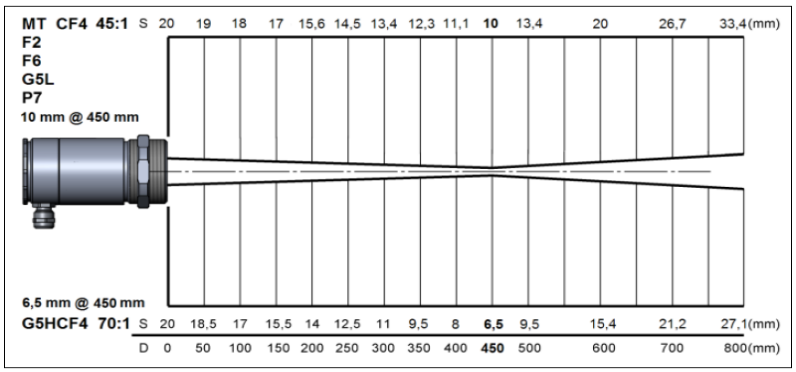

Figure 98. Focal point of the G5H CF4 model pyrometer

By design, the detection of the sample thermal emission, leading to the estimation of its surface temperature (see Annex 2 p.235) is carried out through the solar radiation reflected by the inner mirrors of the kaleidoscope during sample exposure (Figure 92). The pyrometer has a spectral response between 4.8 and 5.2 µm (Figure 99), and is thus considered solar blind, since solar irradiance is located below 2.5 µm. Therefore, pyrometry measurements are not perturbed by the incident solar radiation.

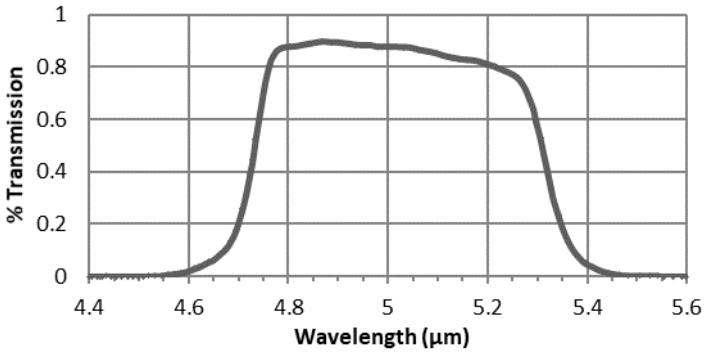

Figure 99. Spectral transmittance of the OPTRIS G5H CF4 pyrometer

3.2.2.2. Heating and cooling rates

Figure 100 shows an example of heating/cooling profile recorded during SAAF cycling test on the surface center (pyrometer) and back center (thermocouple) of a 2 mm-thick TiAlN absorber sample on Inconel. The thermal gradient (in °C/s) gives an image of the heating and cooling rates seen by the sample. The initial heating rate starting from room temperature is around 5°C/s, then between 15 and 25°C/s during the cycles. In this example, backside air cooling with gas flow around 0.0025 g/s was applied to the sample to control its temperature: this “regulated” cooling rate was ranging from -12 to -10°C/s. For the last cooling phase, the air cooling is stopped and the sample is allowed to cool naturally: its natural cooling rate reached around -20°C/s.

Heating and cooling rates may vary with the sample support used (see section 3.2.2.1.4), the sample thickness and the air cooling flow rate, if any. However this example gives an order of magnitude of heating and cooling rate levels available with SAAF. They are much higher than with an electrical furnace (around 20°C/min, see section 3.2.1.3), allowing for thermal shocks and rapid thermal cycling that are only accessible with such a set-up.

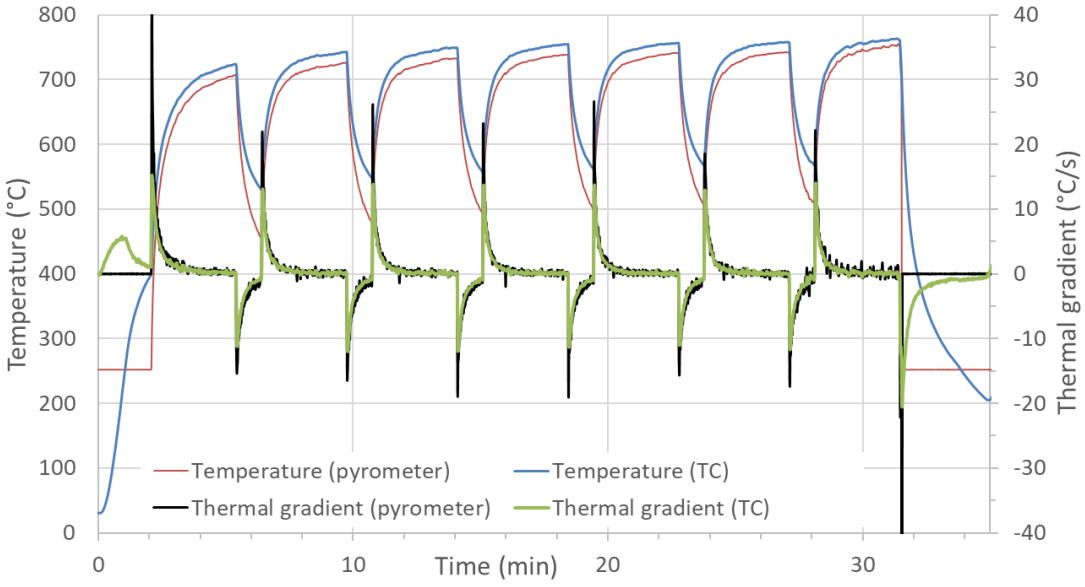

Figure 100. Example of heating/cooling profile with SAAF obtained for TiAlN absorbers

3.2.2.3. Available aging parameters

SAAF allows applying constant solar irradiance for several hours, as well as cycles of high and low solar flux (Figure 101) with chosen amplitude and period, by regulating the shutters opening and closing. The link between shutter aperture and concentrated solar flux after the kaleidoscope was previously calibrated by calorimetry for different values of solar Direct Normal Irradiance (DNI). The sample maximum temperature can be adjusted manually thanks to the air cooling flow rate, when applicable.

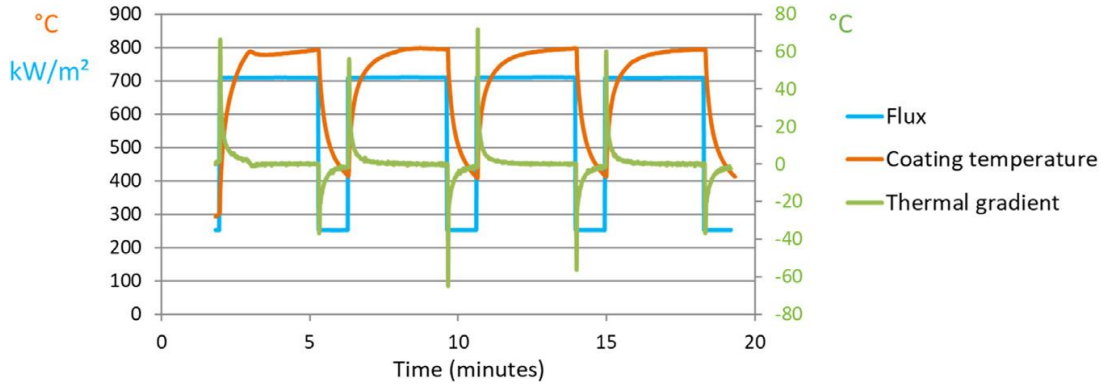

Figure 101. Example of irradiance cycles applied with SAAF, corresponding temperature and thermal gradient (°C/s) [318]

SAAF input parameters are thus:

- the values of concentrated solar flux seen by the sample during the high and low irradiance phases of the cycles (e.g. 700 and 250 kW/m² in Figure 101);
- the durations of these phases (e.g. 200 s and 60 s in Figure 101);
- the air cooling flow rates to regulate the temperature.

The following SAAF data is recorded by the Graphtec GL220 data logger and the computer interface:

- the surface temperature of the sample, given by the pyrometer and/or thermocouple(s);
- the solar DNI value recorded every second by a pyrheliometer on the roof;
- the air flow rate (g/s) for cooling the sample.

3.3. Conclusion on aging

Figure 102 summarizes and compares the available aging parameters for the two aging tools, related to the sources of degradation identified in Chapter 2 (Figure 57 p.70). The use of these two experimental set-ups enables us to compare the impact of the different sources of degradation they are able to provide. Both tools give access to wide temperature ranges, even wider than is pertinent for SSACs. While ALTHAIA set-up allows applying slow thermal cycling for short and long durations, and limited thermal shocks, SAAF allows concentrated solar exposure, rapid thermal cycling for short durations and large thermal shocks. The SAAF UV irradiance level will be discussed in Chapter 5.

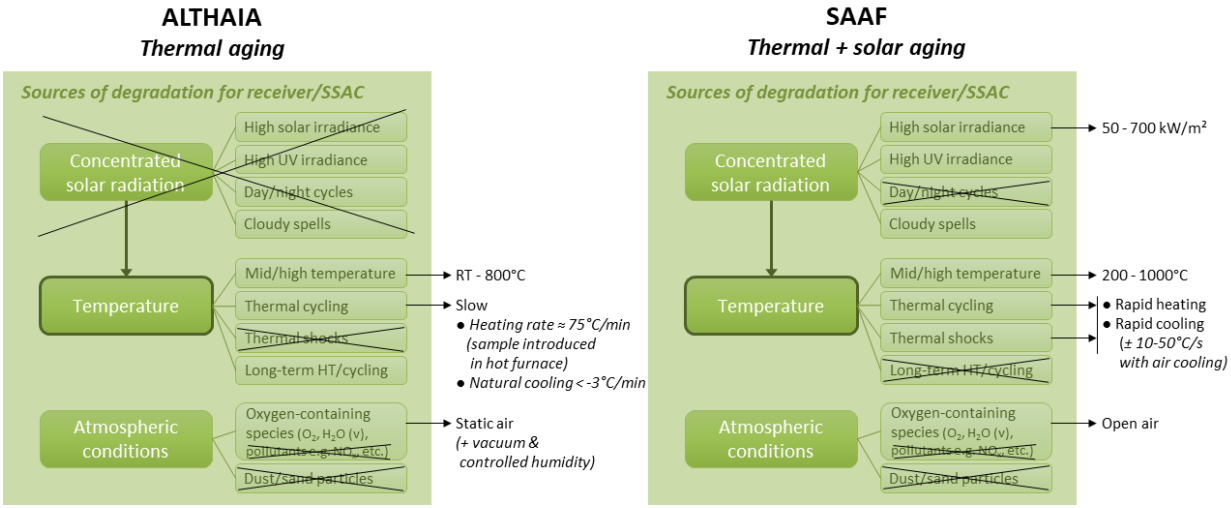

Figure 102. Sources of degradation accessible with the two experimental set-ups

Considering the available aging parameters and their accessible ranges with the two experimental set-ups at our disposal (Figure 102), three main test configurations were retained for this thesis, as explained in Table 11. They will allow exploring the separate and combined effects of thermal aging (Configuration 1, used in Chapter 4), solar aging and solar thermal cyclic aging (Configurations 2 and 3 respectively, used in Chapter 5).

Table 11. Main test configurations selected for this thesis

Configuration	***Configuration 1***	***Configuration 2***	***Configuration 3***
Aging tool	ALTHAIA	SAAF	SAAF
Temperature range	500 - 800°C	450 - 500°C	350 - 700°C
Concentrated solar irradiance	No	Yes Constant (250 or 400 kW/m²)	Yes Cyclic (50-500 kW/m²)
Thermal cycling	Slow (Cumulative 12-24h steps)	No (Cumulative 3.5h steps)	Rapid (High/low irradiance cycles)
Thermal shocks	Limited and repeated	Strong and punctual	Strong and repeated
Total duration	Short (few h) to long (up to 1000h)	Short (up to 15h)	Short (up to 15h)
Interest of study	Effect of thermal aging in air	*Compared with config. 1* ● Additional effect of concentrated solar exposure? ● Necessity to include constant solar aging in SSACs aging procedures?	*Compared with config. 2* ● Additional effect of rapid thermal cycling/shocks? ● Necessity to include cyclic solar aging in SSACs aging procedures?

4. Conclusion

To validate the pertinence of aging procedures, the latter must be tested experimentally, using specific tools and case study solar selective absorber coatings. In this thesis, three different types of SSACs are tested. These absorbers were described in this chapter, looking at the materials, structure and manufacturing techniques used to obtain them. To evaluate the impact of aging, the initial properties of the absorbers and their evolution with aging must be characterized, using techniques and equipment described in this chapter. Their spectral reflectance is systematically measured by spectrophotometry in the 0.25 – 25 µm range. As a complement, the evolution of their surface morphology and chemical composition are periodically followed using SEM and EDS techniques.

A global aging methodology is applied to the SSAC samples. The first step is to ensure the thermal stability of the absorber at typical operating temperatures, in our case 500°C, for at least 100 hours. Once the absorber has proven to be thermal stable in these conditions, more demanding tests can be applied on similar samples to study the effects of different sources of degradation: higher temperatures, longer durations, solar aging, thermal cycling.

Two dedicated experimental benches designed at PROMES-CNRS have been implemented and further developed in this thesis, to allow decorrelating the impact of these potential sources of degradation. Both were presented in this chapter. The first bench (ALTHAIA) allows short and long-term cumulative periodic thermal tests in air, that will be the focus of Chapter 4. The second (SAAF solar furnace) allows materials to be exposed to a real continuous or rapid cyclic concentrated solar flux, more representative of the CSP application, that will be the object of Chapter 5. The applicability and pertinence of these different aging protocols and sources of degradation, related to the technical limits sometimes existing in the application of the desired aging protocols, will be discussed at length in the following chapters.

Chapter 4 - Implementation and critical analysis of purely thermal aging protocols

In this chapter, the impact of purely thermal aging protocols, i.e., using a programmable electrical furnace, will be discussed. Protocols at different aging durations, temperature ranges and atmospheres will be analyzed. For this purpose, the response to these various protocols of the different types of absorbers (see Chapter 3) will be compared. Their optical properties, surface topography and atomic composition will be presented.

First, to ensure the protocols comparability, the equivalence of the series of samples for each type of absorber in their as-deposited state will be studied. Then, the impact of aging for short durations (less than 25h) and long durations (between 100h and 1000h) near the aimed operating temperature (around 500°C) will be discussed. The impact of higher temperatures (> 500°C), thermal cycling and aging atmosphere will also be investigated.

1. Verification of samples equivalence for comparable aging studies

1.1. Definition of sample equivalence

To study the aging of solar selective absorber coatings, different aging protocols must be applied and compared. Therefore, large series of equivalent samples are necessary for aging studies, i.e., samples with the same structure, deposited by the same technique, in the same equipment, with the same experimental parameters, on the same substrates, in the same batch, by the same operator, etc.

In reality, many factors impair the repeatability of the samples manufacturing process, causing small fluctuations between the samples. This is especially the case at the laboratory scale, which often uses small deposition machines, providing limited batches (e.g. 1 to 4 samples at a time). Thus several runs are necessary to obtain the required number of samples, with risks of evolutions in the process conditions (e.g. wear and pollution of sputtering targets). Also, these processes often include manual operation steps, sometimes carried out by different operators, increasing risks of low repeatability. As an example, the W/SiCH samples from PROMES are manufactured in the IDEFIX reactor (Figure 81 p.99) using plasma deposition techniques. Layer thicknesses are controlled by protecting the sample under a shutter, so that the deposition of a specific layer can be stopped abruptly. This shutter is operated manually, so that deposition times may vary by a few seconds for different samples, inducing thickness variations by a few nanometers. Also, plasma generator voltages and powers are not perfectly stable and slightly vary from one batch to another.

Contrarily, manufacturing processes at the industrial scale are designed, optimized, automated, and sometimes equipped with in-line control, to provide large batches of samples, with the highest repeatability possible from one batch to another. As a consequence of the larger size of deposition machines however (e.g. able to treat 4-meter-long tubes), the samples are not always uniform depending on the position of the substrate relative to the material source (sputtering target, gaseous precursor injection, etc.) during manufacturing. This may create differences between samples manufactured during the same batch. In all cases, there can also be small variations of the substrate surface state (roughness, pollution) before deposition.

All these unavoidable variations from one sample/batch to another can induce differences in their microstructure and optical properties. Therefore, their equivalence must be verified before applying aging protocols. The reproducibility and uniformity of the samples can for instance be estimated from the comparison of their optical properties, e.g. using spectral reflectance measurements after manufacturing (as-deposited).

In this work, three types of absorber structures are considered, two produced with research reactors and one with a pilot-scale deposition machine. In all cases, different series of samples were used for aging studies. To be able to compare the impact of the different aging tests, samples equivalence for each type of absorber was investigated.

1.2. Samples of TiAlNx/TiAlNy tandem absorber coatings

For the case of the $TiAlN_x/TiAlN_y$ tandem absorber with TiAlN sublayer and SiNCH antireflective top layer (see Chapter 3 section 1.1, p.95), four different series of samples were used to study the aging behavior of this type of absorber coating (Table 12). The series are named by the year and week when they were manufactured, from 2016 to 2019. Each series corresponds to a single experimental batch (letter A to E for the day of the week) where several samples were fabricated simultaneously (except for series 1830, which was produced in 3 consecutive batches).

Table 12. The different series of samples used to test $TiAlN_x/TiAlN_y$ tandem absorber coating

$TiAlN_x/TiAlN_y$ absorber	Series 1616	Series 1828	Series 1830	Series 1928
Number of samples	10	7	23	20
Number of batches (code)	1 (D)	1 (A)	3 (A, B, C)	1 (E)
Substrate Inconel 625 (thickness 2 mm)				
Ø 1”	10	1	6	-
Ø 2”	-	2	3	5
Substrate SS 304L (thickness 1 mm)				
25 x 30 mm²	-	2	-	6
50 x 50 mm²	-	2	14	9

All samples have the same coating structure as presented in Chapter 3 (Figure 75 p.96), except that series 1616 has two additional sublayers. The coatings were all deposited using the same experimental conditions. A variety of substrates was used: Inconel 625 with diameters 1” and 2” and thickness 2 mm, stainless steel (SS) 304L substrates with dimensions 25 x 30 mm² and 50 x 50 mm² and thickness 1 mm. In the following, the equivalence of the samples is estimated by comparing their optical properties (spectrophotometry), surface topography (SEM) and composition (EDS) in their as-deposited state. Results are not shown for series 1830 because the latter was received after a first heat treatment of 24h at 500°C at HEF. Some results for series 1828 are also not shown for the same reason.

1.2.1. Optical properties

The reflectance spectra of all the samples in their as-deposited state are plotted in Figure 103, showing notable variations and no overall perfect equivalence of all the samples.

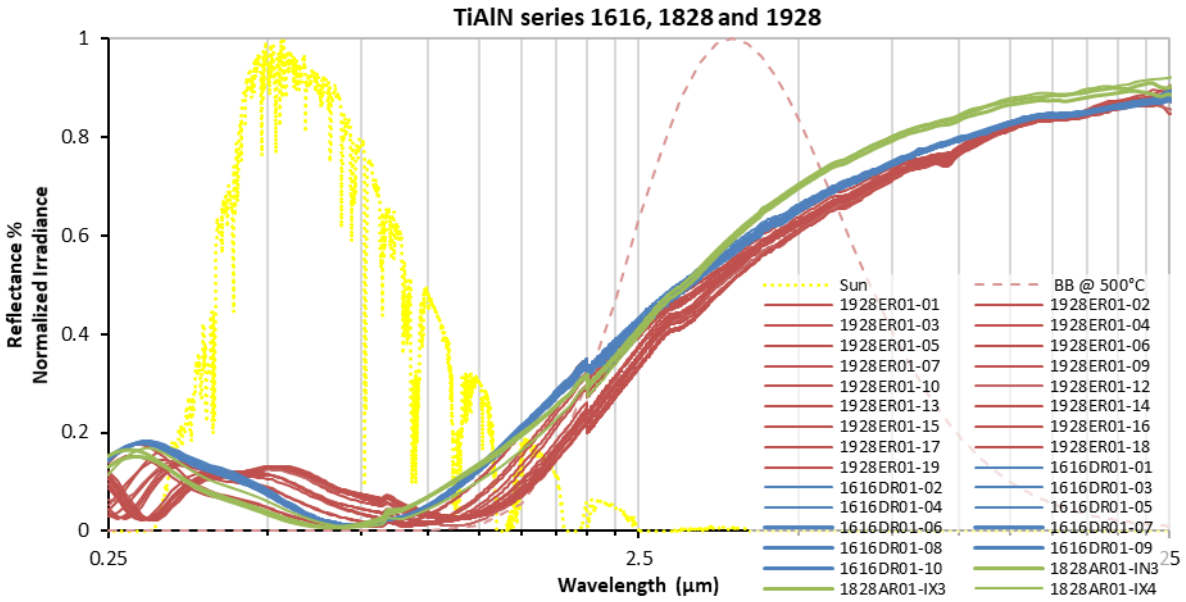

Figure 103. Reflectance spectra of as-deposited absorbers for series 1616 (blue), 1828 (green) and 1928 (red)

Looking at each series separately, it can be seen that the uniformity of the samples is high for the 10 samples of series 1616 (Figure 104), the latter being all deposited on the same type of substrate (Inconel 1"). Uniformity is also good for series 1828 (Figure 105), whatever the type of substrate (Inconel or SS). Series 1928 shows the lowest uniformity, with higher variations of the spectra, especially in the visible region (Figure 106). The lack of uniformity is not due to the substrate nature, as reflectance variations also exist for samples with the same type of substrate.

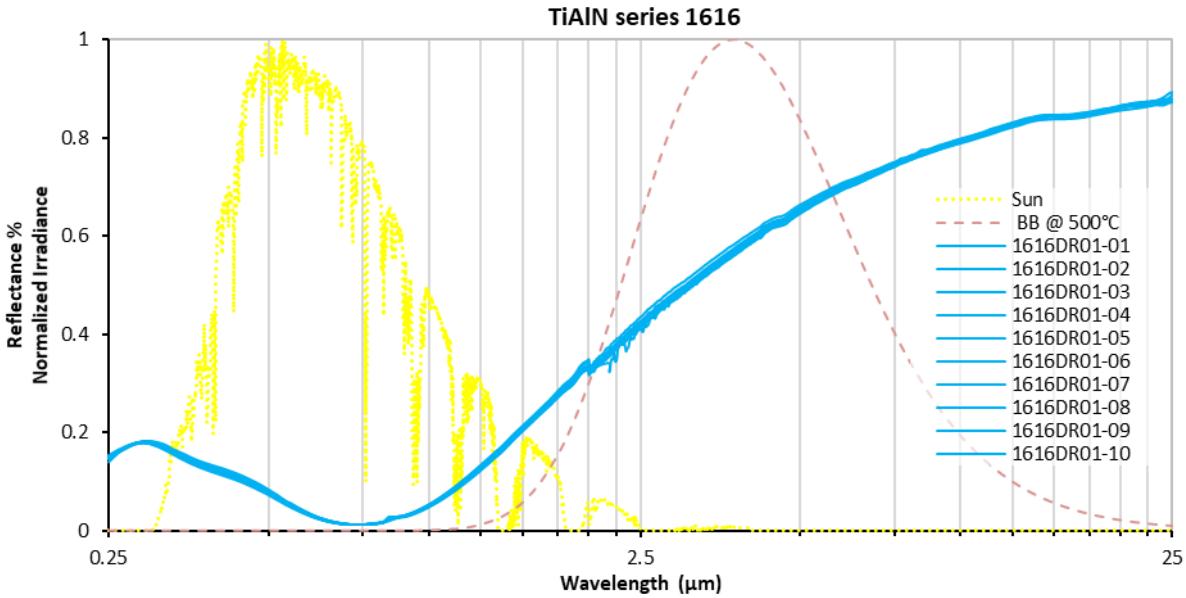

Figure 104. Reflectance spectra of series 1616 as-deposited samples with Inconel substrate

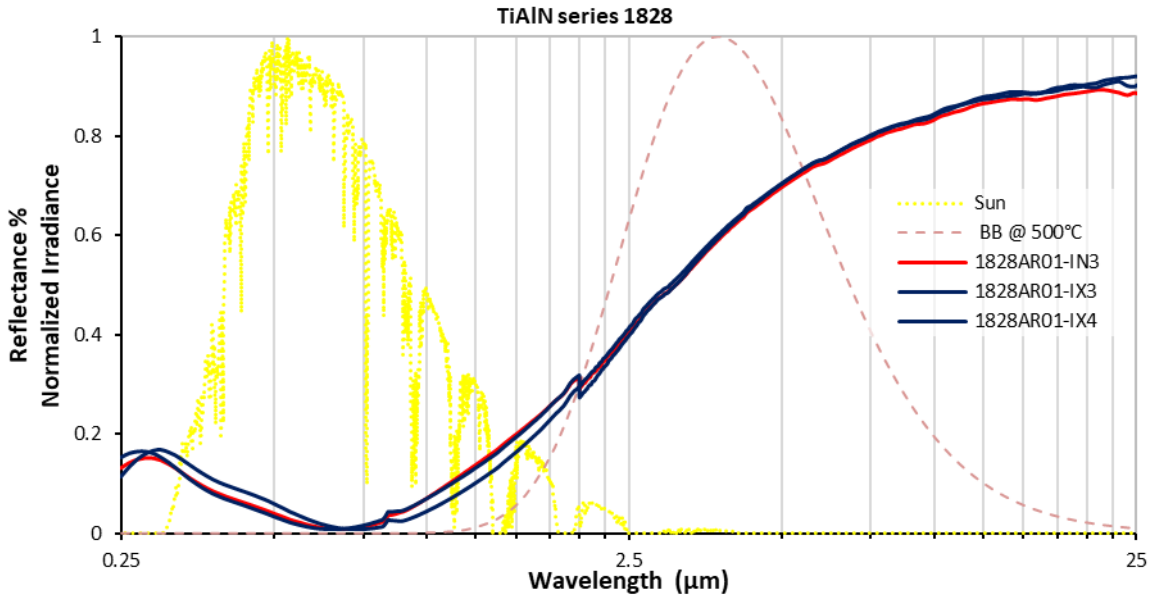

Figure 105. Reflectance spectra of as-deposited series 1828 samples with SS (dark blue) and Inconel (red) substrates

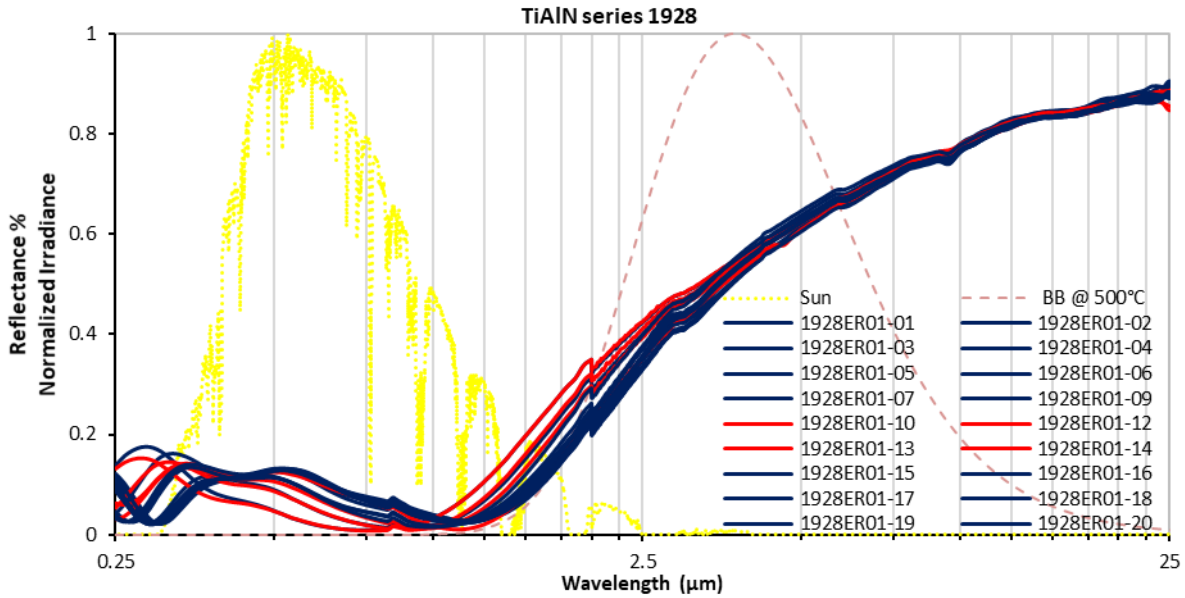

Figure 106. Reflectance spectra of as-deposited series 1928 samples with SS (dark blue) and Inconel (red) substrates

The average optical performances of each series, i.e., their solar absorptance and thermal emittance calculated from reflectance spectra (Figure 103), and resulting heliothermal efficiency, are shown in Table 13 along with their standard deviations [319]. These standard deviation values represent the uniformity (or lack thereof) between samples of each series and the repeatability of the manufacturing process. The error due to the equipment used for reflectance measurements (see Chapter 3 section 2.1, 2.1p.99) and subsequent calculation of optical performance is not taken into account as previous work showed that this error is very low [320] compared to the standard deviation between samples.

As expected from reflectance spectra, series 1616 and 1828 have a high uniformity, reflected by the low standard deviations: up to 0.002 for solar absorptance and 0.004 for thermal emittance, whatever the type of substrate. Series 1928 has a low uniformity, with a standard deviation of 0.009 for solar absorptance and up to 0.011 for thermal emittance.

Table 13. Optical performance of series of samples for $TiAlN_x/TiAlN_y$ tandem absorber coatings (as-deposited)

$TiAlN_x/TiAlN_y$ absorber	Series 1616	Series 1828	Series 1928	All series
Solar absorptance				
All samples (number)	0.915 ± 0.002 (10)	0.927 ± 0.002 *(3)*	0.914 ± 0.009 (18)	0.919 ± 0.008 (30)
Inconel substrate	*0.915 ± 0.002 (10)*	*0.926 (1)*	*0.921 ± 0.009 (4)*	*0.921 ± 0.006 (15)*
SS substrate	-	*0.928 ± 0.002 (2)*	*0.912 ± 0.008 (14)*	*0.923 ± 0.010 (15)*
Thermal emittance @ 500°C				
All samples (number)	0.348 ± 0.004 (10)	0.315 ± 0.004 (3)	0.381 ± 0.011 (18)	0.348 ± 0.024 (30)
Inconel substrate	*0.348 ± 0.004 (10)*	*0.320 (1)*	*0.378 ± 0.013 (4)*	*0.349 ± 0.018 (15)*
SS substrate	-	*0.312 ± 0.002 (2)*	*0.380 ± 0.011 (14)*	*0.335 ± 0.026 (15)*
Heliothermal efficiency @ 500°C				
All samples (number)	0.846 ± 0.002 (10)	0.865 ± 0.002 (3)	0.838 ± 0.011 (18)	0.850 ± 0.011 (30)
Inconel substrate	*0.846 ± 0.002 (10)*	*0.862 (1)*	*0.846 ± 0.012 (4)*	*0.851 ± 0.007 (15)*
SS substrate	-	*0.866 ± 0.001 (2)*	*0.837 ± 0.010 (14)*	*0.856 ± 0.014 (15)*

Comparing between series, the optical performance slightly varies from one series to another. The average solar absorptance is around 0.915 for series 1616 and 0.914 for series 1928, and 0.927 for series 1828 (+ 0.012). The average value for all the series of as-deposited samples is 0.919, with overall standard deviation of 0.008. These values show that there is an acceptably small variation in solar absorptance between the samples of each series and between the series, of less than 1 point of absorptance (i.e., 1% when considering solar absorptance in %) in all cases.

The average thermal emittance is 0.348 for series 1616, 0.315 for series 1828 and 0.381 for series 1928. Emittance is thus the lowest for series 1828 and the highest for series 1928, with a variation of 0.066, i.e., almost 7 points of emittance. As a result, the average thermal emittance for all the series is 0.348 with a standard deviation of 0.024. These values show that there is a higher variation in thermal emittance between the series than in solar absorptance, around 2 points of emittance (i.e., 2% when considering thermal emittance in %).

This larger variation does not appear to be clearly linked to the nature of the substrate, as similar variations are obtained when comparing the series by type of substrate. It therefore arises from variations in the coating architecture. For instance, series 1616 samples have additional underlying layers that do not affect solar absorptance but may affect thermal emittance as they mask the IR-reflective substrate.

The evolution of heliothermal efficiency between the series is naturally directly linked to that of the previous parameters. Series 1616 shows a good and repeatable efficiency (0.846 ± 0.002). Due to its highest solar absorptance and lowest thermal emittance, series 1828 presents the highest efficiency (0.865), with a low variation between samples (± 0.002). The lowest and less uniform efficiency is observed for series 1928 with 0.838 and a high variation of 0.011. Overall, this type of absorber shows a good heliothermal efficiency with an average of 0.850 for all the series, and a small variation of around 1 point.

1.2.2. Surface topography, atomic composition

Naked eye observation (Figure 107) and SEM images at the microscopic scale (Figure 108) both indicate that the surface topography of all analyzed as-deposited samples is uniform and smooth, and similar for all series and substrate types. Figure 108 shows examples for series 1616 (Inconel) and 1928 (SS 304L).

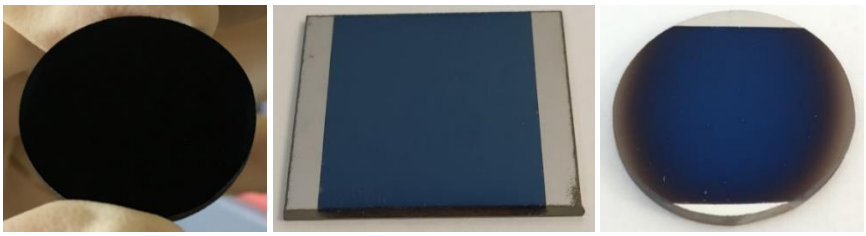

Figure 107. Macroscopic image of TiAlN absorber samples (from left to right, series 1616, 1928 and 1828)

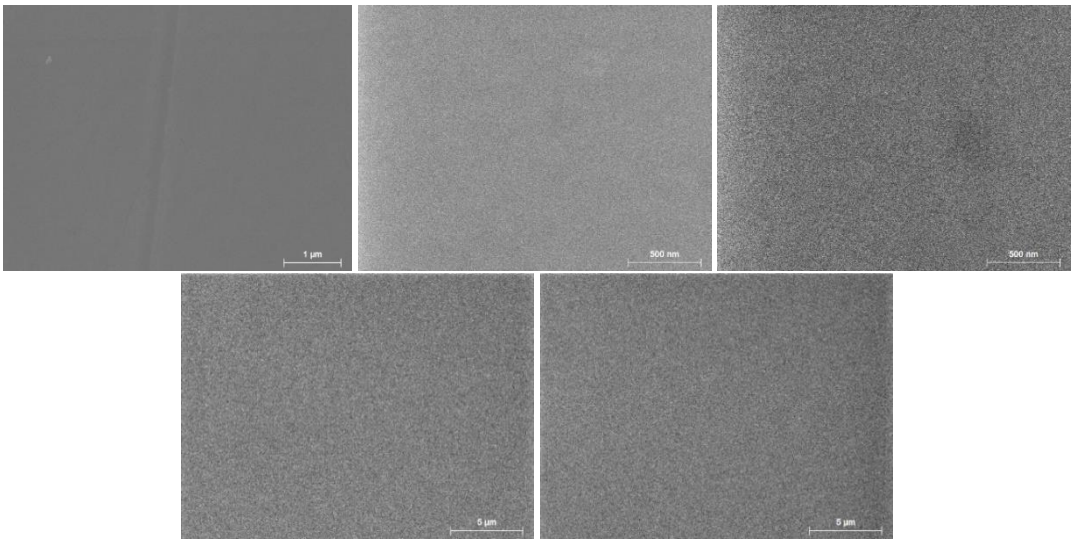

Figure 108. SEM images of as-deposited samples on Inconel (series 1616, top) and SS substrates (series 1928, bottom)

Table 14 shows the atomic percentage of the different chemical elements present in the as-deposited samples of series 1616 and 1928, compared with the uncoated Inconel substrate in the first case.

Table 14. Initial chemical composition in at.% (EDS) of the TiAlN absorber samples on Inconel (series 1616) and stainless steel (series 1928) substrates, compared with uncoated substrates

Series	Substrate	O	Si	Al	Ti	Fe	Cr	Ni	*Mo*	Nb
_	Inconel	-	-	-	0.4	5	24	63	5	2
1616	Inconel	-	4	35	4	3	14	36	3	1
1928	SS 304L	2	5	21	5	48	14	5	-	-

Since the coatings are thin (< 500 nm), elements from the substrates (in blue) are detected underneath, only with smaller amounts than in the uncoated substrates, as can be expected. Indeed, Inconel is a Ni-based alloy with additional Fe, Cr, Mo and Nb contents, while SS is a Fe-based alloy with typical 18-10 Cr-Ni content.

The main elements of the TiAl/TiAlN_x/TiAlN_y/SiNCH absorber structure (in red) are also detected: silicon (4-5 at.%), titanium (4-5 at.%) and aluminum (20-35 at.%). Nitrogen was difficult to detect because of the overlap between N and Ti EDS peaks and the greater content in Ti (Chapter 3 section 2.2 p.101). Carbon was not quantified, due to its low amount in the coating, and the difficulty to distinguish between the carbon present in the coating and the one naturally occurring surface pollution.

The atomic composition in coating elements is similar for both series, except that for series 1616, the content in aluminum (35 at.%) is higher than for series 1928 (21 at.%), due to the two additional sublayers in series 1616. For the same reason, the content in elements detected from the substrate is higher for series 1928 (67 at.% vs. 57 at.% in total), as its coating is thinner.

1.2.3. Conclusions

Four series of samples based on the same TiAl/TiAlN$_x$/TiAlN$_y$/SiNCH absorber configuration were compared in their as-deposited state, to check their equivalence. Indeed, they were not all fabricated at the same time (6 batches over 3 years) and not all on the same types of substrates (Inconel or SS). Meanwhile, large sets of equivalent samples are needed for comparable aging studies. The comparison relied on the results of spectral reflectance measurements and subsequent optical performance calculation, surface topography by SEM and chemical composition by EDS.

The reflectance spectra of all samples are not equivalent (Figure 103). Series 1616 and 1828 both have good optical uniformity, with no notable influence of the type of substrate (Figure 106). Series 1928 has lower uniformity, even when comparing samples with the same type of substrate. Taking into account all series, the average solar absorptance is 0.919 ± 0.008, the average thermal emittance is 0.348 ± 0.024 and the average heliothermal efficiency is 0.850 ± 0.011 (Table 13). These standard deviation values show that the solar absorptance and heliothermal efficiency of all samples is very comparable with a difference of less than 1 point (i.e., 1% if these parameters are considered in %). Meanwhile, thermal emittance fluctuates slightly more distinctly, by 2 points. This can be attributed in part to the higher emittance of series 1616 compared to series 1828, due to its sublayers. The microstructural analysis (surface topography, chemical composition) did not reveal any notable differences between the samples, whatever the series and substrate types.

Overall, the equivalence between these samples is sufficient to consider them for complex aging studies. Although their thermal emittance is not exactly equivalent, their solar absorptance is very similar, and their coating architecture and chemical composition are close enough that their aging behavior should not differ significantly. In any case, for each sample the variation with aging of its optical behavior will be considered relatively to its as-deposited state (e.g. $\Delta\alpha_S$ = α_S (aged) – α_S (as-deposited)) for better comparability with other samples.

1.3. Samples of WAlSiN absorber coatings

For the WAlSiN absorber coating with SiON/SiO$_2$ antireflective layer from CSIR-NAL Bangalore (see Chapter 3 section 1.2, p.97), different series of samples were also used to apply and evaluate different aging strategies (Table 15). In total, 30 samples were manufactured individually, i.e., in a different batch, using the same equipment and the same experimental conditions, to obtain the same absorber architecture (Figure 78 p.97). The substrate nature is also the same (stainless steel 304), only the substrate dimensions vary. Series SSC-0 was kept and studied at CSIR-NAL with their own equipment [195,242,305]. The others were studied at PROMES-CNRS.

Table 15. Description of WAlSiN absorber sample series

WAlSiN tandem absorber		*Number of samples*	*Substrate nature*	*Substrate dimensions*
Studied at CSIR-NAL [242]	***SSC-0***	13	SS304	-
Studied at PROMES-CNRS	***SSC-1***	2	SS 304	Ø 1"
	SSC-2	2	SS 304	32 x 32 x 2 mm^3
	SSC-3	4	SS 304	Ø 1'' + 30 x 30 x 3 mm^3
	SSC-4	2	SS 304	Ø 1''
	SSC-5	10	SS 304	30 x 30 x 3 mm^3
	SSC-6	2	SS 304	30 x 30 x 3 mm^3

1.3.1. Optical properties

The samples received at PROMES were divided into six different series of samples (SSC-1 to 6) according to their optical similarities. Indeed, although they all present a similar profile, some notable differences in their reflectance spectra (Figure 109) were observed between these 22 samples. The samples studied at CSIR-NAL (samples SSC-01 to 08 in Figure 109) show reflectance spectra similar to that of the samples studied at PROMES-CNRS. These differences are typical of small variations of the coating layers thicknesses but not of their inherent chemical nature, as illustrated by reflectance shifts in wavelength but not in intensity. Small variations in the IR range may be caused by slight differences in substrate surface state (polishing, cleaning) and composition.

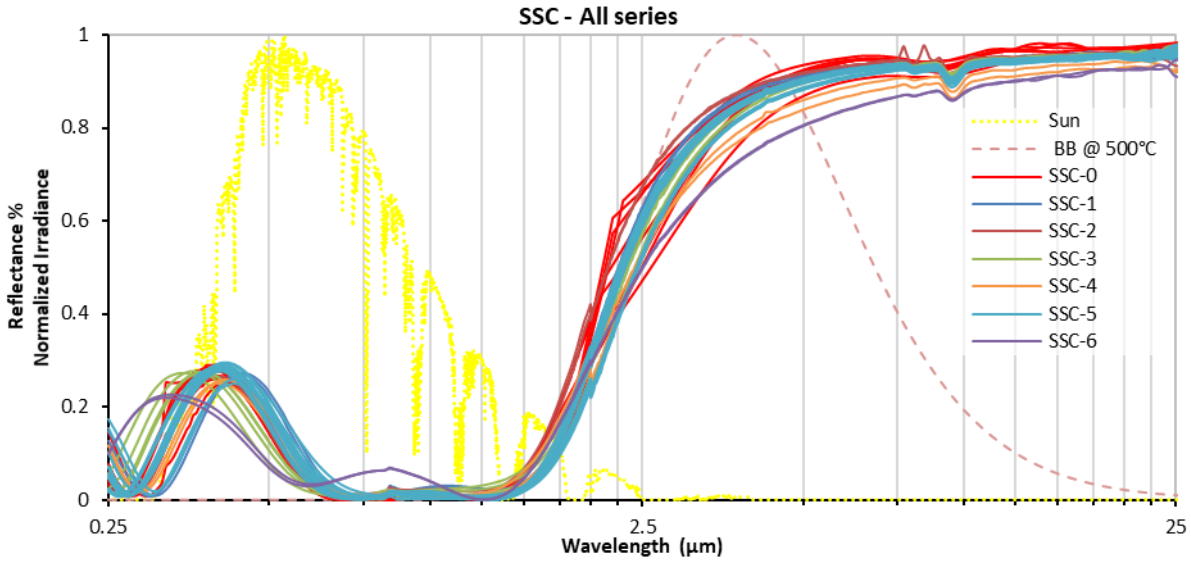

Figure 109. Reflectance spectra of 30 equivalent WAlSiN as-deposited samples (6 series)

Table 16 shows the corresponding optical performance parameters. The latter were calculated from reflectance spectra (see Chapter 1 section 3, p.28), measured at room temperature by spectrophotometry at CSIR-NAL (SSC-0) or PROMES (SSC-1 to 6), using similar equipment. For series SSC-0, solar absorptance was also directly measured at CSIR-NAL using a Devices and Services (D&S) Solar Spectrum Reflectometer (SSR) [242]. The two methods give different values of solar absorptance, as can be expected. Indeed, the calculation of solar absorptance from the reflectance spectrum is based on the standard direct + circumsolar solar spectrum G173-03 AM1.5 [31]. Meanwhile, SSR direct measurement is based on the detection from several photodetectors and weighing of their respective ranges to approach a global (direct + diffuse) solar spectrum. For the sake of comparing with the other series, for which absorptance was estimated from spectral reflectance measured at PROMES, values deduced from spectral reflectance measurements at CSIR-NAL (line 2) will be considered for series SSC-0.

Overall, the variations in reflectance spectra result in variations of the samples good optical performance (Table 16). This type of absorber shows a high value of solar absorptance (0.914 in average, ranging from 0.898 to 0.926) with a low variation between samples (standard deviation of 0.008).

Table 16. Optical properties for the different series of samples for the WAlSiN absorber

WAlSiN tandem absorber	*Solar absorptance*	*Thermal emittance @ 500°C*	*Heliothermal efficiency @ 500°C*
Series studied at CSIR			
SSC-0			
Directly measured [242]	*0.952 ± 0.003*	-	-
Deduced from spectral reflectance	0.919 ± 0.004	0.143 ± 0.022	0.890 ± 0.004
Series studied at PROMES			
SSC-1	0.898 ± 0.001	0.133 ± 0.003	0.872 ± 0.001
SSC-2	0.908 ± 0.009	0.121 ± 0.002	0.884 ± 0.008
SSC-3	0.926 ± 0.002	0.152 ± 0.006	0.896 ± 0.002
SSC-4	0.913 ± 0.001	0.194 ± 0.010	0.874 ± 0.001
SSC-5	0.910 ± 0.003	0.154 ± 0.013	0.880 ± 0.005
SSC-6	0.920 ± 0.002	0.230 ± 0.001	0.874 ± 0.003
Average of series 1 to 6 (PROMES)	0.913 ± 0.009	0.159 ± 0.030	0.881 ± 0.009
Average of series 0 to 6	0.914 ± 0.008	0.155 ± 0.029	0.884 ± 0.008

Thermal emittance at 500°C is also good, with a low average value of 0.155 (ranging from 0.121 to 0.230). As for the previous absorber (section 1.2.1), thermal emittance presents a higher fluctuation between samples, with a similar standard deviation of 0.029 (i.e., 3 points of emittance when the latter is considered in %). Direct measurements of thermal emittance at 82°C at CSIR-NAL on series SSC-0 using an emissometer (model AE1-RD1) did not show this level of standard deviation [242]. Therefore, these fluctuations may also be partly due to the high sensitivity of thermal emittance calculated from reflectance to the chosen concatenation wavelength and the quality of the overlapping between spectra measured in the UV-Vis-NIR and IR ranges using two different spectrophotometers.

Heliothermal efficiency reflects the variations in solar absorptance (0.884 in average, ranging from 0.872 to 0.896) with the same standard deviation of 0.008. Indeed, by definition, solar absorptance has a more direct impact on heliothermal efficiency, compared to thermal emittance (see Chapter 1 section 3.4.2, p.34).

1.3.2. Surface topography, atomic composition

Figure 110 and Figure 111 show macroscopic pictures and SEM images of the samples surface after deposition. No defects are observed in the samples surface morphology, and no differences are notable between the series.

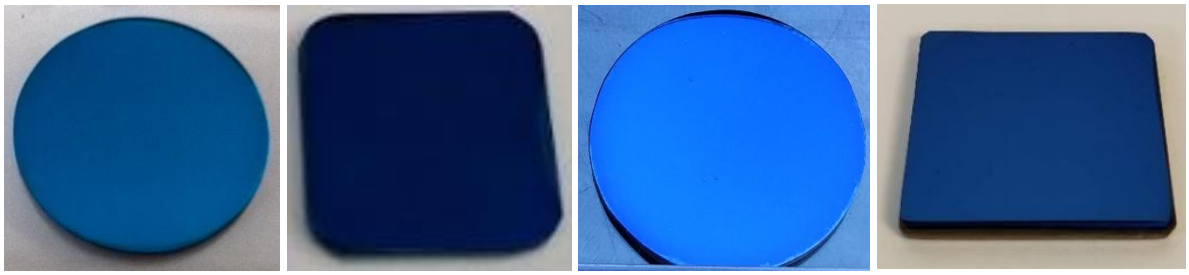

Figure 110. Pictures of the as-deposited surface for series SSC-1, SSC-2, SSC-3 and SSC-5 (from left to right)

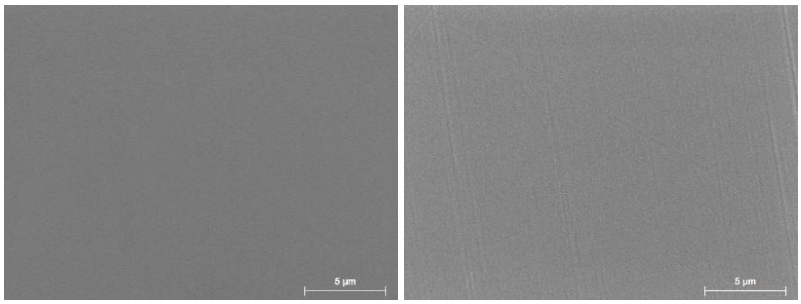

Figure 111. SEM images of the as-deposited surface for series SSC-3 (left) and SSC-5 (right)

Table 17 shows EDS measurements of the atomic composition of the WAlSiN absorber coatings. For each series, average contents and standard deviations were obtained from at least two measurements on each of the several samples considered. In addition, the error on EDS atomic composition is approx. 2%. EDS results indicate that the samples of the different series have close atomic compositions.

Fe and Cr are elements from the SS substrate, detected in similar amounts, indicating that the coatings have similar thicknesses and densities, except for SSC-6 which may be thinner than the others, as the detected content in substrate elements is higher.

Table 17. EDS atomic composition of WAlSiN as-deposited samples (accelerating voltage 15 kV)

Series / Element (at.%)	O	W	Al	Si	N	Ar	Fe	Cr	Ni
SS 304 substrate *(4 samples)*	-	-	-	1 ± 0	-	-	72 ± 0	19 ± 0	8 ± 0
SSC-1 *(2 samples)*	42 ± 1	28 ± 2	9 ± 1	3 ± 1	13 ± 1	2 ± 0	3 ± 1	1 ± 0	-
SSC-2 *(2 samples)*	39 ± 3	32 ± 3	7 ± 1	3 ± 2	14 ± 6	1 ± 0	3 ± 1	1 ± 0	-
SSC-3 *(4 samples)*	36 ± 2	36 ± 2	7 ± 1	1 ± 1	13 ± 1	2 ± 0	4 ± 1	1 ± 0	-
SSC-5 *(2 samples)*	35 ± 1	32 ± 0	10 ± 1	-	15 ± 1	2 ± 0	4 ± 0	1 ± 0	-
SSC-6 *(1 sample)*	11 ± 1	6 ± 1	6 ± 1	-	2 ± 1	1 ± 0	54 ± 1	16 ± 1	5 ± 0

A small quantity of Ar is detected, due to the incorporation in the coatings of energetic Ar^+ ions during the Ar plasma assisted sputtering process (see Chapter 3 section 1.2.2, p.98). O, W, Al, Si and N are elements from the WAlSiN/SiON/SiO_2 coatings. Their relative contents slightly vary depending on the series. However, this is probably related to the EDS technique itself, rather than to notable changes in the coatings compositions.

For instance, the quantification of Si in the presence of W is tricky, as the two elements have overlapping peaks at low energy (see Chapter 3 section 2.2, p. 101), that could only be distinguished using a technique with higher resolution than EDS, such as WDS (Figure 112). W also presents high energy peaks, due to its much larger atomic number, i.e., 74 vs. 14 for Si. Thus it is systematically detected and prioritized during the automated EDS quantification. Therefore, it is credible that the actual amount of Si is significantly higher than estimated by EDS.

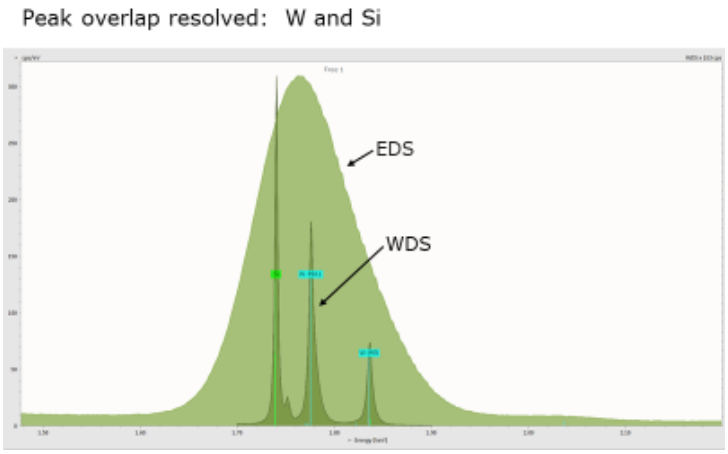

Figure 112. W and Si peak overlap (source: Bruker)

O and N also have low energy overlapping peaks. As they are both light elements, they however cannot be distinguished by higher energy peaks, explaining why N is in some cases not quantified (series SSC-1), virtually increasing the relative content in O.

1.3.3. Conclusions

In this case, the equivalence between samples and series of samples was checked out with a comparison of five series of samples with WAlSiN/SiON/SiO_2 absorber coating. They were fabricated in different batches with the same type of substrate, SS304. Again this comparison is based on the results of spectral reflectance measurements, optical properties, surface topography by SEM and chemical composition by EDS.

Reflectance measurements show similar spectra for all the samples, with slight variations over the whole spectral range (Figure 109). The highest variation occurs at the beginning of the visible region (close to 0.25 µm) and the end of near infrared region (close to 2.5 µm). Series SSC-1, SSC-3 and SSC-4 show a good optical uniformity with the smallest variation in reflectance (Figure 109) and optical properties, especially solar absorptance (Table 16). Series SSC-1 shows the best uniformity considering the close values of solar absorptance and thermal emittance.

Taking into account all series, the average solar absorptance is 0.914 ± 0.008, the average thermal emittance is 0.155 ± 0.029 and the average heliothermal efficiency is 0.884 ± 0.008 (Table 16). The standard deviation of solar absorptance and heliothermal efficiency is thus small, of 1 point. Meanwhile, thermal emittance fluctuates more distinctly by almost 3 points. Microstructural analysis did not show any notable differences between the samples of all series. These optical fluctuations may thus be due to slights variations in layer thicknesses during deposition, especially when considering the complex architecture of this type of absorber, where very thin layers must be deposited (2-3 nm). Indeed, the WAlSiN layer is composed of 18 layers of W_2N and 18 layers of AlSiN over a total thickness of 85 nm (see Chapter 3 section 1.2.1, p. 97).

To conclude on these series, the equivalence between these samples is sufficient for the results of different aging studies to be compared. As shown with the previous absorber, their optical properties are not the same, the solar absorptance values are very close between series, and their structure and chemical composition are close enough that their aging behavior should not change significantly.

1.4. Samples of W/SiCH multilayer absorber coatings

For the W/SiCH multilayer absorber coating (see Chapter 3 section 1.3, p.98), two different series of samples were used as part of our study (Table 18).

Table 18. The different series of samples used to test W/SiCH multilayer absorber coating

W/SiCH absorber coating	Series I4C	Series I9C
Number of samples	3	5
Number of layers in the coating	4	9
Substrate	Inconel	Silicon

The two series have different architectures with different numbers of layers (4 and 9) and different substrate types (Inconel, Si). The series are named after the number of layers of the coating. Series I4C is a W (181 nm) / SiCH (71 nm) / W (8 nm) / SiCH (72 nm) multilayer absorber deposited on an Inconel substrate (Figure 80 p. 99), with a total coating thickness of 331 nm. Series I9C is a multibilayer of four W (2 nm) / SiCH (60 nm) periodic bilayers and an infrared reflective W sublayer with a thickness of 180 nm (total coating thickness of 428 nm), deposited on a silicon substrate for easier material characterization after aging. Because of their very different structures, in this case the two series are not directly meant to be compared with one another. The equivalence within each series is discussed in the following.

1.4.1. Optical properties

Figure 113 and Table 19 show the reflectance spectra and corresponding optical performance of the two series of samples in their as-deposited state.

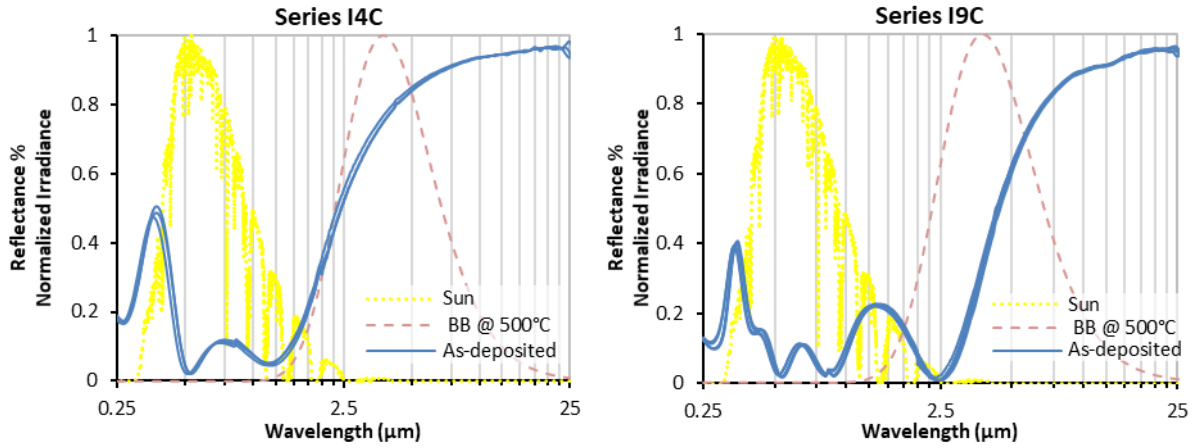

Figure 113. Reflectance spectra of series I4C (left) and series I9C (right)

Table 19. Optical properties for each series of the W/SiCH absorber coating

W/SiCH absorber coating	Series I4C	Series I9C
Solar absorptance	0.871 ± 0.004	0.896 ± 0.001
Thermal emittance @ 500°C	0.190 ± 0.007	0.426 ± 0.008
Heliothermal efficiency @ 500°C	0.833 ± 0.005	0.812 ± 0.001

As expected, the optical behavior is very different when comparing the two series. Series I4C has the best selective behavior with an efficiency equal to 0.833 ± 0.005, as it is an optimized architecture [93]. Contrarily, series I9C is less efficient (0.812 ± 0.001), as its architecture is not optimized. Indeed, it was initially developed for the purpose of generating W-SiCH composites by thermal annealing [194]. As a

result, solar absorptances are close, with a difference of 0.025 (0.896 vs. 0.871). The higher solar absorptance for I9C is due to the larger number of absorptive layers. As a consequence, thermal emittance is also much higher for I9C series, by 0.236 (0.426 vs. 0.190), due to the reflectance spectrum shift towards the infrared range. This shift is in turn due to the nature of the Si substrate, which is not IR-reflective as is the Inconel one, and to the higher number of layers and interfaces intensifying multiple reflections and enhancing optical interferences [194]. On the other hand, within each series the samples are satisfyingly uniform, with standard deviations lower than 1 point of performance (maximum ± 0.007).

1.4.2. Surface topography, atomic composition

Pictures and SEM images of as-deposited W/SiCH samples for series I4C and I9C show a homogenous and smooth surface in both cases (Figure 114). There is no visual difference between the surfaces of each series.

Table 20 shows the atomic content of the different elements present in the as-deposited absorber samples as measured by EDS. For series I9C, the higher content in silicon compared to series I4C is partly due to the Si substrate, which is detected underneath the coating. In a similar manner, elements from the Inconel substrate, Ni and Cr, are detected for series I4C.

Table 20. Initial chemical composition in at.% (measured by EDS)

Series	*Substrate*	*O*	*Si*	*C*	*W*	*Fe*	*Cr*	*Ni*	*Mo*	*Nb*
_	Inconel	-	-	-	-	5	24	63	5	2
I4C	Inconel	1	3	69	21	-	2	5	-	-
I9C	Silicon	1	12	70	16	-	-	-	-	-

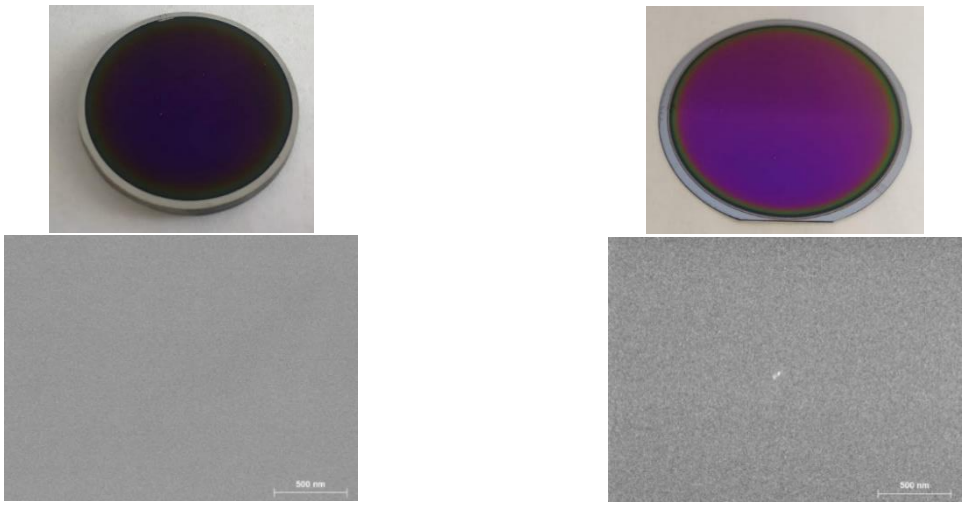

Figure 114. Pictures (top) and SEM images (bottom) of the surface of a sample from series I4C (left) and series I9C (right)

From its architecture, series I9C has a higher content in Si and C, as it comprises four 60 nm-thick SiCH layers (240 nm in total), whereas series I4C has only two SiCH layers (143 nm in total). Meanwhile, the content in W should be equivalent (189 nm in total for series I4C vs. 188 nm in total for series I9C). This is not clearly apparent in Table 20, where the detected content in W is larger by 5 at.% for series I4C. This again can be due to the overlapping of W and Si EDS peaks, rendering the concomitant quantification of these two elements difficult, especially at low Si contents. Therefore, the W content detected for series I9C with more Si (coating + substrate) is probably more realistic. In any case, these two series having different architectures, they have different atomic compositions, as can be expected.

1.4.3. Conclusions

From the as-deposited analysis done on this type of absorber for the different series, due to their different architectures, a high variation of reflectance spectra was observed from one series to another, and as a results a high variation between the optical properties of the absorber, with a higher variation of thermal emittance than solar absorptance. As expected, the equivalence between these series cannot be considered and the two series will be used for testing separate aging protocols.

1.5. Conclusions on sample equivalence

In this section, large sets of samples were compared to determine their equivalence, for each of the three types of absorbers considered in this work: TiAlN and WAlSiN tandem absorbers, and W/SiCH multilayer absorber. The comparison of the samples was based on data obtained with the material characterization techniques available at PROMES-CNRS laboratory: spectrophotometry, SEM and EDS.

The average optical performance calculated from reflectance measurements for each type of absorber is recalled in Table 21. For W/SiCH only the 4-layer series I4C is considered, as it is optimized. The other available series has a different architecture, so each series has been studied separately and their equivalence is not discussed. For WAlSiN, for the sake of comparison, the reported solar absorptance is the one calculated from reflectance spectra using the same method as for the others.

Following Eq.(12) (p.34), solar absorptance has a higher impact on the absorber optical performance than thermal emittance. Therefore, variations in solar absorptance between equivalent samples of the same type of absorber must be limited, typically around 0.01, while variations in thermal emittance can be higher due to its lesser impact, typically lower than 0.1. Thus, the series of samples considered in this study present acceptable variations of their optical properties for a given type of absorber.

Table 21. Average optical performance for each type of absorber

Property / absorber type *(number of samples considered)*	**TiAlN tandem** *(30 samples)*	**WAlSiN tandem** *(30 samples)*	**W/SiCH multilayer** *(3 samples I4C)*
Solar absorptance	0.919 ± 0.007	0.914 ± 0.008	0.871 ± 0.004
Thermal emittance @ 500°C	0.348 ± 0.033	0.155 ± 0.029	0.190 ± 0.007
Heliothermal efficiency @ 500°C	0.850 ± 0.011	0.884 ± 0.008	0.833 ± 0.005

These variations of optical properties tend to indicate that the top layers of the coatings, that by design influence solar absorptance, are very similar, while the underlying layers and substrate surface state, that influence thermal emittance, may vary more from one sample/series/batch to another.

In addition, for a given absorber the surface morphology and chemical composition are similar. This study thus suggests that, for a given absorber type, the series of samples can be considered equivalent enough to be able to compare the results of different aging protocols applied to them. Indeed, their coating architecture and chemical composition are close enough so that their aging behavior and thermal stability should not differ significantly from one series to another.

In any case, in the following, for each treated sample, the variation with aging of its optical response will also be considered relatively to its as-deposited state (e.g. $\Delta\alpha_S$ = α_S (aged) – α_S (as-deposited)). This allows for an enhanced comparability between the aging results obtained on different samples of a given absorber architecture.

2. Thermal aging for short durations in air

When a solar selective absorber coating is designed and developed, even if the thermal stability of its constitutive materials is sometimes known, the aging behavior of the complete architecture is hard to predict, due to the complex aging phenomena discussed at length in Chapter 2. Therefore, the first simple step to test the thermal stability of an absorber is usually to treat samples under thermal radiation for a short duration, at temperatures close to the aimed operating temperature of the absorber. Since their duration is short, such tests can be attempted on equivalent samples in a range of temperatures instead of just one, in order to explore the absorber thermal resistance and find the critical temperature above which stability is no longer ensured. The atmosphere imposed on the coating during these tests also depends on the aimed working conditions, i.e., vacuum or air.

In this way, the first response of the absorber coating with temperature can be precisely observed, using material characterization techniques. In particular, due to the optical nature of CSP applications, the absorber optical properties (spectral reflectance, solar absorptance, thermal emittance, heliothermal efficiency) are chosen as the main parameters to follow this evolution with aging.

As a first step to investigate the aging behavior of absorber coatings, thermal aging tests for short durations of typically up to 24h are applied, usually in air and at various temperatures. The aim of such tests is to observe the response of the as-deposited coating to thermal exposure, usually at a temperature higher than its fabrication temperature. Indeed, depending on their fabrication technique and experimental conditions, coatings are not always stabilized after deposition. They can for instance present porosity or residual stress that may evolve under thermal post-treatment (see Chapter 2 section 3.2.2, p.60). Such microstructural changes may cause variations in their optical properties that can be detrimental to their performance.

2.1. Optical properties

As an illustration of the effect of short duration aging protocols, Figure 115 shows the experimental spectral reflectance of the 3 types of absorbers (TiAlN, WAlSiN, W/SiCH) before and after thermal aging in air for up to 25h, at different temperatures. The aging conditions are recalled in the graph titles.

For the WAlSiN absorber, samples were treated and measured at CSIR-NAL [242], first for 5h at different temperatures between 300 and 600°C in air, then up to 25h on the same samples. The other absorber coatings were treated and measured at PROMES-CNRS for up to 24h at 500°C in air. Some of them were treated for 24h directly from the as-deposited state, while others were first heat treated for 12h then treated again to reach 24h in total. Three series are considered for the TiAlN absorber and two for the W/SiCH absorber (4 and 9 layers). All these samples were treated in ambient air, except the 9-layer W/SiCH (I9C) absorber that was treated in filtered air, i.e., without CO_2 and H_2O. Table 22 (p.135) and Figure 116 (p.137) show the corresponding variations in optical performance. Variations are calculated as the difference between the considered property after aging and before aging (e.g. $\Delta\alpha_S$ = α_S (after 24h) – α_S (as-deposited)). In Figure 116, the first number is the aging temperature in °C and the second number is the aging duration in hours.

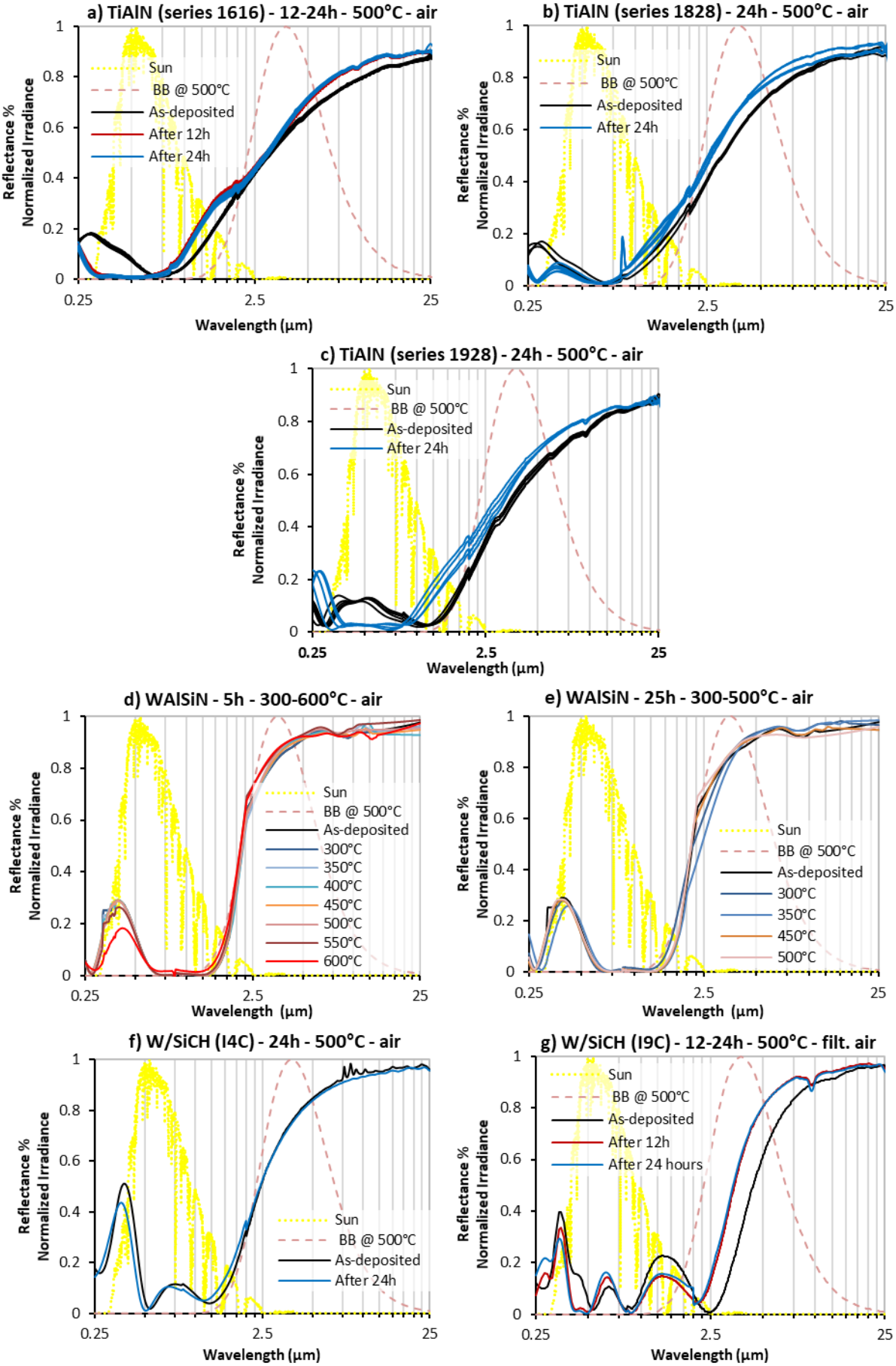

Figure 115. Reflectance spectra of samples of the 3 absorber types, as-deposited and heat treated in air for up to 25h

Table 22. Comparison of optical properties as-deposited and after 12 and/or 24h at 500°C in air (favorable variations are in green, unfavorable ones in red)

Absorber	*State*	*Nb of samples*	*Solar absorptance*	*Thermal emittance @ 500°C*	*Heliothermal efficiency @ 500°C*
TiAlN Series 1616	As-deposited	*10*	0.915 ± 0.002	0.348 ± 0.004	0.846 ± 0.002
	After 12h	*7*	0.904 ± 0.001	0.306 ± 0.005	0.844 ± 0.001
	After 24h	*9*	0.912 ± 0.004	0.302 ± 0.004	0.852 ± 0.005
	Variation after 12h		*-0.011*	*-0.042*	*-0.002*
	Variation after 24h				
	vs. as-deposited		***-0.003***	***-0.046***	***+0.006***
	vs. 12h		***+0.008***	***-0.004***	***+0.008***
TiAlN Series 1828	As-deposited	*3*	0.927 ± 0.002	0.315 ± 0.004	0.865 ± 0.002
	After 24h	*7*	0.911 ± 0.004	0.257 ± 0.008	0.861 ± 0.003
	Variation after 24h		***-0.016***	***-0.058***	***-0.004***
TiAlN Series 1928	As-deposited	*17*	0.914 ± 0.009	0.381 ± 0.011	0.839 ± 0.011
	After 24h	*4*	0.924 ± 0.007	0.329 ± 0.012	0.859 ± 0.005
	Variation after 24h		***+0.010***	***-0.052***	***+0.020***
W/SiCH Series I4C	As-deposited	*1*	0.869	0.195	0.831
	After 24h	*1*	0.882	0.194	0.843
	Variation after 24h		***+0.013***	***-0.001***	***+0.013***
W/SiCH Series I9C	As-deposited	*5*	0.896 ± 0.001	0.426 ± 0.008	0.812 ± 0.001
	After 12h	*1*	0.920	0.288	0.863
	After 24h	*1*	0.912	0.280	0.857
	Variation after 12h		*+0.024*	*-0.138*	*+0.051*
	Variation after 24h				
	vs. as-deposited		***+0.014***	***-0.146***	***+0.045***
	vs. 12h		*-0.008*	*-0.008*	*-0.006*

Overall, the observed evolutions in optical properties, if any, tend to occur after the first hours of thermal aging (5 to 12h), as little difference is later obtained between 5/12h and 24/25h. Also, there is also no notable difference between samples treated cumulatively, i.e., first for 12h then again for 12h to reach 24h of aging in total, and samples treated for 24h directly from their as-deposited state.

For TiAlN absorbers (Figure 115(a-c)), compared to their as-deposited state, reflectance after 12 and 24h of aging clearly evolves. It is reduced in the UV-Vis range but increases in the NIR-IR range (typically above 0.75 µm). As a consequence, solar absorptance varies slightly (max. ± 0.016); thermal emittance notably decreases by several points (max. -0.058, i.e., -6 points); heliothermal efficiency is only slightly affected, with either a very slight decrease (-0.004) or a small increase (+0.020, i.e., +2 points), depending on the concomitant evolutions of solar absorptance and thermal emittance.

The appearance of a very small absorption peak around 9.3 µm (reflectance dip visible in reflectance spectra), typical of Si-O bonds (1075 cm^{-1}) [321], indicates that the coating could be slightly oxidized after its exposure to air. In previous work by HEF-IREIS [295], the optical changes were attributed to variations in layer thicknesses due to aging, especially for the two absorber layers, as measured on SEM images. Short duration thermal aging (12h) in air at a temperature close to that of the aimed application (500°C) leads to slight changes in optical performance, due to the coating microstructural fine tuning: densification and layer thickness variation. Since the absorber was optically optimized using optical simulation before plasma synthesis, due to these changes the absorber architecture is no

longer perfectly optimal. This underlines the critical importance of checking the coating stability after deposition, to validate its performance.

This idea is illustrated by the case of the non-optimized W/SiCH absorber with 9 layers (series I9C), for which aging tests were also carried out for 12 and 24h at 500°C in air. The design of this periodic architecture was not optically optimized in terms of layer thicknesses before synthesis. Aging also affects its reflectance, with a shift towards lower wavelengths in the IR range and a decrease in intensity in the UV-Vis-NIR range (Figure 115(g)). Consequently, contrarily to the previous examples, in this case aging notably improves the absorber performance. As reflectance is slightly higher above 0.5 µm but lower before 0.5 µm, and the spectrum is shifted towards lower wavelengths, there is an increase in solar absorptance by 2 points (+0.024 to reach 0.920), and more importantly a significant decrease of thermal emittance by almost 14 points (-0.138), so that heliothermal efficiency increases by 5 points (+0.051). Complementary studies in PROMES-CNRS during the thesis of D. Ngoue [194] indicated that this improvement is again due to changes in the chemical nature of the coating (oxidation of SiCH with partial replacement of H and/or C by O – here also confirmed by the appearance of an absorption peak near 9.3 µm on reflectance spectra, diffusion of W) and subsequent densification. A study of the kinetics of such phenomena showed that they are initiated at the early stages of heating (during the first 3 hours).

This example shows that an initially non-optimal architecture may evolve into a more efficient one after aging for a short duration. Therefore, the short-term aging behavior of an absorber must absolutely be studied and its initial design can even be adapted accordingly.

For the WAlSiN absorber, several equivalent samples were treated for 5h in air, at different temperatures ranging from 300°C to 600°C, with this time the objective to find a critical temperature beyond which the coatings are no longer stable. Up to 450°C the optical properties remain stable (Figure 115(d) and Figure 116 (top)). At 500°C and above, thermal emittance decreases by up to 2 points, while solar absorptance is stable and even slightly increases at 600°C. Consequently, not only heliothermal efficiency is not degraded by aging but it even tends to slightly improve with temperature, starting at 500°C, reaching an improvement of 0.5 point at 550°C and 600°C. This example again illustrates that absorber coatings can be improved by short duration aging. Also, it demonstrates that aging for short durations is not sufficient to conclude on the existence and value of a critical temperature that would induce optical degradation.

Small changes in the optical properties, mostly thermal emittance, are observed between 5h and 25h of thermal aging for the WAlSiN absorber (Figure 116 (bottom)). However, the calculation of thermal emittance considered here is influenced by the fluctuating quality of the overlap between the spectra acquired in the UV-Vis-NIR and NIR-IR ranges and of the extrapolation in the 16 – 25 µm range (Figure 115(e)). As a matter of fact, direct measurements of thermal emittance at 82°C at CSIR-NAL using an emissometer (model AE1-RD1) did not show any variations [242]. Therefore, the observed variations for this absorber may not be significant, and remain small in any case (maximum 1.5 points of emittance).

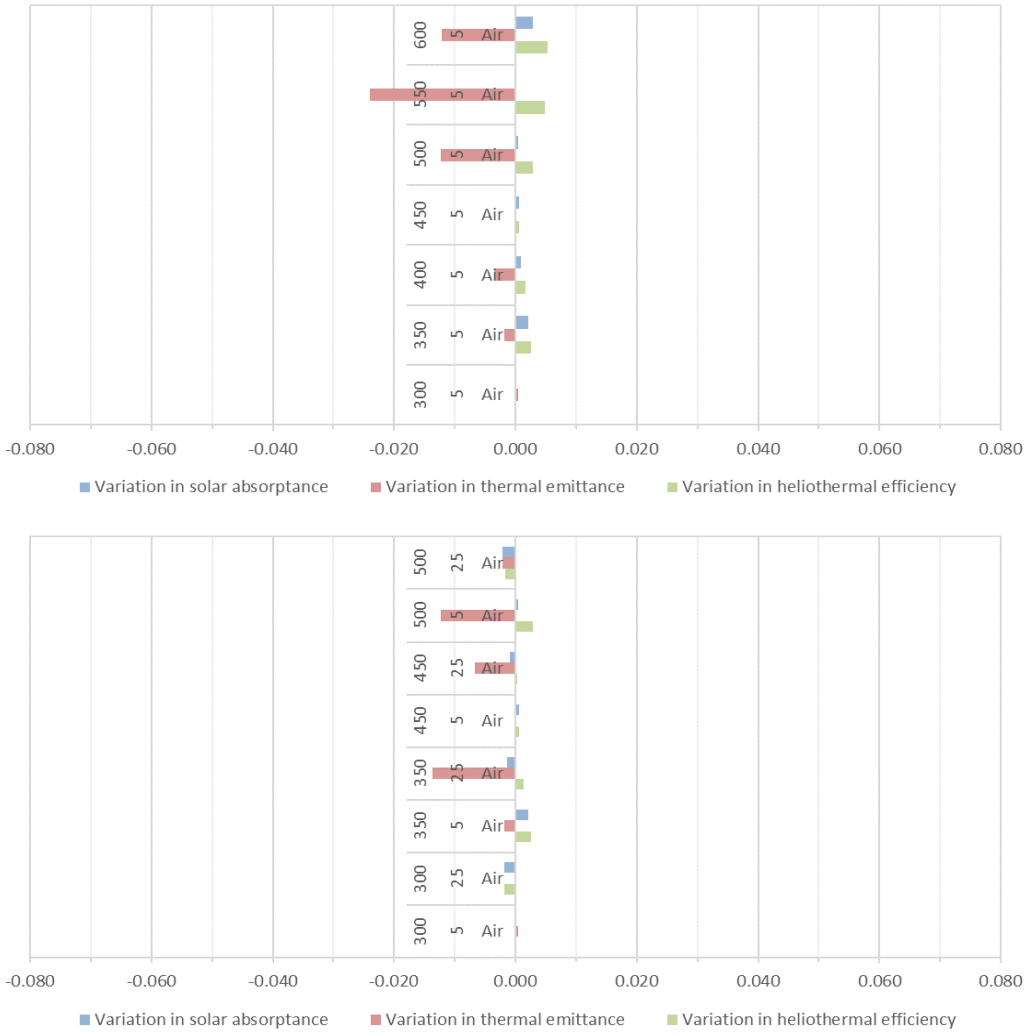

Figure 116. Optical properties variations of WAlSiN absorber with thermal aging at different temperatures in air: (top) after 5h (300 - 600°C); (bottom) after 5 and 25h (300 - 500°C)

2.2. Conclusions on thermal aging for short durations

Overall, short duration thermal aging tends to either slightly degrade or slightly improve the optical performance of initially optimized absorber coatings (using optical design). Indeed, the systematic decrease in thermal emittance is not always enough to compensate for the slight decrease in solar absorptance sometimes observed. Meanwhile, the performance of initially non-optimized absorber coatings can evolve positively with this first aging step. These changes are likely caused by small microstructural evolutions when exposed to temperatures higher than the fabrication temperature. In particular, coating layer thicknesses can vary due to thermal densification. In some cases, an evolution in composition due to oxidation phenomena can also occur and impact optical performance, either positively or negatively. On the whole, this analysis shows that such **short duration tests give valuable indications of the aging behavior of the absorbers**, such as their critical temperature, a relevant parameter indicative of their limit of use. However, they are never enough to conclude on the stability of the coating, let alone its durability. **Longer durations are absolutely necessary to validate or disprove the tendencies observed at short durations**.

In any case, this study indicates that variations in optical properties seem to occur at the early stages (first hours) of thermal aging in air at high temperature, then tend to stabilize. Such short duration thermal aging could thus be considered as a **post processing step for absorber coatings fabrication**,

with the aim of stabilizing the microstructure and properties of the coatings, or even in some cases fine tuning and improving them. This kind of procedure is classically called **curing** in materials engineering. Since absorbers will inevitably be exposed to high temperatures in the final CSP application, this curing step, integrated as the final step in the fabrication process, is **highly recommended** to avoid any notable changes in the coating performance after its installation. Also, as optical properties were not perfectly stabilized after up to 12h, it appears recommendable to increase the duration of the **curing step to typically 24h**, to better ensure the stabilization of the coating microstructure. In the following, unless otherwise stated, a curing step of 24h at 500°C in air was thus systematically applied to the TiAlN and W/SiCH absorbers before any other type of aging.

Finally, even though short duration thermal aging gives access to relevant information of the aging behavior of the absorber coatings, it is mandatory to check if this behavior remains constant with time. Aging tests for longer durations than 24h are thus necessary to verify their durability.

3. Thermal aging for long durations at working temperature in air

Compared to short durations, applying thermal aging on solar absorbers for long durations allows checking whether their optical performance tends to stabilize with time after its first evolution, or if the latter tend to progress further, to finally reach an unacceptable level of degradation. In this way, long duration tests allow studying the absorbers behavior in conditions better approaching the real working conditions in CSP plants, i.e., a high number of hours at high temperature during the lifetime of a CSP plant.

For our study, the aimed working temperature is considered to be around 500°C in air, representative of CSP technologies such as Fresnel or central tower with Direct Steam Generation.

As a consequence:

- Three equivalent samples of the TiAlN absorber (series 1616) were aged for up to 1000h at 500°C in air, cumulatively with steps of approx. 24h;
- During the thesis of D. Ngoue [194], several equivalent samples of the optically non-optimized 9-layer W/SiCH absorber (periodic series I9C) deposited on silicon wafers were treated at 500°C in filtered air (without CO_2 and H_2O) for different durations up to 96h, and some of these results are reported here to complete our analysis of aging protocols;
- In addition, a sample of the optically optimized 4-layer W/SiCH absorber (a-periodic series I4C [93]) deposited on Inconel was also treated at 500°C in ambient air during this thesis, this time cumulatively on the same sample for up to 96h, with steps of 24h;
- During the thesis of K. Niranjan at CSIR-NAL, a sample of the WAlSiN absorber was treated at 450°C in air, cumulatively with steps of 25h until reaching a total duration of 250h, and these results are further exploited here [242].

Their spectral reflectance was measured as-deposited and after each aging step to follow the evolution of the optical properties with aging. Their surface morphology and atomic composition were also measured at intervals by SEM and EDS analyses. The corresponding results are presented in the following subsections.

3.1. Optical properties

Figure 117 shows the reflectance spectra measured before and after each aging step applied to the different absorbers. For the TiAlN absorber, only some of the collected spectra are shown, for clarity. The spectra for the as-deposited state and up to 24h of aging are the same as the ones presented in section 2 on short durations. Table 23, Figure 118 and Figure 119 show the evolutions with aging of the corresponding optical performance parameters: solar absorptance, thermal emittance and heliothermal efficiency at 500°C, and performance criterion in some cases. Table 23 gives the absolute values and variations of these optical properties for TiAlN and W/SiCH absorbers at specific durations, Figure 119 shows absolute values for all aging durations applied to the TiAlN absorber and Figure 118 shows the absolute variation for WAlSiN absorber compared to the as-deposited state, as previously shown for shorter durations.

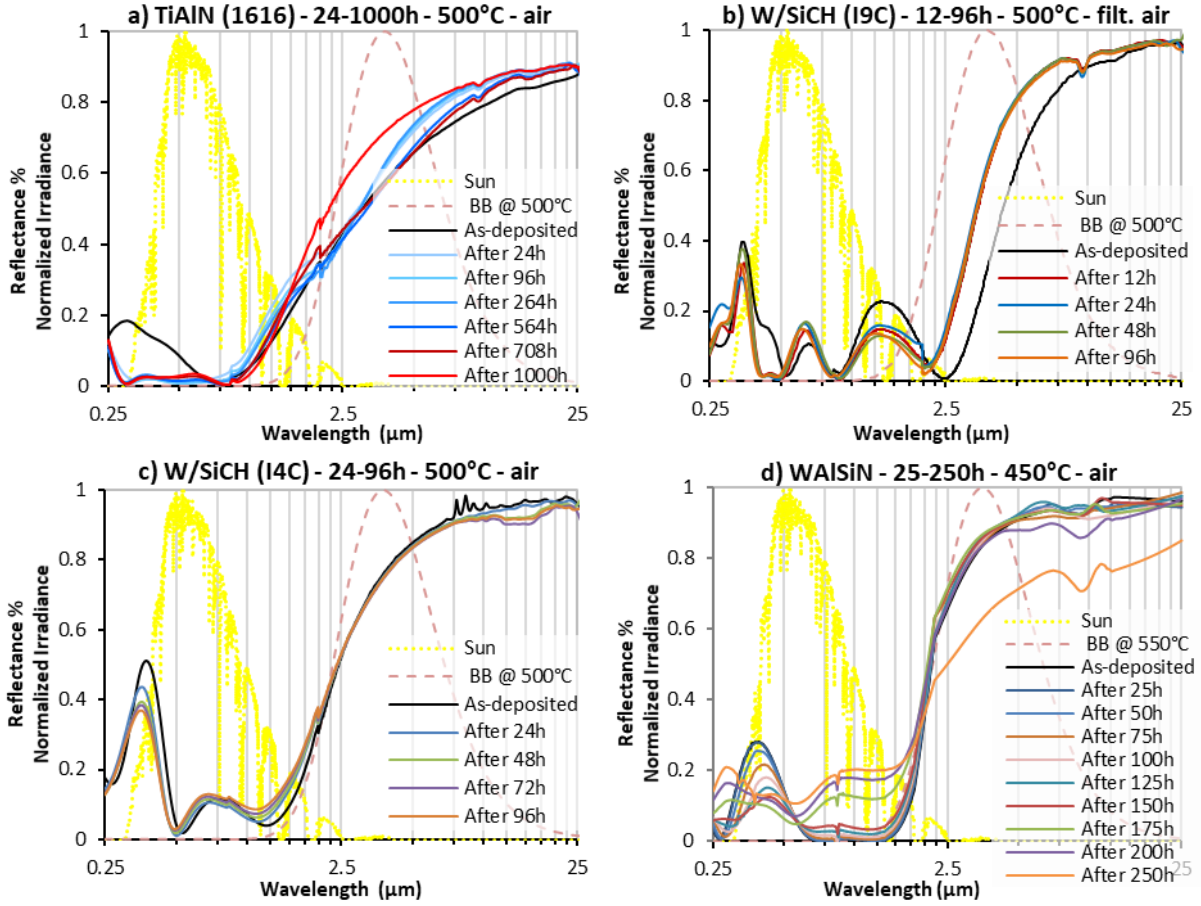

Figure 117. Reflectance spectra of the different absorbers, as-deposited and aged at 450 or 500°C in air for up to 1000h

Overall, the beneficial effect of the curing step (24h aging) discussed in section 2 is again visible here: for TiAlN and W/SiCH absorbers, the decrease in UV-Vis reflectance, coupled with a decrease in thermal emittance due to the increase in NIR-IR reflectance and/or the reflectance blueshift (due to coating densification with aging), leads to an increase in heliothermal efficiency by a few points.

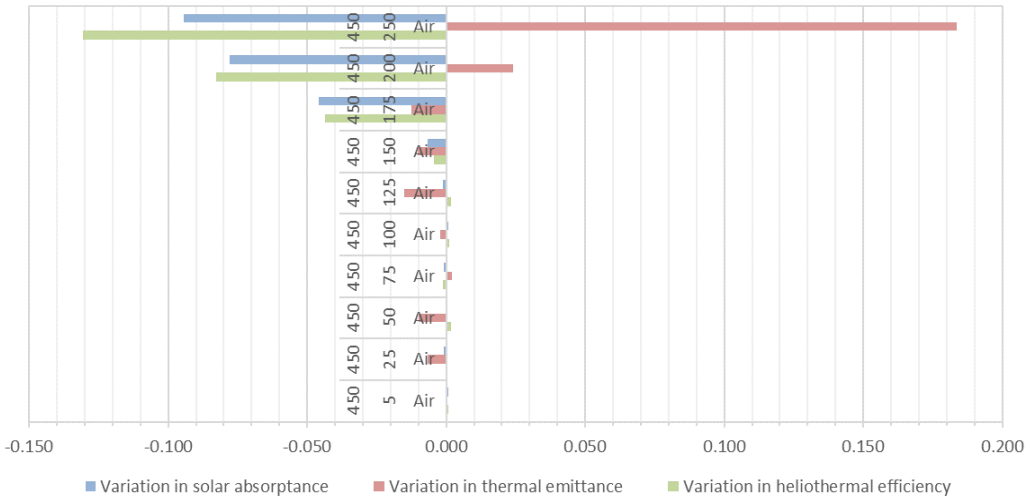

Figure 118. Optical properties variations of the WAlSiN absorber with up to 250h of aging at 450°C in air (the first number is the aging temperature in °C and the second number is the aging duration in h)

Table 23. TiAlN and W/SiCH absorbers optical performance evolution for as-deposited and aged samples at 500°C in air

Absorber	***State***	***Solar absorptance***	***Thermal emittance @ 500°C***	***Heliothermal efficiency @ 500°C***
TiAlN Series 1616	As-deposited (3 samples)	0.915 ± 0.002	0.348 ± 0.004	0.845 ± 0.003
	After 24h (3 samples)	0.912 ± 0.004	0.302 ± 0.004	0.850 ± 0.001
	After 96h (2 samples)	0.920 ± 0.002	0.297 ± 0.007	0.862 ± 0.001
	After 264h (3 samples)	0.926 ± 0.002	0.289 ± 0.005	0.869 ± 0.001
	After 564h (2 samples)	0.932 ± 0.000	0.337 ± 0.009	0.866 ± 0.002
	After 708h (1 sample)	0.921	0.334	0.859
	After 1000h (3 samples)	0.917 ± 0.003	0.230 ± 0.007	0.872 ± 0.002
	Variation after 1000h			
	vs. as-deposited	***+0.002***	***-0.118***	***+0.027***
	vs. 24h (cured)	***+0.005***	***-0.072***	***+0.022***
W/SiCH Series I9C [194]	As-deposited (5 samples)	0.896 ± 0.001	0.426 ± 0.008	0.812 ± 0.001
	After 24h (1 sample)	0.912	0.280	0.857
	After 48h (1 sample)	0.913	0.286	0.856
	After 96h (1 sample)	0.920	0.290	0.863
	Variation after 96h			
	vs. as-deposited	***+0.024***	***-0.136***	***+0.051***
	vs. 24h (cured)	***+0.008***	***+0.010***	***+0.006***
W/SiCH Series I4C (1 sample)	As-deposited	0.869	0.195	0.831
	After 24h	0.882	0.194	0.843
	After 48h	0.875	0.199	0.836
	After 72h	0.871	0.204	0.831
	After 96h	0.863	0.200	0.824
	Variation after 96h			
	vs. as-deposited	***-0.006***	***+0.005***	***-0.007***
	vs. 24h (cured)	***-0.019***	***+0.006***	***-0.019***

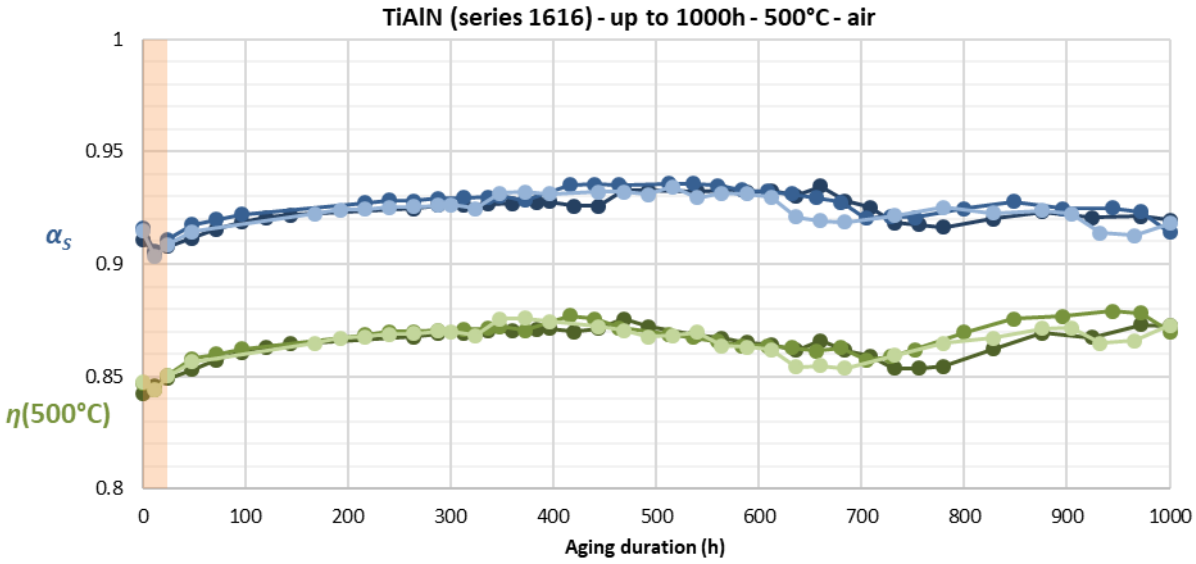

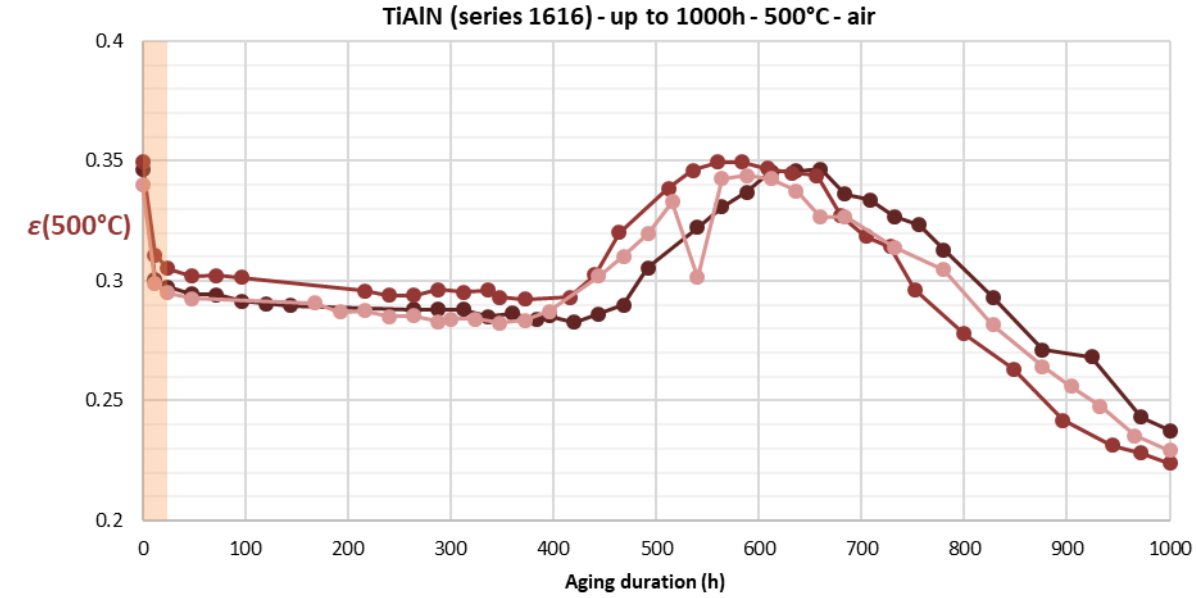

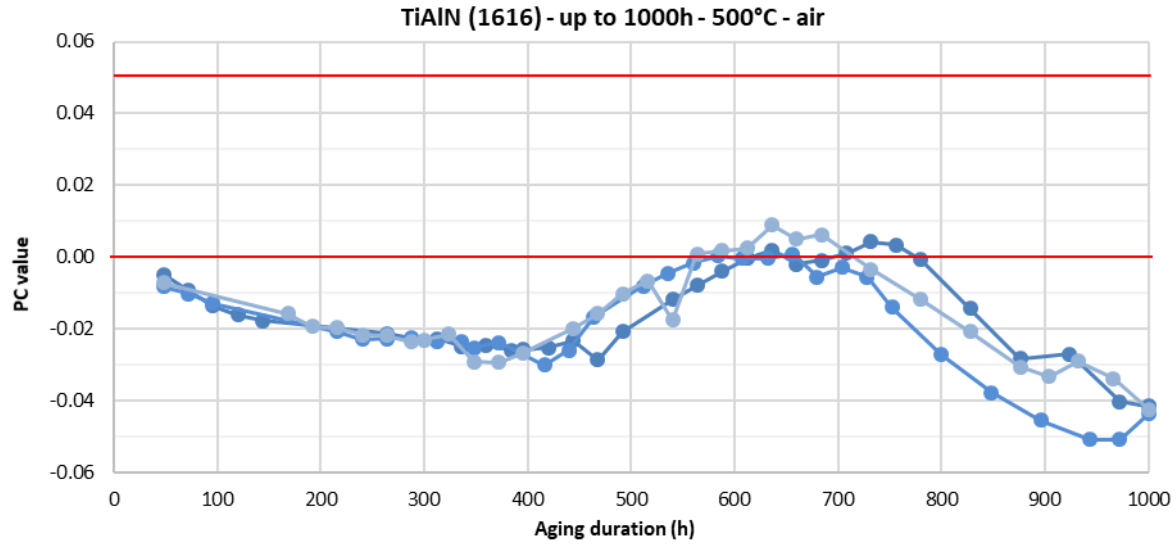

Figure 119. TiAlN absorber optical performance parameters (solar absorptance α_s, thermal emittance ε(500°C), heliothermal efficiency η(500°C), performance criterion PC) evolution with cumulative aging duration at 500°C in air for three equivalent samples (the orange rectangle represents the curing step)

After this curing step, there is no general tendency for the different absorbers. For the TiAlN absorber, the performance continues to improve (i.e., solar absorptance increases by up to 3 points and thermal emittance decreases by 2 points), slightly but steadily, up to approx. 400h of aging (Figure 119). The cut-off wavelength between low and high reflectance behavior is shifted towards lower wavelengths (Figure 117), due to the decrease in coating thickness [295]: a slow densification of the material with cumulative aging may thus be at play. After 400h, thermal emittance suddenly increases again by approx. 5 points to reach its initial value, before going down again after 600h to finally reach values significantly lower than the initial one (-0.118 after 1000h vs. as-deposited). Meanwhile, above 500h solar absorptance decreases again slightly, to practically reach its initial value after 1000h (+0.005 after 1000h, Table 23). These changes derive from the ones in spectral reflectance (Figure 117 (a)), with a slight increase below 0.7 µm where solar irradiation is high, thus reducing solar absorptance, not compensated by the slight reflectance decrease in the NIR region. IR reflectance varies the most, causing the strong variations in thermal emittance. Overall, heliothermal efficiency remains higher than its initial value at all times, up to 1000h of aging (+0.027 vs. as-deposited, Table 23). Also, the performance criterion (PC = $-\Delta\alpha + 0.5\ \Delta\varepsilon$) is very low (below 0.01, Figure 119) and even negative for most of the aging test, clearly illustrating that not only the optical performance is not degraded by aging, but it is even improved by it. Aging is thus beneficial for this type of absorber coating, which demonstrates good thermal stability for long durations at 500°C in air.

For the 9-layer W/SiCH absorber, spectral reflectance varies only slightly after the curing step (Figure 117 (b)), so that the optical properties have not significantly changed after 96h of aging (Table 23). Solar absorptance and thermal emittance slightly increase compared to the cured state (+0.01), resulting in a very slight improvement of the heliothermal efficiency. This absorber is thus thermally stable up to approx. 100h. However, these evolutions are very similar to the ones obtained for the TiAlN absorber after 100h, so that the 9-layer W/SiCH absorber may also still evolve with time if aging tests are continued.

For the 4-layer W/SiCH absorber, reflectance tends to gradually decrease in the UV-Vis (0.25-0.5 µm) and IR regions (> 2.5 µm) whereas it increases in between (0.5-2.5 µm) (Figure 117 (c)). There is also a blueshift of the reflectance minima, indicating a probable decrease in thickness and densification of the coating with aging. After the improvement brought by the curing step, the optical properties tend to degrade slowly with aging, to finally reach a performance after 96h that is slightly lower than the performance of the as-deposited sample (-0.006 in solar absorptance, +0.005 in thermal emittance, -0.007 in heliothermal efficiency), and definitely lower the performance of the cured sample (-0.019 in solar absorptance, +0.006 in thermal emittance, -0.019 in heliothermal efficiency).

For the WAlSiN absorber, the optical properties remain stable up to 150h (Figure 118), despite the decrease in reflectance in the UV region (Figure 117 (d)) that has little impact on solar absorptance, as there is very little solar radiation in this range. As previously discussed, the small variations in thermal emittance below 150h are not significant as they are mostly caused by the poor overlapping of UV-Vis-NIR and IR spectra. Then after 150h of aging the behavior starts to change in a more significant way, first in the solar range where reflectance flattens, with a notable increase beyond 0.5 µm, then also in the infrared region where reflectance strongly decreases. As a consequence, the heliothermal efficiency starts to decrease at 150h (-0.13 after 250h), first due to a dramatic drop in solar absorptance (-0.09 after 250h), then to a strong increase in thermal emittance (+0.18 after 250h).

In the following, material characterization sheds some light into the causes of these evolutions. On this matter, as observed for shorter durations absorption peaks (reflectance dips around 9.3 µm) appear with aging, foreboding some level of oxidation through the formation of Si-O and/or Al-O bonds [321].

3.2. Surface topography

Figure 120 and Figure 121 compare macroscopic and SEM pictures of the surface of the different absorbers in their as-deposited state and after aging at 450 or 500°C in air for different durations.

Absorber	*As-deposited*	*After 24h*	*After 48h*	*After 72h*	*After 96h*	*After 1000h*
TiAlN Series 1616		–	–	–	–	
W/SiCH Series I9C [194]	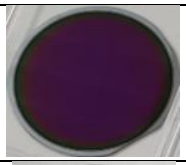	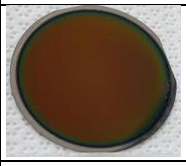	–	–	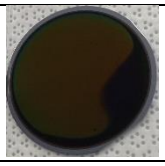	–
W/SiCH Series I4C		–		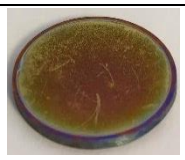	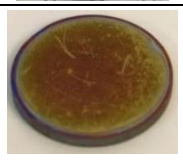	–

Figure 120. Macroscopic images of the absorbers, as-deposited and after aging for different durations at 500°C in air

To the naked eye, the samples, particularly the W/SiCH ones, display changes in color with aging. This change probably reflects a change in thickness due to the densification of the coating [194], as indicated by the blueshift of the reflectance spectra (Figure 117). Local surface defects and edge delamination can also be observed on the TiAlN and 4-layer W/SiCH absorbers deposited on Inconel substrates, while the 9-layer W/SiCH absorber deposited on Si did not suffer from delamination (Figure 120). The phenomena can thus be due to the larger thermal expansion of the metallic alloy substrate (typically 14 x 10^{-6} $°C^{-1}$ at 500°C [322]) compared to the crystalline silicon wafer (4 x 10^{-6} $°C^{-1}$ at 500°C [323]), creating larger tensile mechanical stress in the coating when heated (tension-compression cycle). This example emphasizes the strong influence of the substrate on the aging behavior of absorber coatings. Such macroscopic defects are still visible at larger magnification, provided by SEM analysis. However, when further increasing magnification, the surface appears smooth (apart from the initial polishing tracks of the metallic substrate) and without defects. The morphologic changes appear to only be macroscopic, typical of thermomechanical deterioration and not of dramatic changes of the coating microstructure. This is why the optical properties of these coatings do not drastically change with the applied aging.

Contrarily, for the WAlSiN absorbers, the change in surface morphology is more drastic after 250h (Figure 121), explaining the notable degradation of the optical performance. Indeed, the initially smooth surface changes to a more irregular surface, with the appearance of asperities that strongly deteriorate the selectivity of the material. Thermal emittance is the most affected (Figure 118), due to the size of these asperities, in the micrometer range: they cause light trapping in the IR wavelengths, increasing spectral absorptance and emittance in this range (decrease in reflectance in Figure 117 (d)).

These morphologic and optical changes are also related to the evolution of the material composition with aging, as explained in the following.

<table>
<tr><td>TiAlN
Series
1616</td><td>As-deposited

–</td><td>After 384h at 500°C
 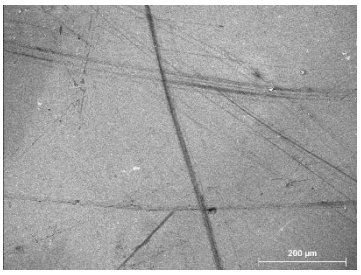
x 150</td><td>After 1000h at 500°C
 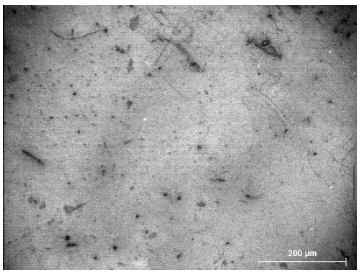
x 150
 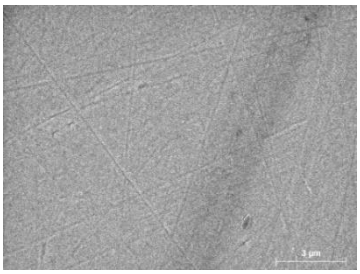
x 8000</td></tr>
<tr><td>W/SiCH
Series I9C
[194]</td><td>As-deposited
 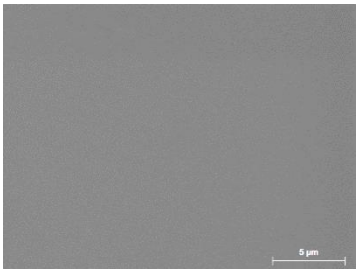
x 5000
 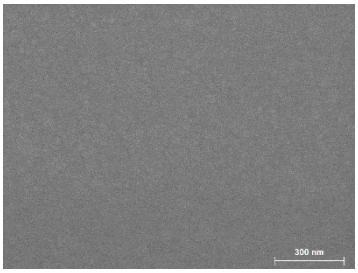
x 80000</td><td>After 96h at 500°C
 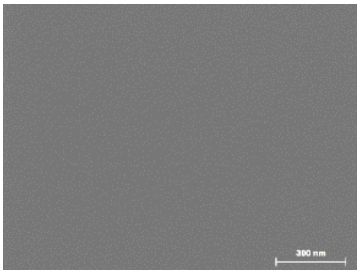
x 80000</td><td></td></tr>
<tr><td>WAlSiN
[242]</td><td>As-deposited

–</td><td colspan="2">After 250h at 450°C
 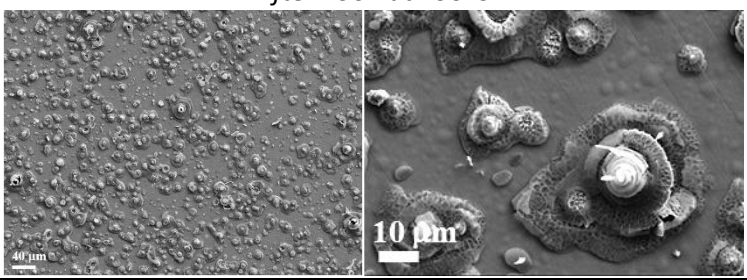 </td></tr>
</table>

Figure 121. SEM images of the surface of the absorbers, after different aging durations at 450°C or 500°C in air

3.3. Atomic composition

The evolutions in the atomic composition of the different absorbers were measured by EDS at intervals. Both the 9-layer W/SiCH and WAlSiN absorbers show a large increase of the oxygen content in the coating after aging (approx. +20-25 at.%, Table 24), indicating their oxidation in the presence of

air. In the W/SiCH absorber, it was previously observed [194] that the incorporation of oxygen happens through the formation of Si-O and W-O bonds, to the detriment of C, which may be expulsed in the form of CO_2 vapor. In a similar manner, in the WAlSiN absorber it is probable that it happens through the formation of W-O, Al-O and/or Si-O bonds, to the detriment of N (which may be expulsed in the form of N_2 and/or NO_x vapors).

Table 24. EDS analysis (at.%) of the 9-layer W/SiCH and WAlSiN absorbers, as-deposited and aged in air

Absorber	*Substrate*	*State*	*W*	*Al*	*Si*	*C*	*N*	*O*
W/SiCH I9C [194]	Silicon	As-deposited	16		12	71		1
		After 12h at 500°C	17		11	54		18
		After 24h at 500°C	17		14	44		25
		After 48h at 500°C	18		11	48		22
		After 96h at 500°C	18		11	50		22
WAlSiN [242]	Stainless steel	As-deposited	20	4	9		19	48
		After 250h @ 450°C (Figure 117 (d))						
		Flat surface	17	4	9		2	68
		Asperities	12	4	8		_	76

For the W/SiCH absorber, oxidation occurs after the first few hours of aging, then the oxygen content seems to stabilize, as reflected by the stabilization of the optical properties. For the WAlSiN absorber, the whole coating is oxidized, forming WO_3 phases [242], and the asperities observed in Figure 117 (d) present an even larger amount of oxygen. Since these asperities contain less W than the flat surface, they are probably made of a metallic oxide based on one of the elements from the stainless steel substrate (e.g. Cr).

The TiAlN absorber, initially oxygen-free by design, also tends to oxidize with aging. The oxygen content in the coating increases progressively as the cumulated aging duration increases, up to approx. 7 at.% after 400h and up to approx. 10 at.% after 1000h (Figure 122).

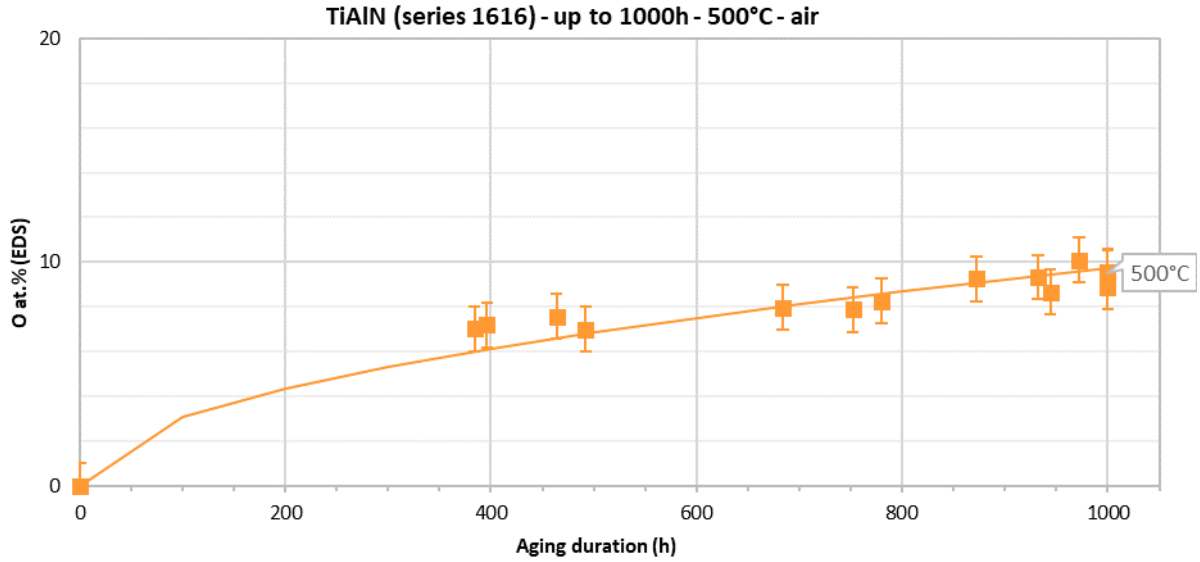

Figure 122. Evolution of the oxygen atomic content (at.%O) in the absorber coating measured by EDS vs. aging duration at 500°C in air

In this case, the evolution of the oxygen content with aging duration was fitted with a parabolic law known as Wagner's law of oxidation (see Chapter 2 section 3.2.1.2, p.57). The latter states that during oxidation a mass gain *Δm* occurs and is related with the square root of time, according to Eq.(34). Here we will assume that the mass gain due to the formation of oxides is proportional to the increase in oxygen content in at.% measured by EDS.

$$\Delta m \propto at.\%\, O \;\propto K \cdot \sqrt{t} \tag{34}$$

This parabolic oxidation profile is typical of the formation of an adhering and stable oxide at the surface of the coating during aging. As further oxidation must happen via oxygen diffusion through this surface oxide, oxidation becomes slower and slower as the oxide gets thicker. Overall, the impact of oxidation is not very strong since the optical properties remain stable even while this oxidation phenomenon goes on (Figure 119).

It is thus possible that oxidation mostly concerns the top SiCNH antireflective layer of the absorber structure, and that the optical indices (*n*, *k*) of the latter are not drastically changed by the incorporation of oxygen in its microstructure, which remains a transparent low-*n* material. These results seem to indicate that the initial SiCNH top antireflective layer may be oxidized into SiO_2, then this layer acts as a barrier against further oxidation, while keeping the antireflective property also characteristic of this oxide material. The observed change in optical properties may additionally be caused by the modification of layer thicknesses and intrinsic chemical nature due to atomic interdiffusion between the coating layers or between the substrate and the coating, which are thermally-induced phenomena, as was previously observed for similar HEF-IREIS coatings [295].

In any case, as oxidation is slowly and constantly increasing, it does not seem to be the cause for the fluctuations in optical properties observed after 400h, especially thermal emittance (Figure 119). Since the physical aspect of the surface evolves towards local defects at the micrometer scale, the changes in optical properties at this second stage of aging are probably due to the impact these defects have on the coating optical response in the IR range, as was observed for the WAlSiN absorber.

3.4. Conclusions on thermal aging for long durations at working temperature

Overall, this analysis shows that changes in coating microstructure, chemical composition and subsequently in optical properties, if any, mostly occur during the first hours of aging (i.e., the curing step), then the coating tends to stabilize or evolve slowly up to at least 100-150h. This evolution is typical of the formation of a protective surface oxide to slow down oxidation, here based on the Si-derived antireflective top layers (SiCNH, SiCH and SiON layers for the TiAlN, W/SiCH and WAlSiN absorbers, respectively) forming silicon oxides [194]. Oxygen incorporation at the level of 10-25 at.% does not necessarily result in a significant change, let alone degradation, in the optical performance of the aged absorber.

However, given enough time (here above 150 to 400h), cumulative aging seems to provoke another stage of aging where the optical performance of the coatings, especially thermal emittance, is degraded by the appearance of defects on their surface. These defects can be purely physical, such as local cracks or delamination, probably resulting from thermomechanical phenomena induced by thermal expansion and repeated thermal cycling (e.g. for the TiAlN and W/SiCH absorbers) [242]. They can also result from chemical changes, e.g. for the WAlSiN absorber highly-oxidized asperities develop on the surface over time. Due to their size, these defects increase the absorption/emission of radiation in the IR region.

For some absorber coatings, the beneficial effect of the curing step is not retained with further aging, again demonstrating that tests for longer durations than the first few hours are absolutely necessary to conclude on the stability of an absorber coating, although many authors claim the thermal stability for their absorber coatings after short durations, sometimes as short as 2h.

In addition, our suggested aging protocol, exposed in Chapter 3 (section 3.1 p.102), is based on the trends observed in this chapter so far. First, the thermal stability is studied for a duration of typically 100h, to be able in most cases to observe sufficient changes on the absorber microstructure and composition – although the examples of the TiAlN and WAlSiN absorbers emphasize that a deterioration may still eventually appear if tests are continued for longer durations at the same temperature. Depending on its aging behavior up to 100h, the absorber can reasonably be further tested or disqualified.

These further tests can be performed for longer durations at the same temperature, close to the aimed working temperature in the CSP applications; or an accelerated aging protocol can be applied at higher temperatures (see Chapter 2 section 4.1.2, p.75), also called “accelerated temperatures”. The interest of such protocols is that it avoids testing for very long durations at the working temperature (e.g. 1000h), as applying higher temperatures supposedly accelerates aging phenomena without changing their nature. This topic will be discussed in the following section.

4. Thermal aging for long durations at accelerated temperatures in air

The TiAlN absorber has demonstrated its good thermal and optical stability for long durations up to 1000h at 500°C in air with a small variation of the optical properties after the high amount of hours. Thus, this absorber type was selected to apply and evaluate a classical accelerated aging protocol. Several equivalent samples of the TiAlN absorber series 1616 were thermally aged for long durations (200 to 450h) in air at different accelerated temperatures from 600°C to 800°C.

The selected temperatures were 600°C, 630°C, 660°C and 690°C, to obtain a lifetime prediction from the accelerated aging tests according to an Arrhenius protocol (see Chapter 2 section 4.1.2.1, p.76). This protocol implies choosing a set of accelerated temperatures in close succession, that are close enough to the aimed working temperature (here 500°C) so that they will provoke similar aging phenomena following an Arrhenius law (e.g. oxidation and diffusion), but high enough so that they will noticeably accelerate them. In addition, tests at even higher temperature of 800°C were also attempted to further explore the coating thermal resistance in air. In all cases, heat treatments with steps of 12 or 24h were applied to follow more precisely the evolution of the samples with aging. Their optical properties were systematically measured after each aging step and material characterization was carried out at intervals.

4.1. Optical properties

Figure 123 shows reflectance spectra measured after aging at the different accelerated temperatures from 600 to 800°C. For clarity’s sake, only some of the aging durations were represented in Figure 123. In all cases, the first step of aging (24h or 40h, in blue) is applied at 500°C, to act as a curing step. Afterwards the accelerated temperature is applied instead. The total number of aging hours seen by the coating takes this first curing step into account. Figure 124 shows the subsequent variations of optical performance (solar absorptance, thermal emittance, heliothermal efficiency and performance criterion at 500°C) for all applied aging durations.

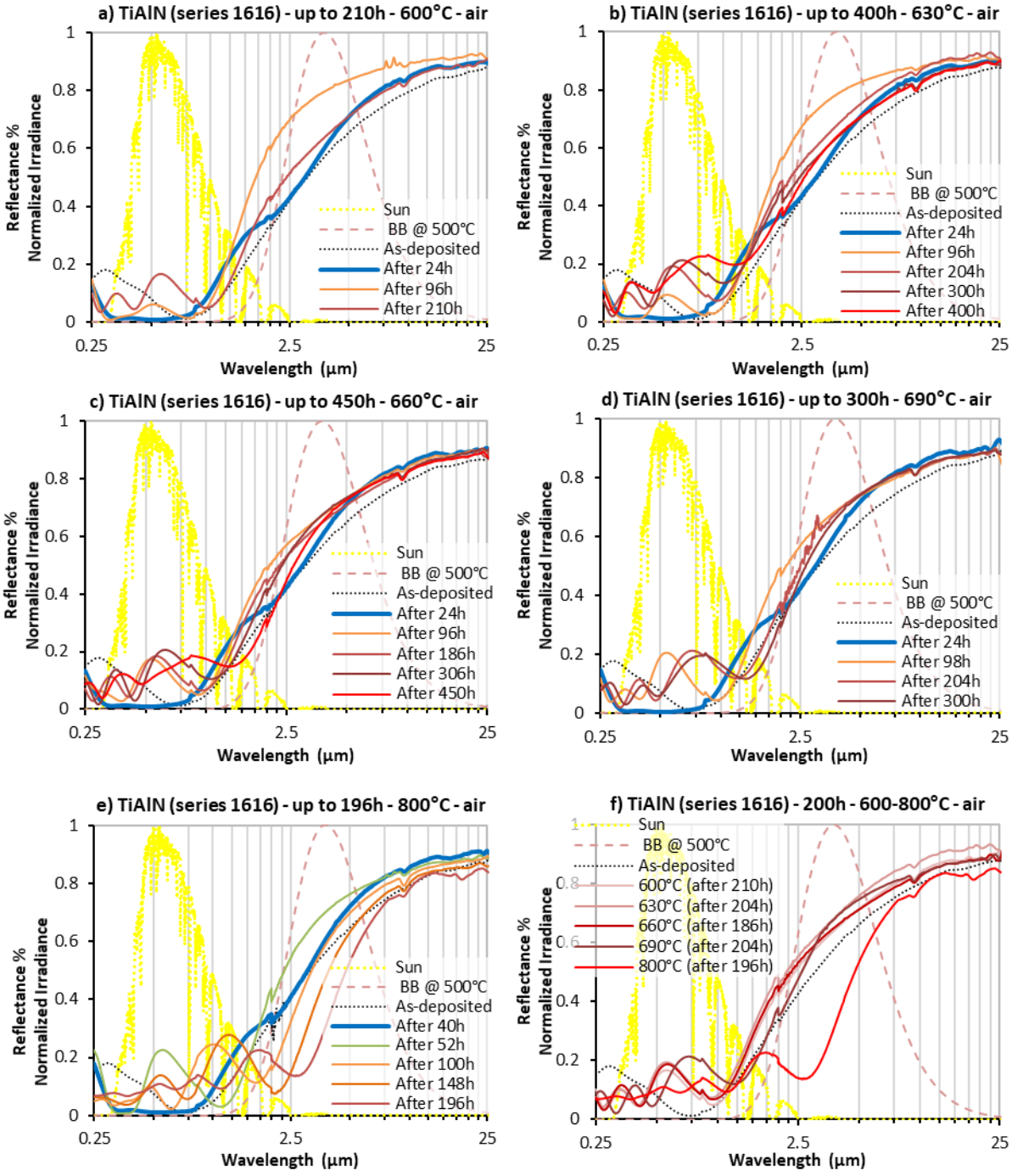

Figure 123. Evolution of the reflectance spectra for the TiAlN absorber aged at different durations and temperatures from 600°C to 800°C in air. The first step of aging (24h or 40h, in blue) is applied at 500°C in air (curing step).

As can be expected, higher variations of reflectance spectra are observed compared to aging tests at 450-500°C (Figure 117 p.139). Whatever the accelerated temperature, the first exposure (up to approx. 100h, light orange in Figure 123) of the samples to a higher temperature than the curing temperature of 500°C (blue in Figure 123) causes a reflectance blue-shift in the IR range beneficial for thermal emittance, as the higher reflectance in the NIR-IR range blocks a larger fraction of the blackbody emission. Thus ε(500°C) decreases by 5 to 17 points, depending on temperature (Figure 124 b)).

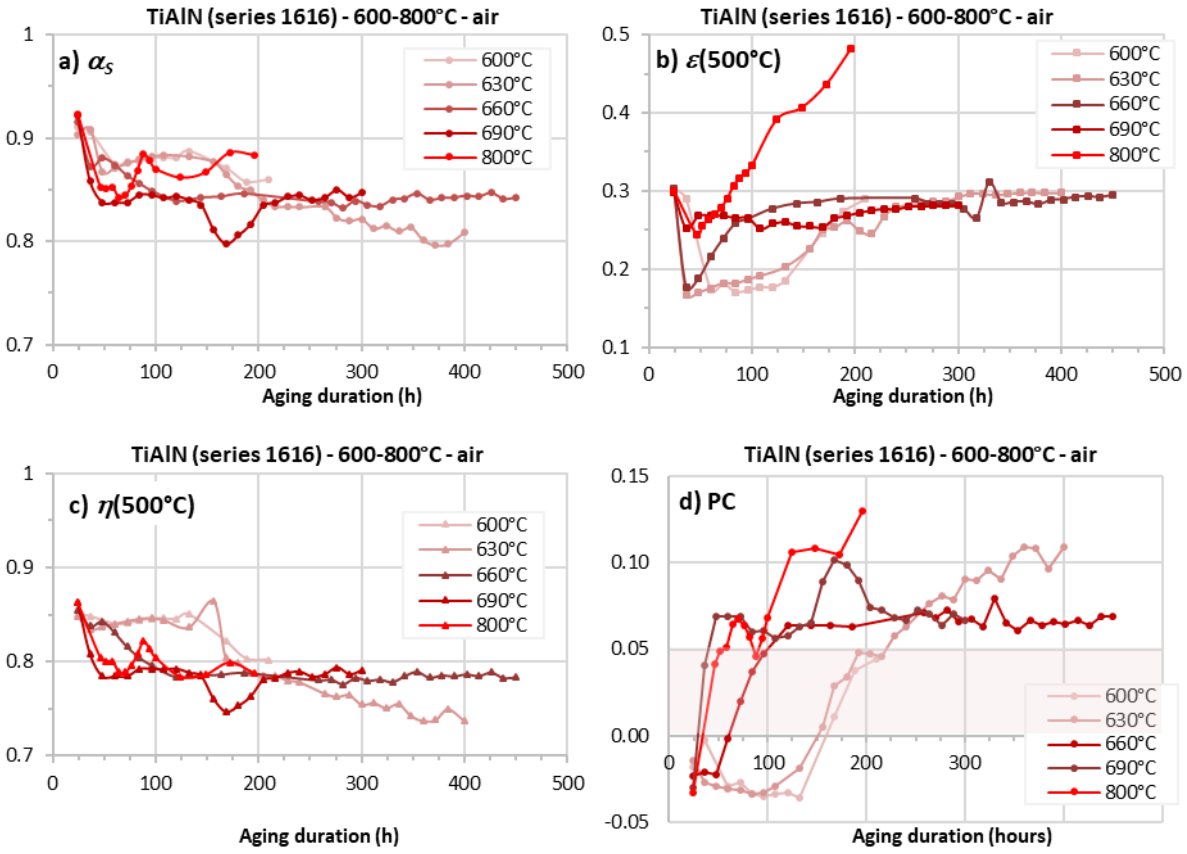

Figure 124. Evolution of optical performance (solar absorptance α_S, thermal emittance ε and heliothermal efficiency η at 500°C, performance criterion PC) with aging at accelerated temperatures in air for up to 450h

The same first evolutions are however detrimental to solar absorptance and heliothermal efficiency, which decrease by up to 9 points (Figure 124 a), c)). Indeed, reflectance tends to increase in the solar range with increasing aging temperature (Figure 123). The observed reflectance oscillations are typical of changes in the coating chemical nature and its subsequent optical behavior, switching from absorptive to semitransparent [194]. The presence of an absorption peak around 9.3 µm [321] indicates that these changes in chemical nature may be due to some level of oxidation.

When increasing the aging duration at a given temperature, the frequency of the UV-Vis oscillations increases, causing the spectra to shift towards higher wavelengths in the whole spectral range. This behavior is typical of an increase in coating thickness [194]. As a consequence, after its first drop, thermal emittance tends to increase again (Figure 124 b)). It reaches its initial value for aging tests up to 690°C then stabilizes, and even strongly exceeds it (+0.18) when aged at 800°C. Meanwhile, solar absorptance mostly stabilizes after its first drop, as the oscillations shift beyond the solar range, so that overall the heliothermal efficiency tends to stabilize or slowly decrease when increasing the aging duration, whatever the accelerated temperature.

When increasing the aging temperature, the amplitude of the reflectance oscillations increases, as clearly visible in Figure 123 f) showing the reflectance spectra of the samples aged for similar durations of approx. 200h at the different temperatures. Figure 125 shows the corresponding optical performance: from 600°C to 690°C, similar decreases of solar absorptance (-0.08 to -0.05) and thermal emittance (-0.09 to -0.06) are observed, while at 800°C there is a strong increase in thermal emittance due to the reflectance red-shift. These results indicate a non-linear relationship between the aging temperature and the deterioration of the absorber, yet they confirm a tendency to accelerate aging when applying higher temperatures.

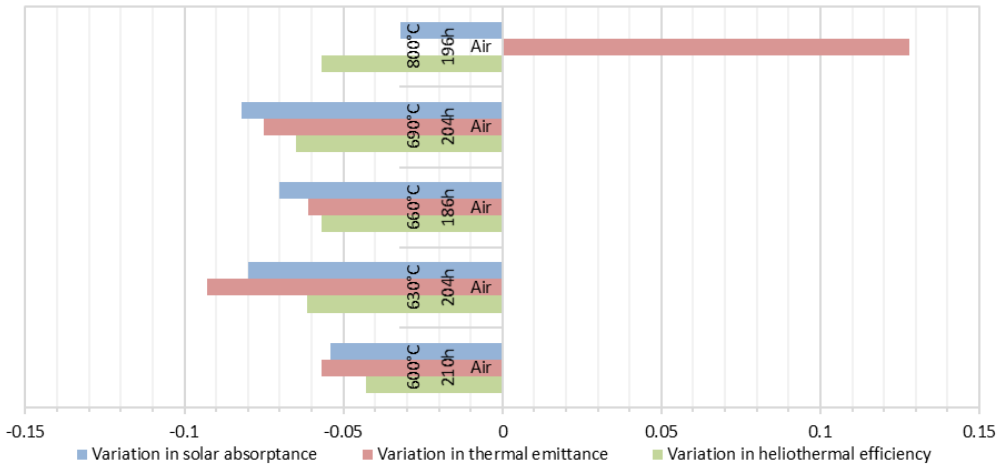

Figure 125. Evolution of optical performance for temperatures from 600°C to 800°C after approx. 200h in air

The acceleration of aging is evidenced by the increase in thermal emittance and performance criterion (PC = $-\Delta\alpha + 0.5\ \Delta\varepsilon$) (Figure 124 b), d)). This increase globally tends to be faster and steeper when increasing the aging temperature. Indeed, at the lowest temperatures (e.g. 630°C), PC remains below 0.05 (the recommended maximal acceptable value before disqualifying the coating) for up to 200h; at 660°C PC exceeds 0.05 after approx. 100h; at 690°C and 800°C, PC is higher than 0.05 before the first 50h of aging. Whatever the aging temperature, the performance criterion increases with time, so that it ends up exceeding the recommended value of 0.05. It is to notice that at the lowest temperatures, PC is negative during the first steps of aging, reflecting the observed decrease in thermal emittance and the corresponding optical improvement.

The surmised changes in chemical nature and increase in thickness of the aged coatings can be linked to the oxidation of the absorber, which was already observed at 500°C (see section 3.3). This point is further discussed in the next section.

4.2. Surface topography, atomic composition

Macroscopic and SEM images of the aged coatings are visible respectively in Table 25 and Table 26 for the different accelerated temperatures and different durations.

To the naked eye (Table 25), the samples rapidly suffer with aging from inhomogeneous changes in color (from dark blue to orange/purple) and aspect (seemingly corrosion spots and stains). SEM images (Table 26) show the appearance of irregularities on the surface. At smaller magnification (scale 200 µm), spots appear on the coating, that are not visible at higher magnification (scale 1-3 µm), indicating that these irregularities have a larger size, in the 10-50 µm range. They may be partly accountable for the visible changes in the aspect of the samples in Table 25.

Table 25. Macroscopic images of TiAlN absorber series 1616 aged in air at accelerated temperatures of 630, 660, 690 and 800°C (to be compared with as-deposited state, Figure 107 p.124)

Aging temp.	Aging duration						
630°C	–	–	–	*After 264h at 630°C* 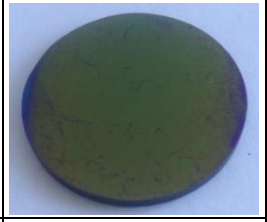	*After 384h at 630°C* 	–	–
660°C	–	–	–	–	*After 366h at 660°C* 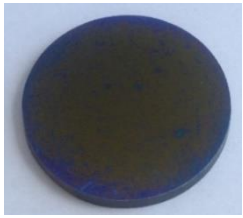	*After 426h at 660°C* 	*After 450h at 660°C* 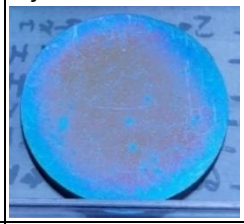
690°C	–	–	*After 156h at 690°C* 	*After 276h at 690°C* 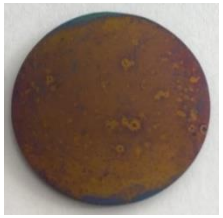	*After 300h at 690°C* 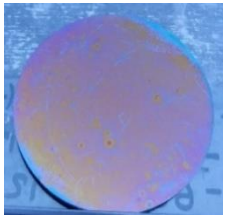	–	–
800°C	*After 88h at 800°C* 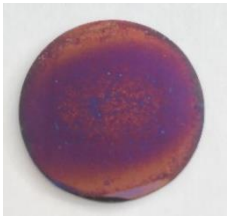	*After 100h at 800°C* 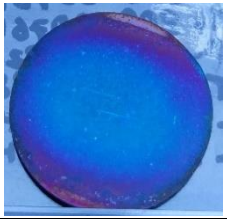	*After 124h at 800°C* 	–	–	–	–

Table 26. SEM images of TiAlN absorber series 1616 aged in air at accelerated temperatures of 630, 660, 690 and 800°C (to be compared with as-deposited state, Figure 108 p.124)

Aging temp.	Aging duration					
				After 288h at 630°C	*After 360h at 630°C*	*After 400h at 630°C*
630°C	–	–	–	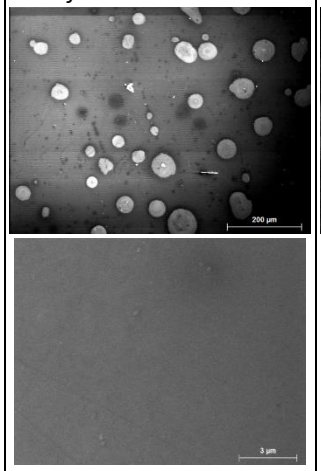	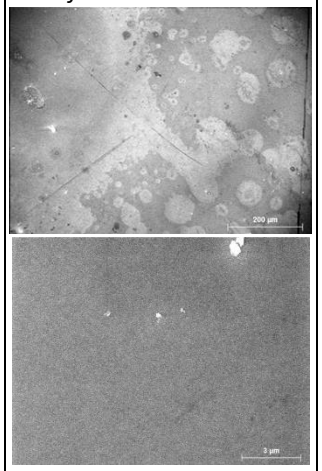	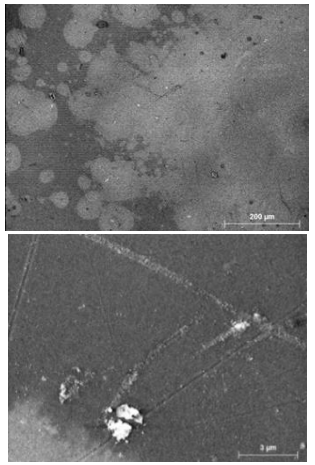
				After 270h at 660°C	*After 390h at 660°C*	*After 450h at 660°C*
660°C	–	–	–	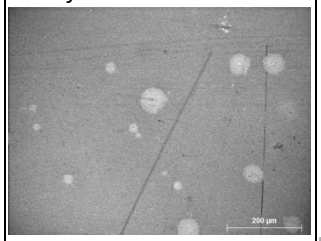	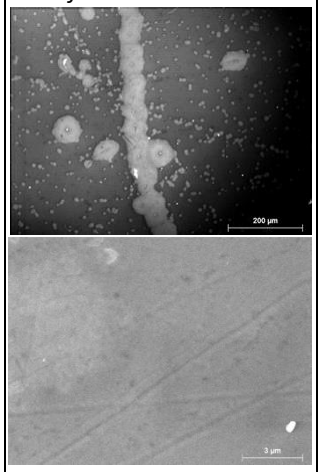	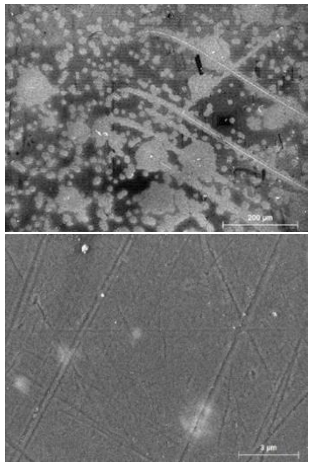

690°C	–	–	*After 180h at 690°C* 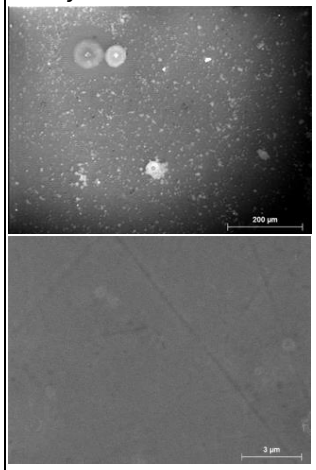	*After 252h at 690°C* 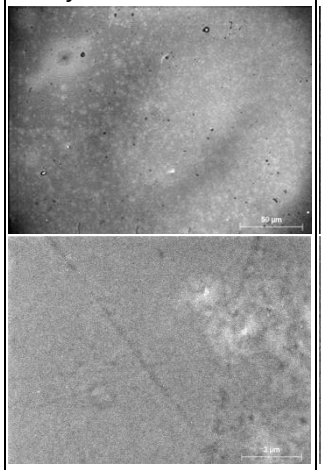	*After 300h at 690°C* 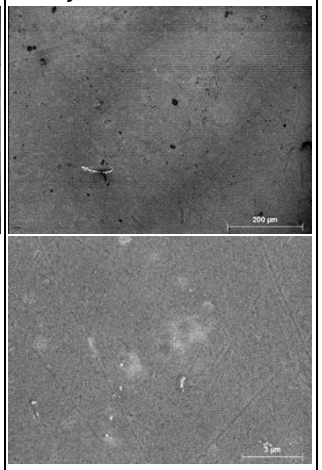	–
800°C	*After 46h at 800°C* 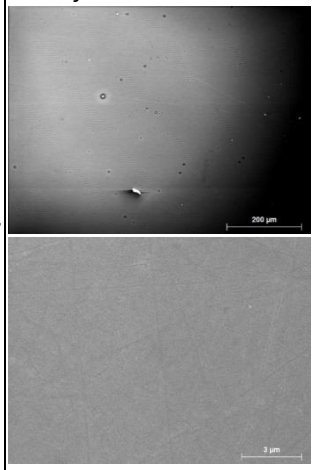	*After 100h at 800°C* 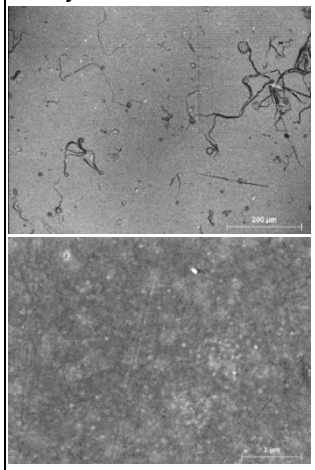	*After 196h at 800°C* 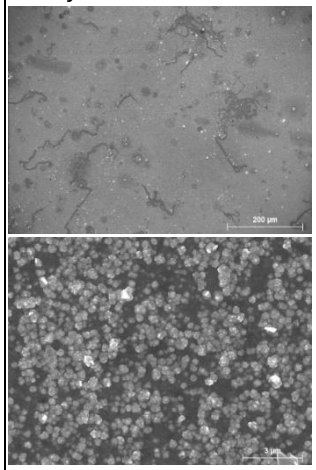	–	–	–

Figure 126 gives a closer look at one of these irregularities on an absorber sample treated at 660°C for 390h, where three areas were analyzed by EDS to obtain their chemical composition. Area 1 represents the main surface of the coating outside of the observed spot (darkest area) while areas 2 and 3 (brightest area) are at the periphery and the center of the spot, respectively.

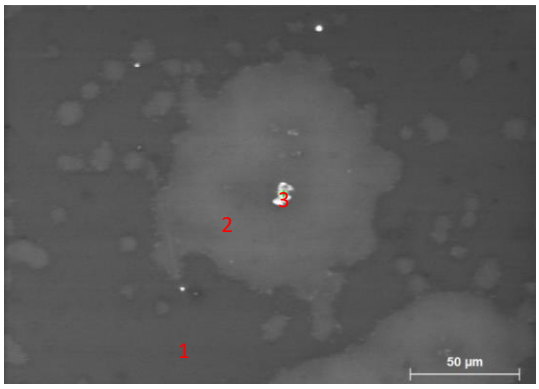

Figure 126. SEM image of an oxide spot that appear with deterioration on the TiAlN absorber.

Figure 127 presents the variation in atomic content, compared to the as-deposited state, of the main elements of the $TiAlN_x/TiAlN_y$/SiNCH coating (O, Si, Al, Ti) and of the Inconel substrate (Ni, Cr, Fe, Nb) for the three areas in Figure 126.

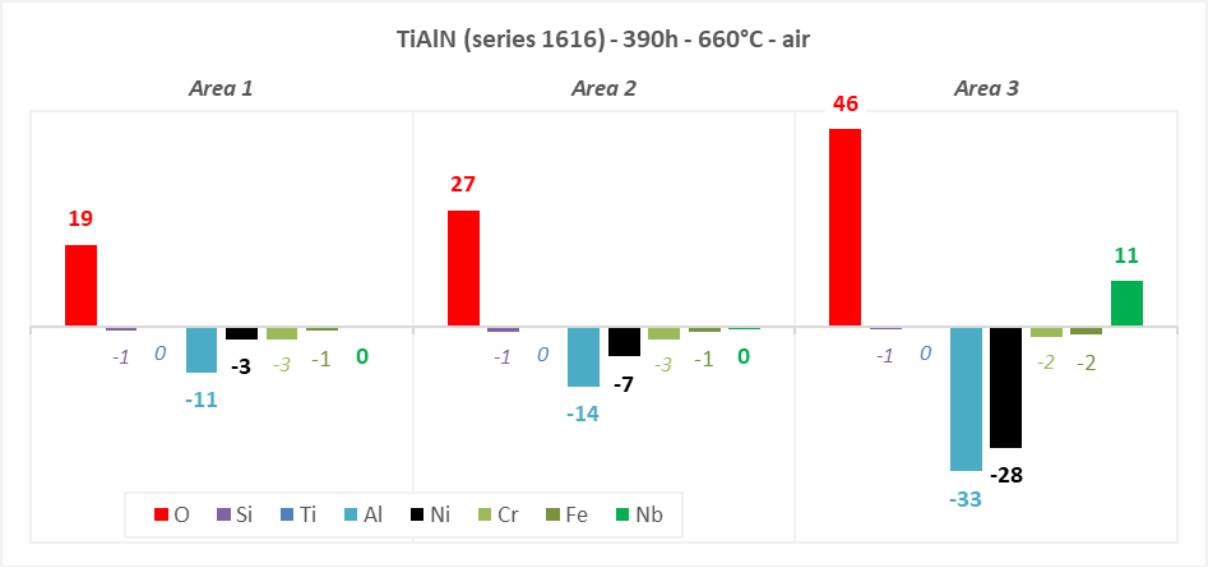

Figure 127. Variation in atomic content (in at.%) for the TiAlN absorber after 390h at 660°C vs. as-deposited state

All areas analyzed on the aged sample present a higher oxygen content than the as-deposited sample, indicating the general oxidation of the sample. The center of the spot (Area 3) has the highest oxygen level (+46 at.% O), more than twice the one detected on the main surface (Area 1, +19 at.% O). Meanwhile, from main surface to center, the detected content in Al decreases (from -11 to -33 at.% Al) while the levels of Ti and Si remain stable.

As for substrate elements, while the contents in Cr and Fe remain stable with a slight tendency to decrease, the content in Ni is clearly lower at the center of the spot, while that of Nb notably increases. These evolutions tend to indicate that the spots appearing at the surface of the aged coatings result from: i) the outward diffusion of substrate elements such as Nb and of coating elements such as Ti, caused by the exposure to high temperatures, and; ii) their oxidation, participating to the growth of an oxide on the sample surface (as inner elements such as Al and Ni are less detected, they are buried deeper into the sample, below its surface).

This hypothesis is supported by EDS analyses over larger areas of the samples showing a significant increase of the oxygen content with increasing temperature and duration (Figure 128), faster than the changes observed at 500°C (Figure 122 p.145). At these higher temperatures, the evolution of the content in oxygen still follows a parabolic law (Eq.(34) p.146), typical of slow and steady oxidation.

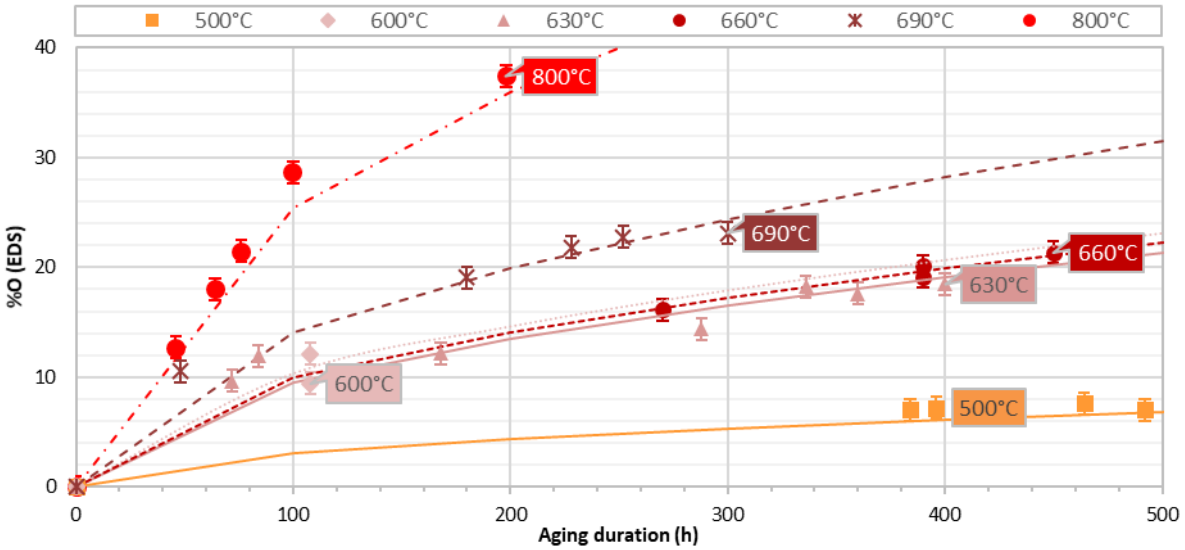

Figure 128. Evolution of at.%O measured by EDS with aging duration at different temperatures

At 800°C the oxidation rather follows a linear tendency at first (< 100h) but then seems to also follow a parabolic law after that, showing similar temperature- and time-dependent oxidation mechanisms at this higher temperature. SEM images of the sample aged at 800°C (Table 26) show that the morphological changes observed at lower temperatures seem to happen at a lower scale, with the appearance of surface asperities at the 100-500 nm scale rather than the 10-50 µm scale, although both seem to be caused by the same oxidation phenomena.

From the EDS results presented in Figure 128, an activation energy for the oxidation phenomena was estimated. First, the parabolic law of oxidation (Eq.(34) p.146) was used to determine the oxidation rate constants $K(T)$ for all accelerated temperatures (600 to 800°C). For this purpose a least-squares method [324] was applied (Eq.(35)): the χ^2 value was minimized using Excel solver, with y_i the experimental at.% O measured by EDS, y the parabolic law (Eq. Eq.(34) p.146) depending on time (aging duration x_i) and K as the parameter to be fitted, σ_i^2 the normally distributed variance of y_i (± 1 at.%) and N the number of experimental points y_i.

$$\chi^2(K) = \sum_{i=1}^{N} \frac{[y_i - y(x_i; K)]^2}{\sigma_i^2} \quad (35)$$

Since oxidation is a temperature-dependent mechanism, the rate constant K depends on temperature and can be expressed using an Arrhenius law (Eq.(22) p.76). The fitted values of $K(T)$ were thus plotted in an Arrhenius plot vs. 1/T to determine by linear regression the activation energy E_a of the oxidation phenomena (Figure 129). E_a is given by the slope of such a plot ($-E_a/R$ with R the gas constant).

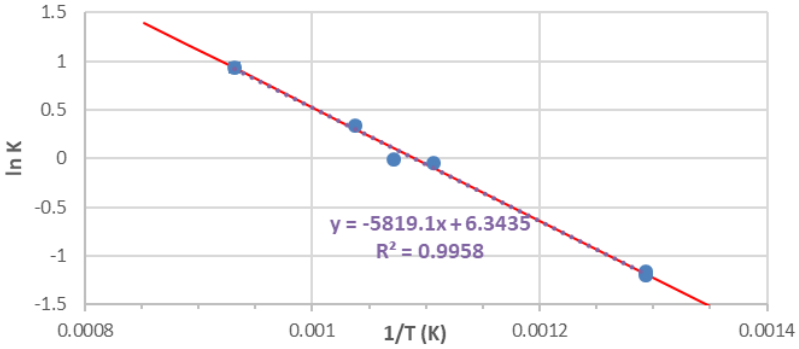

Figure 129. Arrhenius plot of oxidation rate constant *K* vs. temperature *T*

An activation energy of oxidation $E_a \approx 48$ kJ/mol was obtained. This value is low compared to the ones found in the literature for similar TiAlN coatings (e.g. 164 - 376 kJ/mol [325], 136 - 403 kJ/mol [326]). This may confirm that the observed oxidation phenomena do not directly concern the TiAlN absorber layers themselves, but the SiNCH top antireflective layer and/or elements diffusing from the substrate, as previously mentioned. Also, this low activation energy of chemical oxidation is consistent with the slow degradation and stabilization of the optical performance observed when applying accelerated aging (Figure 124). This highlights again that physicochemical changes to the absorber coatings do not necessarily lead to the degradation of their optical properties.

4.3. Lifetime prediction

While such slow and little damaging degradation processes ensure that an absorber coating may be durable, they prevent the application of classical lifetime prediction methods, which are based on the estimation of the activation energy of the optical degradation itself [128,151,327,328]. Indeed, classical lifetime prediction is based on a similar Arrhenius approach as the one presented above, considering the evolution of the optical properties instead of the oxygen content, and deducing an activation energy for the overall degradation in optical performance, leading to the estimation of its yearly decay rate and lifetime (see Chapter 2 section 4.1.2.1) [128,151,327,328]. Contrarily to the above analysis on the oxidation rate, several phenomena may participate in the degradation of optical performance. These phenomena may present different kinetics (rate constants), thus come into play after different aging durations, they may compete or promote one another, etc. They even may not all be thermally-induced phenomena following Arrhenius laws (e.g. formation of cracks). In such cases, it is not possible to obtain a reliable lifetime prediction.

Such is the case for the studied TiAlN absorber. Indeed, the evolution of its optical performance (Figure 124) is not linearly decreasing with time: optical properties first go down then back up and/or stabilize, highlighting that several phenomena occur at different stages of aging. Due to its low activation energy, oxidation is probably one of the first acting phenomena. While this relative resistance to aging is a good hint towards the coating durability, the determination of the activation energy for the optical degradation of this absorber is not possible in this case, thus neither is the prediction of its lifetime.

Moreover, the time scale considered for the estimation of the activation energy influences the determination of the activation energy for optical degradation. For instance Raccurt et al. [151] consider several aging steps, reaching long durations up to 4000h at 450°C and up to 800h at 530°C. In this case however, the time steps between the aging tests are much larger than in our case, 200h to 1000h vs. 24h here. Therefore, it is possible that transitory aging phenomena are detected in our case, that may not have been visible when larger time steps are applied. The protocol applied here may be more sensitive in this regard, more susceptible to fluctuations in optical performance, thus preventing lifetime prediction, but more representative and insightful on the coating aging behavior.

4.4. Conclusions on long durations at accelerated temperatures in air

An accelerated aging protocol at temperatures in the 600-800°C range for durations up to 450h in air was applied to samples of the TiAlN absorber, already stable at 500°C. The degradation of its optical performance was not linear with time or temperature, indicating that several aging phenomena may be competing, with different kinetics. The main aging phenomenon was oxidation, following a parabolic law even at accelerated temperatures. A low activation energy was determined for oxidation. This study is a perfect example that lifetime prediction is not necessarily attainable, depending on the architecture and composition of the coating and on its main degradation mechanisms, which may be complex, competing, present different kinetics, or be too slow to really allow for a notable acceleration of aging.

Tests at accelerated temperatures may give valuable insight on the thermal stability of absorber coatings and its limits at high temperature. However, such accelerated aging protocols can be heavy to implement (requiring several equivalent samples to apply at least 3 aging temperatures for long durations), and they cannot guarantee that the observed degradations are representative of phenomena at lower temperatures, or that lifetime prediction will be possible for the tested absorber coatings. Moreover, the lower the activation energy of the aging phenomena, the lower the acceleration factor provided by accelerated aging tests [327] (see Chapter 2 section 4.1.2.1). Therefore if the aging phenomena have low activation energies, the accelerated tests may require too long, or the testing temperature to apply may be too high to cause similar degradation phenomena, compared to the actual working conditions aimed for the absorber coating. Overall, a cost/benefit analysis is thus to consider in the implementation of such accelerated thermal aging protocols.

5. Influence of other aging parameters

5.1. Influence of thermal cycling

Thermal cycling can be a significant source of degradation in real CSP working conditions (see Chapter 2 section 3.3.2.5, p.68). This section attempts to consider the impact of thermal cycling on two types of absorbers.

In PROMES laboratory, two samples of the TiAlN absorber were treated at 500°C in air to reach similar aging durations:

- a sample of series 1616 was exposed to slow thermal cycling, i.e., cumulatively aged from its cured state (after 24h) up to 120h, by steps of 24h, following 4 heating-plateau-cooling cycles with the temperature profile shown in Figure 90 (p.106).
- a sample of series 1830 was exposed to constant thermal aging, i.e., directly aged from its cured state to 124h, in a single heating-plateau-cooling cycle, with the same heating and cooling ramps as the cycled sample.

In a similar manner, two samples of the WAlSiN absorber coating were treated at CSIR-NAL Bangalore laboratory by K. Niranjan [242], at 400°C in air from their as-deposited state:

- one was exposed to 4 heating-plateau-cooling cycles of 50h, to reach 200h of aging;
- the other was exposed to a single cycle to directly reach 200h of aging.

5.1.1. Optical properties

Figure 130 shows the variation of the reflectance spectra measured for both types of absorbers, applying thermal cycling or constant aging ("no cycling"). Table 27 and Figure 131 show the corresponding variations in optical performance for the TiAlN and WAlSiN absorbers, respectively.

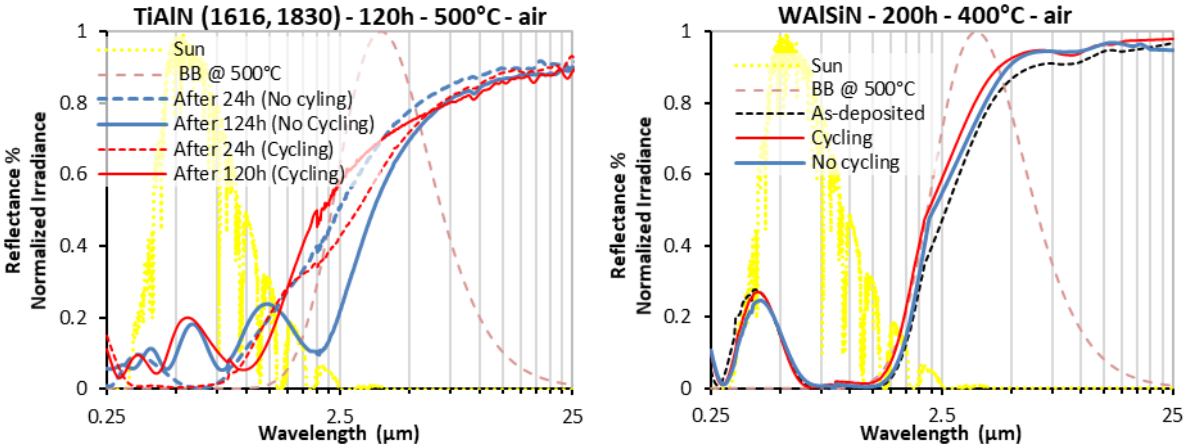

Figure 130. Comparison of the change in reflectance spectrum between cyclic and constant ("no cycling") thermal aging for the two types of absorbers

Table 27. Comparison of optical performance evolution with and without thermal cycling

Absorber	*State*	*Solar absorptance*	*Thermal emittance @ 500°C*	*Heliothermal efficiency @ 500°C*	*PC*
TiAlN Series 1830 *No cycling*	After 24h (cured)	0.906	0.243	0.857	0.092
	After 124h	0.865	0.346	0.797	
	Variation	**-0.041**	**+0.103**	**-0.060**	
TiAlN Series 1616 *Cycling*	After 24h (cured)	0.922	0.298	0.863	0.058
	After 120h	0.844	0.258	0.793	
	Variation	**-0.078**	**-0.040**	**-0.070**	

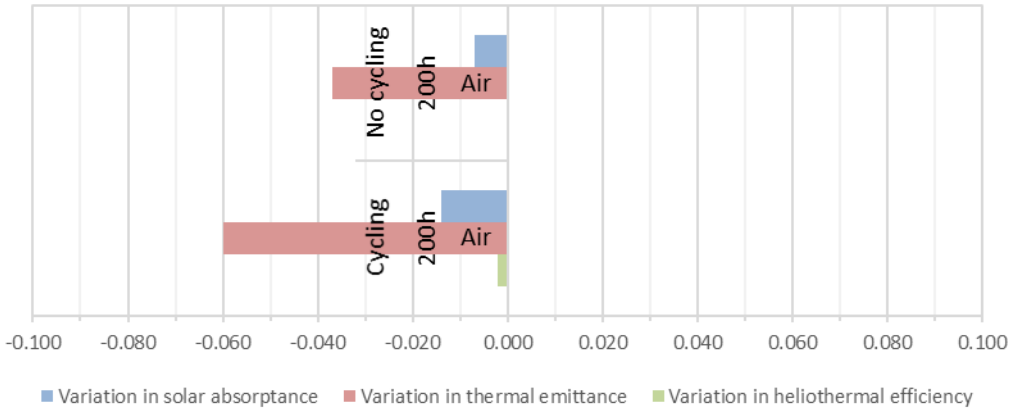

Figure 131. Variation of the optical properties for cycling and non-cycling aging treatments for the WAlSiN absorber

Concerning the TiAlN absorber (Figure 130 left, Table 27), due to a shortage of samples it was not possible to apply these tests on samples of the same series. Series 1830 was received already cured at HEF-IREIS, while series 1616 was cured at PROMES laboratory. Therefore, the reflectance of the two considered samples is different even just after the curing step (24h). It is thus difficult to directly compare their reflectance spectra. Comparing the cured and aged state for each sample, strong oscillations appear after aging in both cases, typical of the changes in composition and thickness

brought on by the oxidation of the coating, as previously discussed. Consequently, reflectance increases in the solar range and shifts towards the IR range.

It seems that the sample treated without cycling (in blue) suffers from a higher variation of reflectance and a larger red-shift, notably increasing its thermal emittance (+0.10), compared to the cycled sample which contrarily presents a drop in emittance (-0.04). Consequently, the performance criterion PC is higher for the sample without cycling (0.09 vs. 0.06), indicating a higher degradation. Reflectance in the solar range is however less affected for the sample without cycling, leading to lower decreases in solar absorptance (-0.04 without vs. -0.08 with cycling) and heliothermal efficiency (-0.06 without vs. -0.07 with cycling) than for the cycled sample.

Concerning the WAlSiN absorber (Figure 130 right, Figure 131), only a small variation of the reflectance spectrum is observed between the cycled and non-cycled samples. Thermal emittance seems to be the most affected, with a larger drop for the cycled sample (-0.06 vs. 0.04). The same goes for solar absorptance to a lesser extent, so that there is no notable change in heliothermal efficiency.

5.1.2. Discussion and preliminary conclusions on thermal cycling

Overall, this study does not show a clear evidence of the impact of slow thermal cycling during aging treatments. On one hand, the considered TiAlN samples may present some initial differences: slightly different architectures (series 1616 has two additional sublayers), different curing facility; so they were hard to compare directly. It is possible that the repeated slow cycles allow the coating to accommodate better to aging, in terms of chemical composition and layer densification, compared to a direct exposure to longer durations. This would explain why a larger degradation is observed without cycling. This could however just be due to the fact that series 1616 is more stable than series 1830 due to its sublayers. On the other hand, the changes observed for the WAlSiN absorber remain very small and may only be due to the method for calculating the optical properties, as previously discussed. In fact, direct measurements of solar absorptance and thermal emittance at CSIR-NAL did not evidence any optical performance changes [242]. Therefore, to conclude on the impact of thermal cycling, a higher number of cycles would need to be applied on truly equivalent samples.

In any case, the tests proposed here, however inconclusive, amounted to applying thermal cycling with a period close to 24h, thus approximating day/night cycles in real CSP working conditions. Thus this type of cyclic test should always be preferred to applying constant thermal loads for long durations. Although highly relevant to the topic, the question of the impact of slow thermal cycling when applying long duration thermal aging tests is too rarely considered in the literature on absorber coatings. This section is thus meant to alert on the importance of conducting thermal cycling tests to predict the performance of absorber coatings, as it can infer damaging thermal stresses produced by the repeated temperature gradients through the coatings.

5.2. Influence of atmosphere during thermal aging

At CSIR-NAL laboratory, equivalent samples of the WAlSiN absorber were aged at 500°C, in vacuum for up to 200h and in air for up to 100h [242]. To study the influence of the atmosphere seen by the absorber coatings during aging, a “vacuum vs. air” comparison of the variations in reflectance (Figure 132) and optical performance (Figure 133) is attempted here. This comparison may allow us to decorrelate the influence of high temperature alone from that of the presence of oxygen during thermal aging. Ambient oxygen is indeed suspected to be the main cause for the absorber thermally-induced oxidation, and often its subsequent optical degradation.

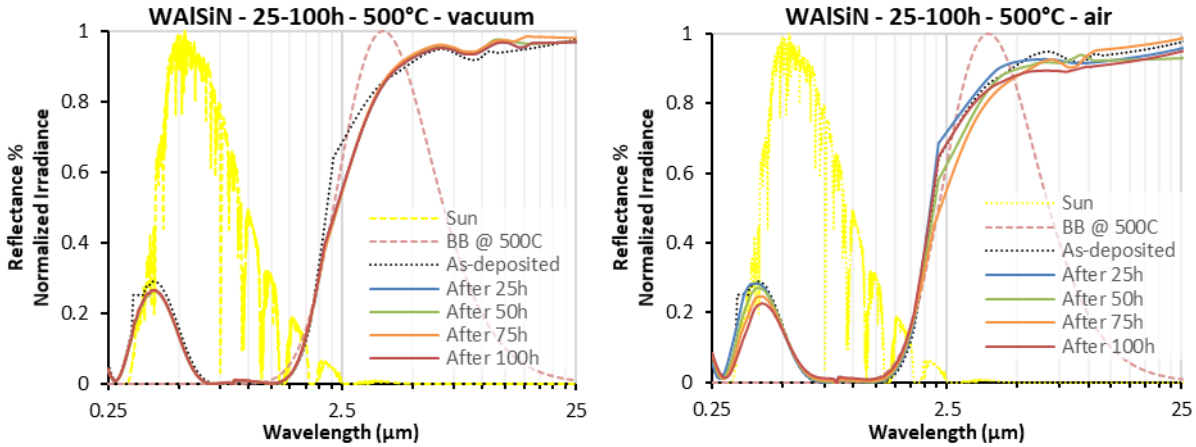

Figure 132. Variation in spectral reflectance of WAlSiN absorber with aging at 500°C in vacuum (left) and air (right) for different durations (25-100h)

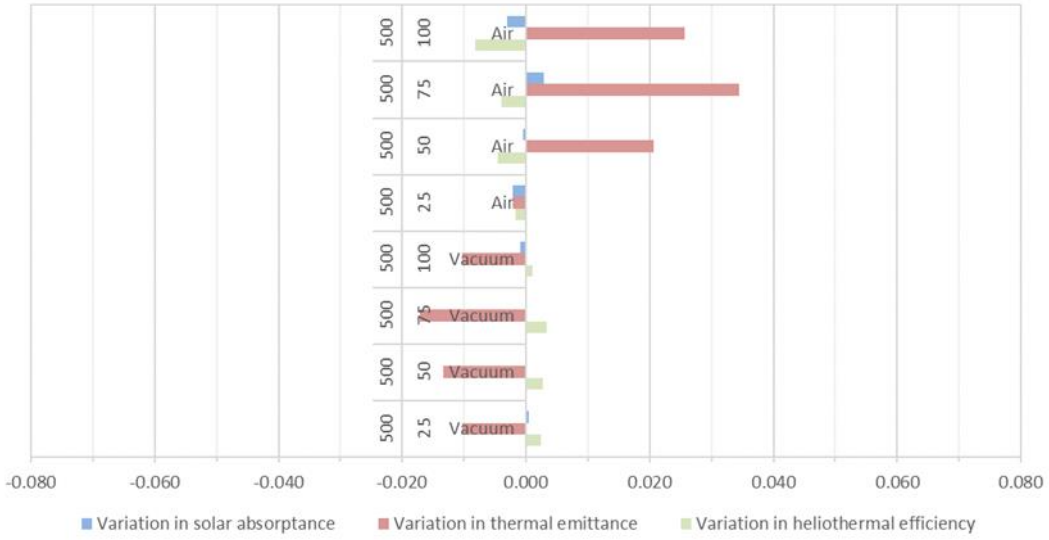

Figure 133. Variation in optical performance of WAlSiN absorber with aging at 500°C in air and vacuum for different durations (25-100h). *N.B. First number is aging temperature in °C and second number is aging duration in h.*

When heat-treating the absorber sample in vacuum, only a minor evolution in the IR reflectance can be observed, causing thermal emittance to slightly decrease (-0.01). Meanwhile, in air the evolution in reflectance is more visible, with a small decrease in reflectance both in the UV-Vis and IR regions. Solar absorptance (and consequently heliothermal efficiency) is barely affected by these evolutions in reflectance as they occur outside of the maximum solar irradiance range (450-700 nm), but they cause thermal emittance to increase (+0.02-0.03).

In this example, the influence of the presence of air during thermal aging is visible but not remarkable, indicating that oxygen does not play a major role in the absorber optical evolution in the considered test conditions. However, since the WAlSiN absorber showed more notable changes when aged at 450°C in air for up to 200h (Figure 117 d) and Figure 118 p.139), it is possible that the differences between vacuum and air tests would be more visible after a longer aging duration. The experiments considered here were not initially designed for the specific purpose of directly comparing the influence of air vs. vacuum, hence tests in air were applied up to a temperature of 500°C and for up to 100h, while tests in vacuum started at 500°C and reached up to 700°C. To complete this study, it would be interesting to carry out aging tests in both vacuum and air at several identical temperatures and longer durations.

In addition the spectral reflectance (Figure 134) and optical performance (Figure 135) of WAlSiN absorber coatings was also compared after aging in air at 400°C and in vacuum at 700°C for up to 200h. Great similarities are observed for the two cases: reflectance slightly varies in the UV-Vis range, resulting in a small drop in solar absorptance (-0.01 at 400°C in air vs. -0.02 at 700°C in vacuum); reflectance is more notably blue-shifted in the IR range, causing a larger drop in thermal emittance (-0.06 at 400°C in air vs. -0.04/-0.07 at 700°C in vacuum).

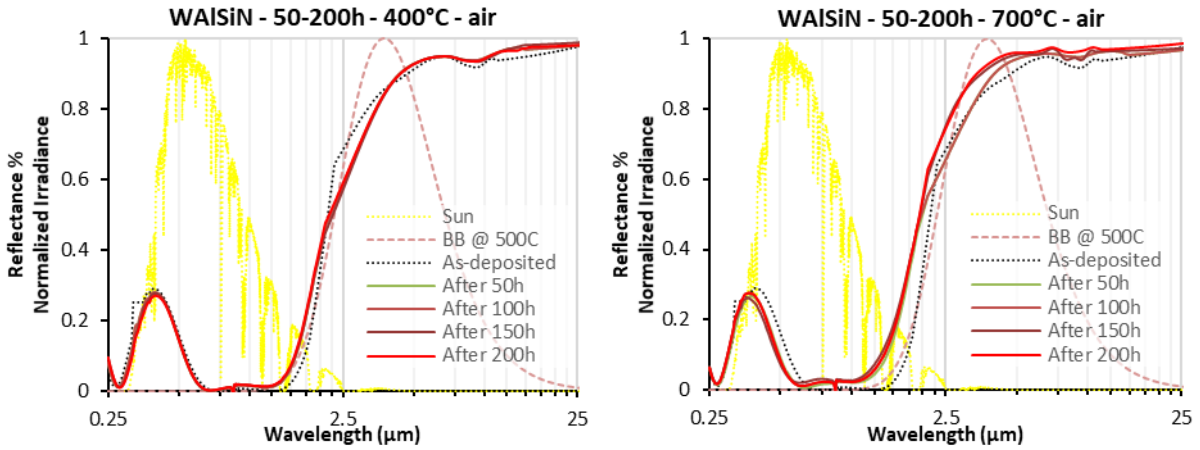

Figure 134. Variations in spectral reflectance of WAlSiN absorber aged at 400°C in air (left) and 700°C in vacuum (right) for up to 200h

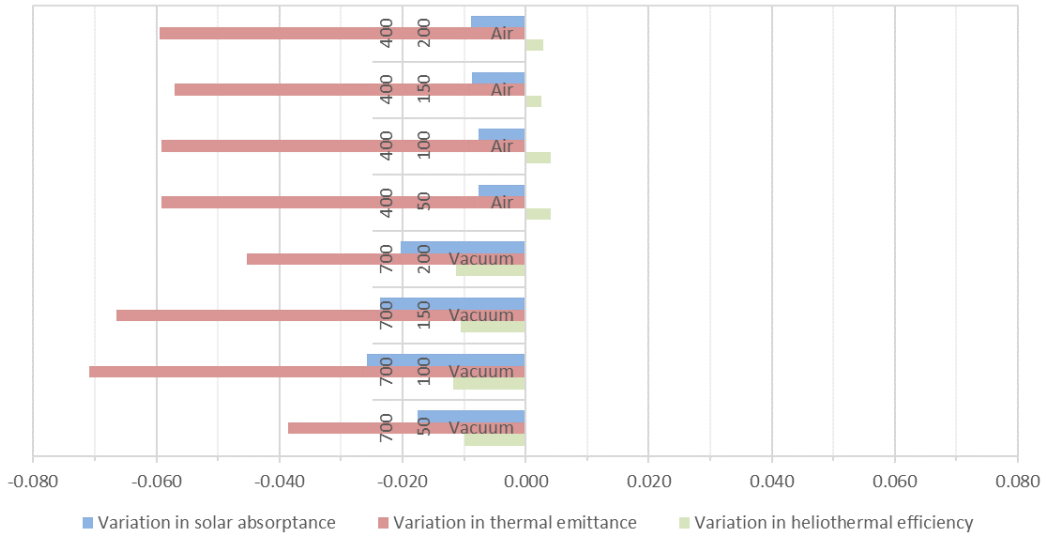

Figure 135. Variations in optical performance of WAlSiN absorber aged at 400°C in air and 700°C in vacuum for up to 200h

This equivalent degradation illustrates that thermally-induced phenomena other than oxidation in the presence of ambient air, e.g. coating densification or atomic diffusion, can result in similar optical degradations. Since they appear at higher temperature (700°C in vacuum vs. 400°C in air), their activation energies are lower than that of oxidation. The presence of ambient air during thermal aging, and the resulting thermally-induced oxidation, thus acts as an acceleration factor for optical degradation. As a consequence, the thermal stability in vacuum is often far higher than in atmospheric conditions, and the critical temperature greatly increases in vacuum. This is why in some CSP technologies such as parabolic troughs, the receiver is evacuated (i.e., the absorber surface works in vacuum instead of air) in order to protect the absorber from oxidation during its lifetime, especially at high temperatures.

In any case, the comparison of vacuum vs. air thermal aging tests, i.e., with and without ambient oxygen, gives valuable insight on the materials aging mechanisms and should be studied by coating developers whenever possible.

Potentially, other elements in the aging (and working) atmosphere can also act as accelerants for the optical degradation of the coating, e.g. water vapor, pollutants, salt sprays, etc. (see Chapter 2). Such experimental work went beyond the scope of this thesis. Preliminary studies were only started regarding the influence of water vapor (thermal aging in ambient air vs. air filtered from H_2O and CO_2).

6. Conclusions on purely thermal aging protocols

Overall, the experimental studies on purely thermal aging presented in this chapter led to the following conclusions and recommendations for coating developers.

Firstly, before studying the aging behavior of a type of absorber coating, the necessary first step is to verify the **equivalence** between the considered samples that will be used in aging protocols. This serves not only to provide an enhanced comparability between the different aging studies, but also to check the repeatability of the coating manufacturing process, especially when working with R&D deposition machines. In any case, the variation in optical performance with aging should always be considered relatively to the as-deposited state of a given sample (e.g. $\Delta\alpha_S$ = α_S (aged) – α_S (as-deposited)).

The second step is to apply **short duration thermal aging** (typically up to 24h) after fabrication to quickly assess the thermal stability of the investigated absorber, at different temperatures around or above the aimed working temperature, and in a relevant atmosphere (ambient air, vacuum, etc.), both depending on the intended CSP technology. This type of test gives valuable indications of the aging behavior of the absorber, such as its **critical temperature** (highest temperature sustainable by the coating without notable degradation), that help define further aging tests. As their duration is short, these tests often have limited impact and can either slightly improve or degrade the absorber. When an improvement is observed, it can be due to a densification of the constitutive layers of the coating and/or, if the aging is applied in air, to the formation of oxides. Both may tune the coating optical properties to provide a better accommodation of the incident solar light. In this case, short duration tests amount to **curing** and can be considered as the final step of the manufacturing process, typically with a duration up to 24h to ensure a stabilization of the coating microstructure.

Valuable as they may be, short duration tests alone are not sufficient to conclude on the durability of the absorber coating. It is thus important to check if the coating observed behavior remains constant with time, especially at its working temperature.

The third step is to apply **longer duration thermal aging around the aimed working temperature**.

- Preferably, **short steps** of 12 to 24h should be applied cumulatively on the same samples, to better follow the evolution of the coating optical performance, and because such **cumulative aging** amounts to thermal cycling with low period and reduced heating/cooling ramps, close to the day/night cycles in CSP applications. In fact, constant heat treatments for long durations may give rise to different aging behaviors, at the risk of not being representative of real working conditions. It is even possible that slow thermal cycling gives occasion to the materials accommodate and stabilize their microstructure between cycles (possibly during the natural cooling phases) and become more resistant to further aging.

- Total aging durations should reach at least **several hundreds of hours**. Indeed, different aging phenomena with different kinetics may be at play, resulting in **different stages of aging**. For instance when aging in air, oxidation may be the first and main aging phenomenon in the first steps of aging. Then oxygen incorporation slows down due to the formation of a stable oxide (following a classical parabolic law of oxidation with $\sqrt{t}$). As a consequence, the optical performance is most changed during the first hours of aging, sometimes positively, then tends to stabilize. Later on, typically above 100h of aging, other phenomena may appear, such as surface defects generated by the slow outward atomic diffusion and surface oxidation of elements (usually metals) from the substrate or from underlayers of the absorber coating. Due to their size in the micrometric range, these defects particularly affect thermal emittance, increasing the absorption/emission of radiation in the IR region and degrading the selectivity.

- Considering the aging phenomena involved, comparing the **effect of different aging atmospheres** can be of interest. For instance, vacuum vs. air tests allow comparing the effect of temperature with or without the presence of ambient oxygen, and thus decorrelate concomitant aging phenomena such as oxidation and atomic diffusion. Such tests reveal that ambient oxygen is clearly the strongest degradation source at high temperature, as the coating critical temperature tends to sharply increase when applying aging under vacuum (e.g. 400°C in air vs. 700°C in vacuum for the WAlSiN absorber).

In any case, this specific study emphasizes the importance of applying long duration aging tests of at least several hundreds of hours at working temperature in order to draw more pertinent conclusions on the long-term thermal stability of absorber coatings.

The expected lifetime of absorber coatings and the solar receivers they cover is typically 25 years (i.e., 73,000h for 8h/day operation). Therefore, to really evaluate their durability in working conditions, aging tests of the absorber coatings at working temperature should ideally be continued for thousands and thousands of hours. To save time and resources, and avoid testing for very long durations, another possibility is to apply long duration aging at **accelerated temperatures higher than the aimed working temperature**. This type of aging protocol allows accelerating the thermally-induced aging phenomena (following Arrhenius laws) without denaturing them, provided the accelerated temperature is not too high, typically no more than 200-300°C higher than the working temperature. Our experimental results validated that **higher and faster evolutions** of the coatings optical performance and microstructure can occur at accelerated temperatures, following at least some of the same aging phenomena as observed at working temperature (e.g. the formation of stable oxide(s)).

Applying aging at several close accelerated temperatures also allows determining the **activation energy** of degradation phenomena. Such activation energy can sometimes be used to predict the lifetime of the coating, based on the estimation of an acceleration factor. The higher the activation energy, the higher the rate constant for the degradation reactions (e.g. oxidation, atomic diffusion), the quicker the aging phenomenon and the more it is accelerated by applying higher temperatures. Therefore it can happen, as observed for the TiAlN absorber, that the activation energy of the degradation phenomenon is so low (e.g. 48 kJ/mol) that a significant acceleration of aging is not attainable using accelerated aging protocols. In such case, it is still necessary to apply very long durations (e.g. > 1000h) to be able to establish the **lifetime and durability** of the absorber coating, demonstrating the limitations of such accelerated aging protocols.

All these aging protocols are found in the literature, although most authors only apply some of them, usually short duration thermal aging at different temperatures, during the development stage of their coatings. Thermal aging tests give access to valuable insight on the behavior of absorber coatings with time, temperature, atmosphere, etc. However, they are based on **purely thermal heating via IR radiation from an electrical furnace**, for practical reasons, as the latter can guarantee long-term, stable, controlled and repeatable aging tests.

Meanwhile, **in real CSP applications, aging conditions are quite different**. The energy that can provoke thermally-induced phenomena is provided by concentrated solar radiation instead of IR radiation, with more energetic photons including UV, and much steeper heating ramps. The receiver is heated on the front (coated) side of the solar receivers, and partly extracted on their rear side by the flow of the heat transfer fluid to be heated, creating large thermal gradients and steeper cooling ramps. Steeper heating/cooling ramps amount to rapid thermal cycling with high amplitude and short period. In order to attempt more representative aging tests and draw a comparison with more classical thermal aging, the next chapter will therefore focus on original aging protocols, closer to the CSP applications, using a unique concentrated solar aging facility developed at PROMES-CNRS laboratory.

Chapter 5 - Implementation and critical analysis of solar aging protocols

Applying thermal aging alone is not enough for a complete analysis of the aging behavior of the absorber related to its application in CSP technologies, especially considering the absence of concentrated solar radiation during the aging treatment, compared to real CSP conditions. Therefore, after the study of the thermal behavior of the absorber in Chapter 4, this chapter will study how the absorbers behave under concentrated solar radiation. Since the latter is also indissociably a heating source for the materials, this type of aging is considered as "solar + thermal" aging, to be compared to purely thermal aging discussed in Chapter 4.

For this purpose, the Solar Accelerated Aging Facility (SAAF) described in Chapter 3 will be used to apply aging on some of the previously considered absorber coatings. First, some limitations and necessary adaptations of the facility for the present study will be presented. In addition to the exposure to concentrated solar radiation, the SAAF also allows applying thermal shocks and rapid thermal cycling, simulating representative CSP receiver conditions. The impact of all these sources of degradation will be studied in this chapter. Based on the results, the necessity of including solar aging in the global aging strategies of absorber coatings, in addition to purely thermal aging, will be discussed.

1. Adaptation of the solar aging facility (SAAF)

The principle of the SAAF facility is detailed in Chapter 3 (section 3.2.2 p.107). This facility was designed and developed in previous work [36,267,268,317,329]. It was further adapted during this thesis to provide a better performance when testing new types of solar selective absorber coatings. The main technical limitations related to our cases of study were identified and solutions were proposed to these limitations, as presented in the following.

1.1. Constraints due to the dimensions of available samples

The samples provided by the different manufacturers presented various shapes, sizes and thicknesses (see Chapter 4 section 1 p.119), that were not all adapted to our existing aging and measurement facilities. These constraints were addressed as explained below.

1.1.1. Compatibility between samples and supports

As mentioned in Chapter 3, different supports to maintain the samples during the solar aging tests were developed in previous work, depending on the shape and dimensions of the samples to be treated at the time (see Table 10 p.111).

Supports 2 and 3 were designed to provide backside air cooling of the sample, to better control and stabilize its temperature during solar exposure. However, for these supports there are specific size requirements: the tested samples must have a square shape, with dimensions of 30 x 30 mm^2 for support 2 and 50 x 50 mm^2 for support 3. As airtightness must be guaranteed, the performance of the backside air cooling system is sensitive to small variations in sample shape, especially for support 3 where the sample must be inserted in the holder cavity. Therefore support 3 could only be used in the case of WAlSiN samples with dimensions 30 x 30 x 2-3 mm^3 [330]. In a similar manner, support 2 could only be used for TiAlN absorber samples with dimensions 50 x 50 x 1 mm^3 (stainless steel substrates). However, the low thickness of these samples was problematic as they suffered bending when exposed to solar irradiance, due to high thermomechanical stress between the irradiated area and the non-irradiated area (see section 2.1.1 p.172). From our observations, a minimum thickness of 2 mm is thus required to avoid sample deformation and ensure a precise study of the aging of absorber coatings.

Support 1 is a previous iteration of Support 3 that had been deteriorated. It could thus be used for the testing of round 2" TiAlN samples in our first experimental campaigns, but in that case no backside air cooling could be applied during the tests, making it harder to control and stabilize the sample temperature.

Due to the limitations of the existing supports, a new sample support (support 4) was later designed at PROMES-CNRS by Roger Garcia (Figure 136). The primary objective of this new support was to allow the treatment of samples of various shapes (round, square, rectangular) and sizes (1" to 2"), while ensuring backside air cooling in all cases. The support has a metallic structure with interchangeable top covers adapted to the different sample sizes. The sample is held by ceramic sticks to limit conductive losses. The air cooling system is less efficient than for supports 2 and 3 as the sample is not sealed to the support, but sufficient to control the maximum temperature of the sample during the aging treatment. This support was used for our second experimental campaign. Thermal studies have been carried out considering previous sample supports by considering the heat transfer scheme of this part of the experimental set-up (support + sample). For this new support, the thermal modeling needs to be considered as part of future analysis on this facility.

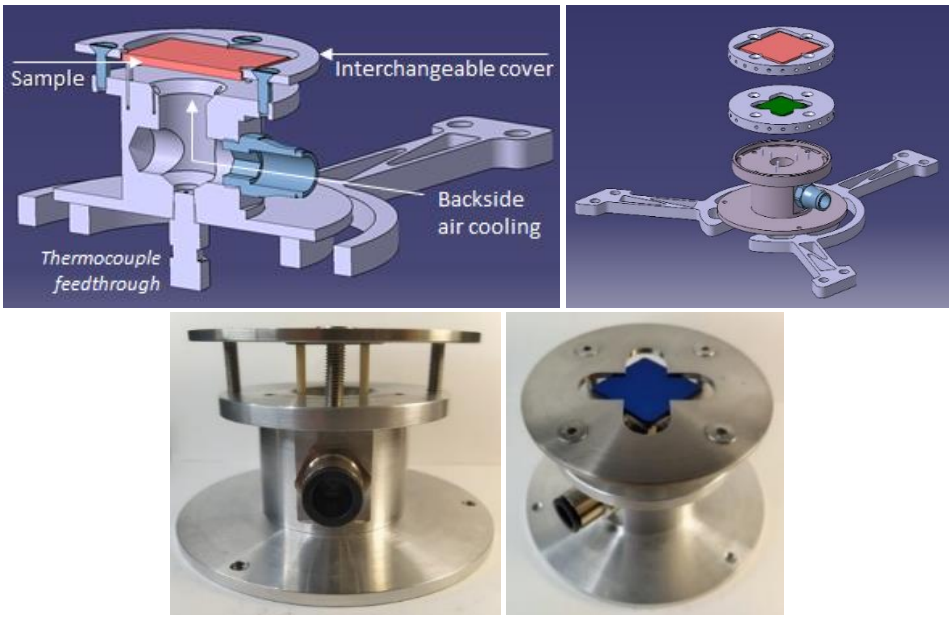

Figure 136. Schematics and pictures of the new sample support configuration (support 4)

1.1.2. Reflectance measurements on aged samples

Normally, once an aging test is completed, the spectral reflectance of the treated sample is measured in the 0.25 - 25 µm using the equipment described in Chapter 3 (section 2.1 p.99), to estimate the optical performance parameters (solar absorptance, thermal emittance, heliothermal efficiency, performance criterion). The IR spectrophotometer (SOC-100 HDR) measures the reflectance from 1.25 to 25 µm. These values are indispensable to estimate thermal emittance.

By design, during a measurement in this apparatus, the sample support (Figure 137, left) must be placed at a specific position: on its left is the reference and along its upper part is the IR source (black body) (see Chapter 3 Figure 84 p.101). Therefore if the sample is larger than the 25 x 25 mm² support, its position is constrained to the right and lower part of the support (Figure 137, right). This is the case for samples treated with SAAF, which are 30 x 30 mm² or 2" in diameter, because the irradiated area is 20 x 20 mm² and the sample must be larger to be properly maintained on the SAAF supports.

Contrarily, to be able to measure the IR reflectance in the central area of the sample, the dimensions of the latter should not exceed 30 mm in diameter (Figure 137, right). Therefore for SAAF-treated samples, the IR reflectance can only be measured on the side of the sample, which is outside of the irradiated central area in most cases (yellow square in Figure 137, right).

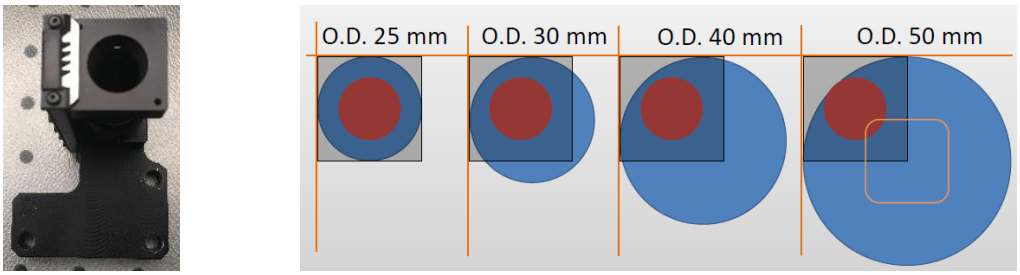

Figure 137. Left: sample support of the SOC-100 HDR IR spectrophotometer. Right: Measured area (red) depending on the diameter (O.D.) of the sample (blue) and its constrained position of the sample support (black). The yellow square represents the irradiated area in the SAAF.

As a preliminary test, reflectance measurements were performed on a solar-aged 2" sample (50.8 mm in diameter), as shown in Figure 138. In area 1 (side), both UV-Vis-NIR and IR reflectance were measured, whereas in area 2 (SAAF-irradiated area) only the UV-Vis-NIR reflectance could be measured because of the abovementioned size constraints in the IR spectrophotometer. No changes in reflectance were observed in area 1 compared to its initial state, whereas in area 2 reflectance was clearly modified by solar aging.

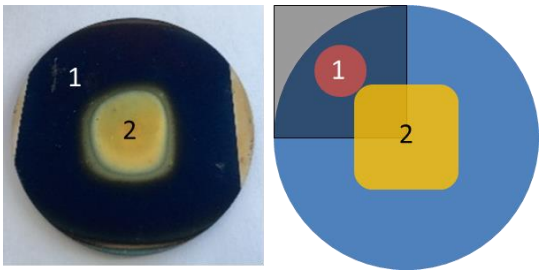

Figure 138. Picture and schematics of a 2" sample irradiated with SAAF in area 2. The red spot is area 1 is the one measured with the IR spectrophotometer.

Therefore, due to these constraints, in most cases the spectral reflectance of the SAAF-treated samples was only measured in the irradiated area using the UV-Vis-NIR spectrophotometer, from 0.25 to 2.5 µm. Solar absorptance can still be calculated in this shortened range, as is often done by coating developers because only one spectrophotometer is needed, although the solar absorptance value calculated in such shortened range is less precise than when considering the whole solar range of 0.28 – 4 µm. Moreover, by design, selective absorber coatings present high reflectance (low absorption) in the NIR-IR range above 1.5 – 2 µm. Thus the value of solar absorptance calculated from reflectance in the 0.25 – 2.5 µm range tends to be overestimated by up to 2 points compared to the solar absorptance calculated in the whole solar range. For this reason, values of solar absorptance presented in this section are not to be directly compared with values presented in the previous chapters, which were calculated using the whole solar range. These overestimated values of solar absorptance are nevertheless useful to study the relative evolution of the aged area at the different stages of aging.

Another solution consists in cutting the sample to be able to measure IR reflectance in the aged area, as shown in Figure 139. However since this is a destructive method, it could only be applied after the last aging step, thus preventing further testing. Thus this solution was only applied to a few samples.

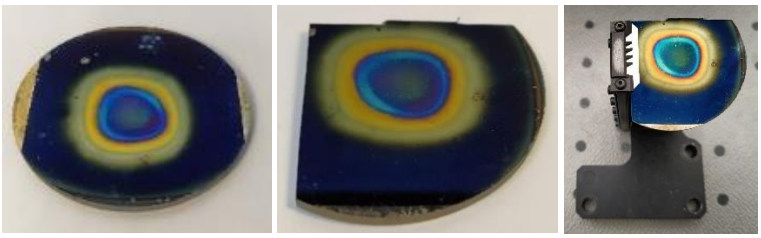

Figure 139. Example of a 2" sample cut for the measurement of reflectance on the aged area

1.2. Temperature measurements on the sample during solar aging

One of the main parameters to follow during the application of aging tests is the temperature of the sample surface. As mentioned in Chapter 3 (section 3.2.2.1.5 p.112), this measurement is done by a pyrometer maintained above the sample, aiming at its surface through the kaleidoscope. With this technique, temperature measurements depend on the surface emittance. Due to the low testing temperatures ($T \leq 500°C$) and low emittance of our samples ($\varepsilon(500°C) < 0.3$) the luminance emitted by our samples is low, so that the signal-to-noise ratio received by the pyrometer from our samples during their irradiation is low. Therefore, pyrometry measurements were not always possible or reliable.

To ensure the measurement of the sample temperature during the aging treatments, the samples or supports were additionally instrumented using K-type thermocouples (TC). Depending on the sample support (see Table 10 p.111) and especially the use of backside air cooling, the temperature of the sample was followed by thermocouples (Figure 140):

- welded on the back center (or back and side) of the sample for support 1 (no backside cooling);
- welded on the front side of the sample for supports 2 and 3 (backside air cooling);
- in contact with the back center of the sample for support 4 (part of the support design).

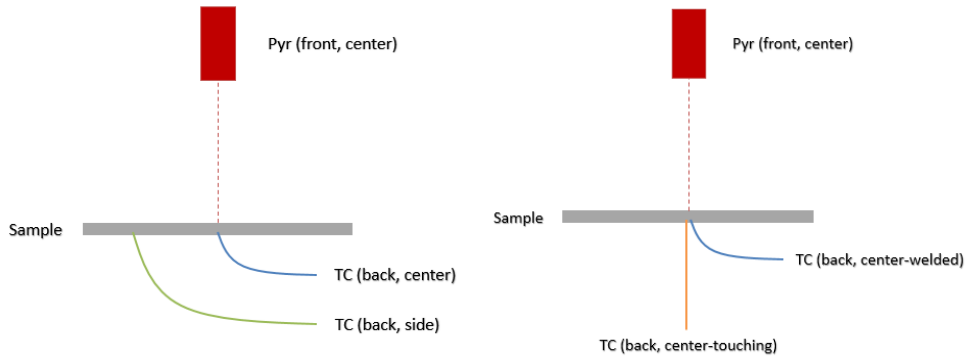

Figure 140. Schematics of sample temperature measurements with SAAF for sample support 1 (left) and 4 (right)

The thermocouples are connected to a Graphtec data logger to record temperature profiles during the experiments. This measurement method can lack reproducibility since there can be fluctuations in the thermocouple positioning, as the thermocouple must be rewelded before every experiment. However, it was used as a complement to pyrometry measurements, especially since the latter do not provide temperature measurement below 250°C.

Typical temperature profiles measured by the pyrometer and the thermocouples can be seen in Figure 141 for supports 1 and 4. For both cases, the back center thermocouple measurement (blue) is consistent with that of the pyrometer on the surface center (red), and is thus considered representative of the sample surface temperature. Measurements on the side of the sample (back or surface) only give a qualitative profile of the temperature variations, as they underestimate the sample temperature by several hundreds of °C. The same goes for the thermocouple touching the center

backside of the sample in support 4 (orange), except that in this case its positioning is more repeatable and a mathematical correlation could be found with the temperature measured by the pyrometer on the sample center front side (Figure 142). In some cases, this correlation could be used for the prediction of the real temperature profile when the pyrometry measurements were not available.

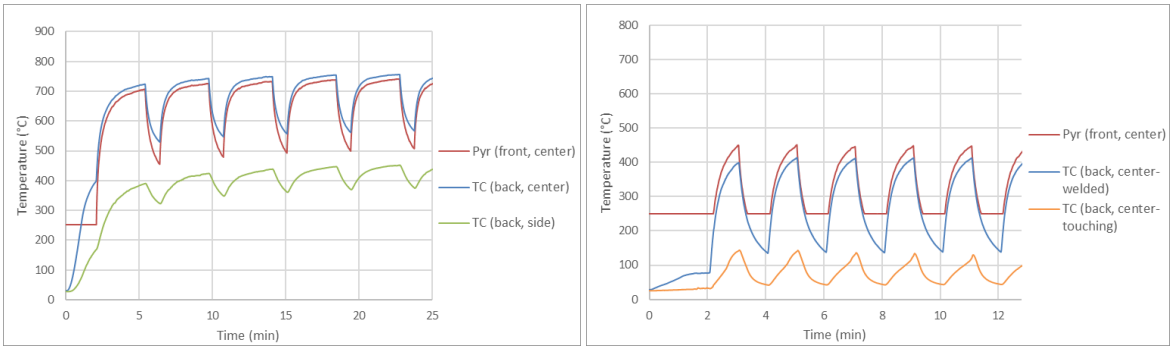

Figure 141. Typical SAAF temperature profiles using support 1 (left) and support 4 (right)

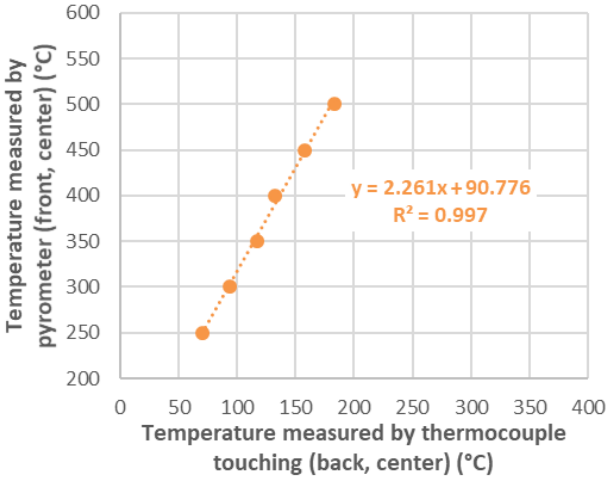

Figure 142. Correlation between temperatures measured by the pyrometer (center, front) and by the thermocouple touching (center, back) of the sample in support 4

2. Comparisons between purely thermal aging and solar aging

A first comparison of the impact of purely thermal aging (Chapter 4) vs. solar aging is attempted in this section, based on the comparison of aging results obtained with ALTHAIA and SAAF facilities. While temperature levels reached by the samples can be close in both types of aging, as explained in the next subsection, their main difference resides in the application of a concentrated solar irradiance on the surface of the sample.

This concentrated solar irradiation can be:

- constant, i.e., at a fixed irradiance (e.g. fixed position of the shutters in SAAF);
- cyclic, i.e., with cycles of high and low irradiance (e.g. two alternating positions of the shutters in SAAF). This amounts to rapid thermal cycling with periods ranging from seconds to minutes, thanks to the high heating/cooling rates.

To isolate as best as possible the additional effect of this irradiation during aging, as a first step the effects of purely thermal aging (ALTHAIA, configuration 1, see Table 11 p.114) and constant solar aging (SAAF, configuration 2) are compared, as defined in the following.

2.1. Main differences between purely thermal aging and solar aging

2.1.1. Temperature profiles

2.1.1.1. Heating and cooling rates

Electrical furnaces such as ALTHAIA are very convenient to apply long-term aging maintaining a very stable temperature profile during the aging treatment. The heating ramps and temperatures of the plateau are easily controlled to the desired values thanks to PID regulation. However, due to their high thermal inertia (as they are made of ceramics), their maximum heating rates are low (e.g. 21°C/min with ALTHAIA, Figure 89 p.105) compared to real CSP conditions, where the sudden exposure to concentrated solar irradiance can lead to high heating ramps for the materials. The only way to obtain a higher heating rate is by introducing the sample directly into the already hot furnace, so the heating rate can reach higher levels (e.g. 73°C/min with ALTHAIA, Figure 89 p.105).

The cooling rate is also determined by the furnace inertia, following a decreasing exponential profile (see Figure 100 p.113). Removing the sample directly from the hot furnace could provide higher cooling rates but it is highly impractical and unsafe. Such heating and cooling rates may be closer to real CSP operating conditions, but this mode of operation can be detrimental to the furnace itself and to the operators. Due to these constraints, the temperature profiles accessible with an electrical furnace can only amount to slow thermal cycling with periods in the range of several hours.

Conversely, solar furnaces such as the SAAF inherently provide more representative CSP conditions, with much higher heating and cooling rates (e.g. ±20°C/s with SAAF, Figure 100 p.113), even when a backside cooling is applied, embodying the heat extraction from the heat transfer fluid in real CSP conditions.

2.1.1.2. Heating duration

Purely thermal aging in electrical furnaces can easily be applied for the desired duration, including very long durations, in a single cycle. Contrarily, due to the intermittence of the solar resource, solar aging tests must be applied cumulatively in different treatments of a few hours at a time, amounting to some level of slow thermal cycling. For this reason, solar aging procedures in solar furnaces under real solar irradiance rarely exceed 100h in total (e.g. between 10 and 20h with SAAF). Long-term “real” solar aging is not possible, which is one of the main drawbacks of this type of aging. This is one of the main reasons why high flux solar simulators have been developed for aging purposes (see Chapter 2 section 4.2.2.2 p.86) to expose the materials for long durations without depending on weather conditions.

2.1.1.3. Temperature fluctuations, effective temperature

During purely thermal aging in electrical furnaces, temperature is well controlled and maintained to the desired level thanks to PID regulation. Due to the natural fluctuations in DNI during the day, in “real” solar aging there can be non-negligible variations in the temperature levels suffered by the solar-aged sample during one of the short aging treatments and/or between these treatments, in the range of ±50-150°C. This is particularly the case if no backside cooling can be applied to the sample during its solar exposure.

Therefore, it is important to monitor the temperature levels suffered by the sample during its consecutive solar aging treatments. For instance, the maximum temperature reached during a test is very relevant to the analysis of the aging behavior of the exposed material. The duration for which the material is subjected to this temperature is also an important factor. Indeed, reaching a high

temperature (e.g. 600°C) during a short overshoot (e.g. 10s) must be less damaging than maintaining a slightly lower temperature (e.g. 550°C) for a much longer duration (e.g. several hours). Therefore, it is also relevant to consider the effective temperature or "time-weighted temperature", considering the time spent at each temperature level. A thermal dose in °C·h can also be estimated by multiplying this effective temperature with the total aging duration.

2.1.1.4. Temperature gradient in the sample

Another major difference with purely thermal aging is the temperature gradient suffered by the irradiated samples, compared to the homogeneous temperature in an electrical furnace. For instance, the temperature distribution seen by an Inconel sample (diameter 50.8 mm, thickness 2 mm) during SAAF treatment was measured, using five thermocouples welded below the sample from its center to its side (Figure 143, right). TC-1 is located at the center and TC-2 to TC-5 are respectively at 6.5 mm, 11.5 mm, 16.5 mm and 21.5 mm from the center. The area irradiated by the concentrated solar flux is ±10 mm from the center (in yellow in Figure 143).

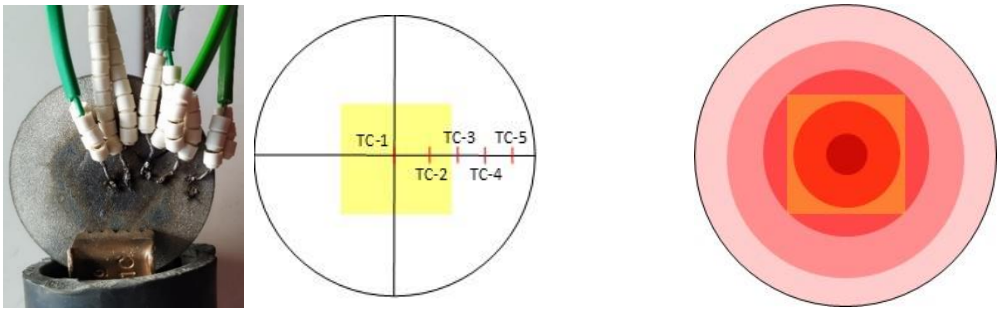

Figure 143. Positions of thermocouples welded on the back of the sample (left) and estimated temperature distribution considering a radial symmetry (right)

The temperature distribution was estimated from these measurements (Figure 144), considering a radial symmetry (Figure 143, right). While temperature is rather homogeneous (± 20°C) in the center of the irradiated area (in yellow), there is a quick drop in temperature on its sides, creating a high temperature gradient of -270°C between the center (0 mm, irradiated) and the edge of the sample (21.5 mm, not irradiated). Such high temperature gradients applied to a coating can be very damaging in themselves, especially at high temperature, as they generate high local thermomechanical stress, which may not be representative of the CSP application.

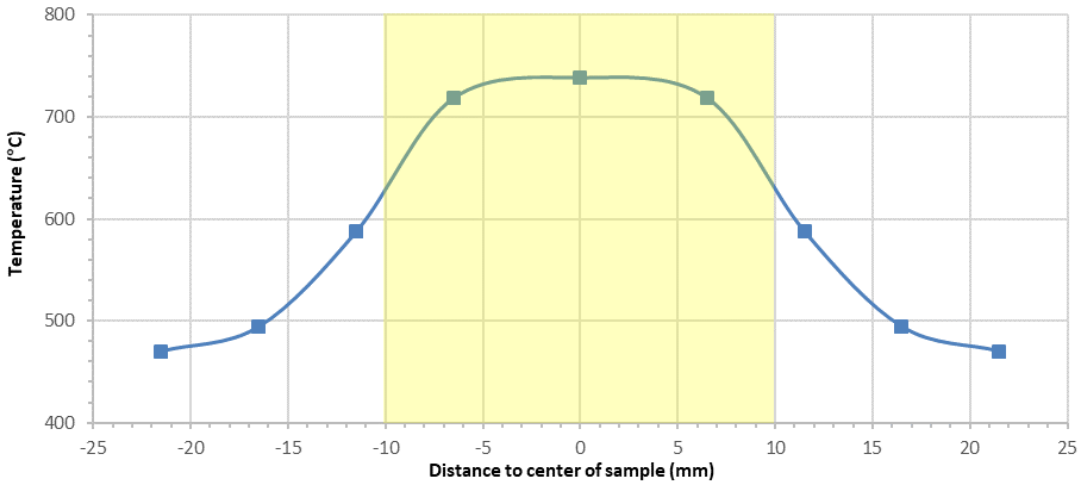

Figure 144. Temperature distribution measured on a sample irradiated in the SAAF

Overall, one must keep in mind that these major thermal differences when analyzing and comparing the results of purely thermal aging and “solar + thermal” aging procedures.

2.1.2. Irradiance profiles

Apart from these thermal considerations, the main difference between purely thermal aging and solar aging is of course the exposure of the tested materials to solar irradiance in solar furnaces compared to infrared radiation in electrical furnaces. In particular, solar irradiance typically contains approx. 3% of ultraviolet radiation (0.28-0.4 µm). UV photons being highly energetic (as energy is inversely proportional to wavelength), they can be potentially damaging for the absorber.

2.1.2.1. Spectral range and irradiance levels

2.1.2.1.1. Solar aging

In concentrated solar technologies, the incident solar spectrum is modified by the reflection on the concentrating mirrors before reaching the absorber. In the SAAF solar experimental set-up, three stages of reflection occur (Figure 145). A heliostat (flat mirror) reflects the incident solar radiation (first reflection) towards a down-facing parabolic mirror (second reflection). These mirrors mainly consist in a silver reflector deposited on mm-thick glass. A kaleidoscope made of four polished aluminum walls is placed at the focal point of the parabola (third reflection), where multiple reflections occur between the four walls to homogenize the concentrated solar flux (see Chapter 3). The sample is placed at the exit of the kaleidoscope.

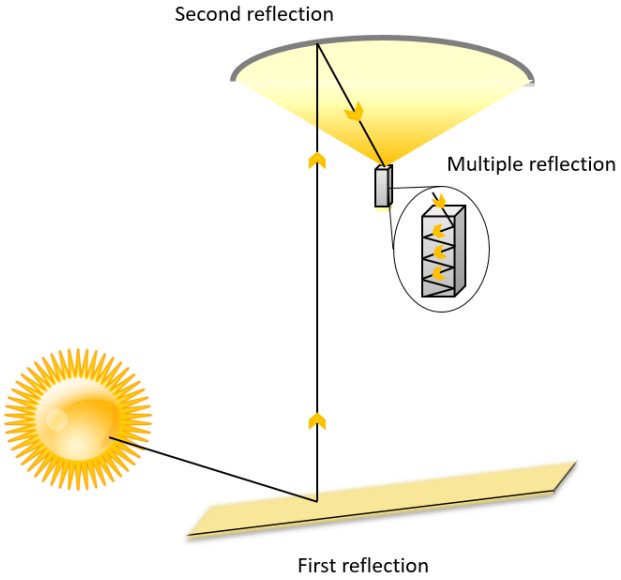

Figure 145. Three main reflection stages in SAAF

Reflectance spectra were measured for the three kinds of reflective surfaces and compared to the solar spectrum calculated for Odeillo using SMARTS software [30] (Figure 146). The heliostat and parabola (silvered-glass mirrors) have a high spectral reflectance except in the 0.28-0.32 µm UV region. The kaleidoscope (polished aluminum) has a lower reflectance below 1 µm, generating optical losses made all the higher by the multiple reflections between its four walls. This may reduce the quantity of UV photons after the third reflection in SAAF.

To better quantify this effect, the modification of the Odeillo incident solar irradiance spectrum after each reflection stage was estimated by multiplying it with spectral reflectance data (Figure 147). A

concentration ratio of C = 15000 was assumed for the parabola at all wavelengths. To account for optical losses due to multiple reflections in the kaleidoscope, an irradiance reduction ratio r = 0.15 was applied, according to Figure 97 p.110. The integration over wavelength of these incident and modified solar spectra (Figure 147) allowed for the comparison of the corresponding flux densities in the UV and solar ranges (Table 28).

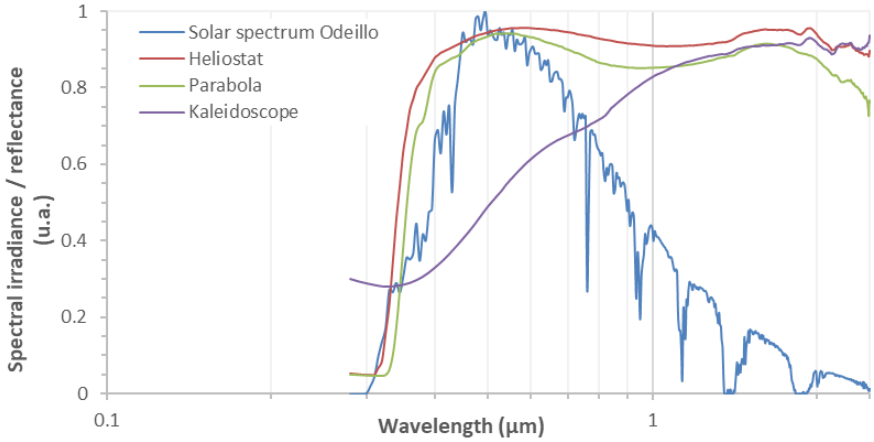

Figure 146. Hemispherical reflectance spectra of the mirrors used in the three reflection stages in SAAF

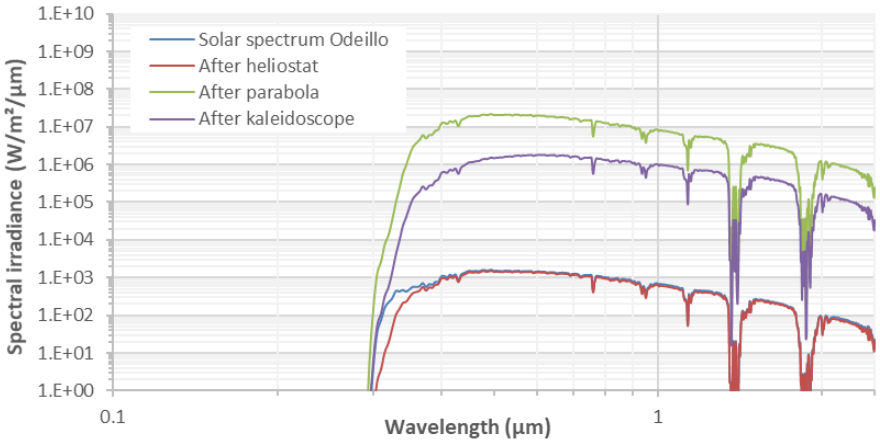

Figure 147. Solar irradiance spectrum in Odeillo before and after each stage of reflection in SAAF (estimated)

Table 28. Estimated flux densities before and after each stage of reflection in SAAF

Flux densities (kW/m²)	Solar spectrum Odeillo	After heliostat	After parabola C = 15000	After kaleidoscope r = 0.15	Received by sample	
					50 kW/m²	500 kW/m²
UV (0.28-0.4 µm)	0.05	0.03	303	14	0.55	5.5
Solar (0.28-2.5 µm)	1.02	0.94	12490	1270	50	500
Fraction of UV (%)	4.7%	3.4%	2.4%	1.1%	1.1%	1.1%

Notably, the solar spectrum in Odeillo has a fraction of UV radiation (0.28-0.4 µm) in the whole solar irradiation spectral range (0.28-2.5 µm) higher (4.7%) than standard solar spectra (3%), due to the high elevation (1650 m) and dry climate in the Pyrenees mountains. This high level of UV radiation is typical of CSP installation sites with high annual solar irradiance. As can be expected from the reflectance spectra of the reflective mirrors in Figure 146, the fraction of UV radiation decreases with each stage of reflection, from 4.7% to 1.1%.

At the first stage, after the heliostat (red vs. blue), UV radiation below 0.35 µm is notably reduced. At the second stage, after the parabola (green) there are some more UV losses, however due to the high concentration ratio of the parabola, UV flux density is high. At the third stage (purple), it is reduced again by the multiple reflections inside the kaleidoscope.

In SAAF, the level of incident solar irradiance can be controlled using shutters. If an irradiance between 50 kW/m² and 500 kW/m² is imposed on the sample, the UV flux density could reach 0.55 to 5.5 kW/m², i.e., more than 10 to 100 times the UV level comprised in the Odeillo solar spectrum. This value is consistent with the one estimated in Chapter 2 (Table 4 p.50) for solar absorbers subjected to a typical solar concentration *C* = 100 (2-3 kW/m²). UV exposure in SAAF is therefore representative of CSP applications. The level of UV radiation seen by samples in solar furnaces is not at all negligible.

The energy *E* of a photon at a wavelength λ is $E\ [J] = h \cdot c/\lambda\ [m]$ (Figure 148). When dividing spectral irradiance (in W/m²/µm) by the energy of the photon (in Joules) corresponding to each wavelength of the incident solar spectrum, the number of incident photons/m²/s/µm can be estimated (1 W ≡ 1 J/s) (Figure 148). When integrating this value over wavelength, a photon flux density (photons/m²/s) can be deduced: only 0.4% of the photon flux density incident on the sample in SAAF concerns photons with an energy above 3.1 eV (i.e., below 0.4 µm), e.g. at 500 kW/m², 1.1 x 10^{19} UV photons/m²/s vs. 2.4 x 10^{21} "solar photons"/m²/s.

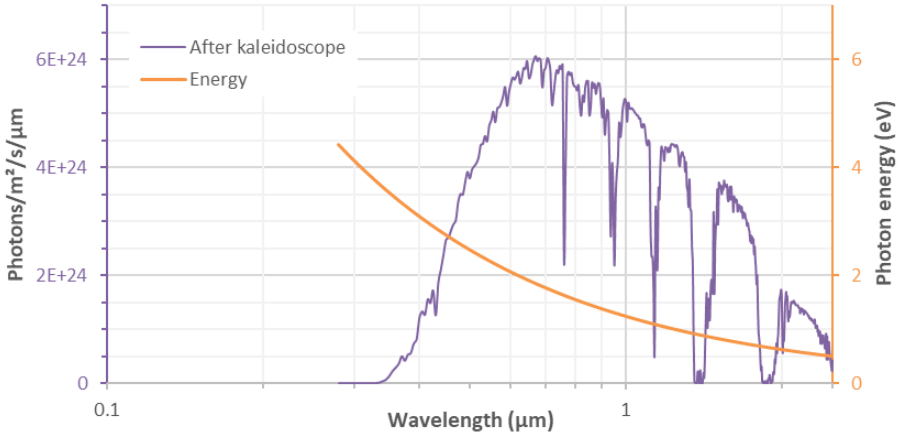

Figure 148. Photon energy and photon flux density/µm after the last stage of reflection in SAAF

Considering that solar selective absorber coatings are solar absorptive by design, they will absorb the majority (i.e., their value of α_S) of the incident solar irradiance they are exposed to. For instance, Figure 149 shows the solar spectral irradiance incident on the sample in SAAF when irradiance is regulated to obtain 50 kW/m² (blue), and the one actually absorbed (orange) by a typical SSAC (sample 1830AR01-07 cured), which depends on its spectral reflectance (green). With a solar absorptance of 0.916, it absorbs approx. 92% of the solar irradiance it is exposed to (45 kW/m²), and up to 94% of the incident UV radiation where the SSAC is more absorptive than in the NIR region, due to its selectivity.

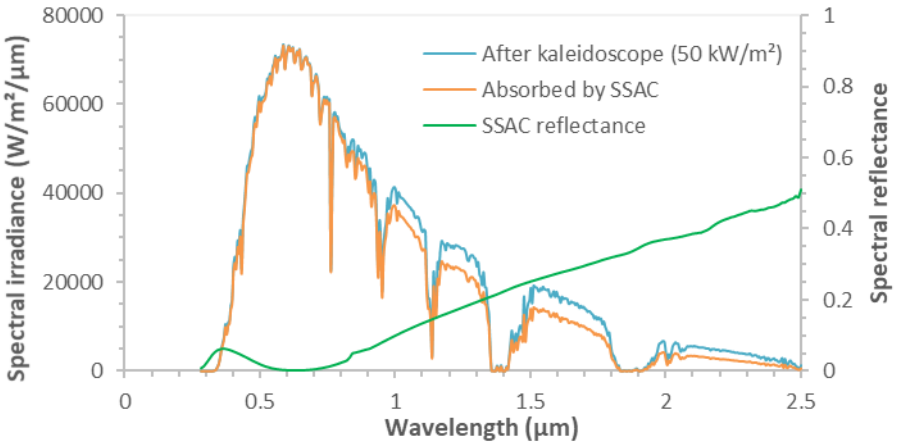

Figure 149. Estimated solar spectral irradiance received (blue) in SAAF at 50 kW/m², and absorbed (orange) by a typical SSAC sample (18301R01-07 cured) depending on its spectral reflectance (green)

2.1.2.1.2. Thermal aging

In an electrical furnace, samples are heated by the infrared irradiation of ceramic heating elements. In ALTHAIA, the sample is placed inside a heated ceramic tube, most likely made mainly of alumina. In Figure 150 (left) the spectral irradiance of the alumina ceramic tube at 500°C (red) was approximated as the spectral blackbody emission (given by Planck's law, brown) multiplied by the spectral emittance of an alumina ceramic (at 1300 K [331], black). It is to notice that the typical irradiance level attained in thermal aging with such configuration is approx. 10 kW/m² (obtained by integrating the red spectrum over wavelength). This is more than 5 times lower than under solar irradiance of 50 kW/m² (Figure 149).

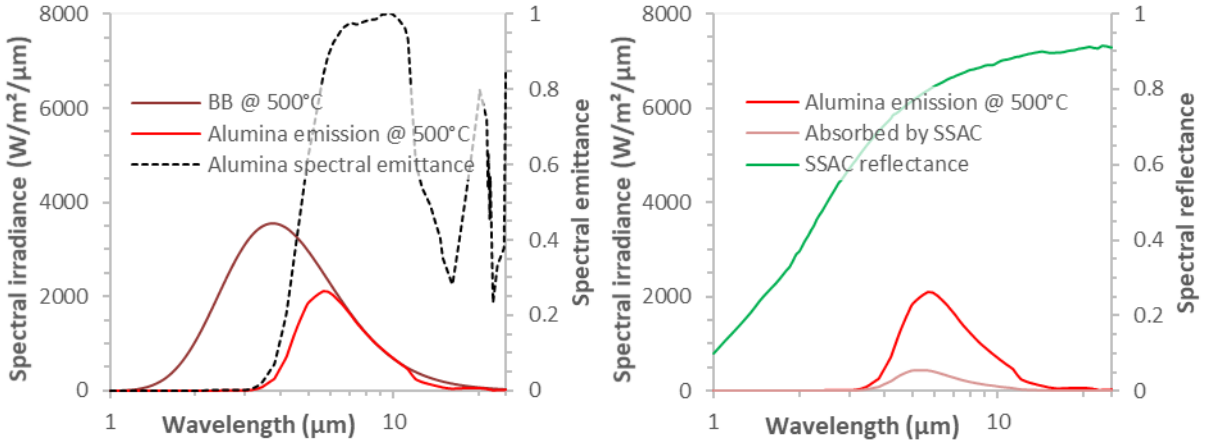

Figure 150. Left: IR spectral irradiance emitted by an alumina ceramic at 500°C (red) estimated from blackbody spectral irradiance at 500°C (brown) and spectral emittance of alumina ceramic (black [331]). Right: Corresponding IR spectral irradiance absorbed (pink) by a typical SSAC sample (18301R01-07 cured) depending on its spectral reflectance (green).

Furthermore, SSACs are highly IR-reflective by design, thus they will absorb only a limited fraction (i.e., their value of $\varepsilon(T)$) of the incident IR irradiance they are exposed to. This was estimated for the same typical SSAC (sample 1830AR01-07 cured) considering its spectral absorptance as 1 minus its spectral reflectance (Figure 150 right, green). Using the approximated emission for the electrical furnace (red), the spectral irradiance actually absorbed by the SSAC (pink) is further reduced, so that only approx. 1.8 kW/m² of the incident 10 kW/m² is absorbed by the coating during purely thermal aging.

2.1.2.1.3. Comparison

Table 29 compares the irradiance levels received and absorbed by typical SSAC samples during purely thermal aging in an electrical furnace and during solar aging in SAAF solar furnace, as estimated in the previous subsections.

Table 29. Estimated irradiance levels received and absorbed by a typical SSAC sample (1830AR01-07 cured) during purely thermal aging in an electrical furnace and during solar aging in SAAF solar furnace for different spectral ranges

Irradiance levels ($kW/m^2 = kJ/m^2/s$) / spectral range	**Purely thermal aging** (ALTHAIA)		**Solar aging** (SAAF 50 kW/m^2)		**Solar/thermal ratio**
	Received	***Absorbed***	***Received***	***Absorbed***	***Absorbed***
UV (0.28 – 0.4 µm)	_	_	0.55	0.52	∞
Solar (0.28 – 2.5 µm)	0.002 [1]	0.001	50	45.3	33000
IR (1 – 25 µm)	10.3	1.8	17.3 [2]	13.4	7

This comparison illustrates the fact that the level of irradiance (in kW/m^2), i.e., energy flux (in $kJ/m^2/s$) absorbed by a solar selective absorber coating is much higher under concentrated solar aging in SAAF than under thermal aging in an electrical furnace. First, solar aging includes energetic UV photons (0.28 – 0.4 µm) that are not at all present during thermal aging. Also, in the solar range (0.28 – 2.5 µm) the energy flux is almost 33000 times higher under solar aging, due to the high solar concentration in SAAF. Even in the IR range (1 – 25 µm), the energy flux is seven times higher under solar aging. These more intense conditions could give rise to larger evolutions of the coatings under concentrated solar aging than under thermal aging.

Considering that irradiance is also the instant energy density (in $kJ/m^2/s$), there may additionally exist a different time scale between:

- **slow thermally-induced physicochemical phenomena in purely thermal aging**, caused by thermal accumulation on the material, until their activation energy can be reached;
- **spontaneous irradiation-induced phenomena in concentrated solar aging** (photon-matter interactions), caused by the more energetic UV-Vis photons that may locally induce chemical bond breaking and formation in the material lattice, especially in combination with high temperature.

This difference in time scale could be further enhanced by the much higher heating rates under concentrated solar aging (tens of °C/s) than thermal aging (tens of °C/min) (see section 2.1.1.1 p.172).

2.1.2.2. Effective irradiance and irradiance dose

In SAAF, similarly to temperature, if irradiance levels incident on the sample are varied during solar aging tests, an effective irradiance ("time-weighted" irradiance, considering the time spent under each irradiance level) can be estimated. An irradiance dose in kWh/m^2 can also be deduced by multiplying this effective irradiance with the total aging duration. It is to notice that contrary to temperature, irradiance levels are not measured during SAAF experiments. Irradiance levels are controlled using the shutter aperture, based on the DNI at the time of the experiment and previous calibrations. Therefore, experimental fluctuations of irradiance levels due to fluctuations in DNI during the test are not taken into account. In the following, setup irradiance levels are used to establish the irradiance profiles.

[1] Spectral irradiance between 0.28 µm and 1 µm is not taken into account, however there is very little blackbody irradiance below 1 µm at 500°C so this is negligible.
[2] Spectral irradiance above 2.5 µm is not taken into account, so this value may be slightly underestimated.

2.2. Influence of concentrated solar irradiation

Despite the discussed differences in aging methods, an analysis of the influence of the exposure to concentrated solar radiation during aging was attempted, by comparing the aging behavior of a sample aged in the ALTHAIA electric furnace (Chapter 4) and a sample aged in the SAAF solar furnace under constant solar irradiance, reaching similar aging temperatures and durations (Table 30). This allows for the comparison of configurations 1 (thermal aging) and 2 (constant solar aging) described in Table 11 p.114. The cured state of the sample (24h at 500°C in air, see Chapter 4) is considered as reference in both cases.

The TiAlN absorber series 1928 was used for this comparison. Sample 1928ER01-20, previously treated in ALTHAIA at 500°C in air, is considered based on the additional 24h single aging step applied after the curing step. Sample 1928ER01-13 was treated in the SAAF at a constant solar irradiance of 400 kW/m², in 4 cycles reaching a total duration of 14h28. Although this could be considered as slow thermal cycling, due to the intermittence of the solar radiation, it is not possible to apply this total duration in one cycle. The corresponding temperature profiles for each cycle are visible in Table 31. Due to the shape and size of the sample, the sample was treated with support 1, hence there was no backside cooling and the temperature tended to fluctuate. It was overall maintained in the 400-580°C range, with a maximum effective temperature of 536°C (treatment 1) and a global effective temperature T_{eff} = 485°C for all treatments. Effective temperature is "time-weighted", i.e., it considers the time spent at each of the different temperature levels seen by the sample during its solar aging and was calculated from the recorded temperature profiles (Table 31). Overall, the two samples were thus subjected to similar temperature levels around 500°C.

Table 30. Number of aging cycles and durations, and resulting macroscopic images of the sample surface

Aging conditions	***Reference***	**Treatment 1**			
Thermal aging ***500°C*** ALTHAIA *Sample 1928ER01-20*	*Cured (24h 500°C air)* -	After 1 cycle (24h) 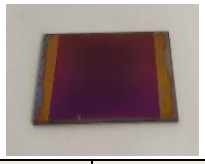			
Aging conditions	***Reference***	**Treatment 1**	**Treatment 2**	**Treatment 3**	**Treatment 4**
Constant solar aging ***400 kW/m²*** SAAF Support 1 (no cooling) *Sample 1928ER01-13*	*Cured (24h 500°C air)* -	After 1 cycle (3h37) -	After 2 cycles (+3h37 = 7h14) 	After 3 cycles (+3h37 = 10h51) 	After 4 cycles (+3h37 = 14h28) 

Table 30 shows the macroscopic pictures of the two samples at the different stages of aging. The sample submitted to thermal aging at 500°C did not show any notable changes in its aspect between the cured and aged state, while a slight discoloration is visible in the irradiated area of the sample treated with constant solar irradiance.

Figure 151 and Figure 152 compare the evolutions in spectral reflectance and solar absorptance for the thermal aging and constant solar aging conditions. Optical variations are small in both cases ($\Delta\alpha_S \leq 0.01$). The reflectance blue-shift could indicate a slight increase in coating thickness in both cases.

Table 31. Temperature profiles obtained with thermal aging at 500°C and constant solar aging at 400 kW/m²

Conditions	Treatment 1
1928ER01-20 1 cycle 24h **T = 500°C** ALTHAIA	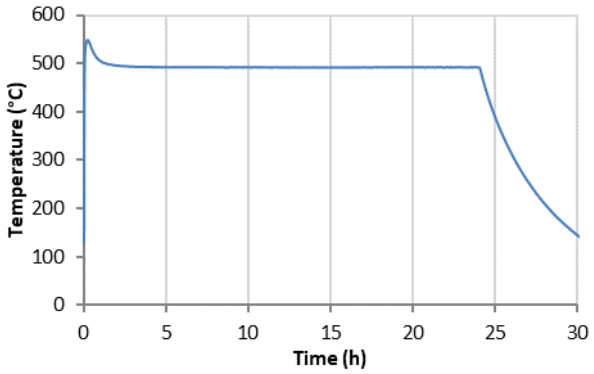

Conditions	Treatment 1	Treatment 2	Treatment 3	Treatment 4
1928ER01-13 400 kW/m² 4 cycles 14h28 **T_{eff} = 485°C** Support 4 (cooling)	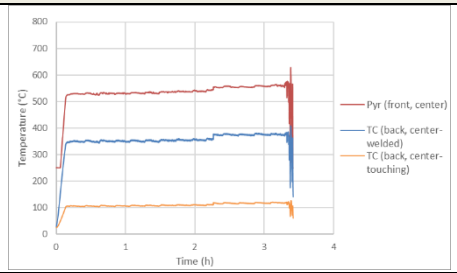	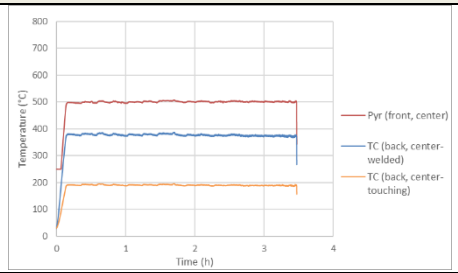	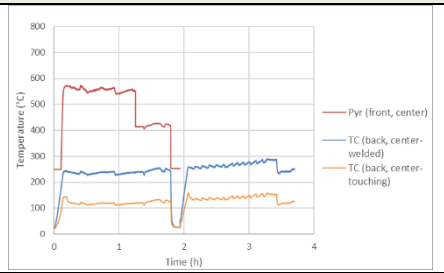	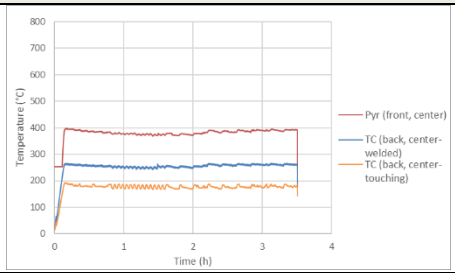
	$T_{eff\text{-}pyr}$ = 536°C, $T_{max\text{-}pyr}$ = 628°C 1 cycle 3h37	$T_{eff\text{-}pyr}$ = 498°C, $T_{max\text{-}pyr}$ = 508°C 1 cycle 3h37	$T_{eff\text{-}pyr}$ = 510°C, $T_{max\text{-}pyr}$ = 574°C 1 cycle 3h37	$T_{eff\text{-}pyr}$ = 383°C, $T_{max\text{-}pyr}$ = 399°C 1cycle 3h37

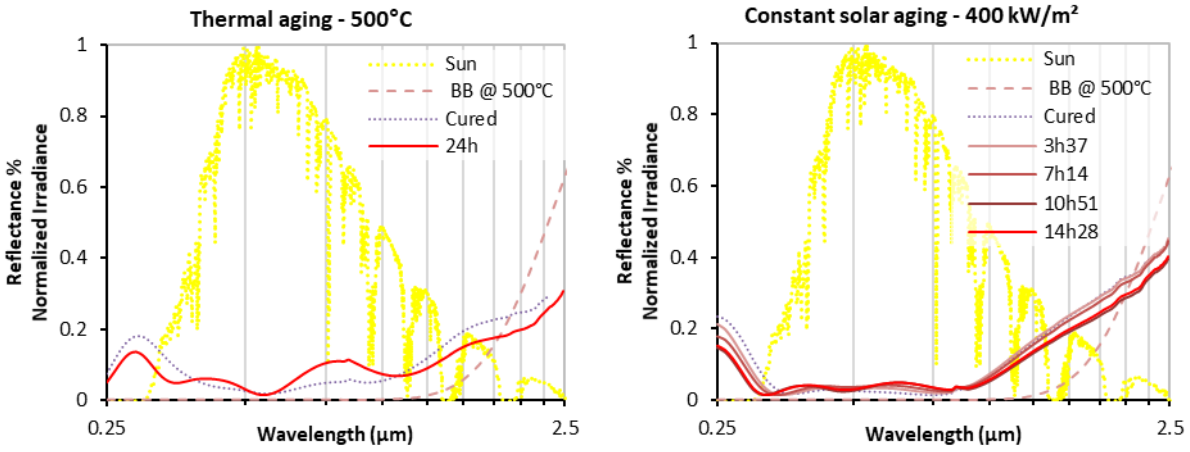

Figure 151. Evolution of the spectral reflectance of the samples with thermal aging and constant solar aging

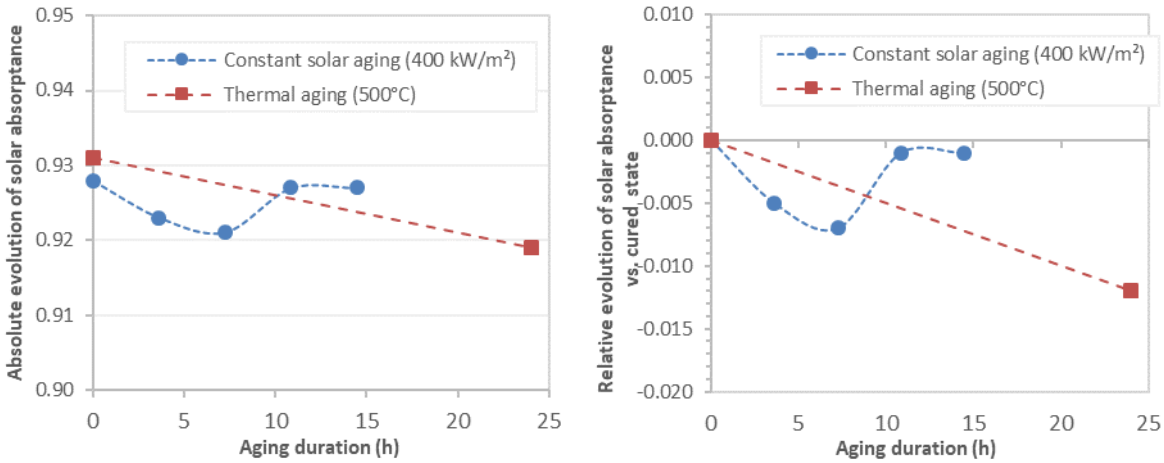

Figure 152. Absolute (left) and relative (right) evolutions of solar absorptance for constant solar aging vs. thermal aging, compared to the cured state (0h)

Overall, **no clear difference was observed between thermal aging and constant solar aging with similar durations** (15-24h) **and temperatures** (approx. 500°C), indicating that **there seems to be no additional influence of the concentrated solar radiation during aging**. Similar results were obtained for the WAlSiN absorber (not shown). Of course, these tendencies will have to be confirmed for longer solar aging durations.

This result could be interpreted in light of the lack of intense UV flux density seen by the material, due to the optical losses in the UV range when the incident solar radiation is reflected by the Ag mirrors of the heliostat (see section 2.1.2 p.174). In any case, it is representative of real CSP applications where absorber materials are subjected to similar conditions, as Ag mirrors are the most used type of solar mirror in CSP.

3. Influence of the sources of degradation during solar aging

In addition to the concentrated solar irradiance level, other sources of degradation can be encountered in CSP conditions, and simulated using the SAAF facility. In particular, rapid thermal cycling with high amplitudes and short periods can occur during cloudy spells, the influence of which can be studied by comparing cyclic solar aging (configuration 3, see Table 11 p.114) with constant solar aging (configuration 2) at similar solar irradiance. Also, the irradiance levels and the irradiance amplitude between the high and low irradiance phases of this rapid cycling, linked to the temperature amplitude

suffered by the sample, can be controlled in the SAAF, and their influence on the aging behavior of the absorber coatings is studied. Indeed, these amplitudes can generate large and potentially damaging thermal shocks in the materials.

For this study, equivalent samples of the TiAlN tandem absorber coating were used. The chosen samples are deposited on an Inconel substrate of 2 mm in thickness and a round shape of 2'' (50.8 mm) in diameter. Considering this, supports 1 and 4 were used. The aging behavior is monitored through the observed changes in macroscopic and SEM images of the samples surface, and the variations in optical properties and chemical composition, considering the different temperature profiles applied during each solar treatment. The variation in optical performance is considered relatively to the cured state (24h at 500°C in air) ($\Delta\alpha_S = \alpha_S$ (aged) – α_S (cured)) for better comparability with other samples.

3.1. Influence of solar irradiance level in constant solar aging

First, the influence of the solar irradiance level during constant solar aging is investigated. To draw a comparison, a sample of series 1830 was exposed to 250 kW/m² for up to 11h20 (using support 1 without backside cooling), and a sample of series 1928 was exposed to 400 kW/m² for up to 14h28 (using support 4 with backside cooling), in four cumulative treatments (Table 32).

Table 32. Number of aging cycles and durations, and resulting macroscopic images of the sample surface

Aging conditions	***Reference***	**Treatment 1**	**Treatment 2**	**Treatment 3**	**Treatment 4**
Constant solar aging ***250 kW/m²*** Support 1 (no cooling) *Sample 1830AR01-08*	*Cured (24h 500°C air)* 	After 1 cycle (6h) -	After 2 cycles (+1h15 = 7h15) -	After 3 cycles (+2h05 = 9h20) 	After 4 cycles (+2h = 11h20) 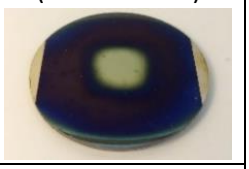
Constant solar aging ***400 kW/m²*** SAAF Support 4 (cooling) *Sample 1928ER01-13*	*Cured (24h 500°C air)* -	After 1 cycle (3h37) -	After 2 cycles (+3h37 = 7h14) 	After 3 cycles (+3h37 = 10h51) 	After 4 cycles (+3h37 = 14h28) 

Table 32 shows macroscopic pictures of the samples surface. The sample treated at 250 kW/m² seems to be the most affected by solar aging, with a change in color from blue to yellow-white in the irradiated area. A similar tendency is suspected for the sample treated at 400 kW/m², only to a lesser extent.

These changes cause evolutions in the sample optical properties (Figure 153) particularly visible after solar aging at 250 kW/m². The oscillations appearing in the reflectance spectrum can be linked to the oxidation of the coating (see Chapter 4), confirmed by EDS measurements where the content in oxygen is increased by aging (Figure 154). Elements from the Inconel substrate (Ni to Mo) tend to be detected in higher quantities after aging, to the detriment of elements from the coating (Al), indicating that the thickness of the coating has decreased, probably due to its densification. Meanwhile, the increase in frequency of the reflectance oscillations could conversely indicate an increase in thickness. However, these oscillations may also appear simply because of a change in the coating chemical and optical nature, from absorptive (TiAlN) to semitransparent (oxide), due to oxygen incorporation [332]. The

fact that the content in Ti does not decrease while that of Al does could indicate that the oxidation of TiAlN may occur via the oxidation of TiN into TiO_x. However, the detected content in Ti is small even in the reference cured state, so this however credible hypothesis cannot reasonably be sustained by EDS measurements only. Complementary analyses such as XPS depth profiles of the aged sample would be necessary to confirm it.

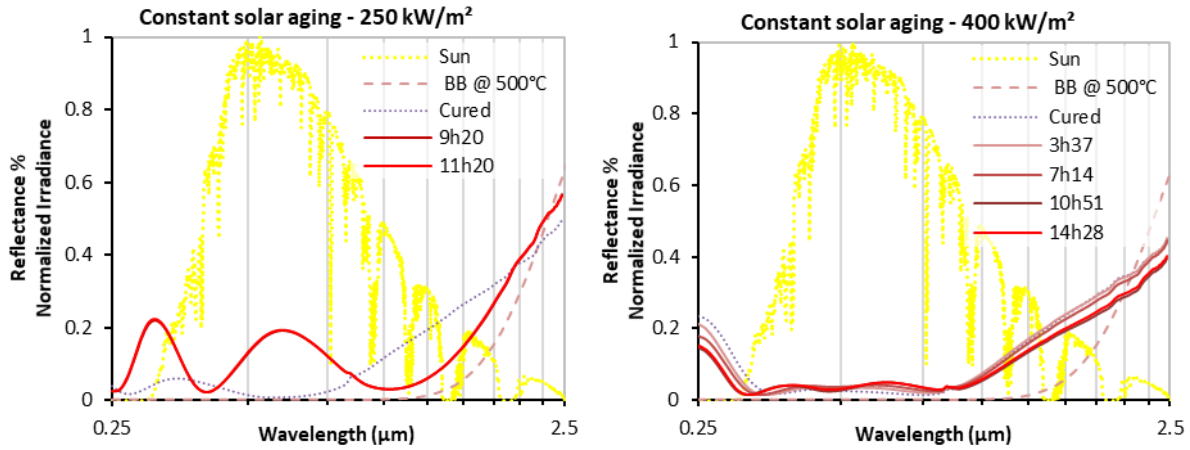

Figure 153. Evolution of the spectral reflectance of the samples with constant solar aging at 250 kW/m² and 400 kW/m²

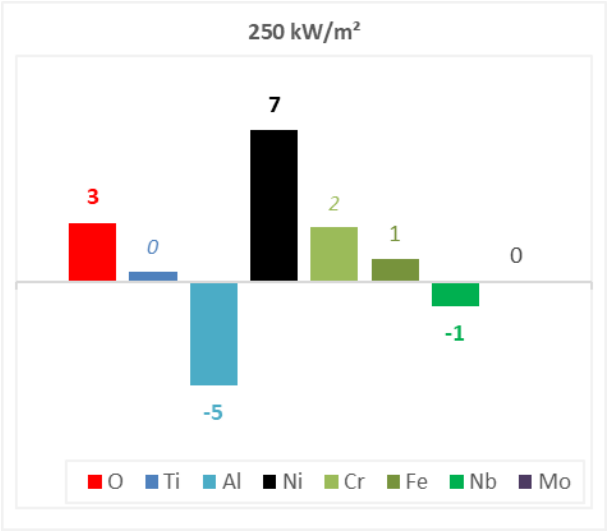

Figure 154. Variation in atomic content (in at.%, measured by EDS) after 11h20 at 250 kW/m² vs. cured state

Following the increase in spectral reflectance, as can be expected the solar absorptance of the sample treated at 250 kW/m² notably decreases compared to the cured state ($\Delta\alpha_S$ = -0.04 after 10h), while that of the sample treated at 400 kW/m² does not significantly change (Figure 155).

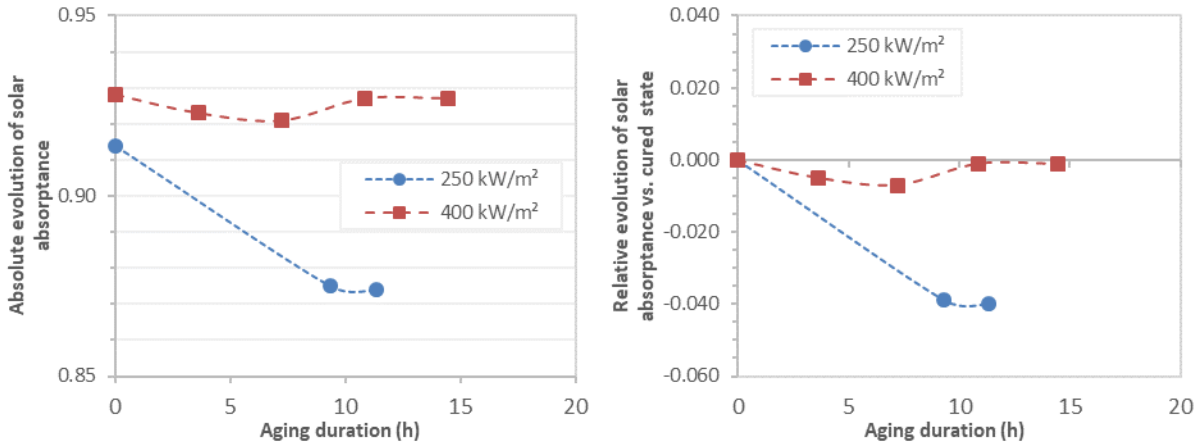

Figure 155. Absolute (left) and relative (right) evolutions of solar absorptance for constant solar aging at 250 kW/m² and 400 kW/m² vs. cured state (0h)

Overall, these results are surprising: it would have been expected that the exposure for similar durations to a higher solar irradiance would lead to a higher deterioration. Indeed, the estimated irradiance dose to which the samples are exposed during 11h20 at 250 kW/m² is significantly lower than during 14h28 at 400 kW/m² (2833 vs. 5787 kWh/m², i.e., half the dose) (Table 34). The higher deterioration observed at 250 kW/m² compared to 400 kW/m² cannot be explained either by a difference in the temperature profiles and levels reached during the tests (Table 33). Indeed, the effective temperature seen by the sample is also lower at 250 kW/m² (422°C vs. 485°C), so that the thermal dose is lower at 250 kW/m² (4783°C·h vs. 7016°C·h). Also, the maximum temperatures are similar, so none of the samples suffered inadvertent overheating beyond the coating critical temperature (this coating is highly stable at 500°C and even higher, see Chapter 4).

In fact, the main difference between these two tests is that the samples do not belong to the same series, and almost a year separates their synthesis. Series 1830 (for the test at 250 kW/m²) was deposited in July 2018 while series 1928 (for the test at 400 kW/m²) was deposited in July 2019. It is thus possible that some fluctuations in the deposition process and subsequent coating architecture, microstructure, composition, etc., appeared between these two deposition campaigns, voluntarily or not. It is also possible that the samples naturally aged differently in ambient conditions during their conservation.

In any case, these experimental results remain inconclusive regarding the effect of the level of concentrated solar irradiance during constant solar aging, since they could not be satisfactorily interpreted with the elements at our disposal. Complementary studies would be needed, using configurations as close as possible to remove any doubt (fresh and truly suitably equivalent samples, same SAAF sample support, etc.).

Nevertheless, the effect of other sources of degradation in solar aging will be presented in the following subsections. In particular, the case of constant solar aging at 250 kW/m² presented here will also be compared to cyclic solar aging applied to a similar sample (series 1830).

Table 33. Temperature profiles obtained with constant solar irradiance of 250 kW/m² and 400 kW/m²

Conditions	Treatment 1	Treatment 2	Treatment 3	Treatment 4
1830AR01-08 250 kW/m² 4 cycles 11h20 **T_{eff} = 422°C** Support 1 (no cooling)	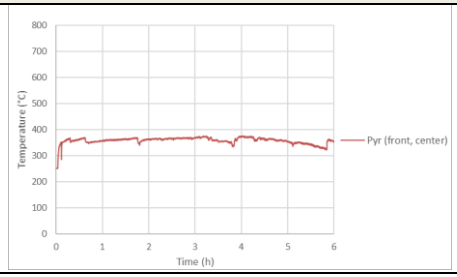	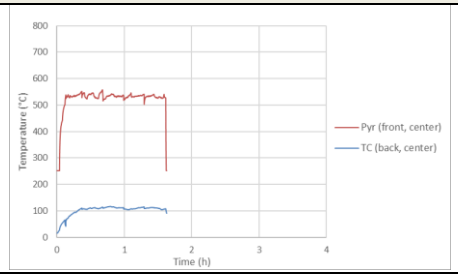	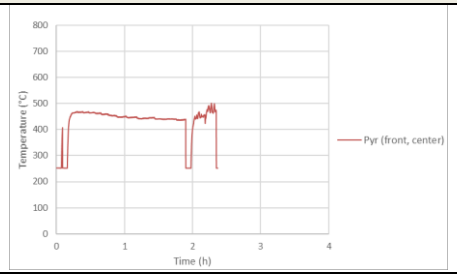	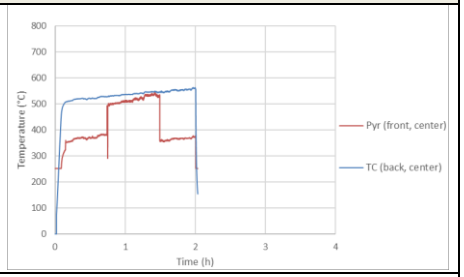
	$T_{eff\text{-}pyr}$ = 359°C, $T_{max\text{-}pyr}$ = 377°C 1 cycle 6h	$T_{eff\text{-}pyr}$ = 529°C, $T_{max\text{-}pyr}$ = 558°C 1 cycle 1h15	$T_{eff\text{-}pyr}$ = 449°C, $T_{max\text{-}pyr}$ = 502°C 1 cycle 2h05	$T_{eff\text{-}TC}$ = 517°C, $T_{max\text{-}TC}$ = 563°C 1 cycle 2h
1928ER01-13 400 kW/m² 4 cycles 14h28 **T_{eff} = 485°C** Support 4 (cooling)	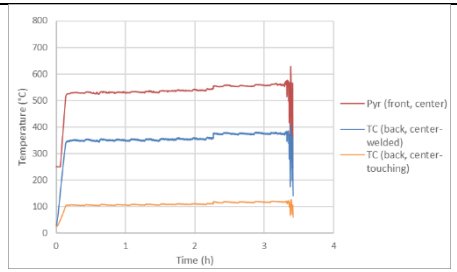	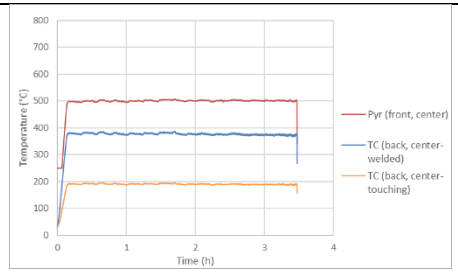	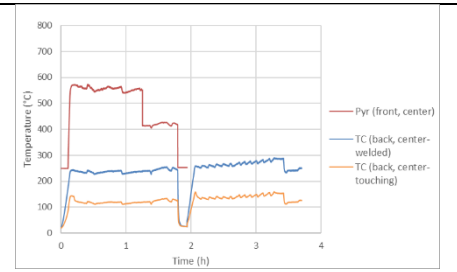	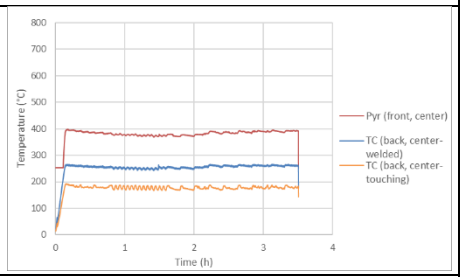
	$T_{eff\text{-}pyr}$ = 536°C, $T_{max\text{-}pyr}$ = 628°C 1 cycle 3h37	$T_{eff\text{-}pyr}$ = 498°C, $T_{max\text{-}pyr}$ = 508°C 1 cycle 3h37	$T_{eff\text{-}pyr}$ = 510°C, $T_{max\text{-}pyr}$ = 574°C 1 cycle 3h37	$T_{eff\text{-}pyr}$ = 383°C, $T_{max\text{-}pyr}$ = 399°C 1cycle 3h37

Table 34. Effective irradiance and dose with constant solar irradiance of 250 kW/m² and 400 kW/m²

Sample	I_{max} (kW/m²)	Total duration (h)	I_{eff} (kW/m²)	Irradiance dose (kWh/m²)	T_{eff} (°C)	Thermal dose (°C·h)
1830AR01-08	250	11.33	250	2833	422	4783
1928ER01-13	400	14.47	400	5787	485	7016

3.2. Influence of cyclic solar aging vs. constant solar aging

In CSP applications, the absorber material may be submitted to sudden variations in the concentrated solar irradiance, for instance during cloudy spells. Here the influence of rapid thermal cycling during solar aging is studied, by comparing the effect on equivalent samples of TiAlN absorber, of: i) constant solar irradiance; ii) repeated cycles oscillating from a high irradiance phase to a low irradiance phase.

A constant irradiation of 250 kW/m² was applied to sample 1830AR01-08, in four cumulative cycles with different durations from 2h to 6h, reaching 11h20 of aging in total (Table 35). Meanwhile, sample 1830AR01-09 was submitted to 225 cycles (16h16) in total, each with a high irradiance phase of 250 kW/m² for a duration of 200s, and a low irradiance phase of 200 kW/m² for a duration of 60s, in four cumulative treatments (Table 35, Figure 156). The samples were treated using support 1 (no backside air cooling, thermocouple welded on the back center of the sample). Both samples were previously cured by the manufacturer (24h at 500°C in ambient air) before solar exposure.

Table 35. Number of aging cycles and durations, and resulting macroscopic and SEM images of the sample surface

Aging conditions	*Reference*	Treatment 1	Treatment 2	Treatment 3	Treatment 4
Constant solar aging *250 kW/m²* Support 1 (no cooling) *Sample 1830AR01-08*	*Cured (24h 500°C air)*	After 1 cycle (6h)	After 2 cycles (+1h15 = 7h15)	After 3 cycles (+2h05 = 9h20)	After 4 cycles (+2h = 11h20)
		-	-	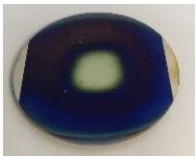	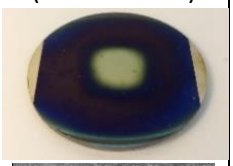
	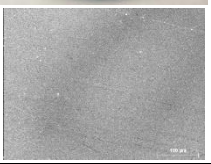	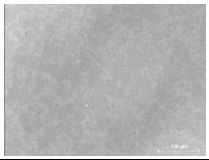		-	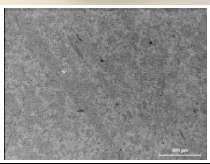
Cyclic solar aging *250-200 kW/m²* ΔI = 50 kW/m² Support 1 (no cooling) *Sample 1830AR01-09*	*Cured (24h 500°C air)*	After 75 cycles (5h25)	After 125 cycles (+3h37 = 9h02)	After 175 cycles (+3h37 = 12h39)	After 225 cycles (+3h37 = 16h16)
		-	-		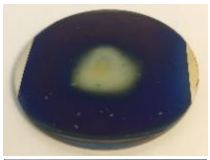
	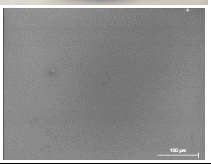			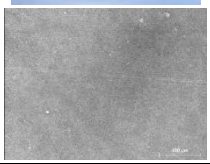	

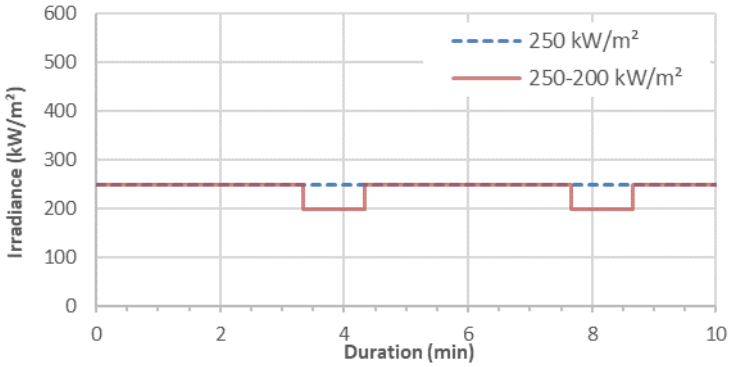

Figure 156. Irradiance levels applied in SAAF (constant solar aging 250 kW/m² vs. cyclic solar aging at 250-200 kW/m²)

Images at macroscopic scale (Table 35) both show surface discoloring, faster under constant irradiation (treatments 3 and 4, 9h20 and 11h20) than under cyclic irradiation (treatment 3, 12h39). Similar changes to the surface are eventually observed. At microscopic scale (SEM images, Table 35), no physical deterioration is observed for both cases, such as cracks or delamination.

In both cases, the samples optical properties (Figure 157 and Figure 159) evolve with their physical aspect. Their discoloring is marked by the appearance of reflectance oscillations that can again be linked to the increase in oxygen content, as measured by EDS (Figure 158), illustrating the coating partial oxidation. As explained in section 3.1, constant solar aging at 250 kW/m² induces a decrease in coating thickness concomitant with a change in chemical nature (oxidation) and subsequent optical behavior from absorptive (TiAlN) to semitransparent (TiAlO). Oxidation also occurs with cyclic solar aging at 250-200 kW/m², only it does not seem to be accompanied by a coating densification, as the content in elements from the coating (Si, Ti, Al) barely evolve after aging. A small decrease in Ni content (main component of the Inconel substrate) could even indicate an increase in coating thickness, maybe due to the growth of an oxide. This is accompanied by a small enrichment in Fe and Mo (substrate elements), that may indicate their outward diffusion inside the coating. These elements could also be oxidized. However, their detected content is low even in the reference cured state (≤ 3 at.%, limit of EDS detection), and this hypothesis would need to be confirmed by more precise means such as XPS depth profiles.

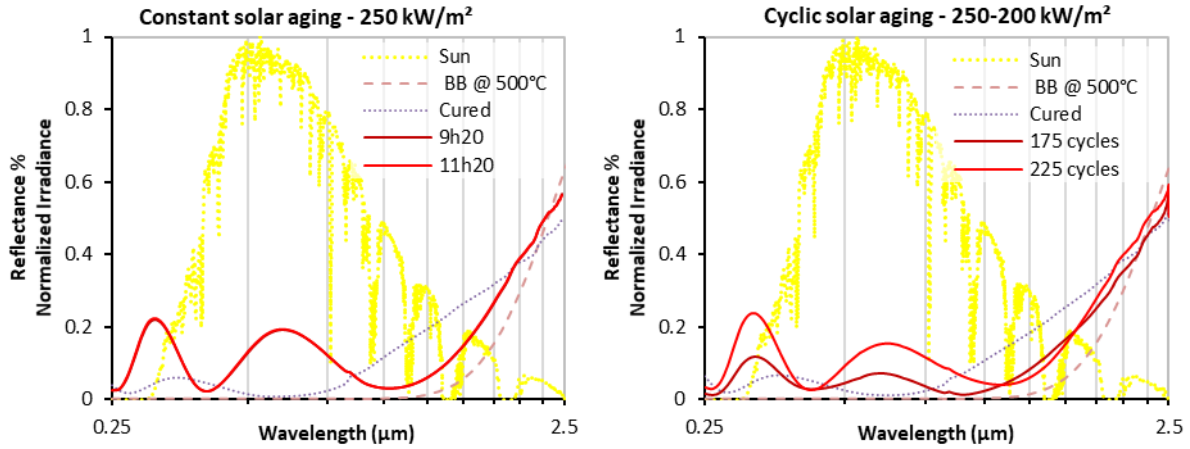

Figure 157. Evolution of sample spectral reflectance with constant (250 kW²) and cyclic (250-200 kW/m²) solar aging

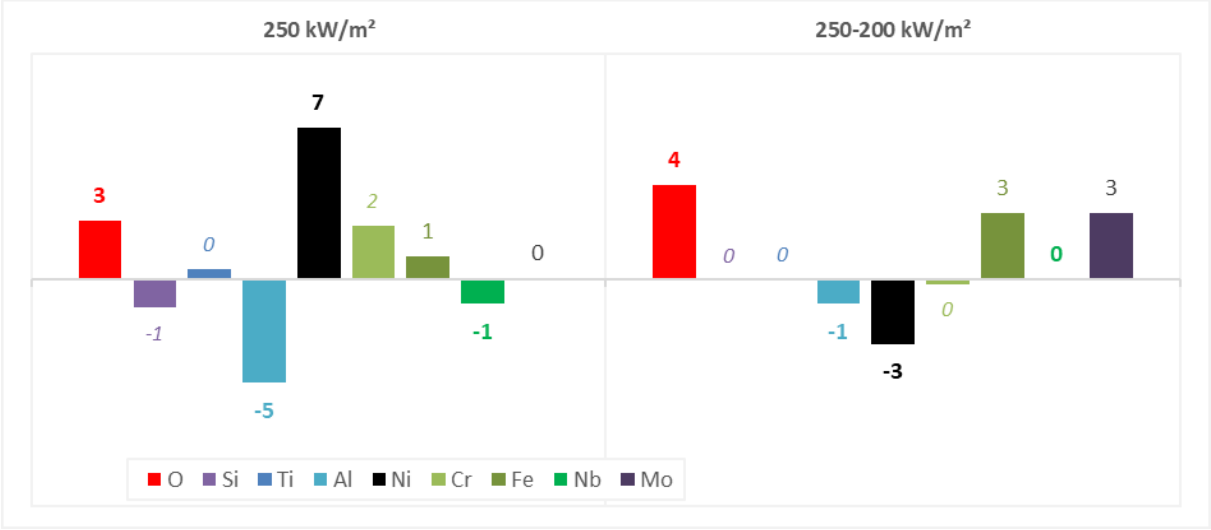

Figure 158. Variation in atomic content (in at.%, measured by EDS after the last treatment) with constant (250 kW²) and cyclic (250-200 kW/m²) solar aging vs. cured state

As a consequence of these evolutions, solar absorptance (Figure 159) decreases more rapidly and more strongly when exposed to constant solar aging at 250 kW/m² ($\Delta\alpha_S$ = -0.04). After the discoloring has settled (third treatment, 9h20 in total), solar absorptance tends to stabilize, as does spectral reflectance. Under cyclic solar aging of 250-200 kW/m², solar absorptance first increases slightly (+0.01), thanks to higher frequency of reflectance oscillations in the solar range, giving rise to a lower reflectance in the NIR range whilst not increasing it in the visible range (maximum solar irradiance around 500 nm). After the last cyclic treatment (16h16 in total), in concordance with the appearance of coating visual discoloring, solar absorptance dropped down to a similar level ($\Delta\alpha_S$ = -0.03) as was observed for constant solar aging.

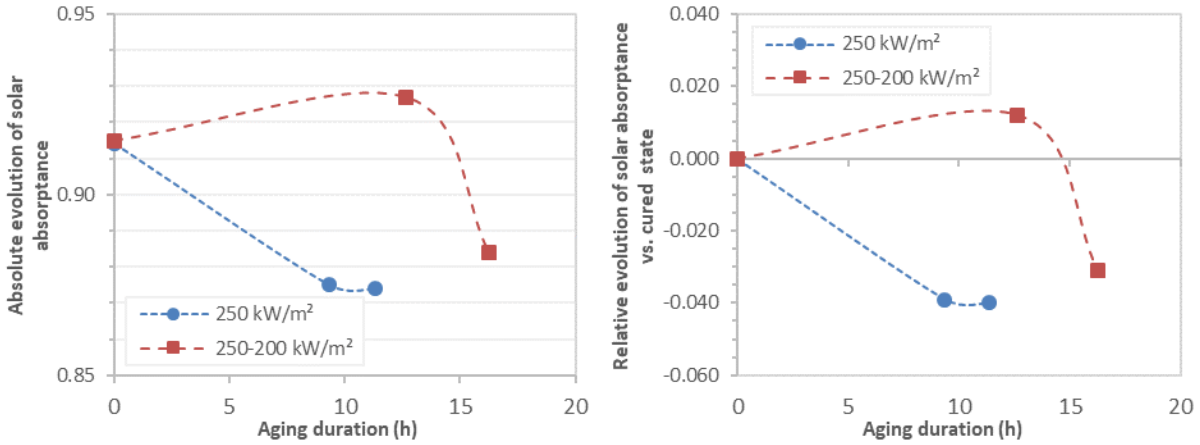

Figure 159. Absolute (left) and relative (right) evolutions of solar absorptance with constant (250 kW²) and cyclic (250-200 kW/m²) solar aging vs. cured state (0h)

This tendency to faster/higher degradation under constant irradiation can be expected, considering the applied conditions. Indeed, the effective irradiance seen by the sample is higher under constant irradiance of 250 kW/m² (I_{eff} = 250 kW/m²) than under cyclic irradiance of 250-200 kW/m² (I_{eff} = 238 kW/m²) (Table 37). In other words, since 1 W ≡ 1 J/s, the energy flux (in kJ/m²/s) received by the sample is higher under this constant irradiance (250 kJ/m²/s vs. 238 kJ/m²/s). Similarly, based on the considerations in section 2.1.2 p.174, a higher irradiance translates into a higher photon flux. The latter are estimated to be 1.18 x 10^{21} photons/m²/s under constant aging vs. 1.13 x 10^{21} photons/m²/s under cyclic aging, in the conditions studied here. Therefore during the same duration, the sample receives (and absorbs) more energy under constant irradiance than under cyclic irradiance, causing faster and higher degradation.

It must be highlighted that these observations are only true because in the chosen test conditions, the high irradiance phase level during cyclic aging is the same as the irradiance level during constant aging (250 kW/m²), thus the low irradiance level and the effective irradiance are lower under cyclic aging than constant aging. That is to say that here the influence of the effective irradiance is highlighted, more than the effect of cycling itself. Therefore, to really isolate the effect of cycling over that of effective irradiance, identical effective irradiance levels would have to be applied (e.g. constant 250 kW/m² vs. cyclic 265-200 kW/m² with 200s/60s cycles).

Another relevant indicator would be the irradiance dose and thermal dose received by the sample. Due to the higher total aging duration under cyclic aging (16h16 vs. 11h20), it is more adequate to compare constant and cyclic aging at closer durations, i.e., after 11h20 at 250 kW/m² (treatment 4) vs. after 12h39 at 250-200 kW/m² (treatment 3). In this case, irradiance doses (approx. 2800-3000 kWh/m²), effective temperatures (approx. 420-430°C), high temperature levels (approx. 540-560°C) are all similar (Table 36). The thermal dose is even higher for cyclic aging (5409°C·h vs. 4783°C·h).

Yet constant solar aging still gives rise to faster and higher degradation than cyclic solar aging ($\Delta\alpha_S$ = -0.04 at 250 kW/m² vs. +0.01 at 250-200 kW/m², Figure 159). This fact is well illustrated in Figure 160, where the evolutions of solar absorptance with irradiance dose (left) and thermal dose (right) are represented. Higher doses in cyclic solar aging are necessary to provoke similar optical degradations.

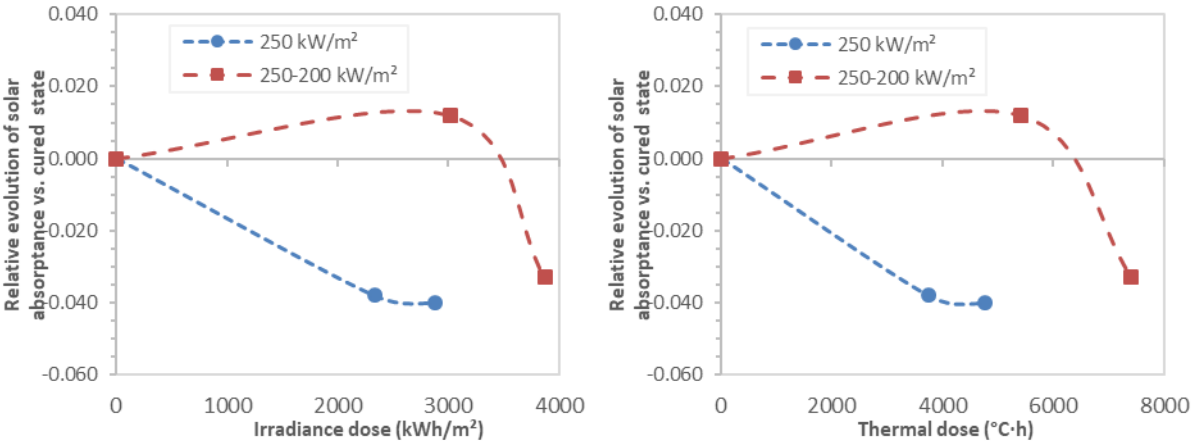

Figure 160. Relative evolutions of solar absorptance with constant (250 kW²) and cyclic (250-200 kW/m²) solar aging vs. cured state (0h), vs. irradiance dose (left) and thermal dose (right) received by the samples

To conclude on the impact of cyclic vs. solar aging, or more accurately on the impact of the effective irradiance applied to the sample during solar aging, it appears that **aging under cyclic irradiation with lower effective irradiance gives slower aging and less damaging than under constant irradiation**, even when applying similar irradiance and thermal doses. This could be due to the fact that a higher effective irradiance translates into higher instant energy and photon flux densities (in J/m²/s and photons/m²/s), that could cause fast chemical reactions due to direct energetic photon-matter interactions (e.g. bond breaking, bond formation). **A higher photon flux density under constant aging could modify the coating surface more quickly during the first stages of aging, accounting for the faster degradation observed**. Given enough time at lower instant photon flux density, the damaging eventually reaches a similar level under cyclic aging.

Finally, in this example, the irradiance level and the amplitude between high and low irradiance phases are moderate (max I = 250 kW/m², ΔI = 50 kW/m²) and the series 1830 coating may be less resistant than others (see section 3.1 p.182). However, it is worth noticing that similar results were obtained with higher irradiance levels and higher amplitudes (400 kW/m² vs. 400-50 kW/m²) on a coating series with apparent higher stability (1928).

After comparing constant and cyclic solar aging, the next section will study the influence of the temperature/irradiance amplitudes during cyclic solar aging at different irradiance levels.

Table 36. Temperature profiles obtained with constant solar irradiance of 250 kW/m² and cyclic solar irradiance of 250-200 kW/m²

Conditions	Treatment 1	Treatment 2	Treatment 3	Treatment 4
1830AR01-08 250 kW/m² 4 cycles 11h20 **T_{eff} = 422°C**	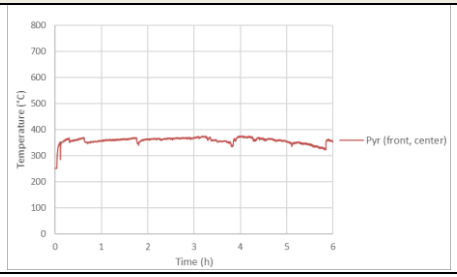	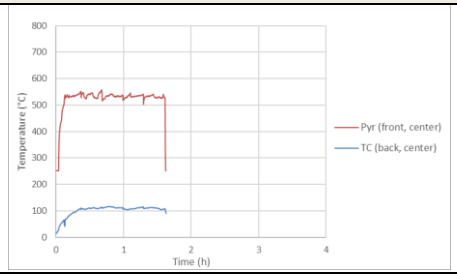	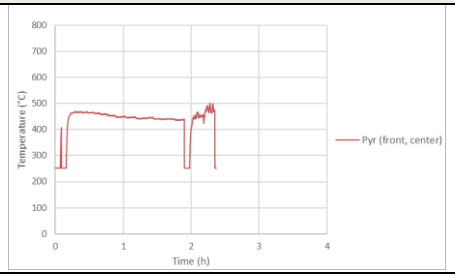	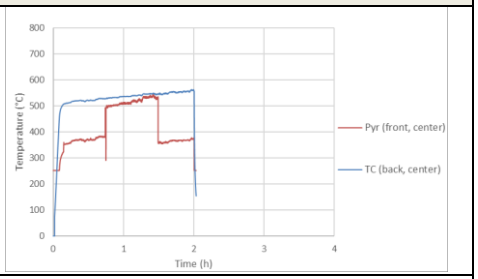
Support 1 (no cooling)	$T_{eff\text{-}pyr}$ = 359°C, $T_{max\text{-}pyr}$ = 377°C 1 cycle 6h	$T_{eff\text{-}pyr}$ = 529°C, $T_{max\text{-}pyr}$ = 558°C 1 cycle 1h15	$T_{eff\text{-}pyr}$ = 449°C, $T_{max\text{-}pyr}$ = 502°C 1 cycle 2h05	$T_{eff\text{-}TC}$ = 517°C, $T_{max\text{-}TC}$ = 563°C 1 cycle 2h
1830AR01-09 250-200 kW/m² 200s/60s 225 cycles 16h16 **T_{eff} = 456°C**	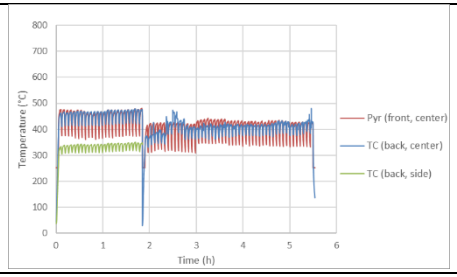	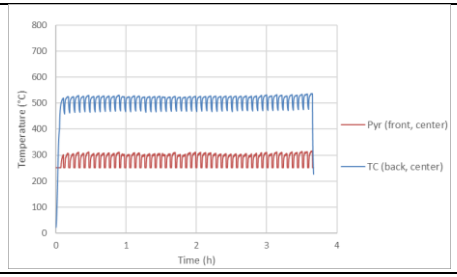	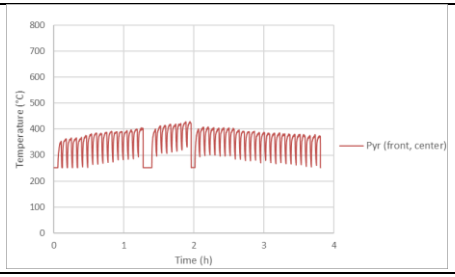	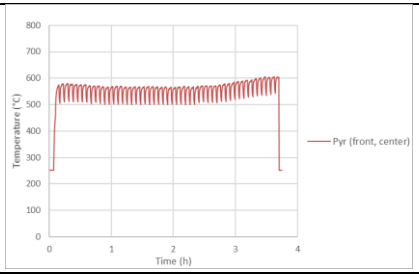
Support 1 (no cooling)	$T_{eff\text{-}pyr}$ = 417°C, $T_{max\text{-}pyr}$ = 481°C 75 cycles 5h25	$T_{eff\text{-}TC}$ = 507°C, $T_{max\text{-}TC}$ = 538°C 50 cycles 3h37	$T_{eff\text{-}pyr}$ = 364°C, $T_{max\text{-}TC}$ = 429°C 50 cycles 3h37	$T_{eff\text{-}pyr}$ = 557°C, $T_{max\text{-}pyr}$ = 606°C 50 cycles 3h37

Table 37. Effective irradiance and dose with with constant solar irradiance of 250 kW/m² and cyclic solar irradiance of 250-200 kW/m²

Sample	State	Number of cycles	I_{max} (kW/m²)	I_{min} (kW/m²)	ΔI (kW/m²)	Duration of I_{max} phase (s)	Duration of I_{min} phase (s)	Time at I_{max} (h)	Time at I_{min} (h)	Total duration (h)	I_{eff} (kW/m²)	Irradiance dose (kWh/m²)	T_{eff} (°C)	Thermal dose (°C·h)
1830AR01-08	After treatment 4	_	250	_	_	_	_	_	_	11.33	250	2833	422	4783
1830AR01-09	After treatment 3	175	250	200	50	200	60	9.72	2.92	12.64	238	3014	428	5409
1830AR01-09	After treatment 4	225	250	200	50	200	60	12.50	3.75	16.25	238	3875	456	7410

3.3. Influence of irradiance/temperature amplitudes in cyclic solar aging

3.3.1. Low-medium irradiance/temperature amplitudes

The influence of the amplitudes in irradiance and temperature during cyclic solar aging was studied by submitting equivalent samples to the two different solar aging conditions presented in Table 38. Sample 1828AR01-IN2 was aged under solar irradiance cycles of 300-250 kW/m² with an amplitude $\Delta I_1 = I_{high} - I_{low}$ = 50 kW/m² (using support 1 without cooling). Sample 1830AR01-03 was tested under cycles of 300-50 kW/m² with an amplitude ΔI_2 = 250 kW/m² (using support 4 with cooling). In both cases, the duration of each cycle is 260s: 200s for the high irradiance phase (300 kW/m²) and 60s for the low irradiance phase (250 or 50 kW/m²) (Figure 161). The cycles were applied in several sets of 50 to 63 of these cycles, representing 3h37 to 4h33 each. Similar total aging durations of approx. 15h were reached.

Table 38. Number of aging cycles and durations, and resulting macroscopic and SEM images of the sample surface

Aging conditions	***Reference***	**Treatment 1**	**Treatment 2**	**Treatment 3**	**Treatment 4**
Cyclic solar aging ***300-250 kW/m²*** ΔI_1 = 50 kW/m² Support 1 (no cooling) *Sample 1828AR01-IN2*	*Cured (24h 500°C air)* 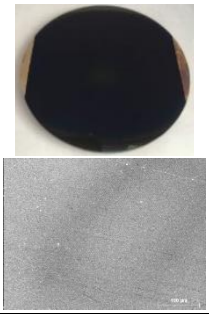	After 50 cycles (3h37) -	After 100 cycles (+3h37 = 7h14) 	After 150 cycles (+3h37 = 10h51) -	After 200 cycles (+3h37 = 14h28) 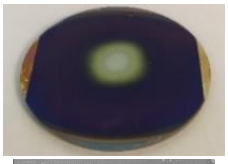
Cyclic solar aging ***300-50 kW/m²*** ΔI_2 = 250 kW/m² Support 4 (cooling) *Sample 1830AR01-03*	*Cured (24h 500°C air)* 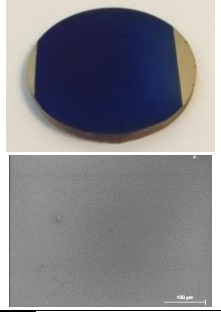	After 50 cycles (3h37) 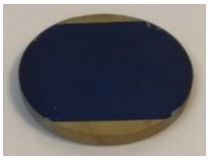	After 100 cycles (+3h37 = 7h14) 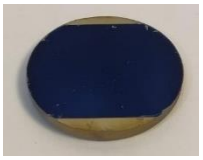	After 163 cycles (+4h33 = 11h47) 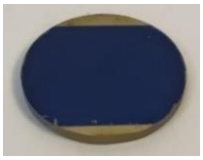	After 213 cycles (+3h37 = 15h24) 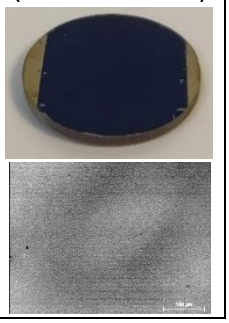

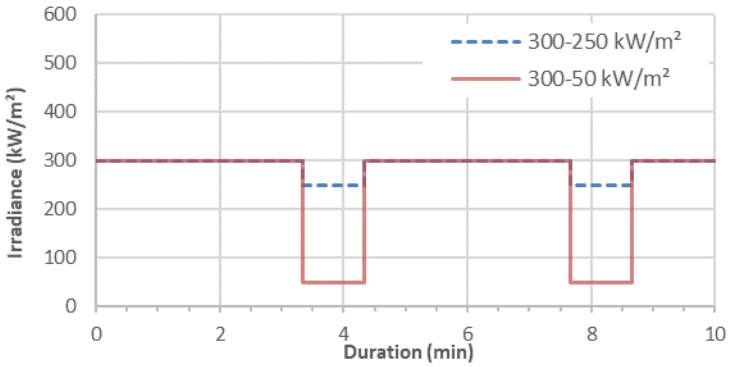

Figure 161. Irradiance levels applied in SAAF (cyclic solar aging at 300-250 kW/m² and 300-50 kW/m²)

Table 38 also shows macroscopic and SEM images of the samples surface after applying the different sets of cycles. To the naked eye, the surface of the sample treated with the irradiance cycle of lower amplitude (300-250 kW/m²) presents a visible change in color from blue to yellow-white in the irradiated area (center of the sample), while for the other sample the surface stays the same after applying all the treatments. At the microscopic scale, SEM images show no differences in surface morphology between cured and aged state, whatever the irradiance cycles.

Figure 162 shows the variations in reflectance spectra after the different aging treatments for the two cyclic conditions. The sample treated at 300-250 kW/m², with the visible change in color, predictably presents the greatest change in optical properties. Reflectance fluctuations appear and intensify with increasing the number of aging cycles, indicating a change in its chemical nature, as previously observed. This is confirmed by EDS measurements done on the TiAlN absorber coatings after the 200 aging cycles (Figure 127): the atomic content in O is slightly increased with aging, while the detected content in elements from the Inconel substrate (Ni to Mo) slightly decreases. Therefore, it is probable that an oxide is slowly growing, as was previously observed with thermal aging on this type of absorber.

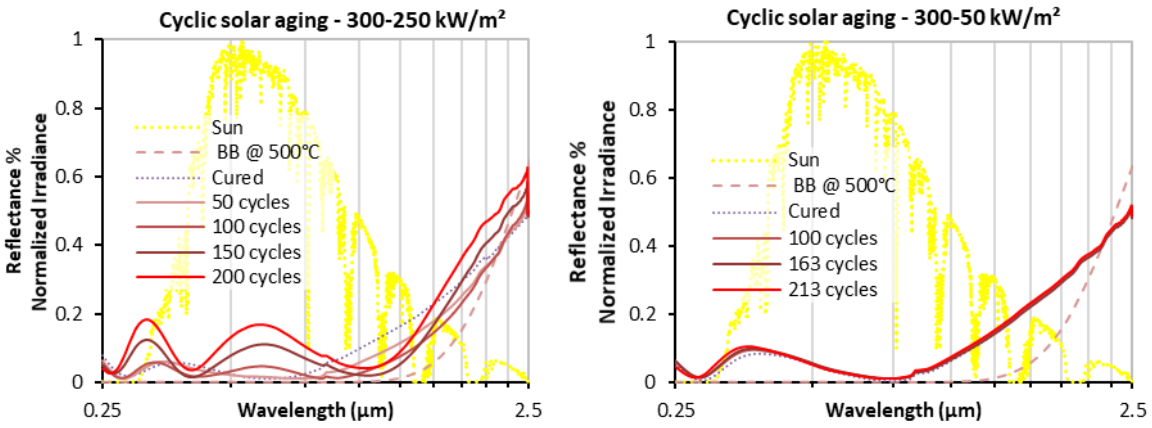

Figure 162. Evolution of the spectral reflectance of the samples treated in SAAF with two different irradiance cycles

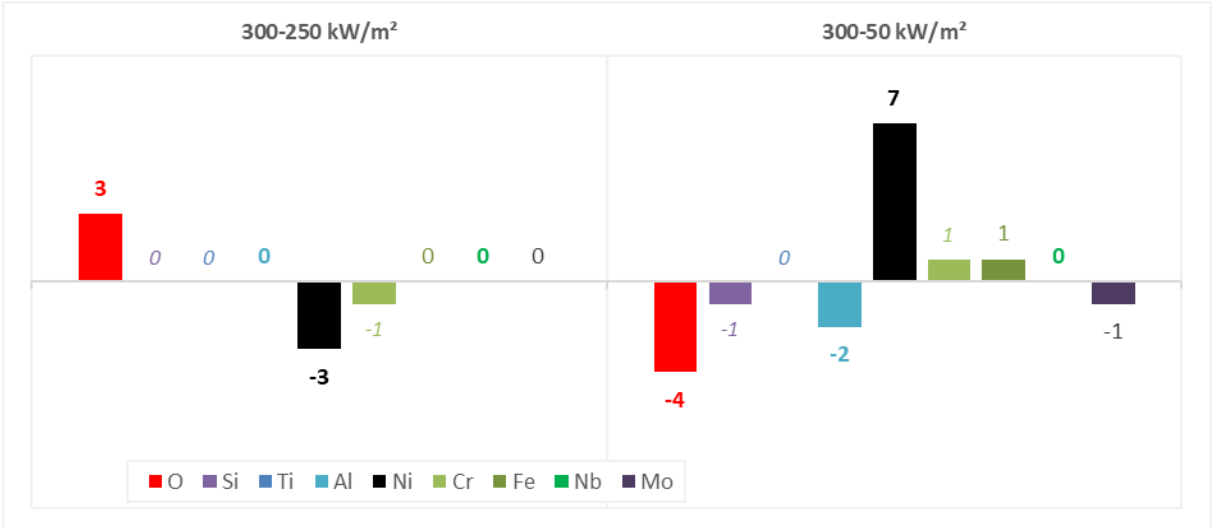

Figure 163. Variation in atomic content (in at.%, measured by EDS) after 200 cycles vs. cured state for the two conditions

As a result, the solar absorptance of the sample treated at 300-250 kW/m² evolves more much notably than that of the sample treated at 300-50 kW/m² (Figure 164). At 300-250 kW/m², it first increases thanks to a decrease in NIR reflectance, then strongly decreases due to the increase in reflectance in the visible range (Figure 162). Meanwhile at 300-50 kW/m², reflectance and solar absorptance barely evolve with aging. EDS measurements after the 200 aging cycles (Figure 127) show that elements from

the substrate are more strongly detected after aging, to the detriment of the elements present in the TiAlN coating (O [3], Ti, Al). These results indicate that the coating tends to thin with aging, probably due to its densification, without notably changing its chemical nature and thus its optical performance.

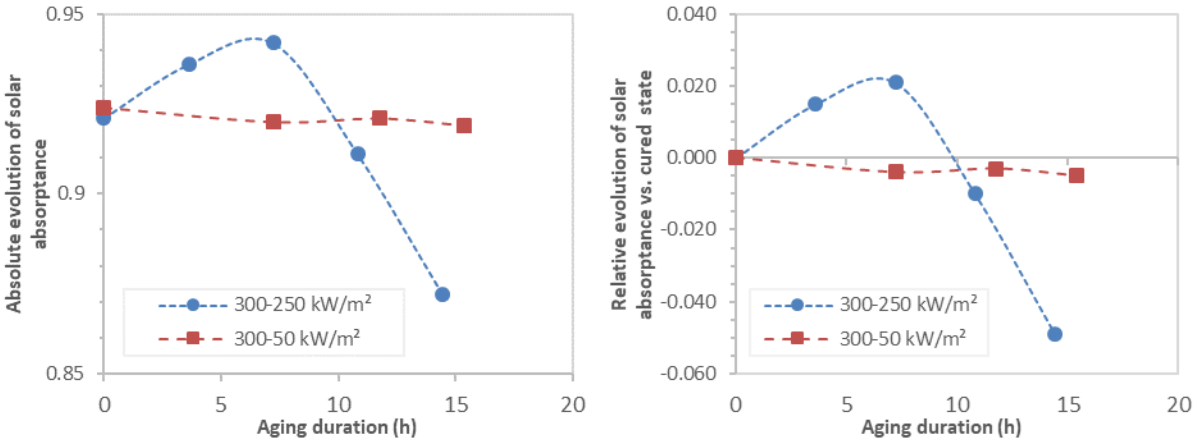

Figure 164. Absolute (left) and relative (right) evolutions of solar absorptance for two cyclic solar irradiations vs. cured state (0h)

Table 39 reports the temperature profiles corresponding to the aging treatments considered here (N.B. pyrometer measurements on the irradiated area are the most reliable but were not systematically possible due to technical problems). The high-low irradiance cycles with irradiance amplitudes ΔI_1 = 50 kW/m² (300-250 kW/m² cycles) and ΔI_2 = 250 kW/m² (300-50 kW/m² cycles) translate into high-low temperature cycles, respectively with temperature amplitudes $\Delta T_1 = T_{high} - T_{low}$ = 100°C (between 550 and 450°C) and ΔT_2 = 250°C (between 500 and 250°C). The highest irradiance amplitude gives rise to the highest temperature amplitude, creating larger thermal shocks to the absorber sample. Therefore, it could be expected that the sample treated with the lowest irradiance/temperature amplitude (300-250 kW/m², ΔI_1 = 50 kW/m², ΔT_1 = 100°C) would be less degraded, yet it is the most affected by aging. Several reasons justify this fact.

First, the effective irradiance seen by the sample is lower for the higher irradiance amplitude, as it takes into account the time spent at both low and high irradiance levels: $I_{eff,\,2}$ = 242 kW/m² for ΔI_2 = 300 – 50 = 250 kW/m² vs. $I_{eff,\,1}$ = 288 kW/m² for ΔI_1 = 300 – 250 = 50 kW/m² (Table 40). The higher degradation observed at lower irradiance/temperature amplitude (ΔI = 50 kW/m², ΔT = 100°C) could thus be caused by a higher effective irradiance and irradiance dose, and subsequently higher energy and photon fluxes, inducing irreversible damage.

Also, with similar high temperature levels T_{high}, a higher temperature amplitude ΔT during cyclic solar aging implies that the effective temperature and thermal dose seen by the sample are necessarily lower. Indeed, the global effective temperature at 300-50 kW/m² (ΔT_2 = 250°C) is lower: T_{eff} = 369°C vs. 524°C for 300-250 kW/m² [4]. This could also explain the lower impact of aging on this sample.

[3] Even though oxygen is not initially present in the TiAlN absorber coating, it is detected after the curing step (24h at 500°C in air) which serves as the reference state for the solar aging tests.

[4] The real effective temperature of the sample exposed at 300-50 kW/m² is probably higher than 369°C. Indeed, pyrometry measurements were incoherent for the last three treatments. Therefore in some cases the temperature profiles considered for the calculation of T_{eff} are the ones measured with the (back, center) thermocouple. The latter tends to be an underestimation of the surface temperature of the sample, as seen during the first treatment (see Table 39).

Additionally, during the 300-250 kW/m² treatments, temperature reached higher levels for longer durations, up to 600°C, due to the natural fluctuations in solar irradiance (DNI) during the day. Indeed, this sample was treated during an early campaign and due to its shape (round, 2" in diameter), support 1 was used for these tests. Therefore, backside air cooling could not be applied, making it harder to control the temperature level during the experiments. Contrarily, the sample treated at 300-50 kW/m² was air-cooled during aging (as support 4 was then available), thus its temperature was better controlled, staying below 550°C at all times, except for a very short overshoot around 630°C.

Overall, this study indicates that **increasing the amplitudes in irradiance and temperature (thermal shocks) during cyclic solar aging does not have a notable impact on absorber coatings microstructure and performance**. In fact, significantly larger amplitudes of solar irradiance (ΔI = 250 vs. 50 kW/m²) and temperature (ΔT = 250°C vs. 100°C) during solar cyclic aging did not affect the materials. Contrarily, the latter were significantly more affected by aging at low cycling amplitudes, due to the higher temperature maintained during the tests (550-600°C for ΔI = 50 kW/m² vs. 500-520°C for ΔI = 250 kW/m²), in combination with the inherent higher effective temperature and effective irradiance (524°C and 288 kW/m² for ΔI = 50 kW/m² vs. 369°C and 250 kW/m² for ΔI = 250 kW/m²). This again underlines the impact of the time actually spent under high solicitation (see section 3.2).

This example is a good illustration that solar aging is indissociably linked to thermal aging during concentrated solar exposure. Most likely, **concentrated solar irradiance and temperature present combined or even synergistic effects, that are very hard to decorrelate using solar aging tools**. An attempt at decorrelating these effects was nevertheless conducted in parallel, on samples of the WAlSiN absorber coating [330,333]. Indeed, the shape of the samples (30 x 30 mm²) allowed the use of support 2 with efficient backside cooling (Table 10 p.111). Thus in this case, the applied concentrated solar irradiance and the resulting temperature of the sample could be controlled more independently: the sample temperature was maintained around or under 400°C whatever the solar irradiance. Applying similar cyclic solar aging (200 cycles of 200s/60s) at 250-200 kW/m² and 250-50 kW/m² did not result in any significant differences in the coating visual aspect and optical performance (in both cases, $\Delta\alpha_S$ and $\Delta\varepsilon \approx$ -0.01 vs. as-deposited). This led to the conclusion that solar cycling had no influence in itself on this absorber coating, as long as the latter was maintained under its critical temperature (limit of thermal stability). Therefore, **temperature remains a critical parameter** for the aging behavior and durability of absorber coatings, probably due to the fact that many of the aging phenomena involved are thermally-induced (oxidation, diffusion, densification, etc.).

In any case, **no impact of rapid thermal shocks** was observed in the studied range (T_{max} = 550°C or ΔT_{max} = 250°C). Therefore to further study the impact of thermal shocks, larger irradiance/temperature amplitudes were also applied, as presented in the following subsection.

Anyway, even when considering an underestimation by 100-150°C, the real effective temperature seen by the sample would still be lower than 524°C, so the conclusion of this comparison remains valid in this regard.

Table 39. Temperature profiles obtained with solar irradiance cycles of 300-250 kW/m² and 300-50 kW/m²

Conditions	Treatment 1	Treatment 2	Treatment 3	Treatment 4
1828AR01-IN2 300-250 kW/m² 200s/60s 200 cycles 14h28 **T_{eff} = 524°C**	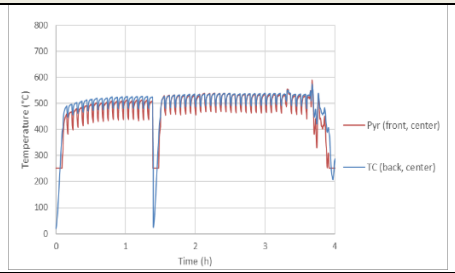	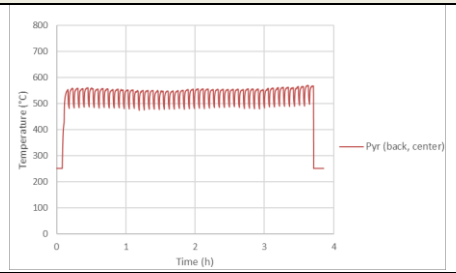	-	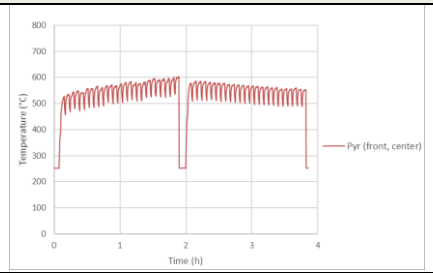
Support 1 (no cooling)	$T_{eff\text{-}pyr}$ = 490°C, $T_{max\text{-}TC}$ = 528°C 50 cycles 3h37	$T_{eff\text{-}pyr}$ = 536°C, $T_{max\text{-}pyr}$ = 570°C 50 cycles 3h37	- 50 cycles 3h37	$T_{eff\text{-}pyr}$ = 548°C, $T_{max\text{-}pyr}$ = 603°C 50 cycles 3h37
1830AR01-03 300-50 kW/m² 200s/60s 200 cycles 15h24 **T_{eff} = 369°C**	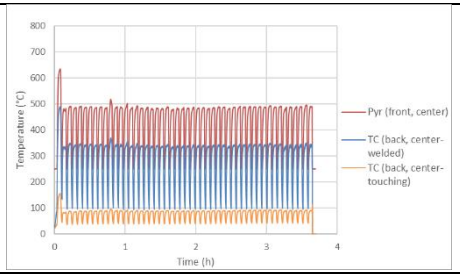	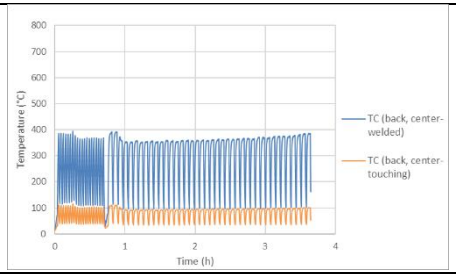	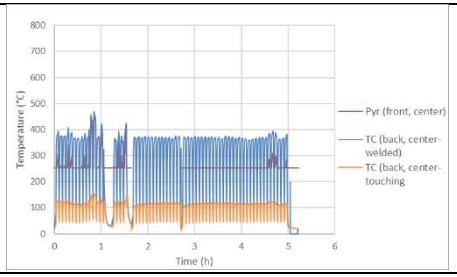	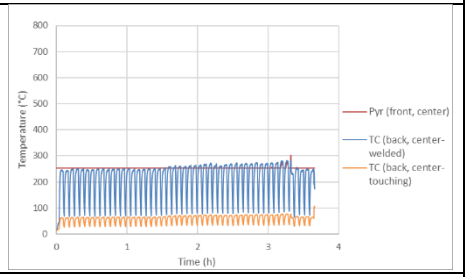
Support 4 (cooling)	$T_{eff\text{-}pyr}$ = 446°C, $T_{max\text{-}pyr}$ = 634°C 50 cycles 3h37	*$T_{eff\text{-}TC}$ = 262°C*, $T_{max\text{-}TC}$ = 395°C 50 cycles 3h37	$T_{eff\text{-}pyr}$ = 326°C, $T_{max\text{-}TC}$ = 469°C 63 cycles 4h33	$T_{eff\text{-}pyr}$ = 269°C, $T_{max\text{-}pyr}$ = 302°C 50 cycles 3h37

Table 40. Effective irradiance and dose with solar irradiance cycles of 300-250 kW/m² and 300-50 kW/m²

Sample	Number of cycles	I_{max} (kW/m²)	I_{min} (kW/m²)	ΔI (kW/m²)	Duration of I_{max} phase (s)	Duration of I_{min} phase (s)	Time at I_{max} (h)	Time at I_{min} (h)	Total duration (h)	I_{eff} (kW/m²)	Irradiance dose (kWh/m²)	T_{eff} (°C)	Thermal dose (°C·h)
1828AR01-IN2	200	300	250	50	200	60	11.11	3.33	14.44	288	4167	524	7569
1830AR01-03	200	300	50	250	200	60	11.83	3.55	15.38	242	3728	369	5676

3.3.2. High amplitudes, impact of high temperature

Cyclic solar aging with large irradiance amplitudes ΔI was applied to three equivalent samples of series 1928 absorber coating. Sample 1928ER01-14 was exposed to 300-50 kW/m² (ΔI = 250 kW/m², support 1), sample 1928ER01-11 to 400-40 kW/m² (ΔI = 350 kW/m², support 4), sample 1928ER01-12 to 500-50 kW/m² (ΔI = 450 kW/m², support 1) (Table 41, Figure 165). In all cases, high and low irradiance phases lasted 60s each. 400 cycles were applied to each sample, for a total duration of approx. 11h to 13h.

Table 41. Number of aging cycles and durations, and resulting macroscopic and SEM images of the sample surface

Aging conditions	***Reference***	**Treatment 1**	**Treatment 2**	**Treatment 3**	**Treatment 4**
Cyclic solar aging ***300-50 kW/m²*** ΔI_1 = 250 kW/m² Support 1 (no cooling) *Sample 1928ER01-14*	*Cured (24h 500°C air)* 	After 25 cycles (0h53) 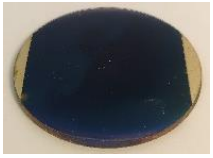	After 125 cycles (+3h20 = 4h13) -	After 225 cycles (+3h20 = 7h33) 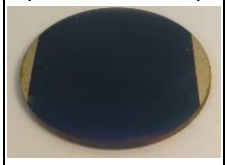	After 325 cycles (+3h20 = 10h53) 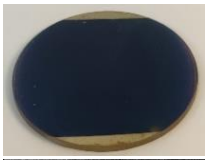 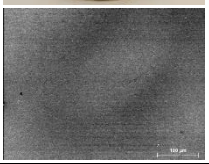
Cyclic solar aging ***400-50 kW/m²*** ΔI_2 = 350 kW/m² Support 4 (cooling) *Sample 1928ER01-11*	*Cured (24h 500°C air)*  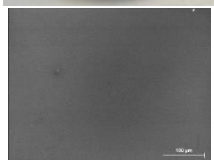	After 100 cycles (3h20) 	After 200 cycles (+3h20 = 6h40) 	After 300 cycles (+3h20 = 10h) 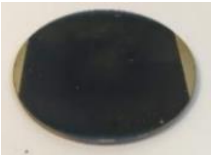	After 400 cycles (+3h20 = 13h20)  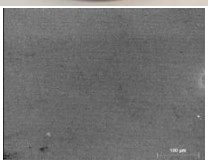
Cyclic solar aging ***500-50 kW/m²*** ΔI_3 = 450 kW/m² Support 1 (no cooling) *Sample 1928ER01-12*	*Cured (24h 500°C air)* 	After 100 cycles (3h20) 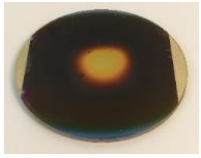	After 200 cycles (+3h20 = 6h40) 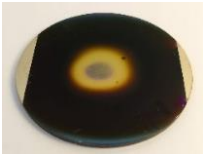	After 300 cycles (+3h20 = 10h) -	After 400 cycles (+3h20 = 13h20) 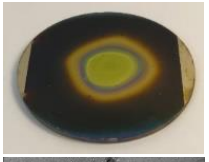 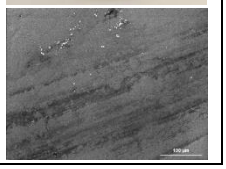

Table 41 shows macroscopic and SEM pictures of the samples after the different treatments. There is no observable change in surface aspect for samples treated at 300-50 kW/m² and 400-50 kW/m². Contrarily, the sample subjected to the highest irradiance level and amplitude (500-50 kW/m²) suffered a significant change, especially a discoloring from blue to yellow in the irradiated area.

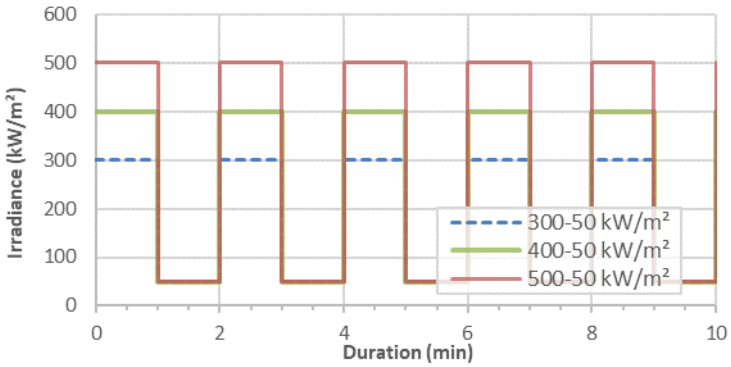

Figure 165. Irradiance levels applied in SAAF (cyclic solar aging at 300-50 kW/m², 400-50 kW/m² and 500 kW/m²)

Figure 166 shows the corresponding evolutions in atomic compositions (EDS) after the last treatment, compared to the cured state. After 400 cycles at 300-50 kW/m², elements from the coating (O to Al) tend to be less detected than in the cured state, while elements from the substrate (Ni to Mo) are slightly more detected, indicating a small decrease in coating thickness with aging, probably due to its densification. The optical properties of this coating are only very slightly affected by aging (Figure 167, Figure 168), consistently with their physical aspect (Table 41). Therefore its thickness must not change very much, nor does its chemical nature.

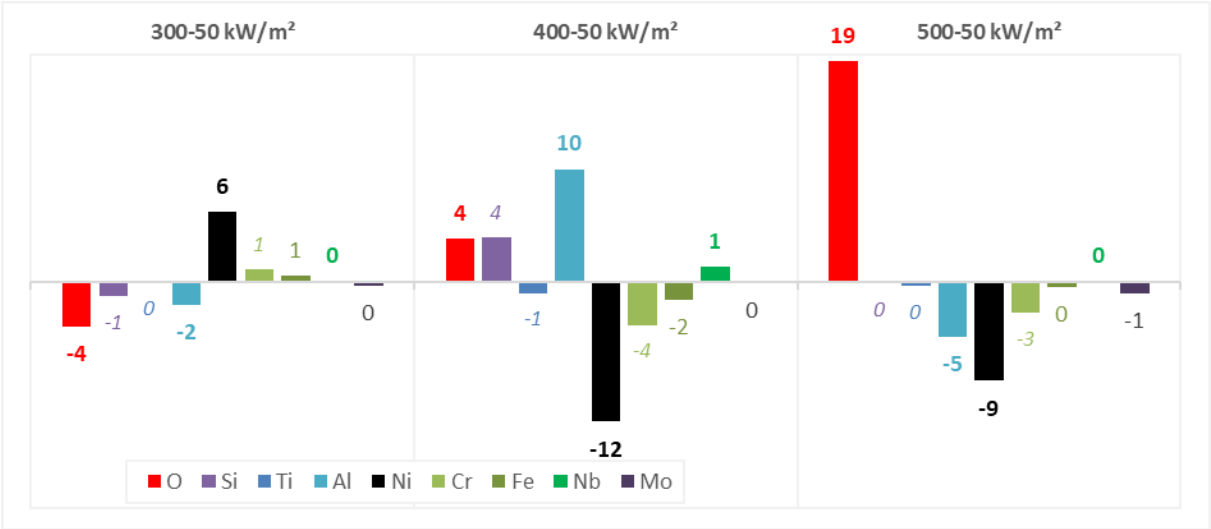

Figure 166. Variation in atomic content (in at.%, measured by EDS) after 200 cycles vs. cured state for the two conditions

After 400 cycles at 400-50 kW/m², elements from the coating are more detected and elements from the substrate are less detected, indicating an increase in the coating thickness. The increase in oxygen content may indicate that this increase could be linked to the coating oxidation. However, there is no visible impact on its optical properties so the changes in chemical nature and thickness must be small.

After 400 cycles at 500-50 kW/m², there is a large increase in the oxygen content, accompanied by a decrease in detected elements from the substrate, indicating a clear oxidation of the coating and an increase in its thickness. The fact that the detected content in Ti does not evolve while that of Al decreases could mean that a titanium oxide tends to form and grow. The hypothesis of an oxide growth is corroborated by the strong evolution of the coating optical properties. Large reflectance oscillations with increasing frequency and amplitude are indeed typical of the formation and growth of a semitransparent oxide in place of the original absorbing material [332]. Consequently, the coating solar absorptance is strongly deteriorated by aging in these harsher conditions ($\Delta\alpha_S$ = -0.25 after 400 cycles).

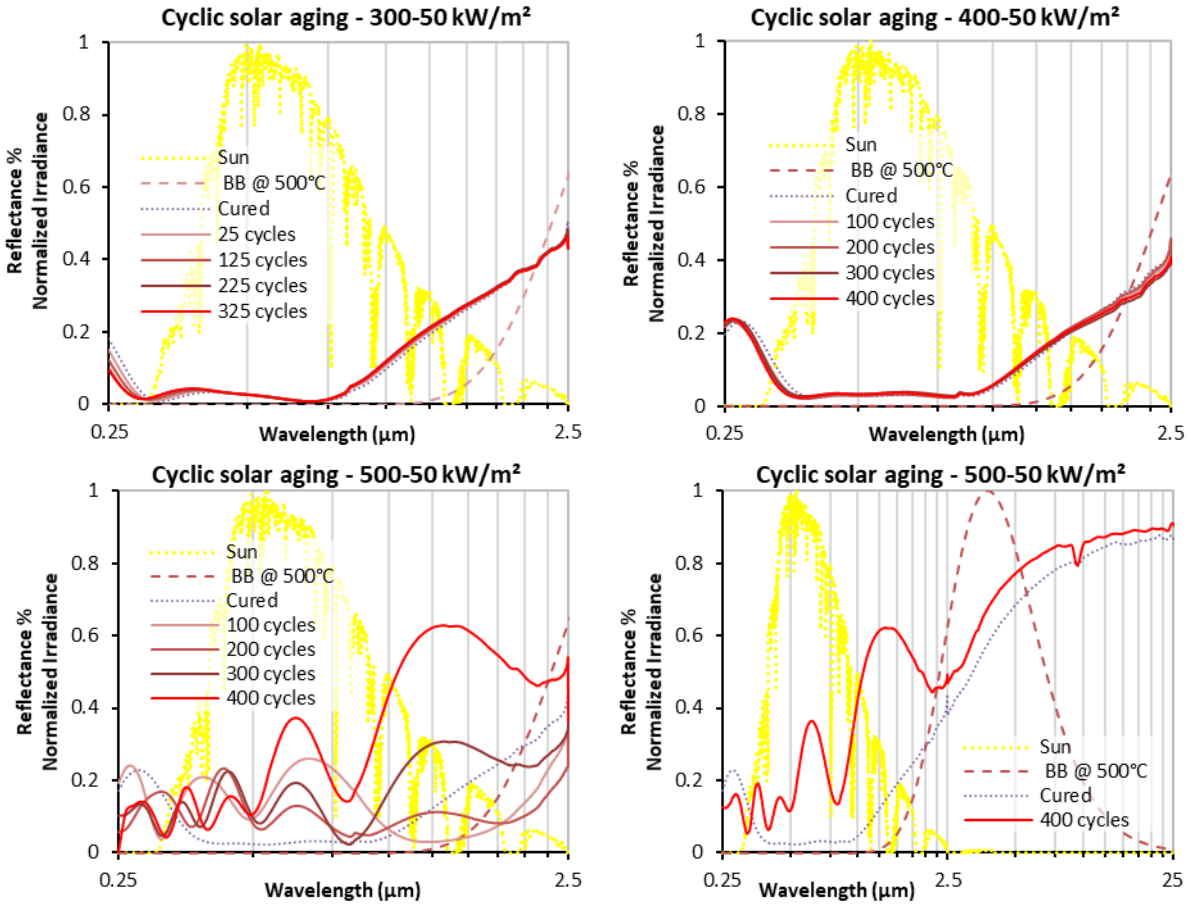

Figure 167. Evolution of spectral reflectance with cyclic solar aging of different amplitudes and high irradiance levels

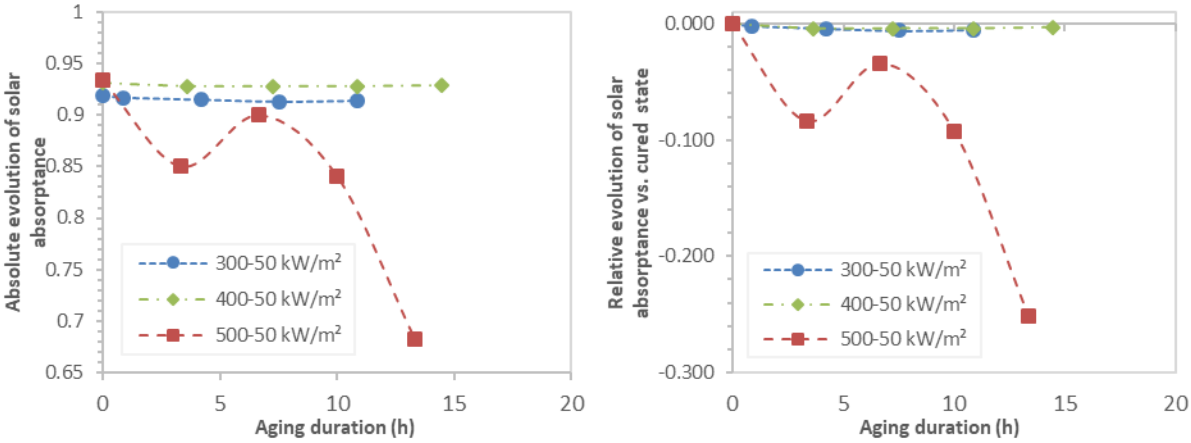

Figure 168. Absolute (left) and relative (right) evolutions of solar absorptance for three cyclic solar irradiations vs. cured state (0h)

Additionally, the sample treated at 500-50 kW/m² was cut after the final treatment to allow for the measurement of its spectral reflectance in the whole spectral range of interest, from 0.25 to 25 µm (Figure 167 bottom right, section 1.1.2 p.168), giving access to its thermal emittance. The latter also decreases strongly with aging, dropping by 8 points (from 0.336 to 0.252). This is directly linked to the evolution in spectral reflectance: as the latter increases in the whole spectral range, it concomitantly causes the strong decreases in solar absorptance and thermal emittance. However, the drop in thermal emittance is not enough to compensate for the degradation of solar absorptance, as the corresponding heliothermal efficiency dramatically drops by almost 25 points (from 0.867 to 0.631).

To better analyze these results, Table 42 shows the temperature profiles recorded during aging tests.

Table 42. Temperature profiles obtained with cyclic solar irradiance of 300-50 kW/m², 400-50 kW/m² and 500-50 kW/m²

Conditions	Treatment 1	Treatment 2	Treatment 3	Treatment 4
1928ER01-14 300-50 kW/m² 60s/60s 325 cycles 10h53 **T_{eff} = 345°C**	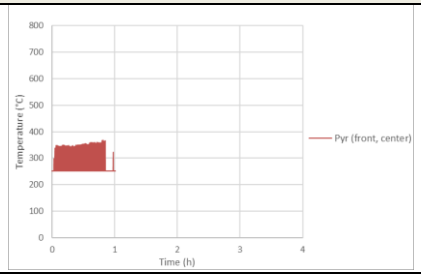	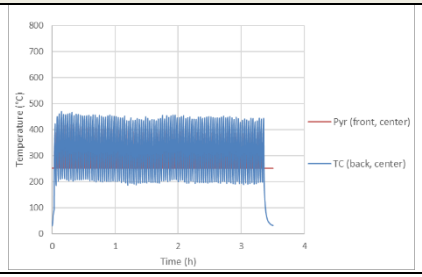	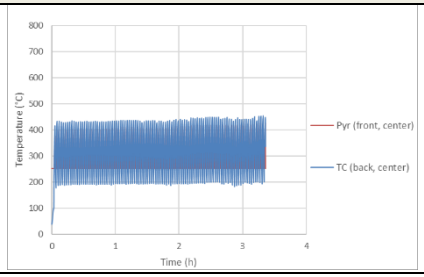	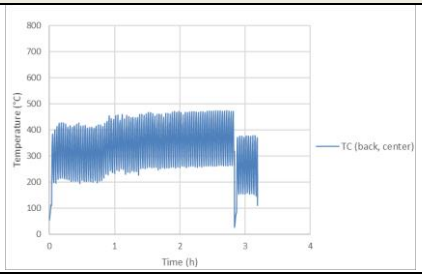
Support 1 (no cooling)	$T_{eff-pyr}$ = 314°C, $T_{max-pyr}$ = 368°C 25 cycles 0h53	$T_{eff-pyr}$ = 349°C, T_{max-TC} = 471°C 100 cycles 3h20	$T_{eff-pyr}$ = 361°C, T_{max-TC} = 454°C 100 cycles 3h20	T_{eff-TC} = 332°C, T_{max-TC} = 474°C 100 cycles 3h20
1928ER01-11 400-50 kW/m² 60s/60s 400 cycles 13h20 **T_{eff} = 390°C**	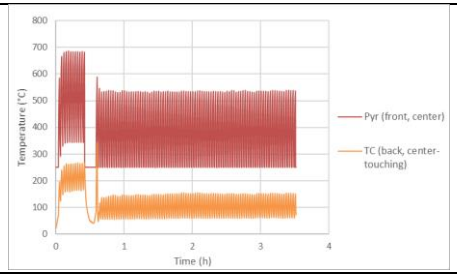	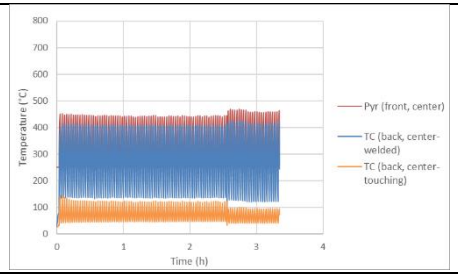	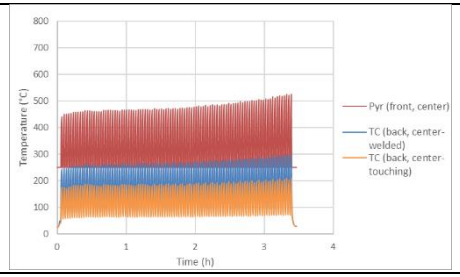	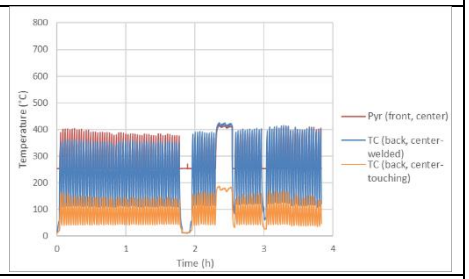
Support 4 (cooling)	$T_{eff-pyr}$ = 429°C, $T_{max-pyr}$ = 687°C 100 cycles 3h20	$T_{eff-pyr}$ =378°C, $T_{max-pyr}$ = 468°C 100 cycles 3h20	$T_{eff-pyr}$ =378°C, $T_{max-pyr}$ = 525°C 100 cycles 3h20	$T_{eff-pyr}$ = 353°C, T_{max-TC} = 425°C 100 cycles 3h20
1928ER01-12 500-50 kW/m² 60s/60s 400 cycles 13h20 **T_{eff} = 516°C**	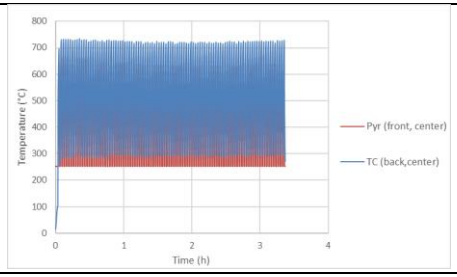	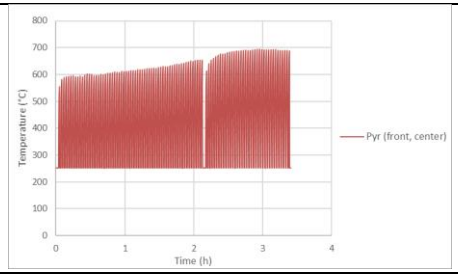	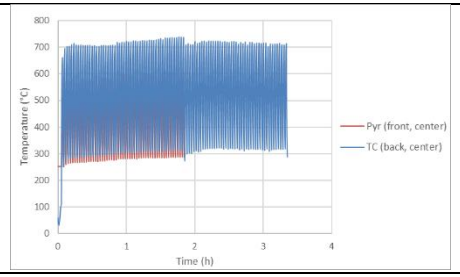	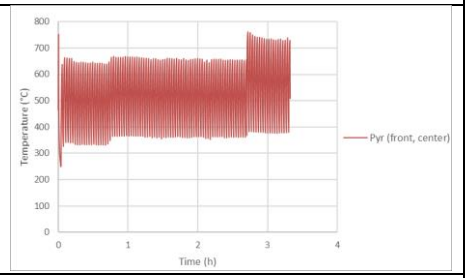
Support 1 (no cooling)	T_{eff-TC} = 513°C, T_{max-TC} = 734°C 100 cycles 3h20	$T_{eff-pyr}$ = 513°C, $T_{max-pyr}$ = 695°C 100 cycles	T_{eff-TC} = 515°C, T_{max-TC} = 739°C 100 cycles 3h20	$T_{eff-pyr}$ = 523°C, $T_{max-pyr}$ = 761°C 100 cycles 3h20

Table 43. Effective irradiance and dose with cyclic solar irradiance of 300-50 kW/m², 400-50 kW/m² and 500-50 kW/m²

Sample	Number of cycles	I_{max} (kW/m²)	I_{min} (kW/m²)	ΔI (kW/m²)	Duration of I_{max} phase (s)	Duration of I_{min} phase (s)	Time at I_{max} (h)	Time at I_{min} (h)	Total duration (h)	I_{eff} (kW/m²)	Irradiance dose (kWh/m²)	T_{eff} (°C)	Thermal dose (°C·h)
1928ER01-14	400	300	50	250	60	60	6.67	6.67	13.33	175	2333	345	3738
1928ER01-11	400	400	50	350	60	60	6.67	6.67	13.33	225	3000	390	5200
1928ER01-12	400	500	50	450	60	60	6.67	6.67	13.33	275	3667	516	6880

Table 44. Temperature profiles obtained with thermal aging at 690°C and cyclic solar aging at 500-250 kW/m²

Conditions	Treatment 1	Treatment 2	Treatment 3	Treatment 4
1616DR01-08 1 cycle 12h **T = 690°C** ALTHAIA	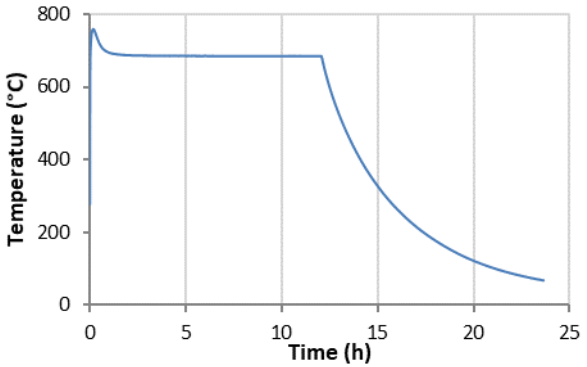			
1830AR01-07 500-250 kW/m² 200s/60s 200 cycles 14h28 **T_{eff} = 708°C**	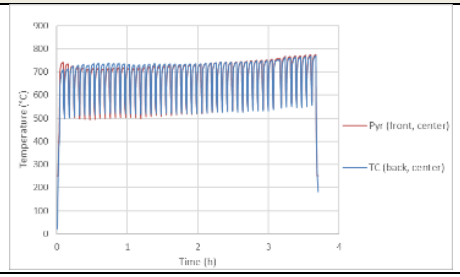	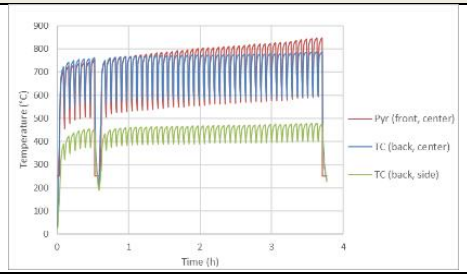	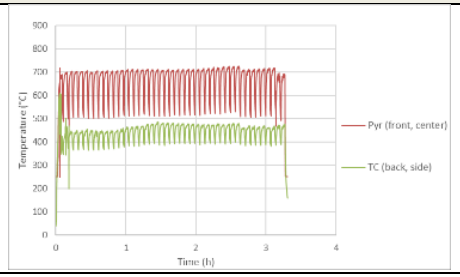	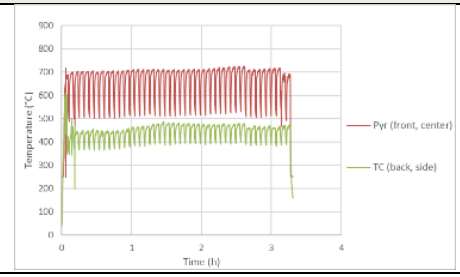
Support 1 (no cooling)	$T_{eff\text{-}pyr}$ = 684°C, $T_{max\text{-}pyr}$= 775°C 50 cycles 3h37	$T_{eff\text{-}TC/pyr}$ = 703/731°C, $T_{max\text{-}TC/pyr}$ = 789/848°C, 50 cycles 3h37	$T_{eff\text{-}pyr}$ = 657°C, $T_{max\text{-}pyr}$ = 726°C 50 cycles 3h37	$T_{eff\text{-}pyr}$ = 759°C, $T_{max\text{-}pyr}$ = 875°C 50 cycles 3h37

During the lowest irradiance aging test at 300-50 kW/m² (I_{eff} = 175 kW/m², Table 43), temperature was also the lowest, in the 200-470°C range, resulting in an effective temperature of 345°C. At 400-50 kW/m² (I_{eff} = 225 kW/m²), temperature was in the 150-550°C range with effective temperature T_{eff} = 390°C and a maximum temperature of 687°C reached for a short time (support 1, no backside cooling). In this second case, temperature was better controlled due the use of backside cooling (support 4), so that the higher irradiance level did not increase the temperature level too much, compared to the 300-50 kW/m². Contrarily, during the highest irradiance test at 500-50 kW/m² (I_{eff} = 225 kW/m²), temperature reached its highest level, in the 300-700°C range, with an effective temperature of 516°C and a maximum temperature of 761°C (support 1, no backside cooling).

Therefore, the observed evolutions in microstructure and optical properties seem to be directly linked to the irradiance and temperature levels seen by the samples during the tests: the higher the irradiance level and amplitude, the higher the temperature, the higher the deterioration. There is a proportionality between irradiance and temperature levels, enhanced by the fact that temperature is not controlled independently with sample backside cooling in two of the three cases. Thus it is difficult to isolate the effects of high irradiance and high temperature, which may well work in synergy.

Anyway, despite a notable difference in irradiance levels and amplitudes between 300-50 kW/m² and 400-50 kW/m² aging tests, no major differences were observed between these two cases. Meanwhile, the corresponding temperature levels are similar (T_{eff} = 345°C vs. 390°C) and remain below the known temperature of thermal stability for such coatings (see Chapter 4). It could thus be argued again that **temperature is a critical, if not predominant, parameter in the solar aging behavior of solar selective absorber coatings**. This question is further discussed in the following subsection.

3.4. Influence of high temperature vs. high solar irradiance

To better distinguish the effects of high temperature and high irradiance, this section compares the aging behavior of TiAlN absorbers under purely thermal aging at 690°C and 800°C (samples 1616DR01-08 and 10, see Chapter 4 section 4 p.147) and under cyclic solar aging conditions reaching similar high temperature levels (T_{eff} = 708°C, T_{max} = 875°C, see Table 44 p.200), thus necessitating even higher irradiance levels of 500-250 kW/m² (200s/60s cycles). Table 45 shows the evolution in surface aspect for the solar-aged sample. Strong changes in color can be observed throughout the treatments. After the first 50 cycles, the irradiated area is yellow-white, then the center of the irradiated area darkens with further treatments. Unfortunately, no pictures were taken of the samples thermally aged at 690°C and 800°C, but no such clear changes in color were observed at similar durations.

Table 45. Number of aging cycles and durations, and resulting macroscopic images of the sample surface

Aging conditions	***Reference***	Treatment 1	Treatment 2	Treatment 3	Treatment 4
Constant solar aging ***500-250 kW/m²*** SAAF Support 1 (no cooling) *Sample 1830AR01-07*	*Cured (24h 500°C air)*	After 50 cycles (3h37)	After 100 cycles (+3h37 = 7h14)	After 150 cycles (+3h37 = 10h51)	After 200 cycles (+3h37 = 14h28)
	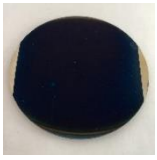	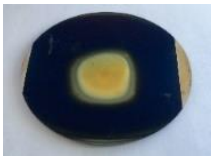	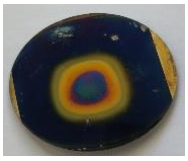	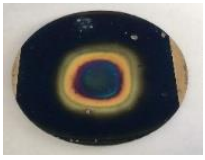	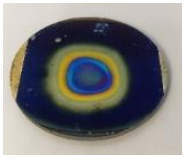

In the meantime, oscillations appear in the UV-Vis-NIR reflectance spectrum after 50 cycles (Figure 169 bottom left), indicating that the coating optical nature changes from absorptive to semitransparent. These oscillations cause a strong solar absorptance drop ($\Delta\alpha_S$ = -0.11, Figure 170 left). After 100 cycles, both the surface color and reflectance spectrum tend to stabilize. The darker irradiated surface gives

rise to a red-shift in spectral reflectance, causing an increase in solar absorptance, though not to its initial level, as well as a large increase in thermal emittance after 200 cycles ($\Delta\varepsilon$ = +0.08, Figure 170).

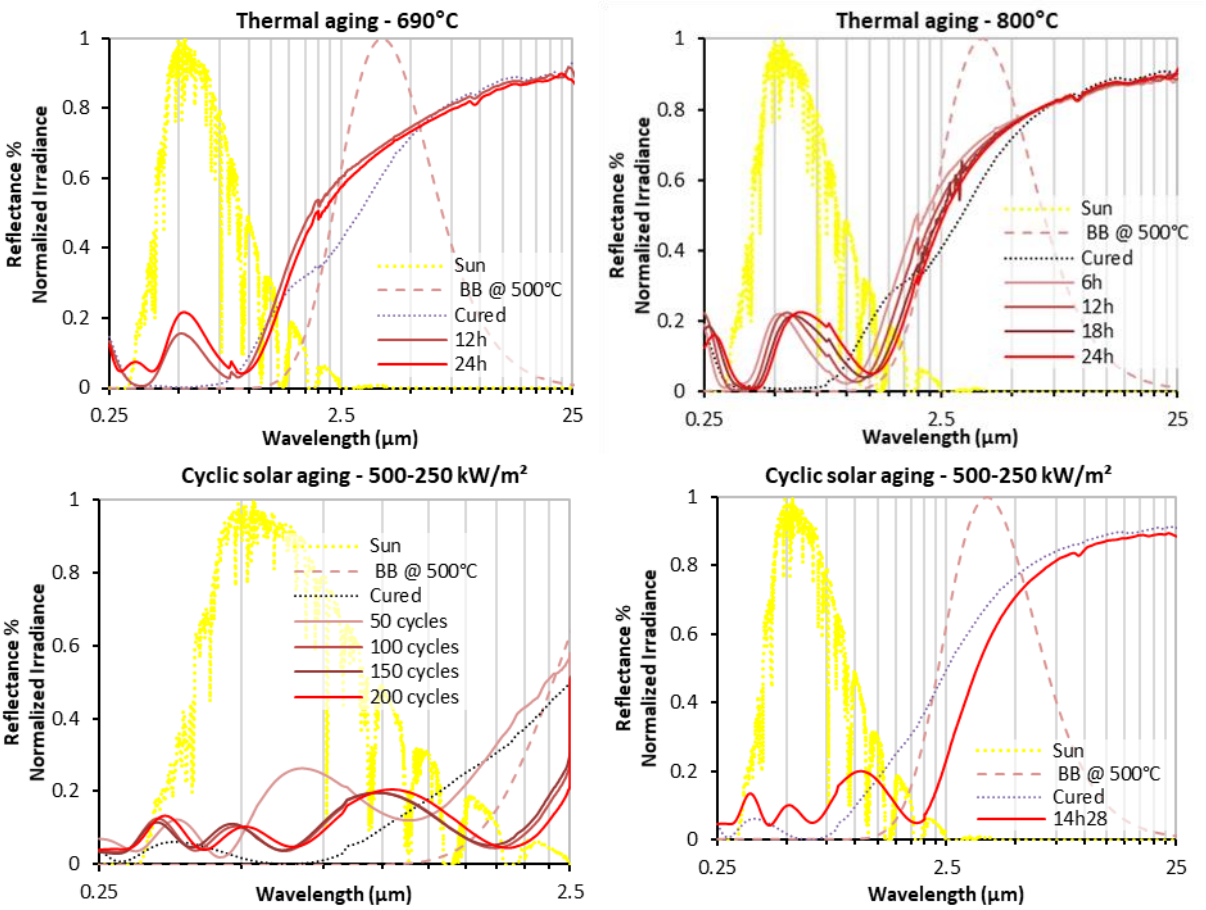

Figure 169. Evolution of spectral reflectance with thermal aging at 690°C (top) vs. cyclic solar aging at 500-250 kW/m² (T_{eff} = 708°C) (bottom)

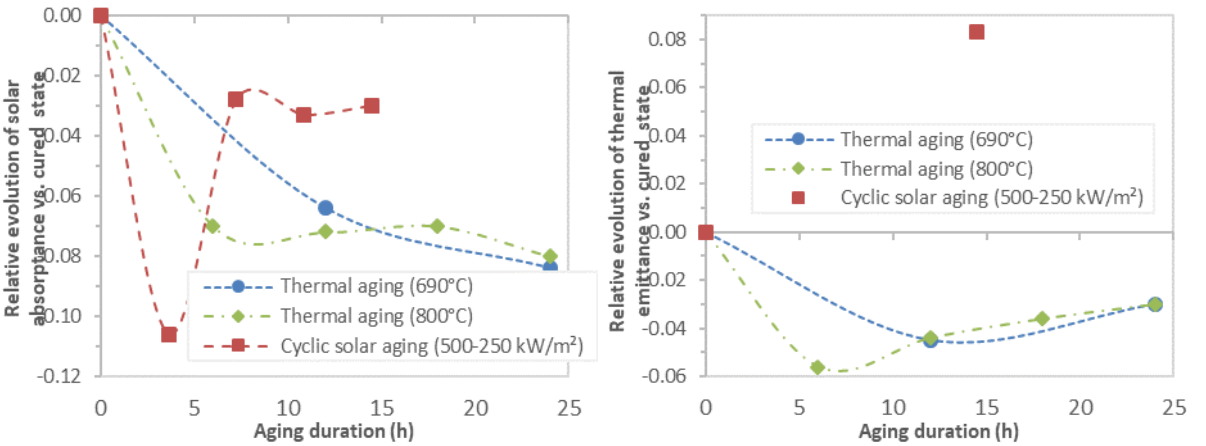

Figure 170. Relative evolutions of solar absorptance (left) and thermal emittance (right) under thermal aging at 690°C and 800°C, and under cyclic solar aging at 500-250 kW/m² (T_{eff} = 708°C)

These evolutions can be correlated to the changes in the material composition observed by EDS (Figure 171). The changes in color and optical properties are linked to a strong increase in the oxygen content, that also tends to stabilize after 100 cycles.

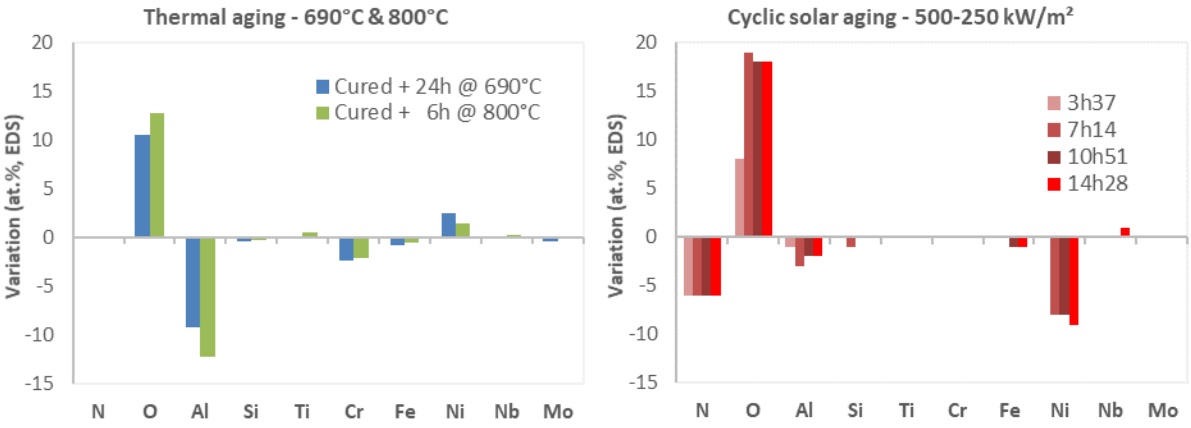

Figure 171. Variations in atomic content (in at.%, measured by EDS): after curing step (24h 500°C) + 24h thermal aging at 690°C and 6h at 800°C, vs. as-deposited state (left); after different durations of cyclic solar aging at 500-250 kW/m² vs. cured state (right)

This increase in oxygen content happens to the detriment of N initially present in the TiAlN absorber, which is no longer detected after 50 cycles. The decrease in elements from the substrate (Ni) indicates that the incorporation of oxygen causes an increase in the coating thickness. As previously observed, such solar aging causes the growth of an oxide, probably in the form of a titanium oxide again. Since the content in Ti does not decrease with the suspected increase in thickness, Ti is not buried under the new oxide but is probably part of it, contrarily to Al since its detected content tends to decrease.

Meanwhile, for thermal aging at similar temperature levels of 690°C and 800°C, similar variations of the coating reflectance spectrum (Figure 169 top) and atomic composition (Figure 171) are observed, indicating that in this case also, the coating is oxidized. However, the consequences on the optical performance are different (Figure 170). Thermal emittance decreases, by down to 5 points at 690°C and 6 points at 800°C, while solar absorptance decreases more steadily, by up to 8 points.

Moreover, if similar chemical phenomena seem to be involved in high temperature thermal aging and high irradiance/ temperature solar aging, the sample under solar aging presents stronger and quicker variations of its visual aspect and optical properties. At similar temperatures, a lower duration under solar aging gives rise to a larger variation in solar absorptance than under thermal aging. Since no additional damaging effect of solar cycling was previously observed (see section 3.2 p.186) the observed changes should not just be due to the high irradiance/temperature amplitudes at 500-250 kW/m². Therefore, these results tend to validate that **there could indeed be an additional and aggravating effect of solar irradiation at high temperature, beyond the effect of high temperature itself**.

4. Discussion and conclusions on thermal and solar aging

In this chapter, the impact of exposing solar selective absorber coatings to concentrated solar irradiance representative of CSP applications ($C \approx 50\text{-}500$) is analyzed in view of **observing the aging phenomena involved, compared to purely thermal aging** studied in Chapter 4. The ulterior motive is to **establish and give recommendations to SSACs developers on the pertinence of including solar aging in their coating failure analysis**, which is usually only centered on thermal aging.

As a forewarning, it is worth noticing that the analysis provided in this chapter is preliminary, as unfavorable technical specificities are to be considered, so that complementary tests will be needed for further validation. For instance, it was found that some of the sample series used for the different tests were not all suitably equivalent in terms of their aging behavior, invalidating the comparison of some of the conditions tested and the decorrelation of some of the sources of degradation, so that these conditions would need to be tested again with more similar samples (see section 3.1 p.182). This highlights the importance of ensuring that large series of perfectly equivalent samples are used, for more comparable aging studies.

Also, in the current SAAF configuration the shutter aperture is the regulated parameter, as a way to control the solar irradiance seen by the sample. This irradiance is only estimated (based on previous calibrations) from the DNI measured at the beginning of the test, although DNI may evolve during the test. Therefore, irradiance is not perfectly regulated, nor is it actually measured. This renders difficult the control of the sample temperature during aging tests, as seen in the irregular temperature profiles presented in this chapter. This is particularly true in this study, since in many cases no backside cooling could be applied due to the shape and size of the samples, that were not adapted to the sample holders available at the time. This is why a new sample holder easily adaptable to different shapes and sizes of samples was developed and will be used in further studies, providing the possibility of backside cooling in all cases, to help with temperature regulation. In parallel, a new SAAF configuration considering the sample temperature as the main regulated parameter was also designed and is under development. It would provide a better control of the temperature profiles imposed on the samples. The comparison of both configurations would help decorrelating the effect of irradiance and temperature.

Moreover, due to incompatible size constraints imposed by the previous sample holders and by the IR spectrophotometer, the IR spectral reflectance in the irradiated area could not be measured in this study, and the evolution of thermal emittance during solar aging is not followed. Thus the conclusions provided here are based solely on the evolution of solar absorptance, which is the main optical parameter for absorber coatings but does not hold information about their selectivity. With the new sample support, smaller samples can be tested, so that this limitation will no longer apply.

Finally, the measurement of sample temperature during solar aging also proved tricky. Indeed, SAAF temperature measurement relies on pyrometry, based on the detection of the irradiance emitted by the hot sample surface around 5 µm. Therefore, low temperatures below 250°C cannot be measured because the emission from the sample at this wavelength is too low, especially since by design solar selective absorber coatings have a low IR emittance. This gives rise to low signal-to-noise ratios that introduce high uncertainties on the measurement of surface temperature by pyrometry. Also, as mentioned the IR emittance could not be measured in the irradiated area after the aging tests, so the emittance implemented in the pyrometer after the first treatment is not the actual emittance of the sample. In addition, the sample emittance can evolve during the aging test itself, causing a drift in the value of temperature given by the pyrometer, compared to its actual value. This effect is clearly visible in Table 44 p.200 (treatment 2) where the maximum temperature read by the pyrometer increases while the one read by the backside thermocouple remains stable. To estimate the uncertainties brought on by these approximations, values of temperature directly given by the pyrometer using the initial emittance as input (e.g. ε_0(5 µm) = 0.219 for sample 1830AR01-07) were compared to corrected values (see correction method in Annex 2.1 p.235) considering the emittance measured on the sample cut after all treatments were applied (ε_4(5 µm) = 0.288): an overestimation of more than 100°C was thus determined. Additional thermocouples were implemented but for obvious reasons they cannot measure the actual temperature of the surface in the irradiated area, so they only give access to an underestimated value of temperature.

Therefore, the temperature profiles provided in this chapter remain approximative. In the future, a solar-blind pyroreflectometry system developed in PROMES-CNRS will be implemented for a more accurate evaluation of surface temperature during SAAF solar aging tests, as it does not rely on the knowledge of the material emittance [334]. Preliminary adaptations of this technique to the SAAF facility have been developed during the SFERA-III EU project, including suitable optics and mechanical supports.

Keeping in mind these practical limitations when analyzing the experimental results obtained in this chapter, some preliminary conclusions can be drawn from this first study.

Under concentrated solar aging, high UV-Vis-NIR solar irradiance levels are reached, irradiating the materials with photons of much higher energy and flux than under IR thermal aging (see section 2.1.2 p.174). Such high irradiance levels could thus give rise to rapid changes in the material microstructure due to photon-matter interactions, that are not accessible with thermal aging. For instance, based on bond dissociation energies in diatomic molecules ($A - B \rightarrow A + B$) and lattice binding energies in crystals [335], energies higher than 3.1 eV (i.e., UV wavelengths below 0.4 µm) are necessary to cause most of these reactions at ambient temperature. In CSP technologies, concentrating optics tend to reduce the UV photon flux but the latter remains high (typically 0.5 to 5 kW/m², see Table 29 p.178), thus probably allowing for lattice rearrangements, especially since the absorber coatings are designed to absorb as much of the incident solar radiation as possible.

Moreover, when absorbing such high solar flux densities, the materials necessarily heat up to reach high levels of temperature. In CSP technologies, part of this heat is extracted by the heat transfer fluid flowing below the absorber. In solar aging facilities, it can be partly extracted using backside cooling. Nevertheless, in both cases the actual temperature profile seen by the absorber coating remains hard to control and regulate, due to high level of incident energy flux provided by solar concentration, compared to the slower heat extraction by convective exchange with the HTF or cooling fluid. So **in addition to high irradiance, absorbers are unavoidably subjected to high temperatures as well**. Therefore, when applying concentrated solar aging, it can be difficult to decorrelate the effects of irradiance and temperature, but their combined effect can be assessed.

Overall, compared to purely thermal aging at similar temperatures, **the combination of high irradiance levels (i.e., high photon and energy fluxes) and high temperature seems to have a stronger and faster effect on the optical performance of the aged absorbers**, especially when applying temperatures higher than the critical temperature of the materials. Similar aging phenomena were observed in both cases, such as oxygen incorporation and oxide growth, but **there could be a synergistic effect between the two sources of degradation, facilitating atomic rearrangements in the material lattice and accelerating such aging phenomena**. Indeed, combining the vibrational energy provided by high temperature with the energy conceded to the lattice via energetic photon-matter interactions, it becomes easier and faster to overcome the energy barriers related to such material evolutions, compared to the energy provided by slow thermal transfers in electrical furnaces.

A simple illustration of this synergy hypothesis lies in the fact that, in some conditions under solar aging, visual changes to the coating surface were observed (strong discoloring in the irradiated area) after only a few hours of aging, when testing at similar temperatures for longer durations under thermal aging did not cause similar evolutions.

Another validation could also be found in the fact that **constant solar aging seems to act faster and more strongly than cyclic solar aging with similar high irradiance level**. Due to the additional lower irradiance phase, the effective (time-weighted) irradiance seen by the tested materials is higher under constant aging. Since this parameter (in kW/m²) is directly linked to the incident photon flux (in photons/m²/s) and energy flux (in J/m²/s, with 1 W ≡ 1 J/s), a higher incident photon flux modifies the coating surface more quickly during the first stages of aging, causing an overall acceleration of aging.

In this light, it seems that **concentrated solar aging representative of CSP applications provide additional photonic phenomena** that may occur at a small physical and time scale (e.g. A°-nm, < s). Due to the energy fluxes involved, they may not be energetic enough to have a large-scale effect on their own. Combined to high temperature, these photonic phenomena mostly seem to **promote and accelerate the thermally-induced aging phenomena obtained when applying purely thermal aging**, without changing their nature and effects at a more "macroscopic" physical and time scale (e.g. µm-mm, hour).

Applying purely thermal aging tests could therefore be sufficient for coating developers in a first approach, provided they are applied at sufficient (representative or accelerated) temperature levels, pertinent working atmosphere and representative durations (several hundreds of hours). Indeed, such aging protocols easily allow investigating the effects of temperature, which is a driving parameter for aging, controlling thermally-induced aging phenomena typical for SSACs, such as oxidation and atomic diffusion.

Despite its more complex implementation, **solar aging remains nonetheless a recommendable step** in the study of the durability of solar selective absorber coatings, as it provides more representative aging conditions, close to the aimed CSP applications, that provoke **additional and possibly synergistic effects in combination with high temperature**. For the analysis of their impact to be more pertinent and valuable, these solar conditions must be as controlled and repeatable as possible, and applied for as long durations as possible, which is more time and resource consuming than simple thermal aging.

General conclusions

As exposed in the first chapter of this thesis, to tackle climate change in a context of ever-expanding energy demand, concentrated solar power (CSP) technologies have been identified as a promising renewable source for heat and electricity generation. These technologies are based on the concentration of the incident solar radiation with mirrors on a solar absorber, inside which flows a heat transfer fluid. This solar absorber must have a high optical performance, achieved through spectral selectivity, i.e., high solar absorptance α_S and low infrared thermal emittance $\varepsilon(T)$, to ensure high solar-to-heat conversion efficiency. Selectivity is obtained with **solar selective absorber coatings** or SSACs (e.g. α_S = 0.95, ε(400°C) = 0.10) deposited on metallic receivers. To increase the global efficiency of CSP technologies and guarantee its deployment, high working temperatures (400-800°C) are desirable, ideally in air to further reduce costs.

Thus as examined in the second chapter, SSACs are subjected to many interconnected **sources of degradation** (e.g. solar radiation with high flux including UV, high temperatures, thermal cycling, thermal shocks, oxidant/corrosive atmospheres) inducing complex **aging phenomena** (e.g. diffusion, oxidation, cracking, fatigue-creep) able to degrade their thermo-optical performance. Therefore, **their aging behavior (thermal stability, durability) must be thoroughly investigated** before they can be implemented in CSP applications. However, after analyzing the literature related to SSACs aging behavior, it was found that the majority of current aging procedures simply consisted in conservative laboratory tests, applying thermal aging in electrical furnaces at moderate temperatures in air or higher temperatures but in vacuum, for rather short durations and without thermal cycling, thus not representative of CSP applications. Also, to this day there is no standardized procedure to evaluate the aging behavior and durability of high temperature SSACs.

After establishing these first assessments based on an extensive literature review, this thesis work developed an experimental study that, in an original manner compared to other studies:

1. was not centered on the analysis of a single type of SSAC that would aim at estimating its reliability and durability. Instead, here three different types of new high temperature air-stable SSACs developed by collaborators (TiAlN and WAlSiN tandem absorber and W/SiC:H multilayer absorber coatings) were considered, with the objective of revealing more **general trends regarding the aging behavior of SSACs**, and thus draw conclusions on the **pertinence of the applied aging procedures** themselves, instead of on the suitability of the coatings;

2. investigated the application of **typical aging procedures** found in the literature for the study of SSACs, using an electrical furnace, i.e., only based on **purely thermal aging**, in order to establish if these procedures are well-suited in a first approach to assess the aging behavior and durability of SSACs, and how to improve them, thus providing **general recommendations to coating developers** for their more pertinent application;

3. additionally investigated **alternative and original aging procedures** for SSACs, more representative of their working conditions in CSP applications, i.e., **solar aging tests** under concentrated solar irradiation in a dedicated solar accelerated aging facility (SAAF) installed at the focal point of a solar furnace, with the objective of **understanding the specific impact on SSACs of several solar aging parameters**, e.g. linked incident solar irradiance and sample temperature profiles, or the additional application of rapid thermal cycling.

4. **compared the impact of purely thermal aging vs. concentrated solar aging** (solar + thermal), to give insight on the **additional impact of the exposure to concentrated solar irradiance** at medium-high temperature, in order to give recommendations to coating developers about the **necessity to include concentrated solar aging protocols** in the durability assessment of their coatings;

5. gathered in-depth knowledge on the **separate impact and possible synergy** between the main sources of degradation affecting SSACs, by decorrelating and/or confronting the observed effects of the different aging parameters accessible;

6. had for ultimate view to propose valuable information to help in **evaluating the possibility and potential establishment of a standardized global aging procedure for SSACs**.

The main conclusions that can be drawn from this original experimental study are the following, and can serve as **recommendations for coating developers**:

1. As a mandatory first step to evaluate the aging behavior of a type of SSAC, large sets of **equivalent samples** should be considered, as far as the repeatability of the manufacturing process allows, in order to apply and compare the effects of several aging conditions on several samples for each condition, and obtain more reliable conclusions. A good equivalence between samples can typically be understood as architectures (in terms of nature and thickness of substrate and coating layers) that are identical or as close as possible, a variation in solar absorptance of 1 point or less ($\Delta\alpha_S \leq 0.01$), and a variation in thermal emittance of 3 points or less ($\Delta\varepsilon \leq 0.03$, as the coatings solar-to-heat conversion efficiency is less sensitive to thermal emittance); in any case, the variation in optical performance with aging should be considered relatively to the reference state of a given sample (e.g. $\Delta\alpha_S = \alpha_S$ (aged) – α_S (as-deposited)).

2. Also, adequate **characterizations of the SSACs materials before and after aging** must be carried out to observe and draw conclusions on the aging behavior, including at least:

    2.1. **spectral optical properties**, in particular hemispherical spectral reflectance, at least in the main UV-Vis-NIR solar range (0.28 – 2.5 µm) to estimate solar absorptance, preferably in the larger and more pertinent UV-MIR "solar selective range" (at least 0.28 – 25 µm), to also estimate thermal emittance and solar-to-heat conversion efficiency, which is the most significant criterion for optical performance. This allows following a potential degradation in performance that would have a direct impact on the global efficiency of the aimed CSP application.

    2.2. **macroscopic pictures of the surface after each aging step**, to keep track of their visual aspect and quickly link it to the other observed evolutions. For instance, a darkening visible to the naked eye can often easily be linked to an increase in solar absorptance. This is a useful and easily accessible information, helpful in the follow-up of the aging behavior. Ideally, these pictures should be taken in a specific photographic studio set-up to avoid parasite reflections on the partially reflective surface.

    2.3. **material composition**, at least to follow the global content in elements (e.g. EDS or WDS), ideally to follow their spatial distribution in the coating (e.g. RBS or XPS depth profiles), as well as **material surface state**, at least to observe major evolutions in microstructure such as cracks or delamination (e.g. optical microscopy, SEM), preferably also to observe evolutions in surface roughness (e.g. AFM, profilometry) which directly influences optical properties. This so as to unveil the aging phenomena at play and understand their consequences on the evolution of the SSACs optical performance.

3. As a mandatory second step, **purely thermal aging** protocols must be implemented:

   3.1. First, **short duration thermal aging** (typically up to 24h) can be applied at different temperatures **around or above the aimed working temperature**, and in the aimed atmosphere (air or vacuum), depending on the intended CSP technology. This type of test is often applied by coating developers as it is easy to implement and gives access to valuable information about the absorber aging behavior (e.g. its **critical temperature**). It often causes slight coating densification and/or oxidation, that can equally result in an improvement or a degradation of the coating optical performance, because **spectral optical properties (optical indices and reflectance) are very sensitive to small variations in thickness and composition**. For instance, the incorporation of oxygen may change the coating optical behavior from absorptive to semitransparent, causing reflectance minima and maxima to appear due to multiple reflections at the coating interfaces. These oscillations increase in frequency and amplitude as the coating thickness increases, so that there is a red-shift of the reflectance spectrum, strongly impacting both solar absorptance and thermal emittance values. If the optical performance improves with short duration aging (typically 24h), it can be considered as the final **curing step** of the fabrication process, instead of an indication of the coating aging behavior. In any case, short duration thermal aging does not provide sufficient information in itself and the **performance evolution trend must be validated by longer duration thermal aging**.

   3.2. As a mandatory next step, **long duration thermal aging** (typically above 100h and up to several thousands of hours) at or near the **aimed working temperature** should be applied to confirm the trends observed at short durations while giving enough time to the coating to stabilize its aging behavior. This should preferably be applied in **short steps** (12-24h) cumulatively on the same samples to better follow the evolution of the coating optical performance and generate slow thermal cycling closer to the CSP application, compared to constant thermal aging. If possible, **long aging durations exceeding several hundreds of hours should be reached**, as several stages of aging may appear with time, due to the different kinetics of the aging phenomena at play (e.g. the slow outward diffusion of metallic elements from the substrate and their subsequent surface oxidation may cause surface defects to appear late in the aging process). Optionally, the comparison of aging tests in **different atmospheres** can help decorrelate competing or synergistic phenomena (e.g. vacuum tests to prevent oxidation processes and better observe the effect of atomic diffusion on the optical performance of the coatings). In any case, this type of aging test gives a **first idea of the long-term thermal stability of SSACs**.

   3.3. As an optional but advised next step, to evaluate SSACs durability, **long duration thermal aging at several accelerated temperatures above the aimed working temperature (max. 200-300°C higher) and close to one another** may be applied. These tests can usually save time and resources by avoiding very long duration testing at the aimed working temperature, as they can accelerate thermally-induced aging phenomena without changing their nature. They may also give access to the **activation energies** of aging/degradation phenomena, that can sometimes be used to predict the lifetime of the coating at working temperature. However, when degradation is ruled by slow reactions, the attainable acceleration of aging is limited and very long durations at accelerated temperatures (e.g. > 1000h) must be applied anyway if one is to establish the SSACs **lifetime and durability**. Since accelerated aging protocols can be heavy to implement and cannot guarantee lifetime prediction, a cost/benefit analysis is to be considered in their implementation.

4. As an optional but highly recommended third step, **concentrated solar aging** can be attempted to test the **SSACs behavior in conditions more representative of CSP applications** (high photon and energy fluxes in the solar range, high heating and cooling rates, etc.), provided suitable facilities are accessible (e.g. solar furnace or high flux solar simulator). Very long durations are not reasonably attainable (due to solar intermittence in solar furnaces or high cost of solar-like lamps in simulators), still such tests provide valuable information on the SSACs aging behavior in more realistic conditions, for instance:

   4.1. In concentrated solar aging, **high incident solar irradiance is indissociable from high surface temperature levels**, even when heat is partly extracted on the absorber backside. It is thus not an adapted method to decorrelate the effects of these two sources of degradation, but instead it reveals their combined effect. The comparison of purely thermal aging and concentrated solar aging highlights that **temperature remains a driving parameter for aging**, as it controls thermally-induced aging phenomena, but concentrated solar irradiance gives rise to **additional photonic phenomena promoting and accelerating thermally-induced aging phenomena, by facilitating atomic rearrangements in the material lattice**. In a first approach, purely thermal aging at appropriate temperatures may thus be sufficient to assess SSACs global aging tendencies, but complementary concentrated solar aging tests are advisable, as they reveal the **synergistic effects between high solar irradiance and high temperature, possibly accelerating SSACs aging in real CSP conditions**.

   4.2. Comparing constant solar aging (typical of stable sunny weather) with short period cyclic solar aging consisting in alternating high and low irradiance phases (typical of cloudy spells), **rapid solar/thermal cycling with the same high irradiance level does not provide additional deterioration** as it in fact reduces the effective temperature/irradiance seen by the materials, so that they are exposed to lower photon and energy fluxes, hindering the abovementioned synergistic effects.

5. In all cases, the **distinction between aging and degradation** must be kept in mind, since an evolution in surface aspect or chemical composition of the SSACs does not necessary lead to a deterioration of their optical performance. In fact, **the relationship between physicochemical aging phenomena** (e.g. oxidation, atomic diffusion, cracks) **and their consequences on SSACs surface optical properties is quite complex and hard to predict**. Indeed, the performance of solar selective absorber coatings (solar absorptance, thermal emittance, solar-to-heat conversion efficiency) intrinsically derives from spectral behaviors (optical indices, reflectance) which are highly sensitive to small changes in the coating chemical/optical nature (e.g. an absorptive nitride or carbide becoming semitransparent when oxidized) and thickness (e.g. an increase in thickness causes a reflectance red-shift increasing thermal emittance). Thus for instance, if it is relatively simple to determine separately the activation energy of an oxidation phenomenon, determining the activation energy leading to a drop in optical performance is not at all straightforward, especially since several aging phenomena are often at play, often with different kinetics, possibly with synergistic or competing effects. For this reason, **a reliable lifetime prediction for SSACs is often hard to obtain**.

6. Finally, if such general recommendations about desirable aging procedures can be established, due to the multiplicity of SSACs architectures and materials explored by coating developers, as well as the variety of CSP technologies, to this day **it remains difficult to propose a unique aging scheme for SSACs with fixed temperature levels and aging durations**. As a start, distinct schemes per type of CSP technology would be better suited, fixing in each case a typical working temperature, to determine temperature levels for purely thermal aging protocols (point 3), as well as a typical solar concentration ratio, to determine concentrated irradiance levels for solar aging protocols (point 4).

Beyond these first recommendations, and in order to complete them, the following paths could be explored, among many possibilities:

1. regarding **purely thermal aging**:

    1.1. since the adsorption of water molecules at the coating surface could enhance and accelerate oxidation/corrosion phenomena, the **specific effect of humid air** at high temperature could be studied, thanks to: i) the comparison of aging behaviors on equivalent samples under ambient air and air filtered from CO_2 and H_2O (tests are underway); ii) the implementation of the full configuration of ALTHAIA facility, which allows controlling the content in water vapor (absolute humidity) contained in the air flow introduced in the low pressure reactor (Figure 91 p.106), so that in addition to the impact of the presence of humidity (compared to dry air tests), the specific impact of the humidity level (water vapor content) could be studied.

    1.2. **additional sources of degradation** could be applied in combination with high temperature, for instance **air pollutants** typically found in the atmosphere, with known corrosive effects (e.g. NO_x compounds), as may be encountered in real CSP conditions.

2. regarding **concentrated solar aging**, complementary aging tests in SAAF facility could be applied:

    2.1. including: i) a more reliable and accurate measurement of sample surface temperature in the irradiated area, not relying on the knowledge of its spectral emittance; ii) the direct and independent regulation of temperature for all tested samples, whatever their dimensions; ii) the follow-up of the thermal emittance of the aged samples in addition to their solar absorptance. All this thanks to the implementation of: i) an in-situ solar-blind pyroreflectometry set-up; ii) another SAAF configuration previously developed for solar curing; iii) the new adaptable sample support developed during this thesis (support 4).

    2.2. in all cases, for **longer durations** than the typical 10 to 15h applied in this work, to better validate the aging tendencies observed, at least reaching 24h to compare with typical thermal aging. One must keep in mind that longer durations (e.g. 100h) would mobilize too much time and resources to be realistic, except if only one aging condition is pursued.

    2.3. to further isolate the **specific effect of rapid solar/thermal cycling**, that was here masked by the predominant influence of the effective irradiance and photon/energy fluxes, cyclic vs. constant solar aging tests with same effective irradiance could be applied on remaining TiAlN absorber samples (e.g. constant 250 kW/m² vs. cyclic 265-200 kW/m² with 200s/60s cycles).

Also, further theoretical and experimental studies would be needed to investigate the apparent coupling and synergy between thermal and photonic effects in CSP applications, compared with purely thermal effects. This is particularly relevant since most aging studies for solar absorbers are conducted in electrical furnaces without the presence of solar photons.

3. regarding **other types of aging**, for instance:

    3.1. **thermomechanical aging protocols** at similar temperature levels than the ones used in purely thermal aging could be investigated, such as fatigue-creep tests with realistic or accelerated mechanical loads compared to the ones encountered in real CSP applications, for instance to account for the presence of a pressurized heat transfer fluid inside the solar receiver, for constraints induced by mismatched thermal expansion coefficients between the different materials of the receiver and coatings, etc. (see Chapter 2);

    3.2. depending on the CSP technology, the absorber coatings may not be protected from other **mechanical degradation phenomena such as particle erosion** in sandy implantation sites, thus their resistance to such sources of degradation could also be tested, using existing facilities usually dedicated to the weathering of concentrating mirrors.

4. Last but not least, the conclusions drawn when applying all the abovementioned aging protocols would need to be **confronted with the real aging behavior of materials that have actually been used in CSP plants for long durations**, in order to validate or reorient them. However, this is rendered difficult by the fact that: i) most SSACs coatings are currently under development, aiming at higher temperature and stability in air, thus will not be used in real CSP installations unless they have first proven their suitability in laboratory aging test conditions; ii) current commercial SSACs in operation could be considered instead, but their working conditions are less demanding (typically, they are operated under vacuum up at 400-580°C or in ambient air below 350°C) and in any case CSP plant operators do not usually share or even collect any information on their aging.

Overall, out of this original thesis work a better understanding and larger view of the general aging behavior of solar selective absorber coatings for high temperature CSP have been gathered, to provide recommendations for more pertinent and global aging procedures, in view of including these recommendations in the potential establishment of a broadly applicable test standard for the investigation and prediction of the thermal stability and durability of these absorber coatings, thus guaranteeing their reliability in real CSP operation and helping in the deployment of CSP technologies for heat and electricity generation.

References

[1] J. Abermann, B. Hansen, M. Lund, S. Wacker, M. Karami, J. Cappelen, Hotspots and key periods of Greenland climate change during the past six decades, Ambio. 46 (2017) 3–11. https://doi.org/10.1007/s13280-016-0861-y.

[2] N. US Department of Commerce, Global Monitoring Laboratory - Global Greenhouse Gas Reference Network. https://www.esrl.noaa.gov/gmd/ccgg/trends/global.html (accessed April 20, 2020).

[3] C. Le Quéré, R.B. Jackson, M.W. Jones, A.J.P. Smith, S. Abernethy, R.M. Andrew, A.J. De-Gol, D.R. Willis, Y. Shan, J.G. Canadell, P. Friedlingstein, F. Creutzig, G.P. Peters, Temporary reduction in daily global CO 2 emissions during the COVID-19 forced confinement, Nature Climate Change. 10 (2020) 647–653. https://doi.org/10.1038/s41558-020-0797-x.

[4] CO2 Emissions from Fuel Combustion 2017, IEA Webstore. https://webstore.iea.org/co2-emissions-from-fuel-combustion (accessed April 20, 2020).

[5] Installed electricity capacity globally by source 2017, Statista. https://www.statista.com/statistics/267358/world-installed-power-capacity/ (accessed April 20, 2020).

[6] Market Report Series: Renewables 2017 – Analysis, IEA. https://www.iea.org/reports/renewables-2017 (accessed April 20, 2020).

[7] Technology Roadmap - Solar Thermal Electricity 2014, IEA Webstore. https://webstore.iea.org/technology-roadmap-solar-thermal-electricity-2014 (accessed April 20, 2020).

[8] Key World Energy Statistics 2017. https://www.oecd-ilibrary.org/energy/key-world-energy-statistics-2017_key_energ_stat-2017-en (accessed April 20, 2020).

[9] Global Solar Atlas. https://globalsolaratlas.info/download/world (accessed April 20, 2020).

[10] Grid Energy Storage - December 2013, Energy.Gov. https://www.energy.gov/oe/downloads/grid-energy-storage-december-2013 (accessed April 27, 2020).

[11] E. González-Roubaud, D. Pérez-Osorio, C. Prieto, Review of commercial thermal energy storage in concentrated solar power plants: Steam vs. molten salts, Renewable and Sustainable Energy Reviews. 80 (2017) 133–148. https://doi.org/10.1016/j.rser.2017.05.084.

[12] T. Okazaki, Electric thermal energy storage and advantage of rotating heater having synchronous inertia, Renewable Energy. 151 (2020) 563–574. https://doi.org/10.1016/j.renene.2019.11.051.

[13] Renewable Capacity Statistics 2019, /Publications/2019/Mar/Renewable-Capacity-Statistics-2019. /publications/2019/Mar/Renewable-Capacity-Statistics-2019 (accessed April 20, 2020).

[14] A. Ummadisingu, M.S. Soni, Concentrating solar power – Technology, potential and policy in India, Renewable and Sustainable Energy Reviews. 15 (2011) 5169–5175. https://doi.org/10.1016/j.rser.2011.07.040.

[15] J.I. Burgaleta, S. Arias, D. Ramirez, GEMASOLAR, THE FIRST TOWER THERMOSOLAR COMMERCIAL PLANT WITH MOLTEN SALT STORAGE, 9.

[16] R. Osuna, R. Olavarría, R. Morillo, M. Sánchez, F. Cantero, V. Fernández-Quero, P. Robles, F. Cerón, J. Talegón, M. Romero, F. Téllez, D. Martínez, A. Valverde, R. Monterreal, R. Pitz-Paal, G. Brakmann, V. Ruiz, M. Silva, P. Menna, PS10, CONSTRUCTION OF A 11MW SOLAR THERMAL TOWER PLANT IN SEVILLE, SPAIN, 9.

[17] Review of commercial thermal energy storage in concentrated solar power plants: Steam vs. molten salts | Request PDF, ResearchGate. https://www.researchgate.net/publication/317266822_Review_of_commercial_thermal_energy_storage_in_concentrated_solar_power_plants_Steam_vs_molten_salts (accessed April 20, 2020).

[18] (PDF) Thermodynamic Assessment of Steam-Accumulation Thermal Energy Storage in Concentrating Solar Power Plants, ResearchGate.

https://www.researchgate.net/publication/335543160_Thermodynamic_Assessment_of_Steam-Accumulation_Thermal_Energy_Storage_in_Concentrating_Solar_Power_Plants (accessed April 20, 2020).
[19] R. Lahlou, P.R. Armstrong, N. Calvet, A.H. Slocum, T. Shamim, Testing of a secondary concentrator integrated with a beam-down tower system under non-liquid cooling strategies, in: Santiago, Chile, 2018: p. 170007. https://doi.org/10.1063/1.5067171.
[20] Z.-J. Zheng, M.-J. Li, Y.-L. He, Optimization of Porous Insert Configuration in a Central Receiver Tube for Heat Transfer Enhancement, Energy Procedia. 75 (2015) 502–507. https://doi.org/10.1016/j.egypro.2015.07.439.
[21] G. Tiryaki, U. Camdali, ENERGY AND EXERGY ANALYSIS OF A SOLAR POWER TOWER SYSTEM WITH A CAVITY RECEIVER, 2017.
[22] G. Barreto, P. Canhoto, M. Collares-Perreira, Modelling and optimisation of porous volumetric receivers in point-focus solar concentration systems, 2020. https://doi.org/10.13140/RG.2.2.24082.81605.
[23] G.K. Manikandan, S. Iniyan, R. Goic, Enhancing the optical and thermal efficiency of a parabolic trough collector – A review, Applied Energy. 235 (2019) 1524–1540. https://doi.org/10.1016/j.apenergy.2018.11.048.
[24] E. Setien, R. López-Martín, L. Valenzuela, Methodology for partial vacuum pressure and heat losses analysis of parabolic troughs receivers by infrared radiometry, Infrared Physics & Technology. 98 (2019) 341–353. https://doi.org/10.1016/j.infrared.2019.02.011.
[25] G. Espinosa-Rueda, J.L. Navarro Hermoso, N. Martínez-Sanz, M. Gallas-Torreira, Vacuum evaluation of parabolic trough receiver tubes in a 50MW concentrated solar power plant, Solar Energy. 139 (2016) 36–46. https://doi.org/10.1016/j.solener.2016.09.017.
[26] W. Platzer, C. Hildebrandt, 15 - Absorber materials for solar thermal receivers in concentrating solar power (CSP) systems, in: K. Lovegrove, W. Stein (Eds.), Concentrating Solar Power Technology, Woodhead Publishing, 2012: pp. 469–494. https://doi.org/10.1533/9780857096173.3.469.
[27] A. Vouros, E. Mathioulakis, E. Papanicolaou, V. Belessiotis, On the optimal shape of secondary reflectors for linear Fresnel collectors, Renewable Energy. 143 (2019) 1454–1464. https://doi.org/10.1016/j.renene.2019.05.044.
[28] R. Abbas, A. Sebastián, M.J. Montes, M. Valdés, Optical features of linear Fresnel collectors with different secondary reflector technologies, Applied Energy. 232 (2018) 386–397. https://doi.org/10.1016/j.apenergy.2018.09.224.
[29] Introduction to Solar Radiation. https://www.newport.com/t/introduction-to-solar-radiation (accessed May 28, 2020).
[30] C. Gueymard, Simple Model for the Atmospheric Radiative Transfer of Sunshine (SMARTS2) Algorithms and performance assessment, FSEC-PF-270-95, 84.
[31] Solar Spectral Irradiance: Air Mass 1.5. https://rredc.nrel.gov/solar//spectra/am1.5/ (accessed April 22, 2020).
[32] C.A. Gueymard, D. Myers, K. Emery, PROPOSED REFERENCE IRRADIANCE SPECTRA FOR SOLAR ENERGY SYSTEMS TESTING, 25.
[33] C. Cintolesi, Large-eddy simulations of conjugate heat transfer with evaporation-condensation and thermal radiation, 2016. https://doi.org/10.13140/RG.2.2.11113.70246.
[34] Soum-Glaude A, Le Gal A, Bichotte M, Escape C, Dubost L, Optical characterization of TiAlNx/TiAlNy/Al2O3 tandem solar selective absorber coatings, Sol. Energy Mater. Sol. Cells. 170 (2017) 254–262. https://doi.org/10.1016/j.solmat.2017.06.007.
[35] A. Dan, A. Soum-Glaude, A. Carling-Plaza, C.K. Ho, K. Chattopadhyay, H.C. Barshilia, B. Basu, Temperature- and Angle-Dependent Emissivity and Thermal Shock Resistance of the W/WAlN/WAlON/Al2O3-Based Spectrally Selective Absorber, ACS Appl. Energy Mater. 2 (2019) 5557–5567. https://doi.org/10.1021/acsaem.9b00743.

[36] A. Boubault, B. Claudet, O. Faugeroux, G. Olalde, J.-J. Serra, A numerical thermal approach to study the accelerated aging of a solar absorber material, Solar Energy. 86 (2012) 3153–3167. https://doi.org/10.1016/j.solener.2012.08.007.
[37] C.E. Kennedy, Review of Mid- to High-Temperature Solar Selective Absorber Materials, 2002. https://doi.org/10.2172/15000706.
[38] R. Winston, Solar Selective Surfaces. By O. P. Agnihotri and B. K. Gupta, Applied Optics. 21 (1982) 292.
[39] Silicone-based thickness insensitive spectrally selective (TISS) paints as selective paint coatings for coloured solar absorbers (Part I) - ScienceDirect. https://www.sciencedirect.com/science/article/abs/pii/S0927024806003485 (accessed March 13, 2022).
[40] I.E. Khodasevych, L. Wang, A. Mitchell, G. Rosengarten, Micro- and Nanostructured Surfaces for Selective Solar Absorption, Advanced Optical Materials. 3 (2015) 852–881. https://doi.org/10.1002/adom.201500063.
[41] C. Heine, R.H. Morf, Submicrometer gratings for solar energy applications, Appl. Opt. 34 (1995) 2476–2482. https://doi.org/10.1364/AO.34.002476.
[42] S.C. Baker-Finch, K.R. McIntosh, Reflection of normally incident light from silicon solar cells with pyramidal texture, Progress in Photovoltaics: Research and Applications. 19 (2011) 406–416. https://doi.org/10.1002/pip.1050.
[43] V. Magnin, J. Harari, M. Halbwax, S. Bastide, D. Cherfi, J.-P. Vilcot, Angle-dependent ray tracing simulations of reflections on pyramidal textures for silicon solar cells, Solar Energy. 110 (2014) 378–385. https://doi.org/10.1016/j.solener.2014.09.025.
[44] M. Bichotte, T. Kämpfe, W. Iff, F. Celle, S. Reynaud, D. Jamon, T. Pouit, A. Soum-Glaude, A. Keilany, L. Dubost, Y. Jourlin, Diffractive gratings to improve TiAlN based spectrally selective solar absorbers, AIP Conference Proceedings. 2033 (2018) 040007. https://doi.org/10.1063/1.5067043.
[45] N. Nguyen-Huu, Y.-L. Lo, Control of Infrared Spectral Absorptance With One-Dimensional Subwavelength Gratings, J. Lightwave Technol. 31 (2013) 2482–2490.
[46] B.J. Lee, L.P. Wang, Z.M. Zhang, Coherent thermal emission by excitation of magnetic polaritons between periodic strips and a metallic film, Opt. Express, OE. 16 (2008) 11328–11336. https://doi.org/10.1364/OE.16.011328.
[47] Y.X. Yeng, M. Ghebrebrhan, P. Bermel, W.R. Chan, J.D. Joannopoulos, M. Soljačić, I. Celanovic, Enabling high-temperature nanophotonics for energy applications, Proc. Natl. Acad. Sci. U.S.A. 109 (2012) 2280–2285. https://doi.org/10.1073/pnas.1120149109.
[48] V. Rinnerbauer, S. Ndao, Y. Xiang Yeng, J.J. Senkevich, K.F. Jensen, J.D. Joannopoulos, M. Soljačić, I. Celanovic, R.D. Geil, Large-area fabrication of high aspect ratio tantalum photonic crystals for high-temperature selective emitters, Journal of Vacuum Science & Technology B. 31 (2012) 011802. https://doi.org/10.1116/1.4771901.
[49] J. Hao, J. Wang, X. Liu, W.J. Padilla, L. Zhou, M. Qiu, High performance optical absorber based on a plasmonic metamaterial, Appl. Phys. Lett. 96 (2010) 251104. https://doi.org/10.1063/1.3442904.
[50] X. Liu, T. Tyler, T. Starr, A.F. Starr, N.M. Jokerst, W.J. Padilla, Taming the blackbody with infrared metamaterials as selective thermal emitters, Phys. Rev. Lett. 107 (2011) 045901. https://doi.org/10.1103/PhysRevLett.107.045901.
[51] E.B. Rubin, S. Shin, Y. Chen, R. Chen, High-temperature stable refractory nanoneedles with over 99% solar absorptance, APL Materials. 7 (2019) 031101. https://doi.org/10.1063/1.5084086.
[52] A. Moreau, C. Ciracì, J.J. Mock, R.T. Hill, Q. Wang, B.J. Wiley, A. Chilkoti, D.R. Smith, Controlled-reflectance surfaces with film-coupled colloidal nanoantennas, Nature. 492 (2012) 86–89. https://doi.org/10.1038/nature11615.
[53] M. Yan, J. Dai, M. Qiu, Lithography-free broadband visible light absorber based on a mono-layer of gold nanoparticles, J. Opt. 16 (2014) 025002. https://doi.org/10.1088/2040-8978/16/2/025002.
[54] J.I. Gittleman, E.K. Sichel, H.W. Lehmann, R. Widmer, Textured silicon: A selective absorber for solar thermal conversion, Appl. Phys. Lett. 35 (1979) 742–744. https://doi.org/10.1063/1.90953.

[55] H.C. Barshilia, S. John, V. Mahajan, Nanometric multi-scale rough, transparent and anti-reflective ZnO superhydrophobic coatings on high temperature solar absorber surfaces, Solar Energy Materials and Solar Cells. 107 (2012) 219–224. https://doi.org/10.1016/j.solmat.2012.06.031.
[56] H. Sai, H. Yugami, Y. Kanamori, K. Hane, Solar selective absorbers based on two-dimensional W surface gratings with submicron periods for high-temperature photothermal conversion, Solar Energy Materials and Solar Cells. 79 (2003) 35–49. https://doi.org/10.1016/S0927-0248(02)00364-1.
[57] N. Selvakumar, H.C. Barshilia, Review of physical vapor deposited (PVD) spectrally selective coatings for mid- and high-temperature solar thermal applications, Solar Energy Materials and Solar Cells. 98 (2012) 1–23. https://doi.org/10.1016/j.solmat.2011.10.028.
[58] A. Dan, H.C. Barshilia, K. Chattopadhyay, B. Basu, Solar energy absorption mediated by surface plasma polaritons in spectrally selective dielectric-metal-dielectric coatings: A critical review, Renewable and Sustainable Energy Reviews. 79 (2017) 1050–1077. https://doi.org/10.1016/j.rser.2017.05.062.
[59] B.O. Seraphin, ed., Solar Energy Conversion: Solid-State Physics Aspects, Springer-Verlag, Berlin Heidelberg, 1979. https://doi.org/10.1007/3-540-09224-2.
[60] Y. Liu, C. Wang, Y. Xue, The spectral properties and thermal stability of NbTiON solar selective absorbing coating, Solar Energy Materials and Solar Cells. 96 (2012) 131–136. https://doi.org/10.1016/j.solmat.2011.09.034.
[61] C.G. Granqvist, G.A. Niklasson, Ultrafine chromium particles for photothermal conversion of solar energy, Journal of Applied Physics. 49 (1978) 3512–3520. https://doi.org/10.1063/1.325263.
[62] G.L. Harding, Evaporated chromium black selective solar absorbers, Thin Solid Films. 38 (1976) 109–115. https://doi.org/10.1016/0040-6090(76)90285-6.
[63] G.A. Niklasson, C.G. Granqvist, Optical properties and solar selectivity of coevaporated Co-Al2O3 composite films, Journal of Applied Physics. 55 (1984) 3382–3410. https://doi.org/10.1063/1.333386.
[64] T.S. Sathiaraj, R. Thangaraj, H. Al Sharbaty, M. Bhatnagar, O.P. Agnihotri, Ni-Al2O3 selective cermet coatings for photothermal conversion up to 500°C, Thin Solid Films. 190 (1990) 241–254. https://doi.org/10.1016/0040-6090(89)90914-0.
[65] J.A. Thornton, J.L. Lamb, Sputter-deposited Pt-Al2O3 selective absorber coatings, Thin Solid Films. 83 (1981) 377–385. https://doi.org/10.1016/0040-6090(81)90644-1.
[66] J. Lafait, S. Berthier, C. Sella, T. Vien, Pt□Al2O3 selective absorber coatings for photothermal conversion up to 600°C, Vacuum. 36 (1986) 125–127. https://doi.org/10.1016/0042-207X(86)90285-X.
[67] Zebib.Y. Nuru, C.J. Arendse, R. Nemutudi, O. Nemraoui, M. Maaza, Pt–Al2O3 nanocoatings for high temperature concentrated solar thermal power applications, Physica B: Condensed Matter. 407 (2012) 1634–1637. https://doi.org/10.1016/j.physb.2011.09.104.
[68] S. John, N. Nagarani, S. Rajendran, Black cobalt solar absorber coatings, Solar Energy Materials. 22 (1991) 293–302. https://doi.org/10.1016/0165-1633(91)90036-K.
[69] Q.-C. Zhang, Y. Yin, D.R. Mills, High efficiency Mo□Al2O3 cermet selective surfaces for high-temperature application, Solar Energy Materials and Solar Cells. 40 (1996) 43–53. https://doi.org/10.1016/0927-0248(95)00078-X.
[70] M. Lanxner, Z. Elgat, Solar selective absorber coating for high service temperatures, produced by plasma sputtering, in: Optical Materials Technology for Energy Efficiency and Solar Energy Conversion IX, International Society for Optics and Photonics, 1990: pp. 240–249. https://doi.org/10.1117/12.20448.
[71] D. Xinkang, W. Cong, W. Tianmin, Z. Long, C. Buliang, R. Ning, Microstructure and spectral selectivity of Mo–Al2O3 solar selective absorbing coatings after annealing, Thin Solid Films. 516 (2008) 3971–3977. https://doi.org/10.1016/j.tsf.2007.07.193.
[72] J. Cheng, C. Wang, W. Wang, X. Du, Y. Liu, Y. Xue, T. Wang, B. Chen, Improvement of thermal stability in the solar selective absorbing Mo–Al2O3 coating, Solar Energy Materials and Solar Cells. 109 (2013) 204–208. https://doi.org/10.1016/j.solmat.2012.11.010.

[73] Q. Zhang, D.R. Mills, New cermet film structures with much improved selectivity for solar thermal applications, Appl. Phys. Lett. 60 (1992) 545–547. https://doi.org/10.1063/1.106602.
[74] Q.-C. Zhang, Metal-AlN cermet solar selective coatings deposited by direct current magnetron sputtering technology, J. Phys. D: Appl. Phys. 31 (1998) 355–362. https://doi.org/10.1088/0022-3727/31/4/003.
[75] Q.-C. Zhang, Direct current magnetron sputtered W–AlN cermet solar absorber films, Journal of Vacuum Science & Technology A. 15 (1997) 2842–2846. https://doi.org/10.1116/1.580837.
[76] Q.-C. Zhang, Development of SS-Aln Cermet Solar Collector Tubes, in: D.Y. Goswami, Y. Zhao (Eds.), Proceedings of ISES World Congress 2007 (Vol. I – Vol. V), Springer, Berlin, Heidelberg, 2009: pp. 1847–1853. https://doi.org/10.1007/978-3-540-75997-3_377.
[77] S. Esposito, A. Antonaia, M.L. Addonizio, S. Aprea, Fabrication and optimisation of highly efficient cermet-based spectrally selective coatings for high operating temperature, Thin Solid Films. 517 (2009) 6000–6006. https://doi.org/10.1016/j.tsf.2009.03.191.
[78] J. Wang, B. Wei, Q. Wei, D. Li, Optical property and thermal stability of Mo/Mo–SiO2/SiO2 solar-selective coating prepared by magnetron sputtering, Physica Status Solidi (a). 208 (2011) 664–667. https://doi.org/10.1002/pssa.201026301.
[79] E. Céspedes, M. Wirz, J.A. Sánchez-García, L. Alvarez-Fraga, R. Escobar-Galindo, C. Prieto, Novel Mo–Si3N4 based selective coating for high temperature concentrating solar power applications, Solar Energy Materials and Solar Cells. 122 (2014) 217–225. https://doi.org/10.1016/j.solmat.2013.12.005.
[80] L. Rebouta, A. Sousa, P. Capela, M. Andritschky, P. Santilli, A. Matilainen, K. Pischow, N.P. Barradas, E. Alves, Solar selective absorbers based on Al2O3:W cermets and AlSiN/AlSiON layers, Solar Energy Materials and Solar Cells. 137 (2015) 93–100. https://doi.org/10.1016/j.solmat.2015.01.029.
[81] A. Antonaia, A. Castaldo, M.L. Addonizio, S. Esposito, Stability of W-Al2O3 cermet based solar coating for receiver tube operating at high temperature, Solar Energy Materials and Solar Cells. 94 (2010) 1604–1611. https://doi.org/10.1016/j.solmat.2010.04.080.
[82] A. Soum-Glaude, I. Bousquet, L. Thomas, G. Flamant, Optical modeling of multilayered coatings based on SiC(N)H materials for their potential use as high-temperature solar selective absorbers, Solar Energy Materials and Solar Cells. 117 (2013) 315–323. https://doi.org/10.1016/j.solmat.2013.06.030.
[83] Q.-C. Zhang, M.S. Hadavi, K.-D. Lee, Y.G. Shen, Zr ZrO2cermet solar coatings designed by modelling calculations and deposited by dc magnetron sputtering, J. Phys. D: Appl. Phys. 36 (2003) 723–729. https://doi.org/10.1088/0022-3727/36/6/315.
[84] Y. Xue, C. Wang, W. Wang, Y. Liu, Y. Wu, Y. Ning, Y. Sun, Spectral properties and thermal stability of solar selective absorbing AlNi–Al2O3 cermet coating, Solar Energy. 96 (2013) 113–118. https://doi.org/10.1016/j.solener.2013.07.012.
[85] H.C. Barshilia, P. Kumar, K.S. Rajam, A. Biswas, Structure and optical properties of Ag–Al2O3 nanocermet solar selective coatings prepared using unbalanced magnetron sputtering, Solar Energy Materials and Solar Cells. 95 (2011) 1707–1715. https://doi.org/10.1016/j.solmat.2011.01.034.
[86] C. Wang, X. Du, T. Wang, L. Zhou, N. Ru, B. Chen, Preparation and optical properties of Nb-NbN multilayer films as solar selective absorptive coatings, Rare Metals. 25 (2006) 355–359. https://doi.org/10.1016/S1001-0521(07)60105-3.
[87] A.R. Shashikala, A.K. Sharma, D.R. Bhandari, Solar selective black nickel–cobalt coatings on aluminum alloys, Solar Energy Materials and Solar Cells. 91 (2007) 629–635. https://doi.org/10.1016/j.solmat.2006.12.001.
[88] E. Wäckelgård, A. Mattsson, R. Bartali, R. Gerosa, G. Gottardi, F. Gustavsson, N. Laidani, V. Micheli, D. Primetzhofer, B. Rivolta, Development of W–SiO2 and Nb–TiO2 solar absorber coatings for combined heat and power systems at intermediate operation temperatures, Solar Energy Materials and Solar Cells. 133 (2015) 180–193. https://doi.org/10.1016/j.solmat.2014.10.022.

[89] A. Schüler, I.R. Videnovic, P. Oelhafen, S. Brunold, Titanium-containing amorphous hydrogenated silicon carbon films (a-Si:C:H/Ti) for durable solar absorber coatings, Solar Energy Materials and Solar Cells. 69 (2001) 271–284. https://doi.org/10.1016/S0927-0248(00)00396-2.
[90] J. Moon, D. Lu, B. VanSaders, T.K. Kim, S.D. Kong, S. Jin, R. Chen, Z. Liu, High performance multi-scaled nanostructured spectrally selective coating for concentrating solar power, Nano Energy. 8 (2014) 238–246. https://doi.org/10.1016/j.nanoen.2014.06.016.
[91] J. Moon, T.K. Kim, B. VanSaders, C. Choi, Z. Liu, S. Jin, R. Chen, Black oxide nanoparticles as durable solar absorbing material for high-temperature concentrating solar power system, Solar Energy Materials and Solar Cells. 134 (2015) 417–424. https://doi.org/10.1016/j.solmat.2014.12.004.
[92] T.K. Kim, B. VanSaders, J. Moon, T. Kim, C.-H. Liu, J. Khamwannah, D. Chun, D. Choi, A. Kargar, R. Chen, Z. Liu, S. Jin, Tandem structured spectrally selective coating layer of copper oxide nanowires combined with cobalt oxide nanoparticles, Nano Energy. 11 (2015) 247–259. https://doi.org/10.1016/j.nanoen.2014.10.018.
[93] L. Di Giacomo, PACVD/PVD de multicouches sélectives pour la conversion thermodynamique de l'énergie solaire, These de doctorat, Perpignan, 2017. http://www.theses.fr/2017PERP0042 (accessed July 15, 2020).
[94] Š.A. Furman, A.V. Tikhonravov, Basics of optics of multilayer systems, Ed. Frontières, Gif-sur-Yvette, 1992.
[95] Å. Andersson, O. Hunderi, C.G. Granqvist, Nickel pigmented anodic aluminum oxide for selective absorption of solar energy, Journal of Applied Physics. 51 (1980) 754–764. https://doi.org/10.1063/1.327337.
[96] M. Born, E. Wolf, Principles of Optics: Electromagnetic Theory of Propagation, Interference and Diffraction of Light, Elsevier, 2013.
[97] C.E. Kennedy, High temperature solar selective coatings, US8893711B2, 2014. https://patents.google.com/patent/US8893711B2/en (accessed May 13, 2020).
[98] L. Rebouta, A. Pitães, M. Andritschky, P. Capela, M.F. Cerqueira, A. Matilainen, K. Pischow, Optical characterization of TiAlN/TiAlON/SiO2 absorber for solar selective applications, Surface and Coatings Technology. 211 (2012) 41–44. https://doi.org/10.1016/j.surfcoat.2011.09.003.
[99] R.N. Schmidt, K.C. Park, R.H. Torberg, J.E. Jensen, High Temperature Solar Coatings, Part I, AST-TDR-63-579, Honeywell Corporation, Hopkins, MN. (1963).
[100] H. Yanbin, Y. Zhiqiang, S. Yueyan, Optical properties of multilayer stack models for solar selective absorbing surfaces, Renewable Energy. 8 (1996) 559–561. https://doi.org/10.1016/0960-1481(96)88918-X.
[101] G.L. Harding, Y. Zhiqiang, S. Craig, S.P. Chow, Sputtered solar selective absorbing surfaces based on aluminum and stainless steel composites, Solar Energy Materials. 10 (1984) 187–207. https://doi.org/10.1016/0165-1633(84)90060-1.
[102] G.A. Niklasson, C.G. Granqvist, Surfaces for selective absorption of solar energy: an annotated bibliography 1955–1981, J Mater Sci. 18 (1983) 3475–3534. https://doi.org/10.1007/BF00540724.
[103] N.P. Sergeant, O. Pincon, M. Agrawal, P. Peumans, Design of wide-angle solar-selective absorbers using aperiodic metal-dielectric stacks, Optics Express. 17 (2009) 22800–22812.
[104] A. Schüler, C. Roecker, J. Boudaden, P. Oelhafen, J.-L. Scartezzini, Potential of quarterwave interference stacks for colored thermal solar collectors, Solar Energy. 79 (2005) 122–130. https://doi.org/10.1016/j.solener.2004.12.008.
[105] M. Farooq, Z.H. Lee, Computations of the optical properties of metal/insulator-composites for solar selective absorbers, Renewable Energy. 28 (2003) 1421–1431. https://doi.org/10.1016/S0960-1481(02)00033-2.
[106] Z.Y. Nuru, C.J. Arendse, T.F.G. Muller, M. Maaza, Structural and optical properties of AlxOy/Pt/AlxOy multilayer absorber, Materials Science and Engineering: B. 177 (2012) 1194–1199. https://doi.org/10.1016/j.mseb.2012.05.028.
[107] R.-C. Juang, Y.-C. Yeh, B.-H. Chang, W.-C. Chen, T.-W. Chung, Preparation of solar selective absorbing coatings by magnetron sputtering from a single stainless steel target, Thin Solid Films. 518 (2010) 5501–5504. https://doi.org/10.1016/j.tsf.2010.04.025.

[108] N. Selvakumar, H.C. Barshilia, K.S. Rajam, A. Biswas, Structure, optical properties and thermal stability of pulsed sputter deposited high temperature HfOx/Mo/HfO2 solar selective absorbers, Solar Energy Materials and Solar Cells. 94 (2010) 1412–1420. https://doi.org/10.1016/j.solmat.2010.04.073.
[109] J.A. Thornton, A.S. Penfold, J.L. Lamb, Sputter-deposited Al2O3/Mo/Al2O3 selective absorber coatings, Thin Solid Films. 72 (1980) 101–110. https://doi.org/10.1016/0040-6090(80)90563-5.
[110] H.C. Barshilia, N. Selvakumar, G. Vignesh, K.S. Rajam, A. Biswas, Optical properties and thermal stability of pulsed-sputter-deposited AlxOy/Al/AlxOy multilayer absorber coatings, Solar Energy Materials and Solar Cells. 93 (2009) 315–323. https://doi.org/10.1016/j.solmat.2008.11.005.
[111] M. Joly, Y. Antonetti, M. Python, M. Gonzalez, T. Gascou, A. Hessler, A. Schueler, Energy-Efficient Sol-Gel Process for Production of Nanocomposite Absorber Coatings for Tubular Solar Thermal Collectors, Proceedings of CISBAT 2013 Cleantech for Smart Cities and Buildings. (2013) 11–16. https://infoscience.epfl.ch/record/195688 (accessed May 13, 2020).
[112] M. Joly, Y. Antonetti, M. Python, M. Gonzalez, T. Gascou, J.-L. Scartezzini, A. Schüler, Novel black selective coating for tubular solar absorbers based on a sol–gel method, Solar Energy. 94 (2013) 233–239. https://doi.org/10.1016/j.solener.2013.05.009.
[113] T. Boström, G. Westin, E. Wäckelgård, Optimization of a solution-chemically derived solar absorbing spectrally selective surface, Solar Energy Materials and Solar Cells. 91 (2007) 38–43. https://doi.org/10.1016/j.solmat.2006.07.002.
[114] Q. Fu, T. Wagner, Interaction of nanostructured metal overlayers with oxide surfaces, Surface Science Reports. 62 (2007) 431–498. https://doi.org/10.1016/j.surfrep.2007.07.001.
[115] J.A. Thornton, J.L. Lamb, Thermal stability studies of sputter-deposited multilayer selective absorber coatings, Thin Solid Films. 96 (1982) 175–183. https://doi.org/10.1016/0040-6090(82)90618-6.
[116] M.G. Hutchins, Spectrally selective solar absorber coatings, Applied Energy. 5 (1979) 251–262. https://doi.org/10.1016/0306-2619(79)90016-3.
[117] W. Graf, F. Brucker, M. Köhl, T. Tröscher, V. Wittwer, L. Herlitze, Development of large area sputtered solar absorber coatings, Journal of Non-Crystalline Solids. 218 (1997) 380–387. https://doi.org/10.1016/S0022-3093(97)00283-4.
[118] M.G. Hutchins, Selective thin film coatings for the conversion of solar radiation, Surface Technology. 20 (1983) 301–320. https://doi.org/10.1016/0376-4583(83)90111-5.
[119] M. Du, X. Liu, L. Hao, X. Wang, J. Mi, L. Jiang, Q. Yu, Microstructure and thermal stability of Al/Ti0.5Al0.5N/Ti0.25Al0.75N/AlN solar selective coating, Solar Energy Materials and Solar Cells. 111 (2013) 49–56. https://doi.org/10.1016/j.solmat.2012.12.010.
[120] H.C. Barshilia, N. Selvakumar, K.S. Rajam, D.V. Sridhara Rao, K. Muraleedharan, Deposition and characterization of TiAlN/TiAlON/Si3N4 tandem absorbers prepared using reactive direct current magnetron sputtering, Thin Solid Films. 516 (2008) 6071–6078. https://doi.org/10.1016/j.tsf.2007.10.113.
[121] A. Carling-Plaza, M.A. Keilany, M. Bichotte, A. Soum-Glaude, L. Thomas, L. Dubost, Demonstration of long-term stability in air at high temperature for TiAlN solar selective absorber coatings, AIP Conference Proceedings. 2126 (2019) 020001. https://doi.org/10.1063/1.5117509.
[122] A. Biswas, D. Bhattacharyya, H.C. Barshilia, N. Selvakumar, K.S. Rajam, Spectroscopic ellipsometric characterization of TiAlN/TiAlON/Si3N4 tandem absorber for solar selective applications, Applied Surface Science. 254 (2008) 1694–1699. https://doi.org/10.1016/j.apsusc.2007.07.109.
[123] H.C. Barshilia, N. Selvakumar, K.S. Rajam, D.V. Sridhara Rao, K. Muraleedharan, A. Biswas, TiAlN/TiAlON/Si3N4 tandem absorber for high temperature solar selective applications, Appl. Phys. Lett. 89 (2006) 191909. https://doi.org/10.1063/1.2387897.
[124] L. Rebouta, A. Pitães, M. Andritschky, P. Capela, M.F. Cerqueira, A. Matilainen, K. Pischow, Optical characterization of TiAlN/TiAlON/SiO2 absorber for solar selective applications, Surface and Coatings Technology. 211 (2012) 41–44. https://doi.org/10.1016/j.surfcoat.2011.09.003.

[125] H.C. Barshilia, Growth, characterization and performance evaluation of Ti/AlTiN/AlTiON/AlTiO high temperature spectrally selective coatings for solar thermal power applications, Solar Energy Materials and Solar Cells. 130 (2014) 322–330. https://doi.org/10.1016/j.solmat.2014.07.037.
[126] J. Feng, S. Zhang, Y. Lu, H. Yu, L. Kang, X. Wang, Z. Liu, H. Ding, Y. Tian, J. Ouyang, The spectral selective absorbing characteristics and thermal stability of SS/TiAlN/TiAlSiN/Si3N4 tandem absorber prepared by magnetron sputtering, Solar Energy. 111 (2015) 350–356. https://doi.org/10.1016/j.solener.2014.11.005.
[127] L. Rebouta, P. Capela, M. Andritschky, A. Matilainen, P. Santilli, K. Pischow, E. Alves, Characterization of TiAlSiN/TiAlSiON/SiO2 optical stack designed by modelling calculations for solar selective applications, Solar Energy Materials and Solar Cells. 105 (2012) 202–207. https://doi.org/10.1016/j.solmat.2012.06.011.
[128] H.C. Barshilia, N. Selvakumar, K.S. Rajam, A. Biswas, Optical properties and thermal stability of TiAlN/AlON tandem absorber prepared by reactive DC/RF magnetron sputtering, Solar Energy Materials and Solar Cells. 92 (2008) 1425–1433. https://doi.org/10.1016/j.solmat.2008.06.004.
[129] J. Jyothi, H. Chaliyawala, G. Srinivas, H.S. Nagaraja, H.C. Barshilia, Design and fabrication of spectrally selective TiAlC/TiAlCN/TiAlSiCN/TiAlSiCO/TiAlSiO tandem absorber for high-temperature solar thermal power applications, Solar Energy Materials and Solar Cells. 140 (2015) 209–216. https://doi.org/10.1016/j.solmat.2015.04.018.
[130] N. Selvakumar, N.T. Manikandanath, A. Biswas, H.C. Barshilia, Design and fabrication of highly thermally stable HfMoN/HfON/Al2O3 tandem absorber for solar thermal power generation applications, Solar Energy Materials and Solar Cells. 102 (2012) 86–92. https://doi.org/10.1016/j.solmat.2012.03.021.
[131] H.C. Barshilia, N. Selvakumar, K.S. Rajam, A. Biswas, Spectrally selective NbAlN/NbAlON/Si3N4 tandem absorber for high-temperature solar applications, Solar Energy Materials and Solar Cells. 92 (2008) 495–504. https://doi.org/10.1016/j.solmat.2007.11.004.
[132] N. Selvakumar, S. Santhoshkumar, S. Basu, A. Biswas, H.C. Barshilia, Spectrally selective CrMoN/CrON tandem absorber for mid-temperature solar thermal applications, Solar Energy Materials and Solar Cells. 109 (2013) 97–103. https://doi.org/10.1016/j.solmat.2012.10.003.
[133] K. Valleti, D. Murali Krishna, S.V. Joshi, Functional multi-layer nitride coatings for high temperature solar selective applications, Solar Energy Materials and Solar Cells. 121 (2014) 14–21. https://doi.org/10.1016/j.solmat.2013.10.024.
[134] Download - Aluminium - ALMECO GROUP. https://www.almecogroup.com/en/pages/631-download (accessed September 7, 2020).
[135] K. Zhang, L. Hao, M. Du, J. Mi, J.-N. Wang, J. Meng, A review on thermal stability and high temperature induced ageing mechanisms of solar absorber coatings, Renewable and Sustainable Energy Reviews. 67 (2017) 1282–1299. https://doi.org/10.1016/j.rser.2016.09.083.
[136] H. Schellinger, M.P. Lazarov, H. Klank, R. Sizmann, Thermal and chemical metallic-dielectric transitions of TiNxOy-Cu absorber tandems, in: Optical Materials Technology for Energy Efficiency and Solar Energy Conversion XII, International Society for Optics and Photonics, 1993: pp. 366–376. https://doi.org/10.1117/12.161977.
[137] H. Schellinger, M.P. Lazarov, W. Assmann, B. Bauer, C. Steinhausen, Improved selective properties of SiO2/TiNxOy-Al tandem absorbers effected by tempering, in: Optical Materials Technology for Energy Efficiency and Solar Energy Conversion XIII, International Society for Optics and Photonics, 1994: pp. 172–181. https://doi.org/10.1117/12.185368.
[138] Products, Home. https://alanod.com/en/products (accessed September 8, 2020).
[139] Thermo Dynamics Ltd. - Sunstrip Solar Absorber Fins. http://www.thermo-dynamics.com/sunstrip.html (accessed September 8, 2020).
[140] asoluna.com, english, Asoluna.Com. https://www.asoluna.com/english (accessed September 8, 2020).
[141] RIOGLASS PTR® 70-4G - Rioglass. https://www.rioglass.com/rioglass-ptr704g/ (accessed September 8, 2020).

[142] Rioglass, Rioglass introduces its next generation “UVAC 7G” receiver tube and sets a new benchmark for thermal output efficiency, Rioglass. (2014). https://www.rioglass.com/rioglass-introduces-its-next-generation-uvac-7g-receiver-tube-and-sets-a-new-benchmark-for-thermal-output-efficiency/ (accessed September 8, 2020).
[143] Archimede Solar Energy. http://www.archimedesolarenergy.it/download.htm (accessed September 7, 2020).
[144] Q.-C. Zhang, Stainless-steel–AlN cermet selective surfaces deposited by direct current magnetron sputtering technology, Solar Energy Materials and Solar Cells. 52 (1998) 95–106. https://doi.org/10.1016/S0927-0248(97)00274-2.
[145] W. Weiss, F. Mauthner, Markets and Contribution to the Energy Supply 2010, (2010) 63.
[146] Q.-C. Zhang, K. Zhao, B.-C. Zhang, L.-F. Wang, Z.-L. Shen, Z.-J. Zhou, D.-Q. Lu, D.-L. Xie, B.-F. Li, New cermet solar coatings for solar thermal electricity applications, Solar Energy. 64 (1998) 109–114. https://doi.org/10.1016/S0038-092X(98)00064-4.
[147] J. Allan, Z. Dehouche, S. Stankovic, L. Mauricette, Performance testing of thermal and photovoltaic thermal solar collectors, Energy Sci Eng. 3 (2015) 310–326. https://doi.org/10.1002/ese3.75.
[148] N. Selvakumar, H.C. Barshilia, K.S. Rajam, Review of sputter deposited mid- to high-temperature solar selective coatings for flat plate/evacuated tube collectors and solar thermal power generation applications, (2010). http://nal-ir.nal.res.in/9637/ (accessed September 7, 2020).
[149] Q.-C. Zhang, D. Mills, A. Monger, Thin film solar selective surface coating, US5523132A, 1996. https://patents.google.com/patent/US5523132A/en (accessed July 16, 2020).
[150] O. Raccurt, A. Disdier, D. Bourdon, S. Donnola, A. Stollo, A. Gioconia, Study of the Stability of a Selective Solar Absorber Coating under Air and High Temperature Conditions, Energy Procedia. 69 (2015) 1551–1557. https://doi.org/10.1016/j.egypro.2015.03.107.
[151] O. Raccurt, F. Matino, A. Disdier, J. Braillon, A. Stollo, D. Bourdon, A. Maccari, In air durability study of solar selective coating for parabolic trough technology, in: 2017: p. 130010. https://doi.org/10.1063/1.4984504.
[152] E. S, D. A, A. A, C. A, F. M, A. Ml, G. A, Optimization procedure and fabrication of highly efficient and thermally stable solar coating for receiver operating at high temperature, Sol. Energy Mater. Sol. Cells. 157 (2016) 429–437.
[153] K. Xu, M. Du, L. Hao, J. Mi, Q. Yu, S. Li, A review of high-temperature selective absorbing coatings for solar thermal applications, Journal of Materiomics. 6 (2020) 167–182. https://doi.org/10.1016/j.jmat.2019.12.012.
[154] Home - SolarPACES. https://www.solarpaces.org/ (accessed November 16, 2020).
[155] J. Karni, Solar-thermal power generation, Annual Review of Heat Transfer. 15 (2012) 37–92. https://doi.org/10.1615/AnnualRevHeatTransfer.2012004925.
[156] L.A. Weinstein, J. Loomis, B. Bhatia, D.M. Bierman, E.N. Wang, G. Chen, Concentrating Solar Power, Chem. Rev. 115 (2015) 12797–12838. https://doi.org/10.1021/acs.chemrev.5b00397.
[157] The Performance of Concentrated Solar Power (CSP) Systems, Elsevier, 2017. https://doi.org/10.1016/C2014-0-03695-7.
[158] G03 Committee, Tables for Reference Solar Spectral Irradiances: Direct Normal and Hemispherical on 37 Tilted Surface, ASTM International, https://doi.org/10.1520/G0173-03R20.
[159] A. Grosjean, Etude, modélisation et optimisation de surfaces fonctionnelles pour les collecteurs solaires thermiques à concentration, These de doctorat, Perpignan, 2018. http://www.theses.fr/2018PERP0002 (accessed July 15, 2020).
[160] R. Reoyo-Prats, A. Carling Plaza, O. Faugeroux, B. Claudet, A. Soum-Glaude, C. Hildebrandt, Y. Binyamin, A. Agüero, T. Meißner, Accelerated aging of absorber coatings for CSP receivers under real high solar flux – Evolution of their optical properties, Solar Energy Materials and Solar Cells. 193 (2019) 92–100. https://doi.org/10.1016/j.solmat.2018.12.030.

[161] A. Soum-Glaude, A. Le Gal, stolarz, On aging protocols for estimating thermal stability and durability of high temperature solar selective coatings, 21th Conference on Concentrating Solar Power and Chemical Energy Systems (SolarPACES 2015). (2015).
[162] I.G. Wright, R.B. Dooley, A review of the oxidation behaviour of structural alloys in steam, International Materials Reviews. 55 (2010) 129–167. https://doi.org/10.1179/095066010X12646898728165.
[163] L.C. Olson, J.W. Ambrosek, K. Sridharan, M.H. Anderson, T.R. Allen, Materials corrosion in molten LiF–NaF–KF salt, Journal of Fluorine Chemistry. 130 (2009) 67–73. https://doi.org/10.1016/j.jfluchem.2008.05.008.
[164] K.L. Summers, D. Chidambaram, Corrosion Behavior of Structural Materials for Potential Use in Nitrate Salts Based Solar Thermal Power Plants, J. Electrochem. Soc. 164 (2017) H5357. https://doi.org/10.1149/2.0501708jes.
[165] J.C. Vidal, N. Klammer, Molten chloride technology pathway to meet the U.S. DOE sunshot initiative with Gen3 CSP, AIP Conference Proceedings. 2126 (2019) 080006. https://doi.org/10.1063/1.5117601.
[166] H. Nakajima, M. Koiwa, Diffusion in Titanium, ISIJ International. 31 (1991) 757–766. https://doi.org/10.2355/isijinternational.31.757.
[167] M. Kotilainen, K. Mizohata, M. Honkanen, P. Vuoristo, Influence of microstructure on temperature-induced ageing mechanisms of different solar absorber coatings, Solar Energy Materials and Solar Cells. 120 (2014) 462–472. https://doi.org/10.1016/j.solmat.2013.09.026.
[168] H.D. Liu, Q. Wan, Y.R. Xu, C. luo, Y.M. Chen, D.J. Fu, F. Ren, G. Luo, X.D. Cheng, X.J. Hu, B. Yang, Long-term thermal stability of CrAlO-based solar selective absorbing coating in elevated temperature air, Solar Energy Materials and Solar Cells. 134 (2015) 261–267. https://doi.org/10.1016/j.solmat.2014.12.009.
[169] F. Cao, D. Kraemer, T. Sun, Y. Lan, G. Chen, Z. Ren, Enhanced Thermal Stability of W-Ni-Al2O3 Cermet-Based Spectrally Selective Solar Absorbers with Tungsten Infrared Reflectors, Advanced Energy Materials. 5 (2015) 1401042. https://doi.org/10.1002/aenm.201401042.
[170] J. Gao, X. Wang, B. Yang, C. Tu, L. Liang, H. Zhang, F. Zhuge, H. Cao, Y. Zou, K. Yu, F. Xia, Y. Han, Plasmonic AgAl Bimetallic Alloy Nanoparticle/Al2O3 Nanocermet Thin Films with Robust Thermal Stability for Solar Thermal Applications, Advanced Materials Interfaces. 3 (2016) 1600248. https://doi.org/10.1002/admi.201600248.
[171] F. Cao, D. Kraemer, L. Tang, Y. Li, A.P. Litvinchuk, J. Bao, G. Chen, Z. Ren, A high-performance spectrally-selective solar absorber based on a yttria-stabilized zirconia cermet with high-temperature stability, Energy Environ. Sci. 8 (2015) 3040–3048. https://doi.org/10.1039/C5EE02066B.
[172] A. Dan, J. Jyothi, K. Chattopadhyay, H.C. Barshilia, B. Basu, Spectrally selective absorber coating of WAlN/WAlON/Al2O3 for solar thermal applications, Solar Energy Materials and Solar Cells. 157 (2016) 716–726. https://doi.org/10.1016/j.solmat.2016.07.018.
[173] A. Antonaia, M.L. Addonizio, S. Esposito, M. Ferrara, A. Castaldo, A. Guglielmo, A. D'Angelo, Adhesion and structural stability enhancement for Ag layers deposited on steel in selective solar coatings technology, Surface and Coatings Technology. 255 (2014) 96–101. https://doi.org/10.1016/j.surfcoat.2014.02.045.
[174] K.P. Sibin, S. John, H.C. Barshilia, Control of thermal emittance of stainless steel using sputtered tungsten thin films for solar thermal power applications, Solar Energy Materials and Solar Cells. 133 (2015) 1–7. https://doi.org/10.1016/j.solmat.2014.11.002.
[175] J. Małecka, Oxidation Activation Energy of Titanium Alloy Based on TiAl(γ) Intermetalic Phase, Advances in Materials Science. 18 (2018) 5–14. https://doi.org/10.1515/adms-2017-0027.
[176] C. Wagner, Beitrag zur Theorie des Anlaufvorgangs, Zeitschrift Für Physikalische Chemie. 21B (1933) 25–41. https://doi.org/10.1515/zpch-1933-2105.
[177] N. Cabrera, N.F. Mott, Theory of the oxidation of metals, Reports on Progress in Physics. 12 (1949) 163–184. https://doi.org/10.1088/0034-4885/12/1/308.

[178] S. Chevalier, P. Juzon, K. Przybylski, J.-P. Larpin, Water vapor effect on high-temperature oxidation behavior of Fe3Al intermetallics, Science and Technology of Advanced Materials. 10 (2009) 045006. https://doi.org/10.1088/1468-6996/10/4/045006.
[179] R. Kremer, W. Auer, Influence of Moisture on the oxidation of γ-TiAl, Materials and Corrosion. 48 (1997) 35–39. https://doi.org/10.1002/maco.19970480107.
[180] Z.Y. Nuru, L. Kotsedi, C.J. Arendse, D. Motaung, B. Mwakikunga, K. Roro, M. Maaza, Thermal stability of multilayered Pt-Al2O3 nanocoatings for high temperature CSP systems, Vacuum. 120 (2015) 115–120. https://doi.org/10.1016/j.vacuum.2015.02.001.
[181] X. Wang, J. Gao, H. Hu, H. Zhang, L. Liang, K. Javaid, F. Zhuge, H. Cao, L. Wang, High-temperature tolerance in WTi-Al2O3 cermet-based solar selective absorbing coatings with low thermal emissivity, Nano Energy. 37 (2017) 232–241. https://doi.org/10.1016/j.nanoen.2017.05.036.
[182] Y. Xue, C. Wang, W. Wang, Y. Liu, Y. Wu, Y. Ning, Y. Sun, Spectral properties and thermal stability of solar selective absorbing AlNi–Al2O3 cermet coating, Solar Energy. 96 (2013) 113–118. https://doi.org/10.1016/j.solener.2013.07.012.
[183] Y. Xue, C. Wang, Y. Sun, W. Wang, Y. Wu, Y. Ning, Preparation and spectral properties of solar selective absorbing MoSi2–Al2O3 coating, Physica Status Solidi (a). 211 (2014) 1519–1524. https://doi.org/10.1002/pssa.201330658.
[184] X.-H. Gao, C.-B. Wang, Z.-M. Guo, Q.-F. Geng, W. Theiss, G. Liu, Structure, optical properties and thermal stability of Al2O3-WC nanocomposite ceramic spectrally selective solar absorbers, Optical Materials. 58 (2016) 219–225. https://doi.org/10.1016/j.optmat.2016.05.037.
[185] X. Duan, X. Zhang, C. Ke, S. Jiang, X. Wang, S. Li, W. Guo, X. Cheng, Microstructure and optical properties of Co-WC-Al2O3 duplex ceramic metal-dielectric solar selective absorbing coating prepared by high velocity oxy-fuel spraying and sol-gel method, Vacuum. 145 (2017) 209–216. https://doi.org/10.1016/j.vacuum.2017.09.002.
[186] X.-H. Gao, H.-X. Guo, T.-H. Zhou, G. Liu, Optical properties and failure analysis of ZrC-ZrOx ceramic based spectrally selective solar absorbers deposited at a high substrate temperature, Solar Energy Materials and Solar Cells. 176 (2018) 93–99. https://doi.org/10.1016/j.solmat.2017.11.018.
[187] C. Zou, W. Xie, L. Shao, Functional multi-layer solar spectral selective absorbing coatings of AlCrSiN/AlCrSiON/AlCrO for high temperature applications, Solar Energy Materials and Solar Cells. 153 (2016) 9–17. https://doi.org/10.1016/j.solmat.2016.04.007.
[188] D. Hernández-Pinilla, A. Rodríguez-Palomo, L. Álvarez-Fraga, E. Céspedes, J.E. Prieto, A. Muñoz-Martín, C. Prieto, MoSi2–Si3N4 absorber for high temperature solar selective coating, Solar Energy Materials and Solar Cells. 152 (2016) 141–146. https://doi.org/10.1016/j.solmat.2016.04.001.
[189] C. Zou, L. Huang, J. Wang, S. Xue, Effects of antireflection layers on the optical and thermal stability properties of a spectrally selective CrAlN–CrAlON based tandem absorber, Solar Energy Materials and Solar Cells. 137 (2015) 243–252. https://doi.org/10.1016/j.solmat.2015.02.010.
[190] J. Feng, S. Zhang, Y. Lu, H. Yu, L. Kang, X. Wang, Z. Liu, H. Ding, Y. Tian, J. Ouyang, The spectral selective absorbing characteristics and thermal stability of SS/TiAlN/TiAlSiN/Si3N4 tandem absorber prepared by magnetron sputtering, Solar Energy. 111 (2015) 350–356. https://doi.org/10.1016/j.solener.2014.11.005.
[191] X.-H. Gao, Z.-M. Guo, Q.-F. Geng, P.-J. Ma, A.-Q. Wang, G. Liu, Enhanced optical properties of TiN-based spectrally selective solar absorbers deposited at a high substrate temperature, Solar Energy Materials and Solar Cells. 163 (2017) 91–97. https://doi.org/10.1016/j.solmat.2017.01.023.
[192] H.C. Barshilia, N. Selvakumar, G. Vignesh, K.S. Rajam, A. Biswas, Optical properties and thermal stability of pulsed-sputter-deposited AlxOy/Al/AlxOy multilayer absorber coatings, Solar Energy Materials and Solar Cells. 93 (2009) 315–323. https://doi.org/10.1016/j.solmat.2008.11.005.
[193] S. Khamlich, R. McCrindle, Z.Y. Nuru, N. Cingo, M. Maaza, Annealing effect on the structural and optical properties of Cr/α-Cr2O3 monodispersed particles based solar absorbers, Applied Surface Science. 265 (2013) 745–749. https://doi.org/10.1016/j.apsusc.2012.11.099.

[194] D. Ngoue, Nanocomposites en revêtement déposé par technologie plasma pour la conversion de l'énergie solaire, Thesis, Université de Perpignan, 2021. http://www.theses.fr/s237939.
[195] K. Niranjan, P. Kondaiah, G. Srinivas, H.C. Barshilia, Optimization of W/WAlSiN/SiON/SiO2 tandem absorber consisting of double layer anti-reflection coating with broadband absorption in the solar spectrum region, Applied Surface Science. 496 (2019) 143651. https://doi.org/10.1016/j.apsusc.2019.143651.
[196] A. Anders, A structure zone diagram including plasma-based deposition and ion etching, Thin Solid Films. 518 (2010) 4087–4090. https://doi.org/10.1016/j.tsf.2009.10.145.
[197] Z. Ke, D. Miao, H. Lei, M. Jianping, W. Jining, L. Xiaopeng, D. Zhejun, M. Jie, Z. Bo, Thermal stability test and ageing mechanisms study of different solar selective absorbing coatings, Surface and Coatings Technology. 323 (2017) 65–71. https://doi.org/10.1016/j.surfcoat.2016.08.092.
[198] Engineering Materials 1 - 5th Edition. https://www.elsevier.com/books/engineering-materials-1/jones/978-0-08-102051-7 (accessed February 19, 2021).
[199] K.D. Bouzakis, M. Pappa, G. Skordaris, E. Bouzakis, S. Gerardis, Correlation between PVD coating strength properties and impact resistance at ambient and elevated temperatures, Surface and Coatings Technology. 205 (2010) 1481–1485. https://doi.org/10.1016/j.surfcoat.2010.07.055.
[200] M.M.M. Bilek, D.R. McKenzie, A comprehensive model of stress generation and relief processes in thin films deposited with energetic ions, Surface and Coatings Technology. 200 (2006) 4345–4354. https://doi.org/10.1016/j.surfcoat.2005.02.161.
[201] Y. Gorash, D. MacKenzie, On cyclic yield strength in definition of limits for characterisation of fatigue and creep behaviour, Open Engineering. 7 (2017) 126–140. https://doi.org/10.1515/eng-2017-0019.
[202] M. Laporte-Azcué, P.A. González-Gómez, M.R. Rodríguez-Sánchez, D. Santana, Deflection and stresses in solar central receivers, Solar Energy. 195 (2020) 355–368. https://doi.org/10.1016/j.solener.2019.11.066.
[203] T. Conroy, M.N. Collins, R. Grimes, A review of steady-state thermal and mechanical modelling on tubular solar receivers, Renewable and Sustainable Energy Reviews. 119 (2020) 109591. https://doi.org/10.1016/j.rser.2019.109591.
[204] Z. Wan, J. Fang, N. Tu, J. Wei, M.A. Qaisrani, Numerical study on thermal stress and cold startup induced thermal fatigue of a water/steam cavity receiver in concentrated solar power (CSP) plants, Solar Energy. 170 (2018) 430–441. https://doi.org/10.1016/j.solener.2018.05.087.
[205] P.A. González-Gómez, M.R. Rodríguez-Sánchez, M. Laporte-Azcué, D. Santana, Calculating molten-salt central-receiver lifetime under creep-fatigue damage, Solar Energy. 213 (2021) 180–197. https://doi.org/10.1016/j.solener.2020.11.033.
[206] J.F. Torres, I. Ellis, J. Coventry, Degradation mechanisms and non-linear thermal cycling effects in a high-temperature light-absorber coating, Solar Energy Materials and Solar Cells. 218 (2020) 110719. https://doi.org/10.1016/j.solmat.2020.110719.
[207] Y. Lalau, O. Faugeroux, E. Guillot, D. Andre, M. Huger, A. Proust, T. Chotard, B. Claudet, IMPACT: A novel device for in-situ thermo-mechanical investigation of materials under concentrated sunlight, Solar Energy Materials and Solar Cells. 172 (2017) 59–65. https://doi.org/10.1016/j.solmat.2017.07.002.
[208] Y. Lalau, O. Faugeroux, B. Claudet, E. Guillot, D. Andre, M. Huger, A. Proust, T. Chotard, A method for experimental thermo-mechanical aging of materials submitted to concentrated solar irradiation, Solar Energy Materials and Solar Cells. 192 (2019) 161–169. https://doi.org/10.1016/j.solmat.2018.12.017.
[209] D. Chen, A. Crisci, R. Boichot, J. Colas, L. Charpentier, M. Balat-Pichelin, M. Pons, F. Mercier, Modeling multilayer coating systems in solar receivers, Surface and Coatings Technology. 399 (2020) 126102. https://doi.org/10.1016/j.surfcoat.2020.126102.
[210] C.M. Koller, R. Hollerweger, C. Sabitzer, R. Rachbauer, S. Kolozsvári, J. Paulitsch, P.H. Mayrhofer, Thermal stability and oxidation resistance of arc evaporated TiAlN, TaAlN, TiAlTaN, and TiAlN/TaAlN coatings, Surface and Coatings Technology. 259 (2014) 599–607. https://doi.org/10.1016/j.surfcoat.2014.10.024.

[211] F. Montero-Chacón, S. Zaghi, R. Rossi, E. García-Pérez, I. Heras-Pérez, X. Martínez, S. Oller, M. Doblaré, Multiscale thermo-mechanical analysis of multi-layered coatings in solar thermal applications, Finite Elements in Analysis and Design. 127 (2017) 31–43. https://doi.org/10.1016/j.finel.2016.12.006.
[212] A.R. Shugurov, M.S. Kazachenok, Mechanical properties and tribological behavior of magnetron sputtered TiAlN/TiAl multilayer coatings, Surface and Coatings Technology. 353 (2018) 254–262. https://doi.org/10.1016/j.surfcoat.2018.09.001.
[213] A. Mège-Revil, P. Steyer, S. Cardinal, G. Thollet, C. Esnouf, P. Jacquot, B. Stauder, Correlation between thermal fatigue and thermomechanical properties during the oxidation of multilayered TiSiN nanocomposite coatings synthesized by a hybrid physical/chemical vapour deposition process, Thin Solid Films. 518 (2010) 5932–5937. https://doi.org/10.1016/j.tsf.2010.05.092.
[214] O.U.O. Mota, R.A. Araujo, H. Wang, T. Çağın, Mechanical Properties of Metal Nitrides for Radiation Resistant Coating Applications: A DFT Study, Physics Procedia. 66 (2015) 576–585. https://doi.org/10.1016/j.phpro.2015.05.077.
[215] C. Ho, A. Mahoney, A. Ambrosini, M. Bencomo, A. Hall, T. Lambert, Characterization of Pyromark 2500 Paint for High-Temperature Solar Receivers, 2012. https://doi.org/10.1115/ES2012-91374.
[216] C.K. Ho, J.E. Pacheco, Levelized Cost of Coating (LCOC) for selective absorber materials, Solar Energy. 108 (2014) 315–321. https://doi.org/10.1016/j.solener.2014.05.017.
[217] N. Birks, G.H. Meier, F.S. Pettit, Introduction to the High Temperature Oxidation of Metals, Cambridge University Press, 2006.
[218] J. Yao, Y. He, D. Wang, J. Lin, High-temperature oxidation resistance of (Al2O3–Y2O3)/(Y2O3-stabilized ZrO2) laminated coating on 8Nb–TiAl alloy prepared by a novel spray pyrolysis, Corrosion Science. 80 (2014) 19–27. https://doi.org/10.1016/j.corsci.2013.08.029.
[219] B. Gorr, L. Wang, S. Burk, M. Azim, S. Majumdar, H.-J. Christ, D. Mukherji, J. Rösler, D. Schliephake, M. Heilmaier, High-temperature oxidation behavior of Mo–Si–B-based and Co–Re–Cr-based alloys, Intermetallics. 48 (2014) 34–43. https://doi.org/10.1016/j.intermet.2013.10.008.
[220] D. Ghosh, S. Mukherjee, S. Das, High temperature oxidation behaviour of yttria (Y2O3) coated low alloy steel, Surface Engineering. 30 (2014) 524–528. https://doi.org/10.1179/1743294414Y.0000000271.
[221] B.A. Pint, K.A. Unocic, K.A. Terrani, Effect of steam on high temperature oxidation behaviour of alumina-forming alloys, Materials at High Temperatures. 32 (2015) 28–35. https://doi.org/10.1179/0960340914Z.00000000058.
[222] D.S. Aydin, Z. Bayindir, M.O. Pekguleryuz, The high temperature oxidation behavior of Mg–Nd alloys. Part II: The effect of the two-phase microstructure on the on-set of oxidation and on oxide morphology, Journal of Alloys and Compounds. 584 (2014) 558–565. https://doi.org/10.1016/j.jallcom.2013.09.110.
[223] G.W. Meetham, M.H.V. de Voorde, Materials for High Temperature Engineering Applications, Springer-Verlag, Berlin Heidelberg, 2000. https://doi.org/10.1007/978-3-642-56938-8.
[224] A. Boubault, C.K. Ho, A. Hall, T.N. Lambert, A. Ambrosini, Durability of solar absorber coatings and their cost-effectiveness, Solar Energy Materials and Solar Cells. 166 (2017) 176–184. https://doi.org/10.1016/j.solmat.2017.03.010.
[225] L. Rebouta, A. Sousa, P. Capela, M. Andritschky, P. Santilli, A. Matilainen, K. Pischow, N.P. Barradas, E. Alves, Solar selective absorbers based on Al2O3:W cermets and AlSiN/AlSiON layers, Solar Energy Materials and Solar Cells. 137 (2015) 93–100. https://doi.org/10.1016/j.solmat.2015.01.029.
[226] D. Dias, L. Rebouta, P. Costa, A. Al-Rjoub, M. Benelmeki, C.J. Tavares, N.P. Barradas, E. Alves, P. Santilli, K. Pischow, Optical and structural analysis of solar selective absorbing coatings based on AlSiOx:W cermets, Solar Energy. 150 (2017) 335–344. https://doi.org/10.1016/j.solener.2017.04.055.
[227] X. Wang, X. Zhang, Q. Li, J. Min, X. Cheng, Spectral properties of AlCrNO-based multi-layer solar selective absorbing coating during the initial stage of thermal aging upon exposure to air, Solar

Energy Materials and Solar Cells. 188 (2018) 81–92. https://doi.org/10.1016/j.solmat.2018.08.008.
[228] M. Bilokur, A.R. Gentle, M.D. Arnold, M.B. Cortie, G.B. Smith, High temperature optically stable spectrally-selective Ti1-xAlxN-based multilayer coating for concentrated solar thermal applications, Solar Energy Materials and Solar Cells. 200 (2019) 109964. https://doi.org/10.1016/j.solmat.2019.109964.
[229] J. Meng, R. Guo, H. Li, L. Zhao, X. Liu, Z. Li, Microstructure and thermal stability of Cu/Zr0.3Al0.7N/Zr0.2Al0.8N/Al34O60N6 cermet-based solar selective absorbing coatings, Applied Surface Science. 440 (2018) 932–938. https://doi.org/10.1016/j.apsusc.2018.01.268.
[230] N. Selvakumar, K. Rajaguru, G.M. Gouda, H.C. Barshilia, AlMoN based spectrally selective coating with improved thermal stability for high temperature solar thermal applications, Solar Energy. 119 (2015) 114–121. https://doi.org/10.1016/j.solener.2015.06.047.
[231] N. Selvakumar, A. Biswas, K. Rajaguru, G.M. Gouda, H.C. Barshilia, Nanometer thick tunable AlHfN coating for solar thermal applications: Transition from absorber to antireflection coating, Solar Energy Materials and Solar Cells. 137 (2015) 219–226. https://doi.org/10.1016/j.solmat.2015.02.008.
[232] Y. Wu, C. Wang, Y. Sun, Y. Ning, Y. Liu, Y. Xue, W. Wang, S. Zhao, E. Tomasella, A. Bousquet, Study on the thermal stability of Al/NbTiSiN/NbTiSiON/SiO2 solar selective absorbing coating, Solar Energy. 119 (2015) 18–28. https://doi.org/10.1016/j.solener.2015.06.021.
[233] J. Feng, S. Zhang, X. Liu, H. Yu, H. Ding, Y. Tian, J. Ouyang, Solar selective absorbing coatings TiN/TiSiN/SiN prepared on stainless steel substrates, Vacuum. 121 (2015) 135–141. https://doi.org/10.1016/j.vacuum.2015.08.013.
[234] Y. Ning, W. Wang, L. Wang, Y. Sun, P. Song, H. Man, Y. Zhang, B. Dai, J. Zhang, C. Wang, Y. Zhang, S. Zhao, E. Tomasella, A. Bousquet, J. Cellier, Optical simulation and preparation of novel Mo/ZrSiN/ZrSiON/SiO2 solar selective absorbing coating, Solar Energy Materials and Solar Cells. 167 (2017) 178–183. https://doi.org/10.1016/j.solmat.2017.04.017.
[235] C. Zou, W. Xie, L. Shao, Functional multi-layer solar spectral selective absorbing coatings of AlCrSiN/AlCrSiON/AlCrO for high temperature applications, Solar Energy Materials and Solar Cells. 153 (2016) 9–17. https://doi.org/10.1016/j.solmat.2016.04.007.
[236] A. AL-Rjoub, L. Rebouta, P. Costa, N.P. Barradas, E. Alves, P.J. Ferreira, K. Abderrafi, A. Matilainen, K. Pischow, A design of selective solar absorber for high temperature applications, Solar Energy. 172 (2018) 177–183. https://doi.org/10.1016/j.solener.2018.04.052.
[237] J. Jyothi, H. Chaliyawala, G. Srinivas, H.S. Nagaraja, H.C. Barshilia, Design and fabrication of spectrally selective TiAlC/TiAlCN/TiAlSiCN/TiAlSiCO/TiAlSiO tandem absorber for high-temperature solar thermal power applications, Solar Energy Materials and Solar Cells. 140 (2015) 209–216. https://doi.org/10.1016/j.solmat.2015.04.018.
[238] Y. Liu, Z. Wang, D. Lei, C. Wang, A new solar spectral selective absorbing coating of SS–(Fe3O4)/Mo/TiZrN/TiZrON/SiON for high temperature application, Solar Energy Materials and Solar Cells. 127 (2014) 143–146. https://doi.org/10.1016/j.solmat.2014.04.014.
[239] P. Song, Y. Wu, L. Wang, Y. Sun, Y. Ning, Y. Zhang, B. Dai, E. Tomasella, A. Bousquet, C. Wang, The investigation of thermal stability of Al/NbMoN/NbMoON/SiO2 solar selective absorbing coating, Solar Energy Materials and Solar Cells. 171 (2017) 253–257. https://doi.org/10.1016/j.solmat.2017.06.056.
[240] M. Bichotte, T. Kämpfe, W. Iff, F. Celle, S. Reynaud, D. Jamon, T. Pouit, A. Soum-Glaude, A. Keilany, L. Dubost, Y. Jourlin, Diffractive gratings to improve TiAlN based spectrally selective solar absorbers, in: Santiago, Chile, 2018: p. 040007. https://doi.org/10.1063/1.5067043.
[241] F. Cao, L. Tang, Y. Li, A.P. Litvinchuk, J. Bao, Z. Ren, A high-temperature stable spectrally-selective solar absorber based on cermet of titanium nitride in SiO2 deposited on lanthanum aluminate, Solar Energy Materials and Solar Cells. 160 (2017) 12–17. https://doi.org/10.1016/j.solmat.2016.10.012.
[242] K. Niranjan, A. Soum-Glaude, A. Carling-Plaza, S. Bysakh, S. John, H.C. Barshilia, Extremely high temperature stable nanometric scale multilayer spectrally selective absorber coating: Emissivity

measurements at elevated temperatures and a comprehensive study on ageing mechanism, Solar Energy Materials and Solar Cells. 221 (2021) 110905. https://doi.org/10.1016/j.solmat.2020.110905.
[243] J. Barriga, U. Ruiz-de-Gopegui, J. Goikoetxea, B. Coto, H. Cachafeiro, Selective Coatings for New Concepts of Parabolic Trough Collectors, Energy Procedia. 49 (2014) 30–39. https://doi.org/10.1016/j.egypro.2014.03.004.
[244] B. Carlsson, M. Koehl, U. Frei, K. Moeller, Accelerated life testing of solar energy materials: Case study of some selective solar absorber coating materials for DHW systems. A report of task 10 solar materials research and development, NASA STI/Recon Technical Report N. 95 (1994). http://adsabs.harvard.edu/abs/1994STIN...9522362C (accessed July 23, 2020).
[245] M. Köhl, K. Gindele, U. Frei, T. Häuselmann, Accelerated ageing test procedures for selective absorber coatings including lifetime estimation and comparison with outdoor test results, Solar Energy Materials. 19 (1989) 257–313. https://doi.org/10.1016/0165-1633(89)90011-7.
[246] S. Brunold, U. Frei, B. Carlsson, K. Möller, M. Köhl, Accelerated life testing of solar absorber coatings:: Testing procedure and results, Solar Energy. 68 (2000) 313–323. https://doi.org/10.1016/S0038-092X(00)00034-7.
[247] B. Carlsson, K. Moeller, U. Frei, M. Koehl, Accelerated life testing of solar absorber coatings, in: Optical Materials Technology for Energy Efficiency and Solar Energy Conversion XIII, International Society for Optics and Photonics, 1994: pp. 79–90. https://doi.org/10.1117/12.185359.
[248] R. Gampp, P. Oelhafen, P. Gantenbein, S. Brunold, U. Frei, Accelerated aging tests of chromium containing amorphous hydrogenated carbon coatings for solar collectors, Solar Energy Materials and Solar Cells. 54 (1998) 369–377. https://doi.org/10.1016/S0927-0248(98)00088-9.
[249] M. Koehl, Durability of solar energy materials, Renewable Energy. 24 (2001) 597–607. https://doi.org/10.1016/S0960-1481(01)00046-5.
[250] B. Carlsson, K. Möller, U. Frei, S. Brunold, M. Köhl, Comparison between predicted and actually observed in-service degradation of a nickel pigmented anodized aluminium absorber coating for solar DHW systems, Solar Energy Materials and Solar Cells. 61 (2000) 223–238. https://doi.org/10.1016/S0927-0248(99)00112-9.
[251] B. Carlsson, K. Möller, M. Köhl, U. Frei, S. Brunold, Qualification test procedure for solar absorber surface durability, Solar Energy Materials and Solar Cells. 61 (2000) 255–275. https://doi.org/10.1016/S0927-0248(99)00111-7.
[252] BS EN 12975-1:2006+A1:2010 - Thermal solar systems and components. Solar collectors. General requirements – BSI British Standards. https://shop.bsigroup.com/en/ProductDetail/?pid=000000000030216715 (accessed September 14, 2020).
[253] A. Soum-Glaude, A. Le Gal, M. Bichotte, L. Dubost, Thermal stability and durability studies of tandem TiAlN high temperature solar selective coatings, 22th Conference on Concentrating Solar Power and Chemical Energy Systems (SolarPACES 2016). (2016).
[254] M. Arntzen, S. Dreyer, J. Specht, T. Kuckelkorn, M. Schmidt, A. Sauerborn, Accelerated Ageing Tests on Schott PTR 70 HCE, SolarPACES, 2011.
[255] N.E. Dowling, Mechanical behavior of materials : engineering methods for deformation, fracture, and fatigue, CERN Document Server. (2012). https://cds.cern.ch/record/2064030 (accessed October 28, 2020).
[256] ASM Handbook, Volume 19: Fatigue and Fracture - ASM International. https://www.asminternational.org/search/-/journal_content/56/10192/25656855/PUBLICATION (accessed October 28, 2020).
[257] S.S. Manson, Behavior of Materials Under Conditions of Thermal Stress, National Advisory Committee for Aeronautics, 1953.
[258] L. Noč, E. Šest, G. Kapun, F. Ruiz-Zepeda, Y. Binyamin, F. Merzel, I. Jerman, High-solar-absorptance CSP coating characterization and reliability testing with isothermal and cyclic loads for service-life prediction, Energy Environ. Sci. 12 (2019) 1679–1694. https://doi.org/10.1039/C8EE03536A.

[259] P. Hartrott, M. Schlesinger, R. Uhlig, J. Jedamski, Fatigue life prediction on ni-base thermal solar receiver tubes, in: 2010.
[260] F. Sutter, A. Fernández-García, P. Heller, K. Anderson, G. Wilson, M. Schmücker, P. Marvig, Durability Testing of Silvered-Glass Mirrors, Energy Procedia. 69 (2015) 1568–1577. https://doi.org/10.1016/j.egypro.2015.03.110.
[261] F. Sutter, J. Wette, F. Wiesinger, A. Fernández-García, S. Ziegler, R. Dasbach, Lifetime prediction of aluminum solar mirrors by correlating accelerated aging and outdoor exposure experiments, Solar Energy. 174 (2018) 149–163. https://doi.org/10.1016/j.solener.2018.09.006.
[262] A. Grosjean, E. Le Baron, A.-C. Pescheux, A. Disdier, Accelerated aging tests and characterizations of solar mirrors: Comparison of combinations of stress factors on degradation, Solar Energy Materials and Solar Cells. 220 (2021) 110851. https://doi.org/10.1016/j.solmat.2020.110851.
[263] H. Chen, W. Gao, T. Liu, W. Lin, M. Li, An experimental study on the effect of salt spray testing on the optical properties of solar selective absorber coatings produced with different manufacturing technologies, Int J Energy Environ Eng. 10 (2019) 231–242. https://doi.org/10.1007/s40095-019-0299-7.
[264] B. Carlsson, K. Möller, M. Köhl, M. Heck, S. Brunold, U. Frei, J.-C. Marechal, G. Jorgensen, The applicability of accelerated life testing for assessment of service life of solar thermal components, Solar Energy Materials and Solar Cells. 84 (2004) 255–274. https://doi.org/10.1016/j.solmat.2004.01.046.
[265] N.C. Park, W.W. Oh, D.H. Kim, Effect of Temperature and Humidity on the Degradation Rate of Multicrystalline Silicon Photovoltaic Module, International Journal of Photoenergy. 2013 (2013) e925280. https://doi.org/10.1155/2013/925280.
[266] D.S. Peck, Comprehensive Model for Humidity Testing Correlation, in: 24th International Reliability Physics Symposium, 1986: pp. 44–50. https://doi.org/10.1109/IRPS.1986.362110.
[267] A. Boubault, Etude du vieillissement de matériaux sous haut flux solaire concentré – Application aux récepteurs surfaciques des centrales solaires thermodynamiques, These en préparation, Perpignan, 2009. http://www.theses.fr/s83622 (accessed July 15, 2020).
[268] A. Boubault, B. Claudet, O. Faugeroux, G. Olalde, Aging of solar absorber materials under highly concentrated solar fluxes, Solar Energy Materials and Solar Cells. 123 (2014) 211–219. https://doi.org/10.1016/j.solmat.2014.01.010.
[269] N. Djohan, R. Estrada, D. Sari, M. Dahrul, A. Kurniawan, J. Iskandar, H. Hardhienata, Irzaman, The effect of annealing temperature variation on the optical properties test of LiTaO3 thin films based on Tauc Plot method for satellite technology, IOP Conf. Ser.: Earth Environ. Sci. 54 (2017) 012093. https://doi.org/10.1088/1755-1315/54/1/012093.
[270] A. Srinivasa Rao, S. Sakthivel, A highly thermally stable Mn–Cu–Fe composite oxide based solar selective absorber layer with low thermal loss at high temperature, Journal of Alloys and Compounds. 644 (2015) 906–915. https://doi.org/10.1016/j.jallcom.2015.05.038.
[271] M. Berenguel, E.F. Camacho, F.J. Garcia-Martin, F.R. Rubio, Temperature control of a solar furnace, IEEE Control Systems Magazine. 19 (1999) 8–24. https://doi.org/10.1109/37.745762.
[272] B. Andrade da Costa, J.M. Lemos, An adaptive temperature control law for a solar furnace, Control Engineering Practice. 17 (2009) 1157–1173. https://doi.org/10.1016/j.conengprac.2009.05.001.
[273] W. Wang, B. Laumert, Simulate a 'Sun' for Solar Research : A Literature Review of Solar Simulator Technology, KTH Royal Institute of Technology, 2014. http://urn.kb.se/resolve?urn=urn:nbn:se:kth:diva-154262 (accessed June 19, 2020).
[274] R.T. Hollingsworth, A SURVEY OF LARGE SPACE CHAMBERS, 15.
[275] R.P. Eddy, Design and construction of the 15-ft-beam solar simulator SS15B, 1968. https://ntrs.nasa.gov/search.jsp?R=19690008610 (accessed July 30, 2020).
[276] R. BARNETT, C. THIELE, Jpl advanced solar simulator design type a(Advanced solar simulator-space environment reproduction), (1963).

[277] P. Kuhn, A. Hunt, A new solar simulator to study high temperature solid-state reactions with highly concentrated radiation, Solar Energy Materials. 24 (1991) 742–750. https://doi.org/10.1016/0165-1633(91)90107-V.
[278] D.S. Codd, A. Carlson, J. Rees, A.H. Slocum, A low cost high flux solar simulator, Solar Energy. 84 (2010) 2202–2212. https://doi.org/10.1016/j.solener.2010.08.007.
[279] Hirsch, A. Zedtwitz, T. Osinga, J. Kinamore, A. Steinfeld, A New 75 kW High-Flux Solar Simulator for High-Temperature Thermal and Thermochemical Research, J. Sol. Energy Eng. 125 (2003) 117–120. https://doi.org/10.1115/1.1528922.
[280] J. Petrasch, A. Steinfeld, A Novel High-Flux Solar Simulator Based on an Array of Xenon Arc Lamps: Optimization of the Ellipsoidal Reflector and Optical Configuration, in: American Society of Mechanical Engineers Digital Collection, 2008: pp. 175–180. https://doi.org/10.1115/ISEC2005-76009.
[281] I. Alxneit, G. Dibowski, R12. 5 solar simulator evaluation report, Solar Facilities for the European Research Area Project, European Union, Brussels, Belgium, Deliverable. 12 (2011).
[282] K.R. Krueger, J.H. Davidson, W. Lipiński, Design of a New 45 kWe High-Flux Solar Simulator for High-Temperature Solar Thermal and Thermochemical Research, J. Sol. Energy Eng. 133 (2011). https://doi.org/10.1115/1.4003298.
[283] C. Dominguez, I. Anton, G. Sala, Solar simulator for indoor characterization of large area high-concentration PV modules, in: 2008 33rd IEEE Photovoltaic Specialists Conference, 2008: pp. 1–5. https://doi.org/10.1109/PVSC.2008.4922739.
[284] An experimental study on the effect of salt spray testing on the optical properties of solar selective absorber coatings produced with different manufacturing technologies | SpringerLink. https://link.springer.com/article/10.1007/s40095-019-0299-7 (accessed November 9, 2020).
[285] O. Raccurt, A. Disdier, Accelerated ageing tests for durability study of solar absorber coatings on metallic substrate for solar thermal energy (STE) application, 9.
[286] Durasol, DURASOL, DURASOL. https://www.durasol.fr/https://www.durasol.fr (accessed January 18, 2021).
[287] IEC 62108:2016 | IEC Webstore | rural electrification, solar panel, photovoltaic, PV, solar power, electricity, LVDC. https://webstore.iec.ch/publication/25938 (accessed January 18, 2021).
[288] IEC 61215-1:2016 | IEC Webstore | rural electrification, solar power, solar panel, photovoltaic, PV, smart city, LVDC. https://webstore.iec.ch/publication/24312 (accessed January 18, 2021).
[289] ISO 22975-3:2014(en), Solar energy — Collector components and materials — Part 3: Absorber surface durability. https://www.iso.org/obp/ui/#iso:std:iso:22975:-3:ed-1:v1:en (accessed November 9, 2020).
[290] F. Wiesinger, F. Sutter, F. Wolfertstetter, N. Hanrieder, A. Fernández-García, R. Pitz-Paal, M. Schmücker, Assessment of the erosion risk of sandstorms on solar energy technology at two sites in Morocco, Solar Energy. 162 (2018) 217–228. https://doi.org/10.1016/j.solener.2018.01.004.
[291] M. Bichotte, L. Dubost, T. Pouit, A. Soum-Glaude, A. Le Gal, H. Glenat, D. Itskhokine, Arc deposited TiAlN selective absorber for high temperature CSP applications, AIP Conference Proceedings. 1734 (2016) 030006. https://doi.org/10.1063/1.4949058.
[292] A. Soum-Glaude, L.D. Giacomo, S. Quoizola, T. Laurent, G. Flamant, Selective Surfaces for Solar Thermal Energy Conversion in CSP: From Multilayers to Nanocomposites, in: Nanotechnology for Energy Sustainability, John Wiley & Sons, Ltd, 2017: pp. 231–248. https://doi.org/10.1002/9783527696109.ch10.
[293] M. Bichotte, T. Kämpfe, W. Iff, F. Celle, S. Reynaud, T. Pouit, A. Soum-Glaude, A. Le Gal, L. Dubost, Y. Jourlin, High efficiency concentrated solar power plant receivers using periodic microstructured absorbing layers, Solar Energy Materials and Solar Cells. 160 (2017) 328–334. https://doi.org/10.1016/j.solmat.2016.10.027.
[294] A. Soum-Glaude, I. Bousquet, M. Bichotte, S. Quoizola, L. Thomas, G. Flamant, Optical Characterization and Modeling of Coatings Intended as High Temperature Solar Selective Absorbers, Energy Procedia. 49 (2014) 530–537. https://doi.org/10.1016/j.egypro.2014.03.057.

[295] M. Bichotte, Réalisation d'un absorbeur solaire sélectif pour centrale CSP associant dépôt en couches minces et texturation de surface, These de doctorat, Lyon, 2017. https://www.theses.fr/2017LYSES013 (accessed May 26, 2021).
[296] Energy - Ireis. https://www.ireis.fr/en/energy.html (accessed October 15, 2020).
[297] The NanoPlaST project, ANR NanoPlaST. https://nanoplast-project.cnrs.fr/ (accessed December 9, 2020).
[298] W. Münz, Titanium aluminum nitride films: A new alternative to TiN coatings, Journal of Vacuum Science & Technology A. 4 (1986) 2717–2725. https://doi.org/10.1116/1.573713.
[299] Industrial deposition of binary, ternary, and quaternary nitrides of titanium, zirconium, and aluminum: Journal of Vacuum Science & Technology A: Vol 5, No 4. https://avs.scitation.org/doi/abs/10.1116/1.574948 (accessed December 4, 2020).
[300] Oxidation of metastable single-phase polycrystalline Ti0.5Al0.5N films: Kinetics and mechanisms: Journal of Applied Physics: Vol 67, No 3. https://aip.scitation.org/doi/abs/10.1063/1.345664 (accessed December 4, 2020).
[301] High-temperature oxidation of ion-plated TiN and TiAlN films | SpringerLink. https://link.springer.com/article/10.1557/JMR.1993.1093 (accessed December 4, 2020).
[302] Y.K. Lee, K.M. Latt, T. Osipowicz, C. Sher-Yi, Study of diffusion barrier properties of ternary alloy (TixAlyNz) in Cu/TixAlyNz/SiO2/Si thin film structure, Materials Science in Semiconductor Processing. 3 (2000) 191–194. https://doi.org/10.1016/S1369-8001(00)00031-7.
[303] M.Y. Kwak, D.H. Shin, T.W. Kang, K.N. Kim, Characteristics of TiN barrier layer against Cu diffusion, Thin Solid Films. 339 (1999) 290–293. https://doi.org/10.1016/S0040-6090(98)01074-8.
[304] A. Schüler, V. Thommen, P. Reimann, P. Oelhafen, G. Francz, T. Zehnder, M. Düggelin, D. Mathys, R. Guggenheim, Structural and optical properties of titanium aluminum nitride films (Ti1−xAlxN), Journal of Vacuum Science & Technology A. 19 (2001) 922–929. https://doi.org/10.1116/1.1359532.
[305] K. Niranjan, P. Kondaiah, A. Biswas, V.P. Kumar, G. Srinivas, H.C. Barshilia, Spectrally Selective Solar Absorber Coating of W/WAlSiN/SiON/SiO2 with Enhanced Absorption through Gradation of Optical Constants: Validation by Simulation, Coatings. 11 (2021) 334. https://doi.org/10.3390/coatings11030334.
[306] Air-oxidation of nano-multilayered CrAlSiN thin films between 800 and 1000 °C - ScienceDirect, (). https://www.sciencedirect.com/science/article/pii/S0257897208009857?casa_token=j-QG7wAc8A8AAAAA:4YDuzqayHDbRPYi5k0MGuXfhY5P9z9Rngk0CVhp5DG69Q3NXL8ERw2fzGocW1VMNo72r5piQUw (accessed December 10, 2020).
[307] R.J. Lad, Multifunctional Silicon Aluminum Oxynitride (SiAlON) Ceramic Coatings for High Temperature Applications, MAINE UNIV AT ORONO LAB FOR SURFACE SCIENCE AND TECHNOLOGY, 2005. https://apps.dtic.mil/sti/citations/ADA444413 (accessed March 22, 2021).
[308] C.M. Lampert, Coatings for enhanced photothermal energy collection II. Non-selective and energy control films, Solar Energy Materials. 2 (1979) 1–17. https://doi.org/10.1016/0165-1633(79)90026-1.
[309] S. Zhao, E. Wäckelgård, Optimization of solar absorbing three-layer coatings, Solar Energy Materials and Solar Cells. 90 (2006) 243–261. https://doi.org/10.1016/j.solmat.2005.03.009.
[310] S. Meziani, A. Moussi, L. Mahiou, R. Outemzabet, Effect of thermal annealing on double anti reflection coating SiNx/SiO2, in: 2015 3rd International Renewable and Sustainable Energy Conference (IRSEC), 2015: pp. 1–5. https://doi.org/10.1109/IRSEC.2015.7454971.
[311] Magnetron sputtering facility - CSIR - NAL. https://www.nal.res.in/en/facilities/magnetron-sputtering-facility (accessed October 19, 2020).
[312] A. Fernández-García, F. Sutter, L. Martínez-Arcos, C. Sansom, F. Wolfertstetter, C. Delord, Equipment and methods for measuring reflectance of concentrating solar reflector materials, Solar Energy Materials and Solar Cells. 167 (2017) 28–52. https://doi.org/10.1016/j.solmat.2017.03.036.

[313] A. Soum-Glaude, Analyses expérimentales et simulation numérique d'un procédé PACVD pour le dépôt de couches minces à vocation mécanique, These de doctorat, Perpignan, 2006. https://www.theses.fr/2006PERP0760 (accessed March 22, 2021).
[314] K. Niranjan, A. Soum-Glaude, A. Carling-Plaza, S. Bysakh, S. John, H.C. Barshilia, Extremely high temperature stable nanometric scale multilayer spectrally selective absorber coating: Emissivity measurements at elevated temperatures and a comprehensive study on ageing mechanism, Solar Energy Materials and Solar Cells. 221 (2021) 110905. https://doi.org/10.1016/j.solmat.2020.110905.
[315] A. Boubault, B. Claudet, O. Faugeroux, G. Olalde, Accelerated Aging of a Solar Absorber Material Subjected to Highly Concentrated Solar Flux, Energy Procedia. 49 (2014) 1673–1681. https://doi.org/10.1016/j.egypro.2014.03.176.
[316] Y. Lalau, Etude du comportement thermomécanique de matériaux céramiques sous irradiation solaire concentrée : développement expérimental et modélisation, These de doctorat, Perpignan, 2017. http://www.theses.fr/2017PERP0061 (accessed July 15, 2020).
[317] R. Reoyo-Prats, Etude du vieillissement de récepteurs solaires : estimation de propriétés thermophysiques par méthode photothermique associée aux outils issus de l'intelligence artificielle, These de doctorat, Perpignan, 2020. http://www.theses.fr/2020PERP0017 (accessed January 25, 2021).
[318] R. Reoyo-Prats, A. Carling Plaza, O. Faugeroux, B. Claudet, A. Soum-Glaude, C. Hildebrandt, Y. Binyamin, A. Agüero, T. Meißner, Accelerated aging of absorber coatings for CSP receivers under real high solar flux – Evolution of their optical properties, Solar Energy Materials and Solar Cells. 193 (2019) 92–100. https://doi.org/10.1016/j.solmat.2018.12.030.
[319] J. Gum, Guide to the expression of uncertainty in measurement - Part 6: Developing and using measurement models, JCGM GUM-6:2020, 103.
[320] A. Salles, Etude du vieillissement thermique des materiaux absorbeurs pour les centrales solaires à concentration, Technical Intership PROMES-CNRS, IUT Mesures Physiques Montpellier-Sète, 2017.
[321] G. Scarel, J.-S. Na, G.N. Parsons, Angular behavior of the Berreman effect investigated in uniform Al2O3 layers formed by atomic layer deposition, J. Phys.: Condens. Matter. 22 (2010) 155401. https://doi.org/10.1088/0953-8984/22/15/155401.
[322] S. Raju, K. Sivasubramanian, R. Divakar, G. Panneerselvam, A. Banerjee, E. Mohandas, M.P. Antony, Thermal expansion studies on Inconel-600® by high temperature X-ray diffraction, Journal of Nuclear Materials. 325 (2004) 18–25. https://doi.org/10.1016/j.jnucmat.2003.10.007.
[323] Y. Okada, Y. Tokumaru, Precise determination of lattice parameter and thermal expansion coefficient of silicon between 300 and 1500 K, Journal of Applied Physics. 56 (1984) 314–320. https://doi.org/10.1063/1.333965.
[324] P.H. Richter, Estimating Errors in Least-Squares Fitting, 31.
[325] P. Panjan, B. Navinšek, M. Čekada, A. Zalar, Oxidation behaviour of TiAlN coatings sputtered at low temperature, Vacuum. 53 (1999) 127–131. https://doi.org/10.1016/S0042-207X(98)00407-2.
[326] J.-L. Huang, B.-Y. Shew, Effects of Aluminum Concentration on the Oxidation Behaviors of Reactively Sputtered TiAlN Films, Journal of the American Ceramic Society. 82 (1999) 696–704. https://doi.org/10.1111/j.1151-2916.1999.tb01819.x.
[327] M. Arntzen, S. Dreyer, J. Specht, T. Kuckelkorn, M. Schmidt, A. Sauerborn, Accelerated Ageing Tests on Schott PTR 70 HCE, (2011).
[328] J.P. Wang, B. Yuan, J. Wang, Y. Luo, Activation Energy Measurement of Cu/SS-AlN/SiAlOx Solar Selective Absorbing Coating, Materials Science Forum. 743–744 (2013) 870–877. https://doi.org/10.4028/www.scientific.net/MSF.743-744.870.
[329] R. Reoyo-Prats, A. Carling Plaza, O. Faugeroux, B. Claudet, A. Soum-Glaude, C. Hildebrandt, Y. Binyamin, A. Agüero, T. Meißner, Accelerated aging of absorber coatings for CSP receivers under real high solar flux – Evolution of their optical properties, Solar Energy Materials and Solar Cells. 193 (2019) 92–100. https://doi.org/10.1016/j.solmat.2018.12.030.

[330] K. Niranjan, A. Carling Plaza, T. Grifo, M. Bordas, A. Soum-Glaude, H.C. Barshilia, Performance evaluation and durability studies of W/WAlSiN/SiON/SiO2 based spectrally selective solar absorber coating for high-temperature applications: A comprehensive study on thermal and solar accelerated ageing, Solar Energy. 227 (2021) 457–467. https://doi.org/10.1016/j.solener.2021.09.026.
[331] B. Rousseau, J.F. Brun, D. Meneses, P. Echegut, Temperature Measurement: Christiansen Wavelength and Blackbody Reference, International Journal of Thermophysics. 26 (2005) 1277–1286. https://doi.org/10.1007/s10765-005-6726-4.
[332] D. Ngoue, (Nano)composites en revêtement déposés par technologie plasma pour la conversion de l'énergie solaire, These de doctorat, Perpignan, 2021. http://theses.fr/2021PERP0011 (accessed October 8, 2021).
[333] M. Bordas, Study of optical properties and aging of absorptive coatings for receivers of thermodynamic solar power plants, End-of-study internship report, Université de Perpignan, 2021.
[334] D. Hernandez, A. Netchaieff, A. Stein, True temperature measurement on metallic surfaces using a two-color pyroreflectometer method, Review of Scientific Instruments. 80 (2009) 094903. https://doi.org/10.1063/1.3208011.
[335] D.R. Lide, ed., CRC Handbook of Chemistry and Physics, 84th ed., CRC Press, 2004.

Annexes

1. SAAF set-up: estimation of the homogenized solar flux received by the sample

The incoming radiation in the SAAF is adjusted by the aperture of the shutters, which varies from 0 to 100%. The shutter aperture is controlled by an external voltage *V* between -5 and 5 Volts. This voltage is converted to a range from 0 to 1 with Eq.(36), to obtain the aperture percentage A_S.

$$A_S = -0.1 \cdot V + 0.5 \tag{36}$$

To calculate the output homogenized flux at the exit of the kaleidoscope placed at the focal of the parabola, calorimetric measurements were carried out in 2017. They consisted in placing a calorimeter at the exit of the kaleidoscope to measure the output flux at different shutter apertures (Figure 172).

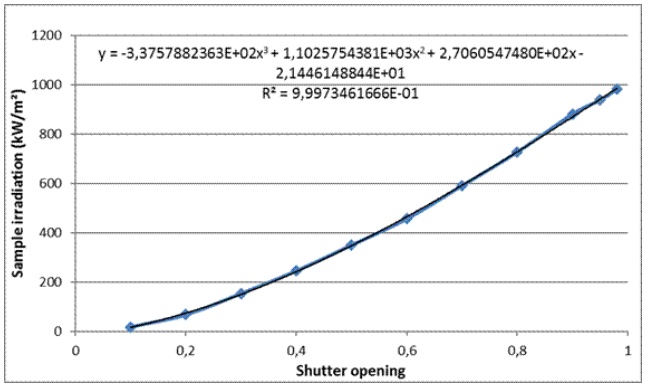

Figure 172. Sample irradiation vs shutter opening for DNI = 1000 W/m²

The results were interpolated to obtain a fitting function. This function is used to establish the aperture command needed to obtain the desired solar flux on the tested sample, placed at the output of the kaleidoscope. The output flux after the kaleidoscope is represented by Eq.(37) vs. the shutters aperture A_S, corrected with the value of Direct Normal Irradiance (DNI) during the experiment. The parameters obtained from Figure 172 are: a_0 = -21.444, a_1 = 270.60, a_2 = 1102.57, a_3 = -337.58.

$$\Phi\ (kW/m^2) = \left(\frac{DNI}{1000}\right) \cdot \left(a_0 + a_1 A_S + a_2 A_S^2 + a_3 A_S^3\right) \tag{37}$$

2. SAAF set-up: pyrometry measurements

In SAAF experimental set-up, the temperature of the surface of the sample exposed to the homogenized concentrated solar flux is measured by a pyrometer. The chosen pyrometer is an Optris CTlaser G5H equipped with CF4 optics. It allows the measurement of temperature between 250°C and 1650°C and has a spectral response in a reduced range between 4.8 and 5.2 µm (see Chapter 3 section 3.2.2.1.5, p.112). It is thus considered as monochromatic at 5 µm.

2.1. Temperature estimation

The estimation of temperature is based on Planck's law of blackbody (BB) radiation (Eq.(38)), which relates the spectral irradiance (radiant exitance) of a blackbody $M_\lambda^0(\lambda, T)$ to its temperature *T*.

$$M_\lambda^0(\lambda,T)_{BB} = \frac{2\pi hc^2}{\lambda^5 \cdot \left(e^{\frac{hc}{\lambda k_B T}} - 1\right)} = \frac{C_1}{\lambda^5 \cdot \left(e^{\frac{C_2}{\lambda T}} - 1\right)} \tag{38}$$

$$C_1 = 2\pi hc^2 = 3.742 \cdot 10^{-16}\ W \cdot m^{-2}\ ;\ C_2 = \frac{hc}{k_B} = 1.44 \cdot 10^{-2}\ m \cdot K$$

The spectral emittance $\varepsilon_\lambda(\lambda,T)$ of a sample at temperature *T* is defined as the ratio between the spectral irradiance $M_\lambda^0(\lambda,T)_{sample}$ emitted by the sample, and the spectral irradiance $M_\lambda^0(\lambda,T)_{BB}$ emitted by a blackbody at the same temperature (Eq.(39)).

$$\varepsilon(\lambda,T) \equiv \frac{M_\lambda^0(\lambda,T)_{sample}}{M_\lambda^0(\lambda,T)_{BB}} \tag{39}$$

The pyrometer detects $M_\lambda^0(\lambda,T)_{sample}$ at 5 µm. The knowledge of the sample spectral emittance $\varepsilon_\lambda(\lambda,T)$ at 5 µm gives direct access to the sample temperature *T* using Eq.(40) derived from combining Eq.(38) and Eq.(39), with λ = 5 µm.

$$T = -\frac{C_2}{\lambda} \cdot ln\left(\frac{C_1 \cdot \varepsilon_\lambda(\lambda,T)}{\lambda^5 \cdot M_\lambda^0(\lambda,T)_{sample}} + 1\right) \tag{40}$$

Thus, the pyrometer calculates the temperature of the sample surface knowing the emittance of said surface, and an emittance value must be input into the device before the measurements. The "real" spectral emittance of the sample at 5 µm can be deduced from its spectral reflectance (measured with SOC-100 reflectometer at room temperature before SAAF experiment), using Eq.(41). If this value is used as input, the pyrometer can directly estimate the sample temperature from Eq.(40).

$$E(\lambda,\theta,T) = 1 - R(\lambda,\theta,T) \tag{41}$$

However this method can be inconvenient, as the emittance input value needs to be changed each time a new sample is tested. Also, the sample emittance may evolve during the experiment during aging, leading to inaccurate temperature estimation.

It is therefore more convenient to use instead a constant approximative emittance value $\varepsilon_\lambda^{\mathrm{app}}(\lambda,T)$ as input for all samples of the same type (e.g. 0.3 for TiAlN absorbers), then later deduce the sample real temperature T_{real} by applying a correction to the temperature profile T_{app} recorded by the pyrometer. This correction considers the real emittance $\varepsilon_\lambda^{\mathrm{real}}(\lambda,T)$ of the given sample measured before the aging test, or the emittance measured after the test if it is very different from its initial value.

By design, the sample irradiance $M_\lambda^0(\lambda,T)_{sample}$ detected by the pyrometer is the same, whatever the input value of emittance. Therefore, from Eq.(38) and (39), Eq.(42) is deduced.

$$M_\lambda^0(\lambda,T)_{sample} = \varepsilon_\lambda^{\mathrm{app}}(\lambda,T) \cdot \frac{C_1}{\lambda^5 \cdot \left(e^{\frac{C_2}{\lambda T_{app}}} - 1\right)} = \varepsilon_\lambda^{\mathrm{real}}(\lambda,T) \cdot \frac{C_1}{\lambda^5 \cdot \left(e^{\frac{C_2}{\lambda T_{real}}} - 1\right)} \tag{42}$$

A temperature correction can be deduced from Eq.(42), as given by Eq.(43).

$$T_{real} = \left[\frac{\lambda}{C_2} \cdot ln\left(\frac{\varepsilon_\lambda^{\mathrm{real}}(\lambda,T)}{\varepsilon_\lambda^{\mathrm{app}}(\lambda,T)}\right) + \frac{1}{T_{app}}\right]^{-1} \tag{43}$$

Such temperature correction is illustrated in Figure 173, where T_{real} of samples with real emittance $\varepsilon_\lambda^{\mathrm{real}}(\lambda,T)$ between 0.10 and 0.20 is plotted for an approximative input emittance $\varepsilon_\lambda^{\mathrm{app}}(\lambda,T)$ = 0.15 and T_{app} detected in the range of 200 to 600°C. At low temperatures, the approximative temperature T_{app} (x-axis) remains close to the real temperature T_{real} (y-axis), by 20 to 30°C. At high temperatures the correction is indispensable, with a difference higher than 100°C between the approximative and real temperature, for a difference of only 0.05 between approximative and real emittance.

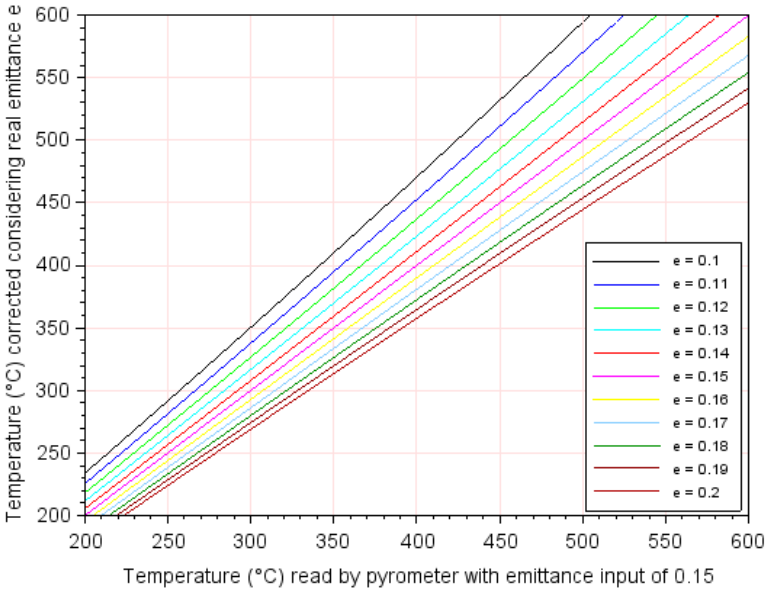

Figure 173. T_{real} vs. T_{app} at $\varepsilon_{\lambda}^{app}(\lambda, T)$ = 0.15 for different values of $\varepsilon_{\lambda}^{real}(\lambda, T)$

2.2. Pyrometer calibration

The pyrometer was calibrated in temperature using a blackbody SR-2 from ECI systems (Figure 174) with ε = 0.99 ± 0.01. The temperature of the blackbody was varied from 250 to 1150°C with a step of 50°C. Table 46 shows the temperature read by the pyrometer with input emittance of 0.98. The pyrometer gives accurate measurements, with maximum relative errors of 2-3% below 700°C.

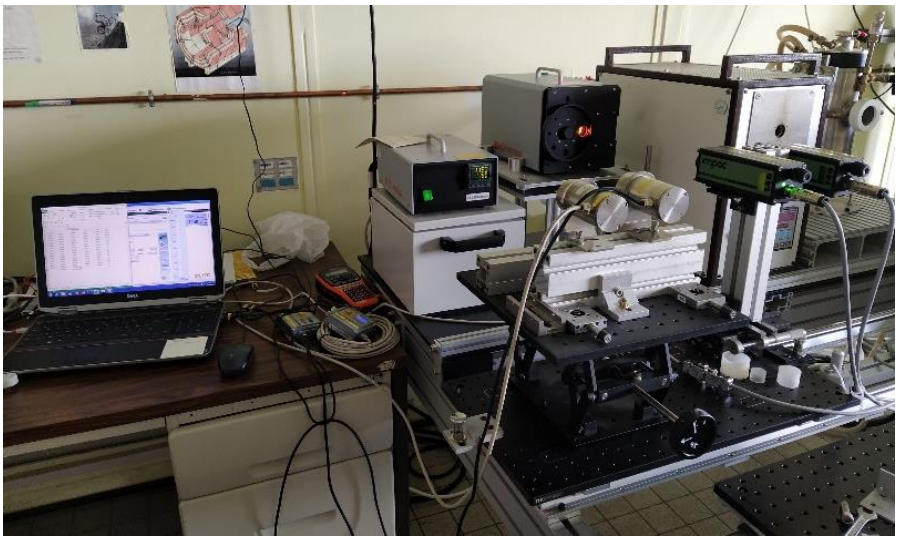

Figure 174. Pyrometer calibration set-up

Table 46. Temperature read by the pyrometer with input emittance of 0.98 vs. real temperature of detected blackbody

SR-2 blackbody T (°C) $\varepsilon = 0.99 \pm 0.01$	**Pyrometer** T (°C) $\varepsilon = 0.98$	**Absolute error with pyrometer** (°C)	**Relative error with pyrometer** (%)
250	256.3	+6.3	+2.5%
300	294.8	-5.2	-1.7%
350	342.6	-7.4	-2.1%
400	389.4	-10.6	-2.7%
450	439.0	-11	-2.4%
500	487.9	-12.1	-2.4%
550	537.2	-12.8	-2.3%
600	586.3	-13.7	-2.3%
650	637.0	-13	-2.0%
700	686.8	-13.2	-1.9%
750	737.0	-13	-1.7%
800	787.5	-12.5	-1.6%
850	838.9	-11.1	-1.3%
900	889.7	-10.3	-1.1%
950	940.5	-9.5	-1.0%
1000	992.7	-7.3	-0.7%
1050	1044.0	-6	-0.6%
1100	1097.0	-3	-0.3%
1150	1149.0	-1	-0.1%

Abstract

Concentrated solar power (CSP) plants provide renewable energy thanks to the concentration of solar irradiation by mirrors upon a solar absorber, which converts it first into heat, enabling large-scale thermal storage to mitigate solar intermittence, then into electricity. The lifetime over which performance is expected to be maintained is typically 25 to 30 years for this technology. However, the latter operates under very demanding conditions for materials (highly concentrated solar irradiance/high temperature combined with oxidant/corrosive atmospheric conditions). The main component exposed to these harsh conditions is the solar absorber, susceptible to high deterioration resulting in high sun-to-heat conversion losses. The solar absorber is often covered with a selective absorber coating, to increase the absorption of solar radiation (high solar absorptance) while reducing radiative thermal losses (low emittance). This solution is optically efficient but requires complex multilayer coating architectures which may easily suffer degradations in CSP conditions of use. It is therefore crucial to prove the durability of new solar absorber coating architectures before they can be used in CSP installations. Aging tests must be applied to study their thermal stability, reliability and potential service life. However, no standardized aging procedures for solar absorber coatings exist today. This thesis work thus provides: i) a critical review of existing aging protocols and tools, and identified aging phenomena; ii) a critical analysis of classical (purely thermal) and original (thermal + concentrated solar) aging protocols based on their experimental application to three types of new selective absorber coatings, using two unique aging tools including a solar furnace. The influence of the main sources of degradation in real CSP operation (high temperature, high concentrated solar irradiation, slow/rapid thermal cycling) is investigated and partly decorrelated, by following the evolution with aging of their optical performance, surface state and chemical composition. This work analyses the pertinence of studied aging protocols and tools, and proposes broadly applicable strategies for solar absorber coating developers.

Résumé

Les centrales solaires à concentration (CSP) fournissent une énergie renouvelable grâce à la concentration de l'irradiation solaire par des miroirs sur un absorbeur solaire, la convertissant en chaleur, stockable à grande échelle pour s'affranchir de l'intermittence solaire, puis en électricité. La durée de vie durant laquelle les performances doivent être maintenues est de 25 à 30 ans pour cette technologie. Cependant, cette dernière opère dans des conditions très exigeantes pour les matériaux (forte concentration solaire/haute température combinées à des atmosphères oxydantes/corrosives). Le composant principal exposé à ces conditions sévères est l'absorbeur solaire. Il peut se détériorer et générer de fortes pertes optiques et thermiques. Les absorbeurs solaires sont souvent recouverts d'un revêtement absorbeur sélectif augmentant l'absorption du rayonnement solaire (forte absorptance solaire) et réduisant les pertes thermiques radiatives (faible émittance). Cette solution très efficace optiquement nécessite des architectures multicouches complexes, qui peuvent se dégrader en conditions d'usage CSP. Il est donc crucial de démontrer la durabilité des nouveaux revêtements absorbeurs solaires sélectifs avant de les utiliser dans des installations CSP réelles. Des tests de vieillissement doivent être appliqués pour étudier leur stabilité thermique, leur fiabilité et leur durée de vie potentielle, mais il n'existe pas à ce jour de procédures de vieillissement standardisées pour les revêtements absorbeurs solaires. Ainsi ce travail de thèse fournit : i) une revue critique des protocoles et moyens de vieillissement existants, et des phénomènes de vieillissement identifiés ; ii) une analyse critique de protocoles de vieillissement classiques (thermiques) et originaux (thermique + solaire concentré), basée sur leur application expérimentale sur trois types de revêtements absorbeurs solaires sélectifs, grâce à deux bancs de vieillissement très originaux dont un four solaire. L'influence des sources de dégradation en conditions d'usage CSP (haute température, forte irradiation solaire concentrée, cyclage thermique lent et rapide) est investiguée et partiellement décorrélée, grâce au suivi des performances optiques, de l'état de surface et de la composition chimique des matériaux vieillis. Ce travail analyse la pertinence des protocoles et moyens de vieillissement étudiés, et tente de proposer une stratégie de vieillissement applicable pour les développeurs de revêtements absorbeurs solaires sélectifs.